INTERNATIONAL DOCTORAL
SCHOOL OF THE USC

Asier
Pereiro Castro

PhD Thesis

Search for flavour anomalies in the quark sector at the LHCb experiment

Santiago de Compostela, 2024

Doctoral Programme in Nuclear and Particles Physics

ESCOLA DE DOUTORAMENTO
INTERNACIONAL DA USC

DOCTORAL THESIS

SEARCH FOR FLAVOUR ANOMALIES IN THE QUARK SECTOR AT THE LHCB EXPERIMENT

Author

Asier Pereiro Castro

Supervisor/s: Bernardo Adeva Andany

Jeremy Peter Dalseno

Tutor: Bernardo Adeva Andany

PHD PROGRAMME IN NUCLEAR AND PARTICLE PHYSICS

SANTIAGO DE COMPOSTELA

— Hello, I am the Doctor by the way
— Doctor... who?
— Just *the Doctor*

ABSTRACT

In this thesis, a time-integrated and flavour-untagged amplitude analysis is performed to four-body decays of the neutral mesons B_s^0 and B_d^0, using data collected by the LHCb experiment during Run 1 and Run 2. Observables to be measured include the investigation of an anomaly in the polarisation of $K^{*0}(892)$ resonances when they arise from decays of B_s^0 and B_d^0 mesons, which seems to point to a break in the universality of the gluonic couplings to the different quark generations in the Standard Model.

These decay channels, besides being a reference for the study of CP-violating and T-violating observables in charmless b-quark decays, have recently been tagged by theoretical groups as the source of a flavour anomaly, which might be connected to other flavour anomalies presented by LHCb in semi-leptonic channels.

The project includes several innovations, both phenomenological and experimental. The formalism that is used to describe the intermediate states considers Lorentz invariant partial waves in the basis of angular momentum, which is more fundamental in quantum mechanics and allows centrifugal barrier factors to be coupled. The multidimensional efficiency is estimated with a new technique that considers fully simulated decays in phase space, based on a GPU-accelerated Kernel Density Estimation method. In addition, several differences between data and MC are corrected for the first time in this analysis. Finally, a new parameterisation is proposed and used to model the strong scalar component present in data, which must be be separated from the vector component.

LIMIAR

Nesta tese realízase unha análise de amplitudes integrada no tempo e en sabor das desintegracións a catro corpos dos mesóns neutros B_s^0 e B_d^0, usando os datos recollidos polo experimento LHCb no Run 1 e no Run 2. Os observables que se miden inclúen a investigación dunha anomalía na polarización das resonancias $K^{*0}(892)$ cando proveñen das desintegracións dos mesóns B_s^0 e B_d^0, que parece apuntar a unha ruptura na universalidade dos acoplos gluónicos ás distintas xeracións de quarks do Modelo Estándar.

Estas canles de desintegración, además de ser referencia para o estudo de observables que violan CP e T en desintegracións de quarks b sen charm, foron recentemente sinaladas por grupos teóricos como a fonte dunha anomalía de sabor, que podería estar conectada con outras anomalías presentadas por LHCb en canles semileptónicas.

O proxecto inclúe varias innovacións, tanto fenomenolóxicas como experimentais. O formalismo usado para describir os estados intermedios considera ondas parciais invariantes Lorentz na base de momento angular, que é máis fundamental na mecánica cuántica e permite acoplar factores de barreira centrífugos. A eficiencia multidimensional será estimada cunha nova técnica que considera sucesos completamente simulados de desintegracións no espazo de fases, baseado nun método de "Kernel Density Estimation" acelerado por GPU. Ademais, varias diferencias entre datos e simulación van a ser corrixidas por primeira vez nesta análise. Finalmente, proponse e úsase unha nova parametrización para modelar a forte compoñente escalar presente nos datos, a cal necesita ser separada da compoñente vectorial.

CONTENTS

GLOSSARY

BDT Boosted Decision Tree 45–47, 49, 56, 65, 84, 133, 134, 137
BSM Beyond the Standard Model 1, 14, 106

CKM Cabibbo-Kobayashi-Maskawa 9–11, 14, 131
CP Charge-Parity 1, 8, 10–12, 14, 15, 17, 19, 20, 22, 27, 28, 30, 32, 33, 37, 87, 128, 130

ECAL Electromagnetic Calorimeter 20
EW Electro-Weak 6–8, 16

FoM Figure of Merit 58–60

HCAL Hadron Calorimeter 20
HLT High Level Trigger 21

IT Inner Tracker 20

KDE Kernel Density Estimation 41, 54, 65, 72, 75, 97, 107
KS Kolmogórov-Smirnov 47, 49

L0 Level-0 21, 44, 71, 75
LFU Lepton Flavour Universality 12, 13
LHC Large Hadron Collider 1, 3, 16–19, 21, 22, 106
LHCb Large Hadron Collider beauty 1, 13, 16–23, 38, 39, 42, 71, 72, 76–79, 85, 106
LQCD Lattice QCD 6

MC Monte Carlo 6, 23–25, 38, 39, 41–43, 45–47, 53–55, 65, 68, 70–73, 75, 80, 84, 89, 90, 101, 102, 133, 137, 142
MVA Multivariate Analysis 39, 45, 46, 64, 79

NP New Physics 1, 13–15, 106, 131

OT Outer Tracker 20

PDF Probability Density Function 24, 25, 29, 55, 68, 71, 73, 85, 87, 90, 92, 104, 129
PID Particle Identification 19, 41–43, 45, 50, 53, 55, 62, 79, 80, 102
pQCD Perturbative QCD 5, 12
PS Pre-Shower 20
PV Primary Vertex 17, 19, 39, 44, 50, 134

QCD Quantum Chromodynamics 4, 5, 16, 17
QCDF QCD Factorisation 5, 6, 12, 13
QFT Quantum Field Theory 2

RGE Renormalisation Group Equation 4
RICH Ring Imaging Cherenkov 19

SCET Soft-Collinear Effective Theory 5, 12
SM Standard Model 1–6, 10–12, 14, 15, 22, 106, 131
SPD Scintillating Pad Detector 20
SV Secondary Vertex 17

TP Triple Product 130
TPA Triple Product Asymmetry 37, 130, 131
TT Trigger Tracker 20

VELO Vertex Locator 17, 19, 20

CHAPTER 1

INTRODUCTION

Particle physics, the study of the fundamental constituents of matter and the interactions that govern them, has profoundly shaped our comprehension of the universe. From the discovery of the electron at the dawn of the 20th century to the recent discovery of the Higgs boson, this field has continually pushed the boundaries of knowledge. The accumulated theoretical and experimental insights have culminated in the most successful theory to date for describing all known particles and their interactions: the Standard Model (SM) of particle physics. Being the most accurate theory we have in science [1], it has been able to predict and explain a wide range of phenomena related to three of the four known fundamental interactions. Despite its successes, the SM leaves several profound questions unanswered inspiring the quest for new physics beyond its scope: the so-called physics Beyond the Standard Model (BSM). These days, we have entered a new paradigm in particle physics, with significant efforts being made in the so-called *precision physics* –i.e., measuring observables that can be predicted by the SM and comparing them, digit by digit, to determine whether they agree with SM predictions within the uncertainty. Any significant deviation might be claimed as a discovery of signatures of New Physics (NP).

Numerous facilities and experiments have been built to discover previously unknown particles, to determine and understand the nature of the interactions among them, and to precisely characterise their properties, leading to the elimination of several theories that were proposed to explain the experimental data. The work described in this thesis has particularly been developed within the Large Hadron Collider beauty (LHCb) experiment, one of the four major detectors operating at the Large Hadron Collider (LHC) accelerator. Although LHCb was originally designed to perform high-precision measurements on Charge-Parity (CP) violation and rare decays, its features have made it unique as a general-purpose detector. The time integrated amplitude analysis of the decays $B^0_{s,d} \to (K^+\pi^-)(K^-\pi^+)$, to be presented in this thesis, is indeed unique, and has remained beyond reach by any other experiment thus far.

These topics, together with a description of the experimental conditions related to this thesis, will be described in further detail in this chapter.

1.1 THEORETICAL ASPECTS

A brief review of the SM is presented and discussed in this section, along with the main concepts and some mathematical developments in the field of flavour physics. The B-meson decays analysed in this thesis are also introduced, together with the current phenomenological and experimental status.

1.1.1 THE STANDARD MODEL OF PARTICLE PHYSICS

The SM is a renormalisable Quantum Field Theory (QFT) describing three out of the four known fundamental interactions, namely electromagnetic, weak, and strong interactions, based on the principle of gauge symmetry. The best model describing gravity is the theory of General Relativity, and since it plays no role at the scales of interest for this thesis it will not be detailed here.

At high energies, the SM is invariant under transformations of the Lie group of symmetry

$$\mathrm{SU}(3)_C \times \mathrm{SU}(2)_T \times \mathrm{U}(1)_Y \ , \tag{1.1}$$

where C is the colour charge, T is the weak isospin, and Y is the weak hypercharge, these being conserved quantities according to Noether's theorem [2].

In QFT, elementary particles are classified based on their spin into two categories: those with half-integer spin are known as *fermions*, and those with integer spin are referred to as *bosons*. Elementary fermions are considered in the SM as the building blocks of matter, and they are further categorised into *quarks*, which participate in the strong interaction, and *leptons*, which do not. There are six fundamental *flavours* of quarks: up (u), down (d), strange (s), charm (c), bottom (b), and top (t), as well as six flavours of leptons: electron (e^-), muon (μ^-), tau (τ^-), and their corresponding neutrinos (ν_e, ν_μ, ν_μ).
Quarks present an additional quantum number called *colour*, with three types: red (r), green (g), and blue (b). Both quarks and leptons have corresponding antiparticles, which have the same mass but opposite quantum numbers (especially, electric charge). Furthermore, colour states for antiquarks can either be anti-red ($\bar{r}$), anti-green ($\bar{g}$), or anti-blue ($\bar{b}$). Quarks have never been observed as free particles; they are always confined in colourless states called *hadrons*. Hadrons can be made up of a quark-antiquark pair, known as *mesons*, where the colour is a combination of a colour and its anti-colour (e.g., red and anti-red), or they can consist of three quarks, known as *baryons*, where each quark has a different colour (red, green, and blue, or anti-red, anti-green, and anti-blue), combining to form a colour-neutral state.
Elementary bosons, on the other hand, are the particles responsible for mediating the fundamental interactions between fermions. Each type of interaction is associated with a specific boson. The photon mediates electromagnetic interactions, $W^\pm$ and Z^0 bosons mediate weak interactions, and gluons mediate strong interactions.

Fermions			$SU(3)_C$	$SU(2)_T$	$U(1)_Y$
e_R^-	μ_R^-	τ_R^-	**1**	**1**	-1
$(\nu_{e_L}, e_L^-)^\top$	$(\nu_{\mu_L}, \mu_L^-)^\top$	$(\nu_{\mu_L}, \tau_L^-)^\top$	**1**	**2**	$-1/2$
u_R	c_R	t_R	**3**	**1**	$2/3$
d_R	s_R	b_R	**3**	**1**	$-1/3$
$(u_L, d_L)^\top$	$(c_L, s_L)^\top$	$(t_L, b_L)^\top$	**3**	**2**	$1/6$
Gauge bosons					
A_μ^a		$a = 1, \ldots, 8$	**8**	**1**	0
W_μ^a		$a = 1, 2, 3$	**1**	**3**	0
B_μ			**1**	**1**	0
Higgs					
$(\phi^+, \phi^0)^\top$			**1**	**2**	$1/2$

TABLE 1.1: Particle content of SM and their transformation properties under the different subgroups

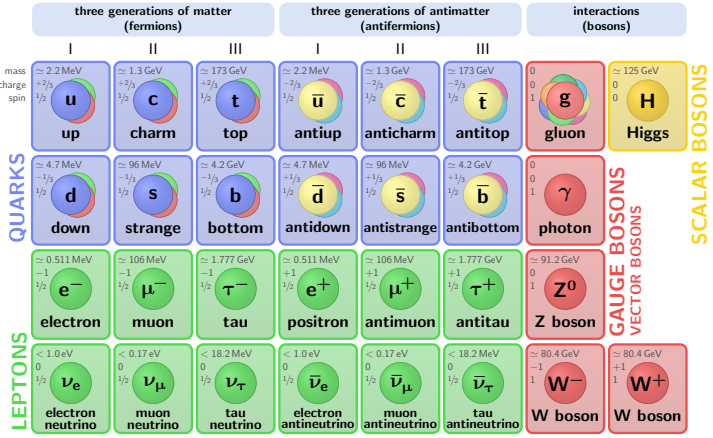

FIGURE 1.1: Particle content of Standard Model.

The discovery of the Higgs boson at the LHC in 2012 confirmed the existence of the Higgs field, responsible for endowing particles with mass through the Higgs mechanism.
A summary of elementary particle content of SM is shown in Fig. 1.1, and their conserved charges under the SM group is shown in Table 1.1.

1.1.1.1 QUANTUM CHROMODYNAMICS

Although most of the significant quark decays occur via weak interactions, especially in the b-quark sector, the strong interaction plays a very important role since quarks have never been observed as free particles, but are confined in hadrons. The finite size of hadrons and the coupling between quarks and gluons must be considered in order to get a precise determination of observables.

The strong interaction is understood by the Quantum Chromodynamics (QCD) non-Abelian gauge field theory, which couples coloured quarks and gluons, and its Lagrangian density [3] is given by

$$\mathcal{L}_{\text{QCD}} = \sum_q \bar{\psi}_{q,a} \left(i\gamma^\mu \partial_\mu \delta_{ab} - g_s \gamma^\mu t^c_{ab} A^c_\mu - m_q \delta_{ab} \right) \psi_{q,b} - \frac{1}{4} G^a_{\mu\nu} G^{\mu\nu}_a \,, \tag{1.2}$$

where repeated indices are implicitly summed over. The γ^μ are the Dirac matrices. The $\psi_{q,a}$ are the Dirac fermion spinor fields representing quarks with flavour q, mass m_q, and colour index a ($a = 1, 2, 3$). The A^c_μ are the gluon fields ($c = 1, \ldots, 8$). The t^c_{ab} matrices are the generators of the SU(3) group, proportional to the Gell-Man matrices, and they encode the fact that a gluon's interaction with a quark rotates the quark's colour in SU(3) space. The parameter $g_s = \sqrt{4\pi\alpha_s}$ is the QCD coupling, which is scale-dependent. Finally, the gluon field strength tensor is defined as

$$G^a_{\mu\nu} = \partial_\mu A^a_\nu - \partial_\nu A^a_\mu - g_s f_{abc} A^b_\mu A^c_\nu \,, \tag{1.3}$$

where f_{abc} are the structure constants of the SU(3) group. The last term in Eq. 1.3, along with

$$\left[t^a, t^b \right] = i f^{abc} t^c \,, \tag{1.4}$$

illustrates the non-Abelian nature of this theory. This non-Abelian characteristic is responsible for the self-interaction of gluons, which allows for three- and four-gluon vertices in Feynman diagrams. Unlike photons, which do not carry electric charge, gluons do carry colour charge, leading to these distinctive interactions.

The coupling constant α_s, as well as the other coupling constants in the SM, is actually non-constant, but depends on the energy scale at which you look at it. This phenomenon is called *running coupling*, and the evolution is governed by the Renormalisation Group Equation (RGE),

$$\mu^2 \frac{d\alpha_s}{d\mu^2} = -(b_0 \alpha_s^2 + b_1 \alpha_s^3 + b_2 \alpha_s^4 + \ldots) \,, \tag{1.5}$$

where μ is the renormalisation scale and b_{n-1} is the n-loop β-function coefficient. The solution to this differential equation only needs for one initial condition (scale reference) and this is typically assigned to the value of α_s at the Z-boson pole mass, $\alpha_s(m_Z) = 0.1180 \pm 0.0009$. The solution with this initial condition, up to 5-loops, is shown in Fig. 1.2. Two main behaviours, the most relevant in QCD, can be qualitatively noted from this plot:

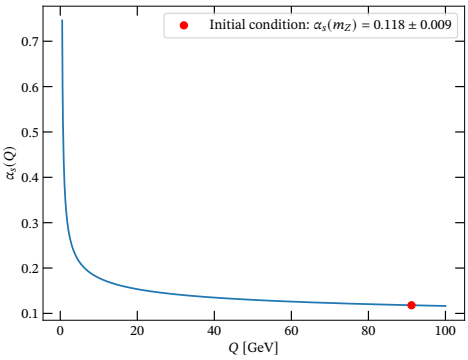

FIGURE 1.2: Solution to Eq. 1.5 using the package RUNDEC [4]. The reference scale has been set to $\alpha_s(m_Z) = 0.1180 \pm 0.0009$ [3], and the result has been obtained with five active quark flavours and up to five loops.

- Confining theory at low relative momenta (low energies, long distances): the coupling constant diverges for small energies, thereby increasing the probability of partonic emissions and confining quarks and gluons into hadrons. Quarks and gluons are produced free and hadronise after a time $t \sim 1/\Lambda_{\text{QCD}}$, which is around a yoctosecond, forming jets. This experimental phenomenon has no formal proof to date, but it is consistent with theory.
- Asymptotically free theory at high relative momenta (high energies, short distances): the coupling constant is at its weakest for high energies, thus strong interactions become weaker and so quarks act to some extent as if they were free and not bound at all. This phenomenon is very well understood in QCD, and more generally in any non-Abelian Yang-Mills theory, and it was proven that QCD is asymptotically free for the number of colours and quarks that are present in the SM. This is the origin of the minus sign in Eq. 1.5, and the discovery was awarded with the Nobel prize in 2004.

This constitutes the main problem of QCD: α_s diverges for low momenta and distances larger than $1/\Lambda_{\text{QCD}} \sim 1/(200\,\text{MeV})$, which is roughly the size of the light hadrons, and they cannot be explored with perturbation theory, thus needing non-perturbative techniques. The following constitute some of the main approaches to solve QCD problems

- Perturbative QCD (pQCD): leverages the asymptotic freedom of QCD, and it is said in the community to be valid for energies above 1 GeV (for which $\alpha_s \approx 0.4$).
- QCD Factorisation (QCDF): separates short-distance (perturbative) and long-distance (non-perturbative) effects in QCD processes. This allows the complex, long-distance physics to be encapsulated in universal functions like partonic distributions, fragmentation functions, or soft functions.
- Soft-Collinear Effective Theory (SCET): effective field theory designed to

systematically handle processes involving different energy scales, and it has been relevant in the calculation of many non-leptonic B-decays.
- Lattice QCD (LQCD): lattice gauge theory is a non-perturbative approach where space-time is discretised into a lattice, allowing the path integrals to be evaluated numerically. Equation 1.2 can be evaluated in huge simulations that in practice can only be achieved by Monte Carlo (MC) techniques.

These do not necessarily have to be used in an exclusive way, but they are often used in conjunction to solve a particular problem. The most relevant for us though is QCDF, which constitutes the main framework in which the observable that will be measured in this thesis is calculated in the SM.

1.1.1.2 ELECTROWEAK THEORY AND HIGGS MECHANISM

Weak interactions exhibit left-handed chirality, which leads to the organisation of quarks and leptons into weak isospin doublets (for left-handed fermions) and weak isospin singlets (for right-handed fermions, excluding neutrinos):

$$Q_i = \begin{pmatrix} U_i \\ D_i \end{pmatrix}_L , \quad q_{R_i} , \quad L_i = \begin{pmatrix} \nu_{\ell_i} \\ \ell_i \end{pmatrix}_L , \quad \ell_{R_i} . \tag{1.6}$$

Here the index $i = 1, 2, 3$ denotes the fermion family number. It is important to note that right-handed neutrinos do not appear in the SM as all their conserved quantities are zero, so they cannot participate in any Feynman diagram.

Electromagnetic and weak interactions are unified within the framework the Electro-Weak (EW) model [5–7], whose Lagrangian density is given by

$$\begin{aligned} \mathcal{L}_{\text{EW}} &= \mathcal{L}_{\text{fermion}} + \mathcal{L}_{\text{gauge}} + \mathcal{L}_{\text{Higgs}} \\ &= \sum_{j=1,2,3} \left[\bar{L}_j i \not{D} L_j + \bar{\ell}_{R_j} i \not{D} \ell_{R_j} + \bar{Q}_j i \not{D} Q_j + \bar{u}_{R_j} i \not{D} u_{R_j} + \bar{d}_{R_j} i \not{D} \ell_{R_j} \right] \\ &- \frac{1}{4} W^a_{\mu\nu} W^{\mu\nu}_a - \frac{1}{4} B_{\mu\nu} B^{\mu\nu} \\ &+ \left(D_\mu \Phi\right)^\dagger \left(D^\mu \Phi\right) + \mu^2 \left(\Phi^\dagger \Phi\right) - \lambda \left(\Phi^\dagger \Phi\right)^2 . \end{aligned} \tag{1.7}$$

Following the *principle of minimal coupling*, the gauge covariant derivative is defined, using the SU(2) and U(1) coupling constants g and g', as follows:

$$D_\mu = \partial_\mu - i \frac{g}{2} \sigma_j W^j_\mu - i \frac{g'}{2} Y B_\mu , \tag{1.8}$$

where σ_j are the Pauli matrices, and W^a_μ ($a = 1, 2, 3$) and B_μ are the SU(2) and U(1) gauge vector fields, respectively. The field strength tensors associated to these fields are defined as

$$\begin{aligned} W^a_{\mu\nu} &= \partial_\mu W^a_\nu - \partial_\nu W^a_\mu + g \, \epsilon^{abc} W^b_\mu W^c_\nu , \\ B_{\mu\nu} &= \partial_\mu B_\nu - \partial_\nu B_\mu . \end{aligned} \tag{1.9}$$

These fields and the gauge bosons $W^{\pm}$, Z^0, and γ are connected through the following relations

$$\begin{aligned} W_\mu^{\pm} &= \frac{1}{\sqrt{2}}\left(W_\mu^1 \mp iW_\mu^2\right) , \\ Z_\mu &= W_\mu^3 \cos\theta_W - B_\mu \sin\theta_W , \\ A_\mu &= W_\mu^3 \sin\theta_W + B_\mu \cos\theta_W , \end{aligned} \tag{1.10}$$

where θ_W is the Weinberg mixing angle. Note that the SU(2)×U(1) gauge symmetry forbids any mass term in the Lagrangian not only the gauge bosons, but also for fermions.
Finally, Φ corresponds to the isospin doublet containing four scalar fields,

$$\Phi(x) = \begin{pmatrix} \phi^+(x) \\ \phi^0(x) \end{pmatrix} = \frac{1}{\sqrt{2}} \begin{pmatrix} \phi_1(x) + i\phi_2(x) \\ \phi_3(x) + i\phi_4(x) \end{pmatrix} , \tag{1.11}$$

with all of them carrying hypercharge $Y = +1$. The field ϕ_1 (ϕ_2) has positive (negative) electric charge, while ϕ_3 and ϕ_4 are neutral.

Once EW symmetry is spontaneously broken, the gauge group is reduced down to the electromagnetic gauge symmetry:

$$\mathrm{SU}(2)_L \times \mathrm{U}(1)_Y \rightarrow \mathrm{U}(1)_{\mathrm{em}} , \tag{1.12}$$

thus generating $W^{\pm}$, Z^0 and fermion masses. This process is known as *Higgs mechanism*. The Higgs field is forced to acquire a vacuum expectation value v in ϕ_3,

$$\Phi_0 = \langle 0|\Phi|0\rangle = \frac{1}{\sqrt{2}} \begin{pmatrix} 0 \\ v \end{pmatrix} , \quad v = \frac{\mu}{\sqrt{\lambda}} \tag{1.13}$$

thereby minimising the Higgs potential in Eq. 1.7. The charge operator,

$$\hat{Q} = \hat{T}_3 + \hat{Y} = \frac{1}{2}\sigma_3 + \frac{1}{2}\mathbb{I}_{2\times 2} = \begin{pmatrix} 1 & 0 \\ 0 & 0 \end{pmatrix} \tag{1.14}$$

leaves Φ_0 in Eq. 1.13 invariant, so $\mathrm{U}(1)_{\mathrm{em}}$ remains unbroken. Although the Higgs field is at its minimum, it can fluctuate around, $\phi_3(x) = v + H(x)$. Substituting this expression in the electroweak Lagrangian, Eq. 1.7, inserting the rotated gauge fields, Eq. 1.10, and expanding the covariant derivative, the electroweak theory leads us to the following set of relations

$$\begin{aligned} &\tan\theta_W = \frac{g'}{g} , \quad e = g\sin\theta_W , \quad e = g'\cos\theta_W , \\ &m_W = \frac{g}{2}v , \quad m_Z = \frac{\sqrt{g^2+g'^2}}{2}v , \quad m_A = 0 , \\ &m_H = \sqrt{2}\mu = 2\lambda v^2 \end{aligned} \tag{1.15}$$

thus determining e, θ_W, m_W, m_Z, m_A, and m_H from the two gauge coupling constants g and g' and the two self-coupling potential constants λ and μ, giving rise to

$v = 246\,\text{GeV}$. Critically, the photon stays massless as observations indicate and the Higgs boson, $H(x)$, which is self-coupled, also acquires mass through this mechanism. These predictions for the masses are valid at lowest order in perturbation theory, but virtual quantum loops add further corrections to these parameters.

1.1.2 CP VIOLATION AND FLAVOUR PHYSICS IN THE STANDARD MODEL

The origin of CP violation lies in the Higgs field. Fermions would be massless, but Yukawa couplings must be added to the EW Lagrangian to give them mass while preserving gauge invariance. These have $Y = 0$ and are invariant under a rotation of the symmetry $\mathrm{SU}(2)_L \times \mathrm{U}(1)_Y$,

$$\begin{aligned}\mathcal{L}_{\text{Yukawa}} &= -G_d^{ij}\,\bar{Q}_{L_i}\Phi\,d_{R_j} - G_u^{ij}\,\bar{Q}_{L_i}\epsilon\,\Phi^*u_{R_j} - G_e^{ij}\,\bar{L}_{L_i}\Phi\,e_{R_j} + \text{h.c.} \\ &= -G_d^{ij}\left(\bar{u}_{L_i}\phi^+ d_{R_j} + \bar{d}_{L_i}\phi^0 d_{R_j}\right) - G_u^{ij}\left(\bar{u}_{L_i}\phi^0 u_{R_j} - \bar{d}_{L_i}\phi^- u_{R_j}\right) \\ &\quad -G_e^{ij}\left(\bar{\nu}_{L_i}\phi^+ e_{R_j} + \bar{e}_{L_i}\phi^0 e_{R_j}\right) + \text{h.c.}\,,\end{aligned} \tag{1.16}$$

where the indices i and j are fermion generation labels, ϵ is the 2×2 antisymmetric tensor, and the Yukawa couplings $G_{u,d,e}$ are 3×3 complex matrices. When the Higgs field acquires a vacuum expectation value (vev),

$$\Phi = \begin{pmatrix}\phi^+\\ \phi^0\end{pmatrix} \xrightarrow{\text{breaking}} \frac{1}{\sqrt{2}}\begin{pmatrix}0\\ v+H\end{pmatrix}\,, \quad \Phi^c = \epsilon\,\Phi^* = \begin{pmatrix}\bar{\phi}^0\\ -\phi^-\end{pmatrix} \xrightarrow{\text{breaking}} \frac{1}{\sqrt{2}}\begin{pmatrix}v+H\\ 0\end{pmatrix}\,, \tag{1.17}$$

then Eq. 1.16 yields the mass terms. Renaming the fermions weak states as f', substituting the Higgs fields, and reorganising the terms as a matrix equation, the Lagrangian is now given by

$$\mathcal{L}_{\text{Yukawa}} = -\frac{v}{\sqrt{2}}\,\bar{d}'_L\,G_d\,d'_R - \frac{v}{\sqrt{2}}\,\bar{u}'_L\,G_u\,u'_R - \frac{v}{\sqrt{2}}\,\bar{e}'_L\,G_e\,e'_R + \text{h.c.} + \ldots\,. \tag{1.18}$$

Remember that mass terms are given, in the Dirac theory, by

$$m\,\bar{f}f = m\,\bar{f}\left[\frac{1}{2}\left(1-\gamma^5\right) + \frac{1}{2}\left(1+\gamma^5\right)\right]f = m\left(\bar{f}_R f_L + \bar{f}_L f_R\right)\,.$$

Therefore, the quarks and leptons mass terms can be identified as

$$M'_u = \frac{v}{\sqrt{2}}\,G_u\,, \quad M'_d = \frac{v}{\sqrt{2}}\,G_d\,, \quad M'_e = \frac{v}{\sqrt{2}}\,G_e\,, \tag{1.19}$$

thereby emerging from a common value, v. Similar terms are originated from H, which lead to the Feynman rules of Higgs boson couplings to fermions. Focusing on the quark sector, the mass matrices are non-diagonal, but they must be diagonalisable since each generation have a different mass,

$$\begin{aligned}U_L^{u\dagger}\,M'_u\,U_R^u &= M_u = \text{diag}\,(m_u, m_c, m_t)\,, \\ U_L^{d\dagger}\,M'_d\,U_R^d &= M_d = \text{diag}\,(m_d, m_s, m_b)\,,\end{aligned} \tag{1.20}$$

where $U_{L,R}$ are unitary matrices. Taking the inverse relation,

$$M'_u = U^u_L\, M_u\, U^{u\dagger}_R \rightarrow \begin{cases} \bar{u}'_L\, M'_u\, u'_R = \left(\bar{u}'_L\, U^u_L\right)\, M_u\, \left(U^{u\dagger}_R\, u'_R\right) \,, \\ \\ \bar{u}'_R\, M'_u\, u'_L = \left(\bar{u}'_R\, U^u_L\right)\, M_u\, \left(U^{u\dagger}_L\, u'_L\right) \,, \end{cases} \tag{1.21}$$

$$M'_d = U^d_L\, M_d\, U^{d\dagger}_R \rightarrow \begin{cases} \bar{d}'_L\, M'_d\, d'_R = \left(\bar{d}'_L\, U^d_L\right)\, M_d\, \left(U^{d\dagger}_R\, d'_R\right) \,, \\ \\ \bar{d}'_R\, M'_d\, d'_L = \left(\bar{d}'_R\, U^d_L\right)\, M_d\, \left(U^{d\dagger}_L\, d'_L\right) \,, \end{cases}$$

one can relate chiral flavour eigenstates q' to chiral mass eigenstates q through the following rotations,

$$\begin{aligned} u'_L &= U^u_L\, u_L \,, \quad d'_L = U^d_L\, d_L \,, \\ u'_R &= U^u_R\, u_R \,, \quad d'_R = U^d_R\, d_R \,, \end{aligned} \tag{1.22}$$

where u is here a shorthand notation for the SU(3) triplet $(u, c, t)^\top$, while d is a shorthand notation for $(d, s, b)^\top$. Thus, $U^{u,d}_{L,R}$ are unknown 3×3 complex matrices.

The quark masses are now understood in the electroweak theory with spontaneous symmetry breaking induced by the Higgs mechanism, which has a significant consequence on the charged current interactions. Remember that the interaction Lagrangian is given by the $V - A$ theory,

$$\mathcal{L}^{cc}_W = -\frac{g}{\sqrt{2}} \left[\left(\bar{u}'_L, \bar{c}'_L, \bar{t}'_L\right) \gamma^\mu W^+_\mu \begin{pmatrix} d'_L \\ s'_L \\ b'_L \end{pmatrix} + \left(\bar{d}'_L, \bar{s}'_L, \bar{b}'_L\right) \gamma^\mu W^-_\mu \begin{pmatrix} u'_L \\ c'_L \\ t'_L \end{pmatrix} \right] \,. \tag{1.23}$$

If the quarks observed in the laboratory are mass eigenstates, then Eq. 1.22 is needed to rotate to the mass basis and this interaction Lagrangian becomes

$$\begin{aligned} \mathcal{L}^{cc}_W &= -\frac{g}{\sqrt{2}} \left[\left(\bar{u}_L, \bar{c}_L, \bar{t}_L\right) U^{u\dagger}_L \gamma^\mu W^+_\mu U^d_L \begin{pmatrix} d_L \\ s_L \\ b_L \end{pmatrix} + \left(\bar{d}_L, \bar{s}_L, \bar{b}_L\right) U^{d\dagger}_L \gamma^\mu W^-_\mu U^u_L \begin{pmatrix} u_L \\ c_L \\ t_L \end{pmatrix} \right] \\ &= -\frac{g}{\sqrt{2}} \left[\left(\bar{u}_L, \bar{c}_L, \bar{t}_L\right) \gamma^\mu W^+_\mu V_{\mathrm{CKM}} \begin{pmatrix} d_L \\ s_L \\ b_L \end{pmatrix} + \left(\bar{d}_L, \bar{s}_L, \bar{b}_L\right) \gamma^\mu W^-_\mu V^\dagger_{\mathrm{CKM}} \begin{pmatrix} u_L \\ c_L \\ t_L \end{pmatrix} \right] \,, \end{aligned} \tag{1.24}$$

where V_{CKM} is the so-called Cabibbo-Kobayashi-Maskawa (CKM) matrix,

$$V_{\mathrm{CKM}} \equiv U^{u\dagger}_L\, U^d_L = \begin{pmatrix} V_{ud} & V_{us} & V_{ub} \\ V_{cd} & V_{cs} & V_{cb} \\ V_{td} & V_{ts} & V_{tb} \end{pmatrix} \tag{1.25}$$

which relates flavour to mass eigenstates in weak charged-current interactions, and hence its elements (moduli squared) may appear in the final observables that

are calculated and measured. Although the matrix has 9 free moduli and 9 free phases, unitarity and quark-field rephasings lead to only 3 real parameters, which are usually written as rotation angles θ_{12}, θ_{23}, θ_{13}, and a single phase, δ,

$$\begin{aligned} V_{\mathrm{CKM}} &= \begin{pmatrix} 1 & 0 & 0 \\ 0 & c_{23} & s_{23} \\ 0 & -s_{23} & c_{23} \end{pmatrix} \begin{pmatrix} c_{13} & 0 & s_{13}e^{-i\delta} \\ 0 & 1 & 0 \\ -s_{13}e^{i\delta} & 0 & c_{13} \end{pmatrix} \begin{pmatrix} c_{12} & s_{12} & 0 \\ -s_{12} & c_{12} & 0 \\ 0 & 0 & 1 \end{pmatrix} \\ &= \begin{pmatrix} c_{12}c_{13} & s_{12}c_{13} & s_{13}e^{-i\delta} \\ -s_{12}c_{23} - c_{12}s_{23}s_{13}e^{i\delta} & c_{12}c_{23} - s_{12}s_{23}s_{13}e^{i\delta} & s_{23}c_{13} \\ s_{12}s_{23} - c_{12}c_{23}s_{13}e^{i\delta} & -c_{12}s_{23} - s_{12}c_{23}s_{13}e^{i\delta} & c_{23}c_{13} \end{pmatrix} \end{aligned} \tag{1.26}$$

where $s_{ij} \equiv \sin\theta_{ij}$ and $c_{ij} \equiv \cos\theta_{ij}$. It is precisely the presence of this irreducible phase in charged-current amplitudes that allows the non-conservation of CP symmetry in the SM.
Another popular parameterisation, which is given as an expansion in powers of the sine of the Cabibbo angle, $\lambda \equiv \sin\theta_{12} \approx 0.22$, is the so-called Wolfenstein parameterisation [8],

$$V_{\mathrm{CKM}} = \begin{pmatrix} 1-\lambda^2/2 & \lambda & A\lambda^3(\rho - i\eta) \\ -\lambda & 1-\lambda^2/2 & A\lambda^2 \\ A\lambda^3(1-\rho-i\eta) & -A\lambda^2 & 1 \end{pmatrix} + O\left(\lambda^4\right) , \tag{1.27}$$

where A, ρ, and η are real numbers of $O(1)$. This parameterisation has the advantage of showing a clear pattern in the CKM matrix; given that λ is a relatively small parameter, the matrix is not that far from the unity matrix. Hence, flavour transitions between quarks of the same family are much more likely than cross-generation hopping.

Another phenomenological aspect of the CKM matrix is the set of unitarity relations, $\left(VV^\dagger\right)_{ij} = \left(V^\dagger V\right)_{ij} = \delta_{ij}$, which lead to twelve complex relations among the matrix elements. The six vanishing relations can be represented as triangles in the complex plane, as would any three two-dimensional vectors. These are called *unitarity triangles*, and the two most important for experiments studying B-meson decays are the following:

$$\begin{aligned} V_{ud}V_{ub}^* + V_{cd}V_{cb}^* + V_{td}V_{tb}^* = 0 \quad (B_d^0 \text{ triangle}) , \\ V_{us}V_{ub}^* + V_{cs}V_{cb}^* + V_{ts}V_{tb}^* = 0 \quad (B_s^0 \text{ triangle}) . \end{aligned} \tag{1.28}$$

Using the Wolfenstein parameterisation,

$$\begin{aligned} O\left(\lambda^3\right) + O\left(\lambda^3\right) + O\left(\lambda^3\right) = 0 \quad (B_d^0 \text{ triangle}) , \\ O\left(\lambda^4\right) + O\left(\lambda^2\right) + O\left(\lambda^2\right) = 0 \quad (B_s^0 \text{ triangle}) . \end{aligned} \tag{1.29}$$

As the sides of the B_d^0 triangle are of similar size, the internal angles are also of the same order of magnitude. These are called α, β, and γ (although the notation ϕ_1,

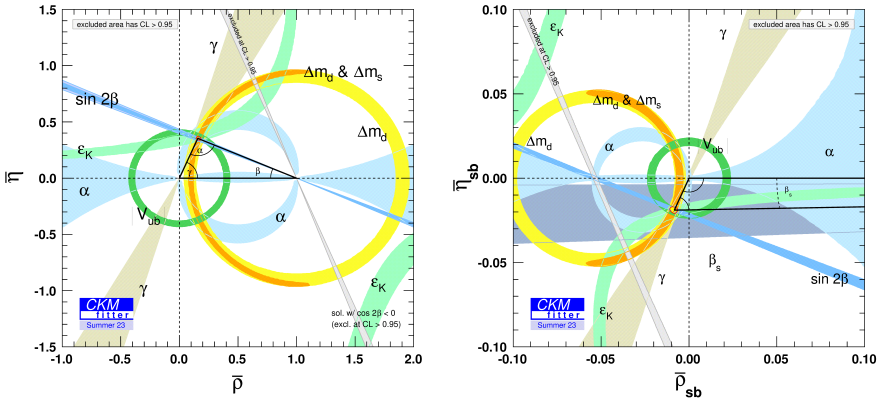

FIGURE 1.3: Latest results on the combination of constraints used in the extraction of Wolfenstein parameters [9, 10]. The figure shows the B_d^0 triangle (left) and B_s^0 triangle (right). Figure taken from [11].

ϕ_2, and ϕ_3 is also used), and are defined through

$$\begin{aligned}
\alpha \equiv \phi_2 &\equiv \arg\left(-\frac{V_{td}V_{tb}^*}{V_{ud}V_{ub}^*}\right) , \\
\beta \equiv \phi_1 &\equiv \arg\left(-\frac{V_{cd}V_{cb}^*}{V_{td}V_{tb}^*}\right) , \\
\gamma \equiv \phi_3 &\equiv \arg\left(-\frac{V_{ud}V_{ub}^*}{V_{cd}V_{cb}^*}\right) .
\end{aligned} \tag{1.30}$$

In the B_s^0 triangle two sides are of similar size and the third one is negligible, leading to a very small angle of $O(\lambda^2)$ and two of $O(90°)$. This small angle, β_s, is defined through

$$\beta_s \equiv \arg\left(-\frac{V_{ts}V_{tb}^*}{V_{cs}V_{cb}^*}\right) , \tag{1.31}$$

and arises when studying CP violation in the B_s^0 sector. Both triangles can be visualised in Fig. 1.3, containing latest results on CKM global fits provided by the CKMFitter collaboration.

No studies of CP violation will be carried out in this thesis, but some CP-violating aspects will be briefly discussed for the decay channels involved here (see Chapter 2).

1.1.3 LIMITATIONS AND PHYSICS BEYOND THE STANDARD MODEL

Although the SM is capable of explaining a wide range of phenomena, it is believed to be an effective low-energy theory of a more general theory. This is quite common in Physics and also occurs, for example, in the Fermi theory for weak

interactions, which is an effective theory of the actual Wff' vertex and is valid for low energies ($q^2 \ll m_W^2$), or in the Newton's law of gravitation theory which is a weak field approximation of General Relativity. Some fundamental questions remain unanswered by the SM, such as:

- Cosmological baryon asymmetry
- Neutrino masses
- Dark matter
- Dark energy
- Hierarchy problem
- Strong CP problem

among others. Several theories have been proposed to extend the SM, such as supersymmetry, leptoquarks or the Z' boson, mainly motivated by tensions between theory and experiment of more than 2σ. Some of the most relevant ones in the field of flavour physics are [12]

- Lepton Flavour Universality (LFU) ratios in exclusive semileptonic $b \to c$ transitions, $R(D^{(*)}) = \mathcal{B}\big(B \to D^{(*)}\tau\bar{\nu}_\tau\big)/\mathcal{B}\big(B \to D^{(*)}\ell\bar{\nu}_\ell\big)$.
- Observables in $b \to s\ell^+\ell^-$ flavour-changing neutral current transitions, particularly the decay rates $\Gamma(B \to K\mu^+\mu^-)$ and $\Gamma(B_s^0 \to \phi\mu^+\mu^-)$, and observables constructed from the $B \to K^*\mu^+\mu^-$ angular distributions.
- Anomalous magnetic moment of the muon, a_μ.
- Unitarity relations which show some tension with unity , $|V_{ud}|^2 + |V_{us}|^2 + |V_{ub}|^2$ and $|V_{ud}|^2 + |V_{cd}|^2 + |V_{td}|^2$.
- Determination of $|V_{ub}|$ and $|V_{cb}|$ from exclusive and inclusive B decay modes.

1.1.4 FLAVOUR ANOMALIES IN QUARK TRANSITIONS

In the context of $B \to VV$ decays, where B is a meson containing a b-quark and V is a massive vector resonance, the observable f_L can be identified as the probability that the two vector mesons are longitudinally polarised. This means their spin vectors are aligned with their momenta, as allowed by $m_V \neq 0$. The alternative configurations are transverse modes, where the spin vectors are orthogonal to their momenta; $f_\perp$ is the probability that both spin vectors are orthogonal, while $f_\parallel$ is the probability that both spin vectors are parallel. By definition, the sum of the three probabilities is 1. These observables and their meaning in the context of the angular distribution will be discussed further in Sec. 2.2 and App. A. The naive counting rules given by the $V - A$ theory suggest

$$f_L \sim 1 - O\left(m_V^2/m_B^2\right) \ , \quad f_\perp \sim f_\parallel \sim O\left(m_V^2/m_B^2\right) \ , \tag{1.32}$$

so that B decays to a pair of light vector mesons should exhibit a strong longitudinal polarisation. This statement is at variance with many measurements from the early 2000s to date, in both charmless and charmed decays [13]. Although the naive behaviour is broken, most of them (though not all) are in very good agreement with the SM once more sophisticated predictions are evaluated in SCET, QCDF, or pQCD. One case which is in tension with SM is the very different polarisation fractions between B_s^0 and B_d^0 modes in decays to $K^{*0}\bar{K}^{*0}$, where the former is around

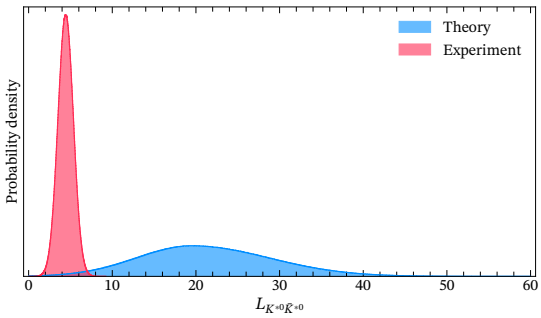

FIGURE 1.4: Comparison between theoretical value versus experimental determination of the observable $L_{K^{*0}\bar{K}^{*0}}$, for which the tension reaches 2.6σ.

20% [14–16] and the latter is around 70% [16, 17]. These particular decay channels are connected through a U-spin flavour symmetry ($s \leftrightarrow d$ exchange), which may help to reduce hadronic uncertainties.

Although the LFU anomalies in $b \to s\ell^+\ell^-$ seem to have vanished [18, 19], its phenomenology guided theorists to propose non-leptonic optimised observables for these and other charmless B-decays [20–22]. For the $B^0_{s,d} \to K^{*0}\bar{K}^{*0}$ case, they propose an observable which is proportional to the ratio between B^0_s and B^0_d longitudinal branching ratios,

$$L_{K^{*0}\bar{K}^{*0}} = \rho(m_{K^{*0}}, m_{\bar{K}^{*0}}) \frac{\mathcal{B}\left(B^0_s \to K^{*0}\bar{K}^{*0}\right)}{\mathcal{B}\left(B^0_d \to K^{*0}\bar{K}^{*0}\right)} \frac{f_L^{B^0_s}}{f_L^{B^0_d}} , \tag{1.33}$$

where $\rho(m_1, m_2)$ stands for the ratio of phase space factors,

$$\rho(m_1, m_2) = \frac{\tau_{B^0_d}}{\tau_{B^0_s}} \left(\frac{m_{B^0_s}}{m_{B^0_d}}\right)^3 \frac{\sqrt{\left(m^2_{B^0_d} - (m_1+m_2)^2\right)\left(m^2_{B^0_d} - (m_1-m_2)^2\right)}}{\sqrt{\left(m^2_{B^0_s} - (m_1+m_2)^2\right)\left(m^2_{B^0_s} - (m_1-m_2)^2\right)}} . \tag{1.34}$$

The theoretical value, first reported in Ref. [22] and updated in Ref. [20], is computed using QCDF and predicted to be $L^{\text{theo}}_{K^{*0}\bar{K}^{*0}} = 19.53^{+9.14}_{-6.64}$, while the experimental value is $L^{\text{exp}}_{K^{*0}\bar{K}^{*0}} = 4.43 \pm 0.92$. The latter was first reported in Ref. [22] based on the measurements from Ref. [16]. Theory and experiment are thus in tension at a 2.6σ level, as illustrated in Fig. 1.4. This was interpreted as a flavour deficit of $b \to s$ transitions versus $b \to d$, in some NP scenarios, in the same way $b \to s\mu^+\mu^-$ decays might be suppressed versus $b \to s e^+e^-$. I shall address this issue in Sec. 3.2, in the light of the LHCb full Run 1 and Run 2 data samples.

1.1.5 $B^0_s \to K^{*0}\bar{K}^{*0}$ AND $B^0_d \to K^{*0}\bar{K}^{*0}$ DECAYS

The $B^0_s \to K^{*0}\bar{K}^{*0}$ and $B^0_d \to K^{*0}\bar{K}^{*0}$ decays, where the K^{*0} will be an abbreviation throughout this thesis of the $K^{*0}(892)$ resonance, are forbidden at tree level in

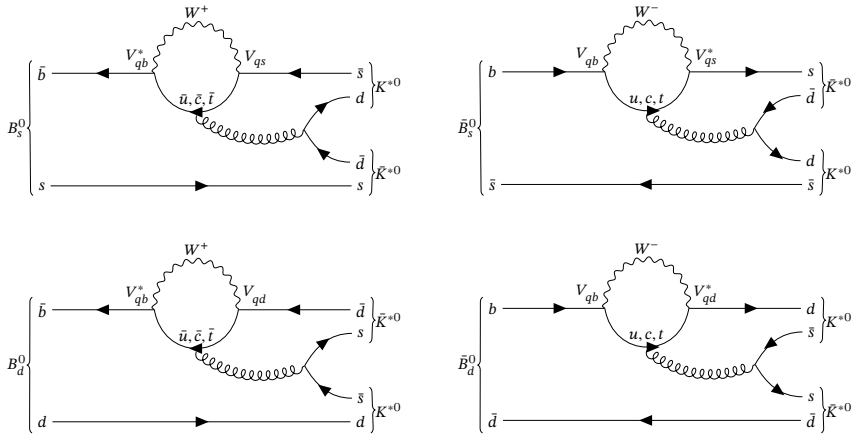

FIGURE 1.5: Leading order Feynman diagrams of $B^0_s/\bar{B}^0_s$ decays to $K^{*0}\bar{K}^{*0}$ (top), and $B^0_d/\bar{B}^0_d$ decays to $K^{*0}\bar{K}^{*0}$ (bottom).

the SM, since the couplings of neutral gauge bosons and quarks are flavour diagonal, but they can occur through virtual quantum loops (flavour-changing neutral currents). In the SM these are dominated by the $b \to sd\bar{d}$ and $b \to ds\bar{s}$ gluonic penguin diagrams, which are shown in Fig. 1.5 along with the CP-conjugated decays. Penguin-dominated decays are interesting in BSM physics searches because they may receive, at similar order, contributions from new (hypothetical) heavy particles, predicted by NP models, and modify observables thus producing a deviation from the SM.

These modes have had considerable interest from the theory community [23–30], in some cases even being dubbed as "golden modes" [21, 31]. They have the almost unique property that both B^0_d and B^0_s mesons have a decay route to an identical final state, thus the two decays are in fact U-spin partners of each other, and the U-spin breaking is only in the relatively small mass difference between the initial states. The branching ratios are small due to the loop suppression, and the B^0_d decay is further suppressed by CKM; even though the production fraction of B^0_d is considerably larger than B^0_s, one expects about a factor of 10 more $B^0_s \to K^{*0}\bar{K}^{*0}$ decays than $B^0_d \to K^{*0}\bar{K}^{*0}$. The subsequent cancellation of hadronic uncertainties is what makes them attractive modes from a theoretical standpoint. Similarly, given the identical final state, one expects many of the experimental uncertainties to also cancel in ratios. These are the main motivations to define the observable $L_{K^{*0}\bar{K}^{*0}}$ as in Eq. 1.33.

Beyond the motivation of measuring $L_{K^{*0}\bar{K}^{*0}}$, there is also a lot of interest in measuring these amplitudes in their own right. There has been a long-standing puzzle in these (and related) decays, regarding the longitudinal polarisation fractions of the vector-vector components. Nominally a $B \to VV$ decay involves a (pseudo)scalar (*i.e.* spin-0) initial state decaying to two vectors (spin-1) making the overall decay amplitude a coherent sum of three interfering helicity amplitudes:

A_0, A_+ and A_-. Due to helicity suppression of the A_+ and A_- transversely polarised amplitudes, it is typically the longitudinally polarised A_0 that dominates. However, previous measurements of f_L in $B_s^0 \to K^{*0}\bar{K}^{*0}$ decays [15, 16] (and also in the related $B_d^0 \to \rho^0 K^{*0}$ and $B_d^0 \to \phi K^{*0}$ decays) suggest a much lower value of f_L. Consequently, a precise measurement of these amplitudes will provide useful input to understand the dynamics of these penguin-dominated modes.

The experimental determination of K^{*0} resonances suffer from a strong contamination of very wide spin-0 resonances and non-resonant contributions. The K^{*0} ($\bar{K}^{*0}$) is usually reconstructed at experiments from $K^+\pi^-$ ($K^-\pi^+$) pairs, but additional resonances such as the $K_0^*(700)$ or $K_0^*(1430)$ also decay into these final states, and their parameterisation across the phase space is not trivial at all.

Another interesting topic related to these decays is the CP-violating phase originated in the interference between B_s^0 (B_d^0) meson-antimeson mixing and decay, the so-called $\phi_s^{d\bar{d}}$ ($\phi_d^{s\bar{s}}$). Although it will not be measured in this thesis, it is the natural next step and requires a full time-dependent and flavour-tagged amplitude analysis. Let us first analyse the B_s^0 case. The individual amplitude for a given partial wave, or helicity, h, can be written as the sum of the contributions from virtual u, c, and t internal loops in the penguin amplitudes [23],

$$A_h = V_{tb}^* V_{ts} P_{t,h} + V_{cb}^* V_{cs} P_{c,h} + V_{ub}^* V_{us} P_{u,h} \ . \tag{1.35}$$

Using the B_s^0 unitarity triangle, one of the three contributions can be removed. Of course the final result cannot depend on the specific quark that is removed.

- If c-quark is eliminated, and defining $P_{ij,h} \equiv P_{i,h} - P_{j,h}$, the amplitude can be written as

$$\begin{aligned} A_h &= V_{tb}^* V_{ts} P_{tc,h} + V_{ub}^* V_{us} P_{uc,h} \\ &= \underbrace{\left|V_{tb}^* V_{ts}\right|}_{O(\lambda^2)} e^{-i\phi_M/2} P_{tc,h} + \underbrace{\left|V_{ub}^* V_{us}\right|}_{O(\lambda^4)} e^{i\gamma} P_{uc,h} \ , \end{aligned} \tag{1.36}$$

  and thus $\phi_s^{d\bar{d}} = \phi_M - 2\phi_D = 0 + O(\lambda^4)$ in the SM.
- If t-quark is eliminated, the amplitude now reads

$$\begin{aligned} A_h &= V_{cb}^* V_{cs} P_{ct,h} + V_{ub}^* V_{us} P_{ut,h} \\ &= \underbrace{\left|V_{cb}^* V_{cs}\right|}_{\in\mathbb{R},\, O(\lambda^2)} P_{ct,h} + \underbrace{\left|V_{ub}^* V_{us}\right|}_{O(\lambda^4)} e^{i\gamma} P_{ut,h} \ . \end{aligned} \tag{1.37}$$

  How can ϕ_M be cancelled now? The solution is simple: if all $O(\lambda^4)$ terms are neglected, then $\mathrm{Im}\left(V_{tb}^* V_{ts}\right) = O(\lambda^4)$ has also to be neglected. Hence, $V_{tb}^* V_{ts} \in \mathbb{R}$ and $\phi_M = 2\arg\left[V_{tb}^* V_{ts}\right] = 0 + O(\lambda^4)$.

Thus, a measurement of a high value for this phase, relative to λ^4 and within the experimental uncertainty, might indicate the presence of NP. The B_d^0 case has very

similar equations, which can be obtained through a U-spin rotation,

$$\begin{aligned} A_h &= V_{tb}^* V_{td}\, P_{t,h} + V_{cb}^* V_{cd}\, P_{c,h} + V_{ub}^* V_{ud}\, P_{u,h} \\ \text{removing charm:} \quad &= V_{tb}^* V_{td}\, P_{tc,h} + V_{ub}^* V_{ud}\, P_{uc,h} \\ &= \underbrace{\left|V_{tb}^* V_{td}\right|}_{O(\lambda^3)} e^{i\beta}\, P_{tc,h} + \underbrace{\left|V_{ub}^* V_{ud}\right|}_{O(\lambda^3)} e^{i\gamma}\, P_{uc,h} \\ \text{removing top:} \quad &= V_{cb}^* V_{cd}\, P_{ct,h} + V_{ub}^* V_{ud}\, P_{ut,h} \\ &= \underbrace{\left|V_{cb}^* V_{cd}\right|}_{\in\mathbb{R},\, O(\lambda^3)} P_{ct,h} + \underbrace{\left|V_{ub}^* V_{ud}\right|}_{O(\lambda^3)} e^{i\gamma}\, P_{ut,h}\ , \end{aligned} \tag{1.38}$$

but very different consequences, since all contributions are of the same order in λ. In this case there is no simple way to obtain a prediction for the EW phase $\phi_d^{s\bar{s}}$, needing for an evaluation of the penguins.

1.2 EXPERIMENTAL ASPECTS

This section introduces the main features of the LHCb experiment at CERN, along with a description of each of its sub-detectors.

1.2.1 THE LARGE HADRON COLLIDER

The LHC [32] is the world's most powerful particle accelerator, situated at CERN, near Geneva, on the French-Swiss border. Operating since 2008, the LHC consists of a two-ring-superconducting hadron accelerator and collider housed in a 27 km tunnel more than 100 m underground. Although it is designed to collide proton beams with a centre-of-mass energy of 14 TeV and a luminosity of 10^{34} cm^{-2} s^{-1}, it can also collide heavy Pb ions with an energy per nucleon of 2.8 TeV and a peak luminosity of 10^{27} cm^{-2} s^{-1}. The project took advantage of the infrastructure built for the LEP (Large Electron-Positron collider) machine, which was an e^+e^- annihilation machine.

A proton beam consists of 2808 bunches of protons, with a nominal spacing of 25 ns (or, in terms of frequency, 40 MHz). Two beams travel through each tube, in opposite directions, and collide at four main interaction points, where the four main LHC experiments are located:

- ATLAS (A Toroidal LHC ApparatuS) and CMS (Compact Muon Solenoid): these are general-purpose detectors, and became very popular in 2012 for the discovery of the Higgs boson [33, 34]. While their main objectives are direct searches of new particles or interactions, like extra dimensions, supersymmetric particles, vector-like quarks/leptons, etc., they are highly competitive in the fields of QCD and flavour physics.
- ALICE (A Large Ion Collider Experiment): this experiment was conceived as a general-purpose detector for heavy-ion physics. Its main objectives are general QCD studies and the nature of the quark gluon plasma, by analysing lead-lead collisions.

- LHCb (Large Hadron Collider beauty): this detector focuses in the study b- and c-hadron decays, which are produced at small angles at the LHC. While its initial objectives were the study of CP violation and rare decays, it was shown that it can act as a general-purpose detector, being competitive in the discovery of tetraquarks [35] and pentaquarks [36], the measurement of the W boson mass [37], or direct searches for new particles [38, 39].

In the case of ALICE and LHCb, the luminosity is reduced in order to have an adequate number of collisions according to the design of the experiments. In the case of LHCb, the luminosity at the collision point is of $O(10^{32})$ cm^{-2} s^{-1}, two orders of magnitude less than those of ATLAS and CMS. This allows to have around a single p-p interaction per bunch crossing, thereby facilitating the separation between the Primary Vertex (PV), where the b- or c-hadrons are produced, and the Secondary Vertex (SV), where they decay.

1.2.2 THE LARGE HADRON COLLIDER BEAUTY EXPERIMENT

The LHCb experiment [40, 41] is a single-arm forward spectrometer dedicated to the study of heavy flavour physics at the LHC, *i.e.*, decays from hadrons containing at least one c-quark or b-quark. At high energies of $O(1\text{ TeV})$, simulations showed that $b\bar{b}$ pairs are produced predominantly at small angles with respect to the beamline, as shown in Fig. 1.6. This phenomenon is well understood in QCD [42], the heavy quark pair production being dominated by gluon fusion. The gluon distribution function sampling of the cross section at leading order is given by

$$x_{1,(2)} \propto \frac{m_T}{\sqrt{S}} \left(e^{(-)y_b} + e^{(-)y_{\bar{b}}} \right) , \tag{1.39}$$

where $\sqrt{S}$ is the hadronic centre-of-mass energy, and $y_{b,\bar{b}}$ are the outgoing heavy quark rapidities. The partonic energy to create a $q\bar{q}$ pair must be sufficient, $\sqrt{\hat{s}} = \sqrt{x_1 x_2 S} \geq 2m_q$, and the most likely case is the collision of a high-x gluon with a low-x gluon, so the outgoing heavy quarks are produced forwardly.

The detector, whose layout is shown in Fig. 1.7, was designed to exploit this, covering an angular acceptance from 10 mrad to 300 (250) mrad in the bending (non-bending) plane. In terms of pseudorapidity, η, defined from the production angle θ as

$$\eta \equiv -\ln\left[\tan\left(\frac{\theta}{2}\right)\right] , \tag{1.40}$$

the detector covers the range $1.6 \leq \eta \leq 4.9$. The detector is composed of different subdetectors with very specific responsibilities, which are described in the following sections as well as the trigger system.

1.2.2.1 VERTEX LOCATOR

The Vertex Locator (VELO) [45] is the flagship subdetector of LHCb, specifically designed to track particles originating from the interaction point of p-p collisions. Its primary function is to precisely determine the position, and thus separate, of

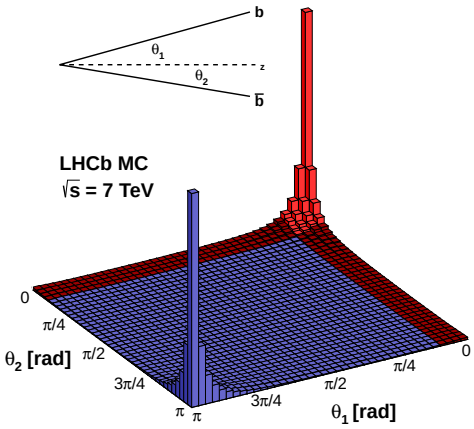

FIGURE 1.6: Simulation of $b\bar{b}$ pairs production at the LHC, showing the very small production angles at high energies. This result was produced at $\sqrt{s} = 7$ TeV, but similar results are obtained for 8 and 14 TeV. The figure was taken from [43].

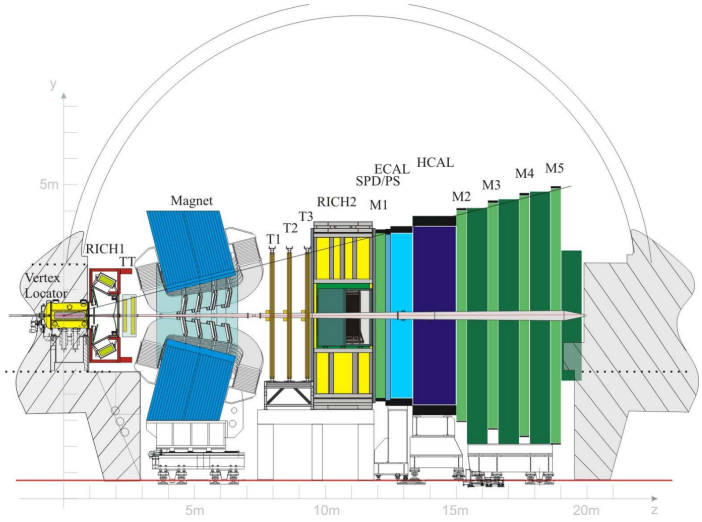

FIGURE 1.7: LHCb detector layout. Figure taken from [44]

primary and secondary vertices, a task which is vital for reconstructing the trajectories of B mesons and other short-lived particles produced in the collisions. The lifetimes of the B or D mesons are of the order of picoseconds, and the relativistic boost due to the high energies increase them so they end up flying millimetres, or even centimetres, before decaying; their decay products are tracked with extreme precision to enable the study of CP violation and rare decays.

The VELO is positioned very close to the LHC beamline, with a minimum distance of a few millimetres from the proton beams, and consists of two retractable halves that are retracted during beam injection to prevent damage and are moved into their operational positions once the beam is stable. This unique movable design ensures the safety of the detectors while maintaining proximity to the beam. The VELO is made up of 21 stations, surrounding the interaction point region, each one containing two silicon strips sensors. One of them, the R-sensor, measures the radial coordinate, whereas the other, the ϕ-sensor, measures the azimuthal coordinate. This information, together with the known spacing between stations, provides the (cylindrical) coordinates of a hit. Three or more hits are required to form a track, and from the information of all tracks the PV coordinates can be inferred.

1.2.2.2 RING IMAGING CHERENKOV

The Ring Imaging Cherenkov (RICH) detectors [46–48] exploit the angle of emission of Cherenkov light emitted by charged particles when they travel through a medium faster than the speed of light in that medium. The speed of light c cannot be surpassed by a massive particle, but in a material with refractive index $n > 1$ the phase velocity of light is c/n, and relativistic particles can easily exceed this speed; when this happens, photons are emitted like the shock front that is generated when an aircraft travels faster than the speed of sound in the air. The Cherenkov radiation is emitted in a cone, with an angle, with respect to the particle trajectory, given by

$$\cos\theta_C = \frac{1}{n\beta} , \tag{1.41}$$

where $\beta = v/c$ is the speed of the particle. In terms of the momentum, $p = \gamma m v$, this reads

$$\cos\theta_C = \frac{\sqrt{p^2 + m^2c^2}}{np} , \tag{1.42}$$

so the charged particle can by identified by its mass if its momentum is known and the Cherenkov angle is measured. This basic principle plays a very important role in the Particle Identification (PID) strategy of LHCb.

LHCb has two RICH detectors: RICH-1 is located upstream of the magnet and covers the range $1 < p < 60$ GeV/c, and RICH-2 is downstream and covers $15 < p < 100$ GeV/c. RICH-1 utilises aerogel and C_4F_{10} as radiating material, while RICH-2 uses C_4F. The hybrid pixel photon detectors used to detector the Cherenkov radiation are housed in magnetic shielding and can detect wavelengths between 200 and 600 nm.

1.2.2.3 MAGNET

The LHCb magnet is a warm[1] dipole [49–51] which provides a strong magnetic field that bends the trajectory of charged particles, according to the Lorentz force, and allows the determination of their momentum using the tracking system. The dipole is composed of two identical aluminium coils, and provides field integral of $\oint \vec{B} \cdot d\vec{l} = 4$ Tm. The y-component of the magnetic field is mapped as a function of the depth in the detector, z-coordinate, and is known to an accuracy of $\delta B/B \sim 10^{-4}$. The magnet polarity is periodically inverted to control any potential systematic errors in CP asymmetries.

1.2.2.4 TRACKING SYSTEM

The tracking system was designed to precisely reconstruct the trajectories of charged particles as they pass through the detector. The system consists of the Trigger Tracker (TT) [52, 53], which is located upstream of the magnet, and the T-stations (T1-T3), placed downstream of the magnet. Each T station is made up of two sub-detectors, or regions: the detector closest to the beam is called Inner Tracker (IT) [54], and the outer region is called Outer Tracker (OT) [55]. The TT and the IT were developed under the same silicon technology, which is more expensive but provides a better spatial resolution; this technology is especially intended for areas of high density of tracks, such as those close to the beamline. The OT is made of straw drift tubes, since the track density is lower. The information is combined with that from the VELO to apply several track reconstruction algorithms [56], ending up with an excellent momentum resolution $\delta p/p$ that varies from 0.5% at low momentum to around 1% at 200 GeV/c.

1.2.2.5 CALORIMETRY SYSTEM

The LHCb calorimeters [57] are designed to measure the energies and positions of electrons, photons and hadrons as well as to participate in their identification and in the trigger system. In order to discriminate between the different classes of particles, the calorimeter system consists of lead wall sandwiched between a Scintillating Pad Detector (SPD) and a Pre-Shower (PS) detector, and these are followed by a conventional arrangement of an Electromagnetic Calorimeter (ECAL) and a Hadron Calorimeter (HCAL). The SPD discriminates whether the particles are charged, if they leave signal, or neutral, if they do not, and allows electrons to be separated from photons; the PS detector identifies electromagnetic particles, and mostly separates electrons from pions and photons from neutral hadrons; the ECAL measures the energy of electrons and photons which produce showers inside it; finally, the HCAL measures the energy of the hadrons. The principle of operation of calorimeters is to stop the particles and measure the energy they leave behind, as well as to prevent their further passage through the detector.

Ideally, electrons/positrons leave a signal in the SPD, PS, and the ECAL; photons do so in the PS and the ECAL; hadrons do so in the SPD and the HCAL.

[1] Warm here means that it works at normal ambient temperature.

1.2.2.6 MUON SYSTEM

The muon system is the last line of detection in LHCb and is designed to detect the most penetrating known particles, excluding neutrinos: muons. Muons with energies greater than $O(1\,\text{GeV})$ are highly penetrating due to their relatively long lifetime, low interaction cross section with hadronic matter and atomic shells, and intermediate mass, which reduces bremsstrahlung effects. Therefore, they can pass through the entire detector without being stopped, leaving a very clean signature in this muon detectors.

The muon system [58–60] is composed of five rectangular stations (M1-M5) placed perpendicular to the beamline. M1 is located in before the calorimeters, and allows to improve the p_T measurement in the trigger; M2-M5 are situated downstream of the calorimeters, interleaved by iron absorbers. Hits in the muon chambers can be associated with hits in tracking system, thereby producing a probability that a track is associated to a muon. Muons play a very important role in the whole trigger system and in subsequent offline analysis.

1.2.2.7 TRIGGER STRATEGY

Trigger systems are critical pieces of particle physics experiments. Given that it is almost impossible to be sure if a particle is a real particle or is a combination of random hits in the detectors, or is random noise in the electronics, or is not the kind of particle that is supposed to be, measurements typically require a lot of candidates and produce results based on statistical knowledge. Proton bunch crossing happens at LHC at a rate of 40 MHz and it is not possible to store all the events, since the output rate can easily reach a petabyte per second; thus, trigger systems help to select and save only information that may contain interesting candidates.

The LHCb trigger [61] uses as main strategy the search for high-p_T tracks, originated in heavy hadron decays, and displaced vertices, originated from the lifetime of b- and c-flavoured hadrons in the range of the picosecond. The trigger has two stages: the Level-0 (L0), based on hardware, and the High Level Trigger (HLT), based on software.

The L0 trigger is designed to reduce the raw event rate from 40 MHz, from which only around 10 MHz of interactions are visible, to about 1 MHz, at which the full detector can be read out. It is implemented in custom FPGAs and has a fixed latency of 4 microseconds. Hardware triggers, due to their low level nature, do not allow to perform flexible and sophisticated selections, so this system just looks for high-E_T hadron, electron, and photon clusters in the calorimeters and high-p_T muons in the muon system. The information from the sub-detectors is sent to the L0 Decision Unit, which performs simple and quick arithmetic computations and computes a boolean decision. Different *trigger lines* are implemented with custom selection criteria, *e.g.*, L0HadronDecision, L0MuonDecision, L0DiMuonDecision, etc. Events passing any of these are sent via a Gigabit Ethernet network to the Event Filter Farm, an infrastructure where around 2000 CPU nodes execute the HLT in parallel.

The HLT is a C++ application that reduces the event rate from 1 MHz to a few kHz,

operating in two stages: HLT1 and HLT2. The HLT1 uses information from the tracking system and perform a quick reconstruction of the tracks, which together with the information from the vertices is transformed into a boolean decision. Events passing HLT1 are sent to HLT2, where more sophisticated selection criteria, such as vertex displacement or invariant mass requirements, are applied. The output from HLT2 is finally written into tapes for further (offline) analysis. These are classified in different streams in files called `.DST` (Data Summary Tape). For example, those events with B-hadron candidates are saved in the `BHADRON.DST`, those containing high-p_T dimuon candidates are saved into `DIMUON.DST`, etc.

Physicists run the so-called *stripping* selections to further reduce the big size of these DSTs. Stripping selections contain very analysis-specific set of requirements, producing as output a `.root` files which can be analysed with ROOT, Python or whatever program programming language or tool the analyst decides to use. This will be the starting point of the analyses to be presented in this thesis.
There are several C++ tools that may be added to the stripping configuration to create high level variables in the final ROOT files, such as the decay-time or the pseudorapidity, from lower level information coming from the sub-detectors.

1.2.2.8 DATA DESCRIPTION

The LHC, as usual in particle physics, operates in runs. The data to be analysed in this thesis belong to the LHCb Run 1, that were collected in 2011 at $\sqrt{s} = 7$ TeV and in 2012 at $\sqrt{s} = 8$ TeV, and to the Run 2, that were collected in 2015-2018 at $\sqrt{s} = 13$ TeV. All data correspond to p-p collisions and the total luminosity recorded is of about 9 fb^{-1}, 3 fb^{-1} collected in Run 1 and 6 fb^{-1} collected in Run 2. Half of all data samples were taken with one polarity of the magnet, and half with the other.

1.3 OBJECTIVES AND METHODOLOGY

As previously discussed, the experimental measurement of $L_{K^{*0}\bar{K}^{*0}}$ is in tension with the SM at 2.6σ. The observable is constructed from ratios of branching fractions and polarisation fractions. Previous LHCb measurements of these modes have only used the Run 1 data. The discovery of the $B_s^0 \to K^{*0}(892)\bar{K}^{*0}(892)$, and the first amplitude analysis of it, was made with 35 pb^{-1} of data collected in Run 1 [62]. This measurement was updated with the 2011 data and measured the amplitudes in the $K^{\pm}\pi^{\mp}$ mass range of $\pm 150\,\text{MeV}/c^2$ around the $K^{*0}(892)$ pole [14]. The first time-dependent analysis of $B_s^0 \to K^{*0}\bar{K}^{*0}$, which measured $\phi_s^{d\bar{d}}$, was presented in Ref. [15] and used the full Run 1 dataset. The first amplitude analysis of $B_d^0 \to K^{*0}(892)\bar{K}^{*0}(892)$ was presented on the full Run 1 dataset in Ref. [16]. The key findings of these previous analyses were values of longitudinal polarisation fractions in $B^0_{s,d} \to K^{*0}\bar{K}^{*0}$ of $f_L^{B_d^0 \to K^{*0}\bar{K}^{*0}} = 0.724 \pm 0.051 \pm 0.016$ and $f_L^{B_s^0 \to K^{*0}\bar{K}^{*0}} = 0.240 \pm 0.031 \pm 0.025$. The ratio of branching fractions was determined to be $\mathcal{B}(B_d^0 \to K^{*0}\bar{K}^{*0})/\mathcal{B}(B_s^0 \to K^{*0}\bar{K}^{*0}) = 0.0758 \pm 0.0057 \pm 0.0025$ [16] and the CP-violating weak phase was found to be $\phi_s = (-0.10 \pm 0.13 \pm 0.14)$ rad [15].

To shed light on this matter, a new analysis is needed that leverages the full potential of the statistics collected in Runs 1 and 2 of the LHCb experiment. The measurement of polarisation fractions requires a time-integrated amplitude analysis of both B_s^0 and B_d^0 meson decays to $K^{*0}\bar{K}^{*0}$, and constitutes the final goal of this thesis. The analysis is done in collaboration with a small research group within LHCb. The aspects related to data selection and branching fraction measurements are primarily carried out by another PhD student from a joint program between the University of Warwick and Monash University. The author of this thesis has focused almost entirely on implementing the full pipeline of the amplitude analysis, including not only its core but also handling the scalar component, describing the acceptance, implementing data/MC corrections, evaluating the transversity results, and assessing the main systematic uncertainties. Minor contributions were made to data selection and mass fitting, primarily in their interface to the amplitude analysis and also to part of the MC generation.

The analysis has been designed paying special attention to previous analyses, with special emphasis on the systematics. As the Run 1 time-dependent amplitude analysis was systematically dominated [15], the increase in data sample size alone to include Run 2 would not lead to meaningful improvements in measurement precision. Thus, significant advances in the methodology addressing the leading causes of systematic uncertainty must be introduced to mitigate this scenario.

While these advances are discussed in detail throughout this thesis, they are also summarised below:

1. Switching the spin description from transversity to covariant formalism
   As the transversity spin amplitudes are not eigenstates of orbital angular momentum L, the production Blatt-Weisskopf barrier factors of the $K^{*0}\bar{K}^{*0}$ intermediate state for the A_0 and $A_\parallel$ polarisations are undefined. In the previous analysis, the $L = 0$ barrier factor was chosen for the baseline, while the alternative form for $L = 2$ had to be trialled in the systematics. This issue affects all $B \to VV$ studies at LHCb that still rely on the transversity formalism for amplitude analysis. Covariant spin amplitudes are eigenstates of L and as such, the appropriate production barrier factor can be applied without further systematic study.
2. Integrating by flat phase space MC instead of $B^0_{s,d} \to K^{*0}\bar{K}^{*0}$ signal MC and using new efficiency modelling methods
   Data includes not only the $K^{*0}\bar{K}^{*0}$ intermediate states of interest, but further contributions from scalar amplitudes and non-interfering background events, both of which are distributed more uniformly throughout phase space. The use of $B^0_{s,d} \to K^{*0}\bar{K}^{*0}$ MC to integrate the signal PDF, which populates a very specific area of phase space, is not sufficient to constrain the effects from these additional states, negatively impacting the precision of the signal $K^{*0}\bar{K}^{*0}$ component in turn. Furthermore, in previous analyses the efficiency was computed directly from the MC using normalisation weights, whose uncertainties are directly proportional to the size of the simulation sample. This analysis uses both a significantly increased MC sample and also a new methodology, which exploits Kernel Density Estimation, to provide a semi-

parametric continuum description of the phase space efficiency.

3. Fitting the S–wave contribution down to threshold
   This analysis focuses, and has focused in the past, on a limited region of the phase space – the $K^{\pm}\pi^{\mp}$ mass region near the $K^{*0}(892)$. The $K^{*0}(892)$ resonance has the pole at $(m_0, \Gamma_0) \sim (895, 50)\,\mathrm{MeV}/c^2$, so analyses typically focus in the region of three widths around the mass pole, *i.e.*, $\sim [750, 1050]\,\mathrm{MeV}/c^2$. This time it is performed right down to the $K\pi$ mass threshold, $m(K^{\pm}) + m(\pi^{\mp}) \sim 633\,\mathrm{MeV}/c^2$, in order to better determine the S–wave shape and to explore different models, something that has not been done so far.

To do so, several mathematical and computational techniques are used and some of them are briefly described in the following sections.

1.3.1 MAXIMUM LIKELIHOOD FIT

The quantum amplitudes are described along the analysis phase space and depend on complex coefficients that modulate each contribution, as well as additional parameters of the lineshapes describing the resonances involved. The parameters are measured from experimental and data and then physics quantities of interest are derived from them. In order to find the optimal values that best fit the model to the data, a maximum likelihood fit is performed. Given a dataset of measurements $\{x_i\}_{i=1}^{N}$, a Probability Density Function (PDF) $\mathcal{P}(x|\theta)$ can be constructed to model the random variable x, which depends on a set of parameters θ. The likelihood function can be constructed as,

$$\mathcal{L}(\theta) = \prod_{i=1}^{N} \mathcal{P}(x_i|\theta) \,, \tag{1.43}$$

which can be interpreted as the joint probability of getting such set of measurements, given some vector of parameters θ. To address possible numerical problems, it is more common to write the negative log-likelihood,

$$-2\log\mathcal{L}(\theta) = -2\sum_{i=1}^{N} \log\mathcal{P}(x_i|\theta) \,, \tag{1.44}$$

where the factor 2 is a convenience. This multidimensional functions behaves like a χ^2 and can be used to find the optimal set of parameters by minimising its gradient, a task which is in general impossible to solve analytically. Furthermore, this principle only works if the PDF is normalised,

$$\int \mathcal{P}(x|\theta)dx = 1 \,. \tag{1.45}$$

The evaluation of this integral for a large number of dimensions can, in practice, only be achieved by means of MC techniques, as is done in this thesis.. Using a MC sample of n events, this is estimated as

$$\int \mathcal{P}(x|\theta)dx \approx \alpha \sum_{i=1}^{n} \mathcal{P}(x_i|\theta) \,, \tag{1.46}$$

where α is a constant proportional to the integration volume, which can be ignored as it plays no role in the likelihood.

The negative log-likelihood is described in the analysis framework as a function of all relevant parameters and the minimum is searched using the MINUIT 2 minimiser.

1.3.2 PARALLELISATION ON CPU AND GPU

The analysis code relies heavily on parallelisation techniques, as the amount of data and calculations to be processed is considerable. Equations 1.44 and 1.46 are parallelised on CPU using the `OpenMP` API, assigning the computation of the PDF of each event to a thread. To take full advantage of parallelisation and reduce computational times, the fits are run on an `AMD Threadripper 3990X` with 64 (128) physical (logical) cores.

The parallelisation on GPU is also explored. A GPU is specifically designed for parallel tasks, and consists of thousands of smaller, simpler cores, optimised for handling many calculations simultaneously. The determination of the multidimensional efficiency with millions of events involved is accelerated with two `NVIDIA RTX 3090` devices.

1.3.3 MACHINE LEARNING CLASSIFICATION TECHNIQUES

Some classification tasks are tackled using Boosted Decision Trees (BDT), a machine learning algorithm highly effective at distinguishing between two data categories based on information from multiple variables. A common task in particle physics is to reduce combinatorial background by training this algorithm to differentiate between pure samples of combinatorial and signal MC data. This is applied in the analysis of these decays, and while it is not a focus of the work conducted for this thesis, it will be briefly explained in Sec. 3.1 for the sake of completeness.

A similar algorithm used here involves employing a BDT to compute a set of weights that align two samples, making them appear the same by utilising information from multiple variables. This algorithm is called `GBReweighter`, which is part of the `hep_ml` package, and is mainly used in the data/MC correction of the hadronic L0 trigger.

CHAPTER 2

PHENOMENOLOGY OF THE DECAYS

Some of the most important expressions of decay and oscillation of neutral mesons are derived in this chapter. The phenomenology of the decays to be explored in this thesis is presented, including a thorough description of covariant spin formalism and the models used to describe the vector and scalar components.

2.1 MIXING AND DECAY OF NEUTRAL MESONS

The study of $B^0_{s,d} \to (K^+\pi^-)(K^-\pi^+)$ decays is conducted in the general framework of the mixing and decay of heavy neutral mesons [63]. Both B^0_s and B^0_d mix with their antiparticles and can decay to the final state of interest, either directly or after mixing. Given the relations between mass and flavour eigenstates,

$$\begin{aligned} |P_H\rangle &= p\,|P^0\rangle + q\,|\bar{P}^0\rangle \ , \\ |P_L\rangle &= p\,|P^0\rangle - q\,|\bar{P}^0\rangle \ , \end{aligned} \tag{2.1}$$

and the phenomenological time evolution of the mass eigenstates,

$$\begin{aligned} |P_H(t)\rangle &= e^{-im_H t} e^{-\Gamma_H t/2}\ |P_H\rangle \ , \\ |P_L(t)\rangle &= e^{-im_L t} e^{-\Gamma_L t/2}\ |P_L\rangle \ , \end{aligned} \tag{2.2}$$

a state initially produced at $t = 0$ as P^0 or $\bar{P}^0$ can be determined at any time t via the following relations:

$$\begin{aligned} |P^0(t)\rangle &= g_+(t)\,|P^0\rangle + \frac{q}{p}\,g_-(t)\,|\bar{P^0}\rangle \ , \\ |\bar{P}^0(t)\rangle &= \frac{p}{q}\,g_-(t)\,|P^0\rangle + g_+(t)\,|\bar{P^0}\rangle \ , \end{aligned} \tag{2.3}$$

with

$$g_{\pm}(t) = \frac{1}{2}\left[e^{-im_H t}\, e^{-\Gamma_H t/2} \pm e^{-im_L t}\, e^{-\Gamma_L t/2}\right] . \tag{2.4}$$

It is useful to have the following expressions

$$\begin{aligned} |g_{\pm}(t)|^2 &= \frac{1}{4}\left[e^{-\Gamma_H t} + e^{-\Gamma_L t} \pm 2\, e^{-\Gamma t}\cos\left(\Delta m\, t\right)\right] \\ &= \frac{e^{-\Gamma t}}{2}\left[\cosh\left(\frac{\Delta\Gamma}{2}\, t\right) \pm \cos\left(\Delta m\, t\right)\right] , \\ g_{+}^{*}(t)\, g_{-}(t) &= -\frac{e^{-\Gamma t}}{2}\left[\sinh\left(\frac{\Delta\Gamma}{2}\, t\right) + i\sin\left(\Delta m\, t\right)\right] , \end{aligned} \tag{2.5}$$

where $\Delta m = m_H - m_L$, $\Gamma = \frac{1}{2}\left[\Gamma_H + \Gamma_L\right]$ and $\Delta\Gamma = \Gamma_L - \Gamma_H$. Writing the transition amplitudes through the S-matrix at $t = 0$ as,

$$\begin{aligned} A_f &= \langle f|\, S\, |P^0\rangle , \\ \bar{A}_f &= \langle f|\, S\, |\bar{P}^0\rangle , \end{aligned} \tag{2.6}$$

the decay rates of flavour eigenstates to the final state f can be written, substituting Eq. 2.3 and using Eq. 2.5, as

$$\begin{aligned} \Gamma\left(P^0(t) \to f\right) &= \frac{1}{N|_{t=0}}\frac{dN\left(P^0(t) \to f\right)}{dt} = N|_{t=0}\left|\langle f|\, S\, |P^0(t)\rangle\right|^2 \\ &= \left|A_f\right|^2\left[|g_{+}(t)|^2 + \left|\lambda_f\right|^2 |g_{-}(t)|^2 + 2\,\mathrm{Re}\left(\lambda_f\, g_{+}^{*}(t)\, g_{-}(t)\right)\right] , \end{aligned} \tag{2.7}$$

$$\begin{aligned} \Gamma\left(\bar{P}^0(t) \to f\right) &= \frac{1}{N|_{t=0}}\frac{dN\left(\bar{P}^0(t) \to f\right)}{dt} = N|_{t=0}\left|\langle f|\, S\, |\bar{P}^0(t)\rangle\right|^2 \\ &= \left|A_f\right|^2\left|\frac{p}{q}\right|^2\left[|g_{-}(t)|^2 + \left|\lambda_f\right|^2 |g_{+}(t)|^2 + 2\,\mathrm{Re}\left(\lambda_f\, g_{+}(t)\, g_{-}^{*}(t)\right)\right] , \end{aligned} \tag{2.8}$$

where

$$\lambda_f \equiv \frac{q}{p}\frac{\bar{A}_f}{A_f} \tag{2.9}$$

is a key parameter in neutral meson mixing, and contains information about the oscillation, the decay, and their interference. If p and q have a phase difference due to the flavour mixing,

$$\frac{q}{p} = \left|\frac{q}{p}\right| e^{i\phi_M} , \tag{2.10}$$

and there is no direct CP violation, so that $\bar{A}_f$ is obtained from A_f by changing the sign of the CP-violating (*i.e.* weak) part of the phase,

$$\begin{aligned} A_f &= |A|\, e^{i\phi_D} e^{i\delta_D} , \\ \bar{A}_f &= \eta_f\, |A|\, e^{-i\phi_D} e^{i\delta_D} , \end{aligned} \tag{2.11}$$

then

$$\lambda_f = \left|\frac{q}{p}\right| e^{i(\phi_M - 2\phi_D)}, \tag{2.12}$$

where ϕ_M and ϕ_D are the phases of the weak mixing and decay amplitudes and δ_D the phase of the strong amplitude, contains relevant information of CP violation in mixing in its modulus and CP violation in the interference between mixing and decay in its effective weak phase, ϕ_s, which was discussed in Sec. 1.1.5.

Equations 2.7 and 2.8 can be written as

$$\begin{aligned} \Gamma\left(P^0 \to f\right) &= \left|A_f\right|^2 \frac{e^{-\Gamma t}}{2}\left(H + I\right) , \\ \Gamma\left(\bar{P}^0 \to f\right) &= \left|A_f\right|^2 \left|\frac{p}{q}\right|^2 \frac{e^{-\Gamma t}}{2}\left(H - I\right) , \end{aligned} \tag{2.13}$$

with

$$\begin{aligned} H &\equiv \left(1 + \left|\lambda_f\right|^2\right)\cosh\left(\frac{\Delta\Gamma}{2}t\right) - 2\,\mathrm{Re}\,\lambda_f \sinh\left(\frac{\Delta\Gamma}{2}t\right) , \\ I &\equiv \left(1 - \left|\lambda_f\right|^2\right)\cos\left(\Delta m\, t\right) + 2\,\mathrm{Im}\,\lambda_f \sin\left(\Delta m\, t\right) . \end{aligned} \tag{2.14}$$

Inserting the definition of λ_f and assuming no CP violation in B mixing, i.e. $|q/p| = 1$, the final expressions for the time-dependent decay rate of a $B^0_{s,d}$ meson to the final state f are found, which can be condensed into a single equation,

$$\begin{aligned} \mathcal{P}(\mathbf{x}, t, q) \propto e^{-t/\tau}\Bigg[& \left(\left|A_f(\mathbf{x})\right|^2 + \left|\bar{A}_f(\mathbf{x})\right|^2\right)\cosh\left(\frac{\Delta\Gamma}{2}t\right) \\ & -2\,\mathrm{Re}\left(A_f^*(\mathbf{x})\;\bar{A}_f(\mathbf{x})\right)\sinh\left(\frac{\Delta\Gamma}{2}t\right) \\ & +q_{\mathrm{tag}}\left(\left|A_f(\mathbf{x})\right|^2 - \left|\bar{A}_f(\mathbf{x})\right|^2\right)\cos\left(\Delta m\, t\right) \\ & +2q_{\mathrm{tag}}\,\mathrm{Im}\left(A_f^*(\mathbf{x})\;\bar{A}_f(\mathbf{x})\right)\sin\left(\Delta m\, t\right)\Bigg] , \end{aligned} \tag{2.15}$$

where $\Gamma = 1/\tau$ and $q_{\mathrm{tag}} = \pm 1$ is the flavour of the initial B-meson, with $q_{\mathrm{tag}} = +1$ for $B^0_{s,d}$ and $q_{\mathrm{tag}} = -1$ for $\bar{B}^0_{s,d}$. The variable $\mathbf{x}$ represents a generic point of the n-body phase space.

As this analysis is a time- and flavour-integrated analysis of the $B^0_{s,d} \to K^{*0}\bar{K}^{*0}$ decays, an integration over the flavour states (sum over the discrete values of q_{tag}) and the decay time must be done. The final expression is given by

$$\begin{aligned} \hat{\mathcal{P}}(\mathbf{x}) &= \sum_{q_{\mathrm{tag}}=\pm 1}\int_{t_1}^{t_2} dt\, \mathcal{P}(\mathbf{x}, t, q_{\mathrm{tag}}) \\ &\propto \left(\left|A_f(\mathbf{x})\right|^2 + \left|\bar{A}_f(\mathbf{x})\right|^2\right)\int_{t_1}^{t_2} dt\, e^{-t/\tau}\cosh\left(\frac{\Delta\Gamma}{2}t\right) \\ &\quad - 2\,\mathrm{Re}\left(A_f^*(\mathbf{x})\,\bar{A}_f(\mathbf{x})\right)\int_{t_1}^{t_2} dt\, e^{-t/\tau}\sinh\left(\frac{\Delta\Gamma}{2}t\right) , \end{aligned} \tag{2.16}$$

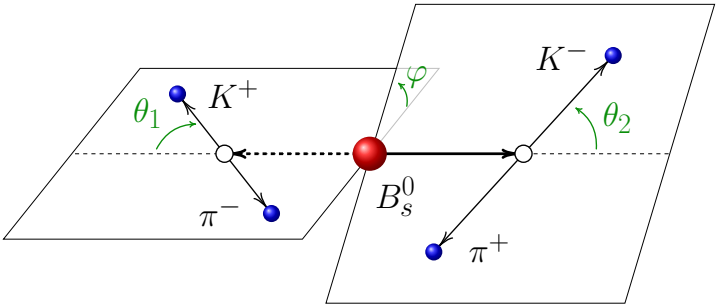

FIGURE 2.1: Definition of helicity angles

which is the PDF that will be used to extract physical parameters via a maximum likelihood fit to the data. No assumption has been made for the explicit expressions $A_f(\mathbf{x})$ and $\bar{A}_f(\mathbf{x})$. Their structure across the phase space will be discussed in the next subsections.

2.2 TRANSVERSITY FORMALISM

The decays $B^0_{s,d} \to (K^+\pi^-)(K^-\pi^+)$ have been studied in the past through amplitude analyses [14–16]. The kinematics of the decay of a mother particle at rest to an N-particle final state ($N \geq 3$) can be described by $4N - 4 - 3 - N = 3N - 7$ independent variables ($4N$ for the 4-momenta of the N daughters, 4 for conservation of energy and momentum, 3 for angles in mother's centre-of-momentum about which the daughters' momenta can be rotated without changing the kinematics, and N for the mass-energy relations of the daughters). Therefore, only 5 variables are independent for a 4-body decay.

The choice for previous analyses of this 5-dimensional basis was $m_1 \equiv m(K^+\pi^-)$, $m_2 \equiv m(K^-\pi^+)$, $\cos\theta_1$, $\cos\theta_2$ and φ. The first two are the invariant masses of both $K\pi$ pairs and allow for separation of the different resonant and non-resonant components, while the last three are referred to as helicity angles, which are schematised in Fig. 2.1. The variable θ_1 (θ_2) is the angle between the direction of motion of the K^+ (K^-) in the $K^+\pi^-$ ($K^-\pi^+$) rest frame, and the $K^+\pi^-$ ($K^-\pi^+$) in the $B^0_{s,d}$ rest frame, while φ is the angle between the two decay planes.

The time-integrated differential decay rate can be written as

$$\frac{1}{\Gamma}\frac{d^5\Gamma}{dm_1\,dm_2\,d\Omega} = \left|\sum_i A_i\, f_i(m_1, m_2, \theta_1, \theta_2, \varphi)\right|^2 \det J(m_1, m_2)\ , \tag{2.17}$$

where the A_i are a set of complex amplitudes, f_i are dynamical functions describing the behaviour of each contribution in the five-dimensional space and $\det J(m_1, m_2)$ is the determinant of the Jacobian of the transformation from the 4-body phase

space,

$$\begin{aligned}\det J(m_1, m_2, \Omega) &\equiv \left| \frac{\partial \Phi_4}{\partial(m_1, m_2, \Omega)} \right| \\ &= q(m_B; m_1, m_2)\, q(m_1; m_K, m_\pi)\, q(m_2; m_K, m_\pi) \ ,\end{aligned} \tag{2.18}$$

with

$$q(M; m_1, m_2) = \frac{\sqrt{\left(M^2 - (m_1 + m_2)^2\right)\left(M^2 - (m_1 - m_2)^2\right)}}{2\,M} \ , \tag{2.19}$$

which is referred to in the following as the break-up momentum. The vector-vector (VV) amplitudes are usually given in the helicity formalism (A_0, A_+, A_-) or in the transversity basis (A_0, $A_\parallel$, $A_\perp$), the latter being the default choice for amplitude analyses as they are CP eigenstates. While A_0 is common to both, transversity and helicity amplitudes are related by the following expressions:

$$\begin{aligned}A_\parallel &= \frac{1}{\sqrt{2}}(A_+ + A_-) \ , \\ A_\perp &= \frac{1}{\sqrt{2}}(A_+ - A_-) \ .\end{aligned} \tag{2.20}$$

Additionally, the strong physics S-wave component present in data has to be modelled and included in Eq. 2.17. Three contributions have to be taken into account: vector-scalar (VS), scalar-vector (SV) and scalar-scalar (SS). The first two are in an $L = 1$ wave, while the last one is in an $L = 0$ wave.

The decay-rate written as a function of these angles and CP eigenstates can be used to disentangle each contribution through the corresponding angular analysis.

Additional information about the angular distribution and the different partial integrals is given in App. A.

2.3 COVARIANT SPIN FORMALISM

The transversity formalism has some limitations from a physical point of view, as it is only valid in the limit of a zero-width resonance, which is not the case for the $K^{*0}(892)$ ($\Gamma_0 \sim 50\,\text{MeV}$). Relativity induces extra dynamic effects along the lineshape of the resonance. Intuitively, for some regions in phase space, the resonance is unable to generate sufficient angular momentum to conserve spin. The Blatt-Weisskopf barrier factors [64] correct the amplitude to account for this spin-dependent effect. Their expressions used in this analysis, for an orbital wave L, are given by

$$\begin{aligned}L = 0: &\quad B_L(q) = 1 \ , \\ L = 1: &\quad B_L(q) = \frac{1}{\sqrt{1 + (qR)^2}} \ , \\ L = 2: &\quad B_L(q) = \frac{1}{\sqrt{9 + 3\,(qR)^2 + (qR)^4}} \ ,\end{aligned} \tag{2.21}$$

where q is the break-up momentum defined in Eq. 2.19 and R denotes the resonance size measured in inverse energy units, under the assumption that it is contained within a square potential well. It is then necessary to describe the intermediate states as eigenstates of angular momentum and assign them the corresponding barrier factors. The states given by A_0 and $A_\parallel$ are linear combinations of S and D waves and are therefore not suitable for this purpose.

Due to the aforementioned limitations imposed by the transversity amplitude formalism, this analysis adopts the formalism for integer spin based on the work of W. Rarita and J. Schwinger [65–67] in which the total amplitude is constructed by the corresponding spin wavefunctions. In such a covariant framework all of the amplitudes are necessarily Lorentz invariant.

Consider a massive spin-J particle with 4-momentum p^μ and spin projection s_z and let $\epsilon_J^{\mu_1\cdots\mu_J}(p, s_z)$ be its wave function, or rank-J polarisation tensor. The Rarita-Schwinger conditions to be fulfilled read as

$$\begin{aligned} \text{orthogonal}: &\quad p_\mu\, \epsilon_J^{\cdots\mu\cdots} = 0\,, \\ \text{symmetric}: &\quad \epsilon_J^{\cdots\mu_i\cdots\mu_j\cdots} = \epsilon_J^{\cdots\mu_j\cdots\mu_i\cdots}\,, \\ \text{traceless}: &\quad g_{\mu\nu}\, \epsilon_J^{\cdots\mu\cdots\nu\cdots} = 0\,. \end{aligned} \tag{2.22}$$

This polarisation tensor would naively have 4^J independent components. Symmetric tensors of rank-J have $1/2(J^2+3J+2)$ independent components and tracelessness imposes $1/2(J^2-J)$ constraints, leaving $2J+1$ independent components as suitable to completely describe the spin-J object.

Since higher spin states can be generated from spin-1 states, it is natural to discuss the spin-1 case first. The polarisation tensor $\epsilon_\mu(p, s_z)$ has 3 independent components, and because spin describes how a state behaves under spatial rotations, the time component must vanish. In a particle's rest frame, where the 4-momentum is given by $k^\mu = (m, 0, 0, 0)$, the components for the different projections of spin are given by

$$\begin{aligned} \epsilon_\mu(k, 0) &= (0, 0, 0, 1) \quad \text{(longitudinal)}\,, \\ \epsilon_\mu(k, \pm 1) &= \mp\frac{1}{\sqrt{2}}(0, 1, \pm i, 0) \quad \text{(transverse)}\,. \end{aligned} \tag{2.23}$$

In order to describe an arbitrary reference frame these can be Lorentz-transformed to any 4-momentum $p^\mu = (E, p_x, p_y, p_z)$ so that $\epsilon_\mu(p, s_z) = \Lambda_\mu^\nu(p, k)\, \epsilon_\nu(k, s_z)$, resulting in

$$\begin{aligned} \epsilon_\mu(p, 0) &= \frac{1}{m}\begin{pmatrix} p_z \\ p_z p_x/(E+m) \\ p_z p_y/(E+m) \\ m + p_z^2/(E+m) \end{pmatrix} \quad \text{and} \\ \epsilon_\mu(p, \pm 1) &= \frac{\pm 1}{\sqrt{2}m}\begin{pmatrix} p_x \mp i p_y \\ m + p_x\left(p_x \mp i p_y\right)/(E+m) \\ \mp i m + p_y\left(p_x \mp i p_y\right)/(E+m) \\ p_z\left(p_x \mp i p_y\right)/(E+m) \end{pmatrix}. \end{aligned} \tag{2.24}$$

Spin-2 polarisation tensors can be generated by coupling two spin-1 states, automatically satisfying the Rarita-Schwinger conditions from Eq. 2.22,

$$\epsilon^{\mu\nu}(p, s_z) = \sum_{s_{z_1}, s_{z_2}} \langle 1 s_{z_1}, 1 s_{z_2} | 2 s_z \rangle \; \epsilon^{\mu}(p, s_{z_1}) \, \epsilon^{\nu}(p, s_{z_2}) \; , \tag{2.25}$$

where $\langle 1 s_{z_1}, 1 s_{z_2} | 2 s_z \rangle$ are the Clebsch-Gordan coefficients from the general theory of angular momentum in quantum mechanics.

Another key object is the projection operator, which has $2J$ indices for a spin-J state, and is defined as

$$P_J^{\mu_1 \ldots \mu_J \; \nu_1 \ldots \nu_J}(p) = \sum_{s_z} \epsilon^{\mu_1 \ldots \mu_J}(p, s_z) \, \epsilon^{* \nu_1 \ldots \nu_J}(p, s_z) \; . \tag{2.26}$$

For spin-1 states, this is reduced to

$$P_1^{\mu\nu}(p) = \sum_{s_z} \epsilon^{\mu}(p, s_z) \, \epsilon^{* \nu}(p, s_z) = -g^{\mu\nu} + \frac{p^{\mu} p^{\nu}}{m^2} \; . \tag{2.27}$$

This popular expression, sometimes known as the tangent projector to a hypersurface in the context of differential geometry, that has the ability to align any 4-vector with the polarisation tensor by removing the normal component. For spin-2 states this is calculated as

$$\begin{aligned} P_2^{\mu_1\mu_2 \; \nu_1\nu_2}(p) &= \sum_{s_z} \epsilon^{\mu_1\mu_2}(p, s_z) \, \epsilon^{* \nu_1\nu_2}(p, s_z) \\ &= \frac{1}{2}\left[P_1^{\mu_1\nu_1}(p) \, P_1^{\mu_2\nu_2}(p) + P_1^{\mu_1\nu_2}(p) \, P_1^{\mu_2\nu_1}(p) \right] - \\ &\quad \frac{1}{3}\left[P_1^{\mu_1\mu_2}(p) \, P_1^{\nu_1\nu_2}(p) \right] \; . \end{aligned} \tag{2.28}$$

Recall that the trace of a projection equals the dimension of the subspace onto which it projects,

$$\mathrm{Tr}(P_J) = \sum_m (P_J)_{m\,m} = 2J + 1 \; . \tag{2.29}$$

Another useful object that has to be introduced is the angular momentum operator, a rank-J tensor representing the orbital wave between two decay products. For a decaying particle $A \to B + C$, it is constructed by projecting the relative momentum $q_A = p_B - p_C$ onto the spin-J subspace of particle A, as depicted in Fig. 2.2,

$$L_{\mu_1 \ldots \mu_J}(p_A, q_A) = (-1)^J P_{\mu_1 \ldots \mu_J \; \nu_1 \ldots \nu_J}(p_A) \, q_A^{\nu_1} \ldots q_A^{\nu_J} \; . \tag{2.30}$$

Finally, it is sometimes necessary to add the Levi-Civita tensor, $\varepsilon_{\mu\nu\alpha\beta}$, to ensure the amplitudes behave correctly under CP as it introduces a minus sign under the exchange of two indices (particles).

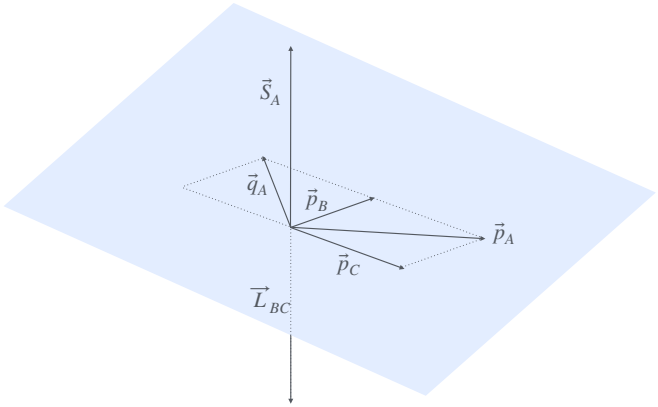

FIGURE 2.2: Visual description of the 3-momentum, angular momentum and spin vectors involved. Vectors $\vec{p}_{B,C}$, and hence $\vec{q}_A$, do not necessarily need to be in the same plane.

2.3.1 SPIN DENSITIES

In the analysis region that is considered the $K\pi$ pairs can be in vector (V) or scalar (S) states. Due to the conservation of angular momentum, there are three possible orbital waves for VV states: $L = 0, 1, 2$ (S, P, D). As VS and SV states are not eigenstates of the CP operator, the following rotated states are considered

$$\begin{aligned} |VS^+\rangle &= \frac{1}{\sqrt{2}}\big(\,|VS\rangle + |SV\rangle\,\big)\,, \\ |VS^-\rangle &= \frac{1}{\sqrt{2}}\big(\,|VS\rangle - |SV\rangle\,\big)\,. \end{aligned} \tag{2.31}$$

that are eigenstates of both CP and angular momentum operators. These, together with the double scalar state, SS, constitute the six possible states that contribute to the total amplitude.

The individual spin wave functions are constructed as a Lorentz scalar by contracting the polarisation tensors with the corresponding orbital waves,

$$\begin{aligned} A^S_{VV}: &\quad S \propto \epsilon_\mu(V_1)\,\epsilon^\mu(V_2)\,, \\ A^P_{VV}: &\quad S \propto \varepsilon_{\mu\nu\alpha\beta}\,L^\beta(V_1,V_2)\,\epsilon^\alpha(V_1)\,\epsilon^\nu(V_2)\,p^\mu(B)\,, \\ A^D_{VV}: &\quad S \propto L_{\mu\nu}(V_1,V_2)\,\epsilon^\mu(V_1)\,\epsilon^\nu(V_2)\,, \\ A^+_{VS}: &\quad S \propto \epsilon_\mu(V_1)\,L^\mu(V_1,S_2) + \epsilon_\mu(V_2)\,L^\mu(S_1,V_2)\,, \\ A^-_{VS}: &\quad S \propto \epsilon_\mu(V_1)\,L^\mu(V_1,S_2) - \epsilon_\mu(V_2)\,L^\mu(S_1,V_2)\,, \\ A_{SS}: &\quad S \propto 1\,, \end{aligned} \tag{2.32}$$

where $V_{1,2} \equiv |K^\pm\pi^\mp\rangle_{J=1}$ and $S_{1,2} \equiv |K^\pm\pi^\mp\rangle_{J=0}$.

Two tricks are used to avoid excessive computations and to handle sums over unobservable spins:

1) It can be easily shown that the projection operator acts over orbital tensors as

$$P^{\mu_1 \dots \mu_J \ \nu_1 \dots \nu_J}(p)\, L_{\nu_1 \dots \nu_J}(p,q) = L^{\mu_1 \dots \mu_J}(p,q) \tag{2.33}$$

2) The sum over the internal unobservable spin projections can be passed through a magnitude squared. Therefore, polarisation tensors can be substituted by angular momentum tensors of equal rank.

The final set of spin densities used in this analysis is

$$\begin{aligned}
A^S_{VV}: &\quad S \propto L_\mu(p_{V_1}, q_{V_1})\, L^\mu(p_{V_2}, q_{V_2})\ , \\
A^P_{VV}: &\quad S \propto \varepsilon_{\mu\nu\alpha\beta}\, L^\beta(p_B, q_B)\, L^\alpha(p_{V_1}, q_{V_1})\, L^\nu(p_{V_2}, q_{V_2})\, p^\mu(B)\ , \\
A^D_{VV}: &\quad S \propto L_{\mu\nu}(p_B, q_B)\, L^\mu(p_{V_1}, q_{V_1})\, L^\nu(p_{V_2}, q_{V_2})\ , \\
A^+_{VS}: &\quad S \propto L_\mu(p_{V_1}, q_{V_1})\, L^\mu(p_B, q_B) + L_\nu(p_{V_2}, q_{V_2})\, L^\nu(p_B, q_B)\ , \\
A^-_{VS}: &\quad S \propto L_\mu(p_{V_1}, q_{V_1})\, L^\mu(p_B, q_B) - L_\nu(p_{V_2}, q_{V_2})\, L^\nu(p_B, q_B)\ , \\
A_{SS}: &\quad S \propto 1\ .
\end{aligned} \tag{2.34}$$

On the technical side, all tensors are implemented in the fit framework using the `qft++` library [68].

2.4 LINESHAPES

To describe the decay of the intermediate states,

$$V \to K^\pm \pi^\mp\ , \quad S \to K^\pm \pi^\mp\ ,$$

dynamical functions dependent on the $K\pi$ invariant mass have to be considered. The vector mode is purely dominated, in the mass window that is analysed, by the $K^{*0}(892)$ resonance, and its decay is parameterised through a relativistic Breit-Wigner (BW) function

$$T(s) = \frac{1}{m_0^2 - s - i\sqrt{s}\,\Gamma(s)}\ , \tag{2.35}$$

where $\sqrt{s} = m_{K\pi}$, m_0 is the pole mass, Γ_0 is the width of the resonance at the pole and the energy-dependent width, for an angular momentum L, is given by

$$\sqrt{s}\,\Gamma(s) = m_0 \Gamma_0 \left(\frac{m_0}{\sqrt{s}}\right) \left(\frac{q_{K\pi}(s)}{q_0}\right)^{2L+1} \left(\frac{B_L(q_{K\pi}(s))}{B_L(q_0)}\right)^2\ , \tag{2.36}$$

where $q_{K\pi} \equiv q(m_{K\pi}; m_{K^\pm}, m_{\pi^\mp})$, $q_0 \equiv q(m_0; m_{K^\pm}, m_{\pi^\mp})$ and B_L are the barrier factors defined in Eq. 2.21. This general formula is particularised for $L = 1$.

The scalar contribution is dominated by the broad resonances $K_0^*(700)$, or κ, and $K_0^*(1430)$, and describing it accurately presents significant modelling challenges. The approach to describe these scalars is built on top of the re-scattering lineshapes from Ref. [69]. Additionally, the authors of this reference report that the pole

Parameter	Value
α	1.15
s_0	$(1.1\,\text{GeV})^2$
$\Sigma_{K\pi} = m_K^2 + m_\pi^2$	$(0.496\,\text{GeV})^2 + (0.13957\,\text{GeV})^2$
$\Delta_{K\pi} = m_K^2 - m_\pi^2$	$(0.496\,\text{GeV})^2 - (0.13957\,\text{GeV})^2$
$s_A = \left(\Sigma_{K\pi} + 2\sqrt{4\,\Delta_{K\pi} + m_K^2 m_\pi^2}\right)/5$	$0.236\,\text{GeV}^2$
B_0	0.403 ± 0.006
B_1	0.173 ± 0.031

TABLE 2.1: Parameters used in the re-scattering lineshape. Pion and kaon masses differ a bit from those used in this analysis, but changing them would require a re-scaling of B_0 and B_1.

position for $K_0^*(700)$ falls deep in the complex plane and cannot be described by any of the standard lineshapes used in experimental particle physics. These functions are obtained in the framework of Chiral Perturbation Theory from Roy-Steiner equations, guaranteeing that they fulfil unitarity, causality, analyticity, and crossing symmetry across the complex plane. Although the parameterisations for the scalar wave cover the case of isospins $I = 1/2$ and $I = 3/2$, only the former is considered in this analysis since the decay is dominated by a gluonic penguin ($I = 0$). The explicit expression for the parameterisation is given by

$$T^{\text{scat}}_{\pi K-\pi K}(s) = \frac{1}{\cot\delta_0^{1/2}(s) - i}\,, \tag{2.37}$$

with

$$\cot\delta_0^{1/2}(s) = \frac{\sqrt{s}}{2\,q(s)(s - s_A)}\left(B_0 + B_1\,\omega(s)\right)\,, \tag{2.38}$$

where $q(s)$ is the break-up momentum of Eq. 2.19, s_A is the Adler zero and $\omega(s)$ is a conformal transformation given by

$$\omega(y) \equiv \omega(y(s)) = \frac{\sqrt{y(s)} - \alpha\sqrt{y_0 - y(s)}}{\sqrt{y(s)} + \alpha\sqrt{y_0 - y(s)}}\,, \tag{2.39}$$

where

$$y(s) = \left(\frac{s - \Delta_{K\pi}}{s + \Delta_{K\pi}}\right)^2\,, \quad y_0 \equiv y(s_0)\,. \tag{2.40}$$

The numeric values used for α, s_0, s_A, together with the parameters B_0 and B_1 that come from a constrained fit to scattering data, are taken from the same reference and are given in Table 2.1.

An additional term is proposed to take into account the direct production of these resonances in the B-decay, besides the possible re-scattering after the process

of hadronisation. This new lineshape results from a production function about which little is known, combined with the S-matrix for re-scattering,

$$T(s) = P(s)\, S^{\text{scat}}_{\pi K-\pi K}(s) = P(s)\left(1 + i\, T^{\text{scat}}_{\pi K-\pi K}(s)\right) , \tag{2.41}$$

being $P(s)$ an unknown production function that is parameterised via a quasi-model-independent approach, as a complex polynomial

$$P(s) = \left(1 + c_1^{\text{abs}} X(s) + c_2^{\text{abs}} X^2(s) + \dots\right) e^{i\left(c_1^{\text{arg}} X(s) + c_2^{\text{arg}} X^2(s) + \dots\right)} , \tag{2.42}$$

with c_i^{abs} and c_i^{arg} a set of parameters that must be determined from a fit to data, and the transformation

$$X(s) = 2\,\frac{\sqrt{s} - \sqrt{s_{\text{min}}}}{\sqrt{s_{\text{max}}} - \sqrt{s_{\text{min}}}} - 1 , \quad X(s) \in [-1, 1] , \tag{2.43}$$

causes the coefficients c_i to have numerical values of $O(1)$. Critically, Watson's theorem ensures the preservation of the phase motion from scattering across the complex plane. An alternative parameterisation of these scalars is considered as a source of systematic uncertainty and addressed later in Sec. 4.1.2.

2.5 FIT BASIS

Although many $B \to VV$ analyses use the five variables discussed in Sec. 2.2, i.e.,

$$\left\{\cos\theta_1,\, \cos\theta_2,\, \varphi,\, m_1,\, m_2\right\} , \tag{2.44}$$

the 4-body phase space, Φ_4, is best suited for this analysis. This is nothing other than the set of 4-vectors generated under the 4-body phase-space element. For a general decay $M \to 1\,2\,\dots\,n$ with 4-vectors $P \to p_1\, p_2\, \dots\, p_n$, this is given by

$$d\Phi_n \equiv \delta^4\left(P - \sum_i p_i\right) \prod_i \frac{d^4 p_i}{(2\pi)^3}\delta\left(p_i^2 - m_i^2\right) , \tag{2.45}$$

where the Dirac-deltas dictate conservation laws, and $d^4 p_i = d^3 p_i / E_i$ is the Lorentz-invariant phase space element.
In this setup, the quantities entering the fit are the 4-vectors of each final state particle. Data events whose 3-momenta have been adjusted to satisfy a B mass constraint fulfil Eq. 2.45, and normalisation events generated with the equation also do. Model and efficiency plots will often be projected in the variables from Eq. 2.44, but thanks to this choice of fit basis, they could be projected in any other set of five independent variables, such as exotic.
The notation Φ_4 or $\mathbf{x}$, or $\mathbf{y}$, will be used indistinctly to refer to a generic point in the four-body phase space, especially in Sec. 3.2.

2.6 AMPLITUDE MODEL

The total amplitude for the $B^0_{s,d} \to (K^+\pi^-)(K^-\pi^+)$ decays is modelled as the coherent sum over all intermediate state amplitudes $A_i(\Phi_4)$,

$$A(\Phi_4) = \sum_i a_i \, A_i(\Phi_4) \, , \tag{2.46}$$

where $a_i = x_i + iy_i$ are complex strong coefficients that modulate each contribution, and are free parameters of the model that must be determined from fits to data. The isobar approach, which assumes that the four-body decay process can be factorised into subsequent two-body decay amplitudes [70–72], is used to construct each partial wave, $A_i(\Phi_4)$, as

$$A_i(\Phi_4) = B_{L_B}(\Phi_4)\Big[B_{L_{K^+\pi^-}}(\Phi_4)\, T_{K^+\pi^-}(\Phi_4)\Big]\Big[B_{L_{K^-\pi^+}}(\Phi_4)\, T_{K^-\pi^+}(\Phi_4)\Big] S_i(\Phi_4) \, , \tag{2.47}$$

where B_{L_B} ($B_{L_{K^\pm\pi^\mp}}$) is the production (decay) barrier factor depending on the orbital wave between B ($K^\pm\pi^\mp$) decay products, $T(s)$ are 2-body mass propagators and S_i are the spin densities from Eq. 2.34. The amplitude for $\bar{B}$ is obtained, using Eq. 2.9 and assuming $a_i = \bar{a}_i$, as

$$\bar{A}(\Phi_4) = \sum_i a_i \, \lambda_i \, \bar{A}_i(\Phi_4) = \sum_i a_i \, \lambda_i A_i(\bar{\Phi}_4) \, , \tag{2.48}$$

where $\bar{\Phi}_4$ is the CP-conjugated 4-body phase space, obtained as

$$K^+(\vec{p}_1)\,\pi^-(\vec{p}_2)\,K^-(\vec{p}_3)\,\pi^+(\vec{p}_4) \xrightarrow{CP} K^-(-\vec{p}_1)\,\pi^+(-\vec{p}_2)\,K^+(-\vec{p}_3)\,\pi^-(-\vec{p}_4) \, .$$

It is interesting to note that, using this covariant approach, there is no requirement to explicitly incorporate any CP eigenvalue into the individual contributions, as would occur with the transversity formalism.

CP symmetry is assumed to be conserved in this thesis since all previous measurements of weak phases for these decay channels show results compatible with zero, either the global weak phase $\phi_s^{d\bar{d}}$ [15] or polarisation-dependent weak phases in Triple Product Asymmetries (TPAs) [14].

CHAPTER 3

TIME-INTEGRATED AMPLITUDE ANALYSIS

This chapter presents a time-integrated amplitude analysis of $B^0_{s,d} \to (K^+\pi^-)(K^-\pi^+)$ decays using the full dataset collected by the LHCb experiment during Run 1 and Run 2. The overall view of this analysis, as designed, involves three main components: data selection, branching fraction measurement, and amplitude analysis. While the branching fraction measurement is conducted independently of the amplitude analysis, data selection has a direct impact on it. Decisions and procedures made during data selection affect the amplitude analysis, and thus, despite being performed by a PhD student from a joint programme between the University of Warwick and Monash University, the key elements of the selection process are detailed in this chapter. In addition, the chapter describes the full construction of the amplitude analysis, including the determination of the efficiency across phase space and time, the evaluation of all data-driven MC corrections, and the model of background decays within the phase space.

3.1 DATA SELECTION

As mentioned above, this section includes a summary of all relevant information regarding the data selection process. The only contributions of the author of this thesis to this block are the generation aof some signal MC samples and their model testing, as well as the interface between data selection and mass fitting to the amplitude analysis where required. Therefore, candidate selection and mass fitting are included here *to provide the necessary context for the amplitude analysis*. The purpose of this step of the analysis is to construct the cleanest possible datasets from hadronic streams (subsets of recorded data containing B-hadron candidates), which are largely plagued by background decays. Additionally, several MC samples of both signal and background processes are simulated to understand the physics

of interaction with the detector and, where possible, are processed in the same way as the data. Finally, a sophisticated four-body mass fit is performed on selected data to estimate the number of events for each signal and background contribution.

3.1.1 DATA SAMPLES

This analysis uses the full LHCb dataset collected during Run 1 (2011–2012) and Run 2 (2015–2018). During tuple[1] construction, the `DecayTreeFitter` algorithm [73] is used to constrain some of the variables given some PV and/or mass hypothesis:

- PV only constraint. These variables are used for selection and invariant mass modelling of the B-candidate mass.
- PV and B^0_d mass constraint. These variables are used when computing the helicity angles and intermediate (K^{*0} and $\bar{K}^{*0}$) masses when fitting the $B^0_d \to K^{*0}\bar{K}^{*0}$ amplitude.
- PV and B^0_s mass constraint. These variables are used when computing the helicity angles and intermediate (K^{*0} and $\bar{K}^{*0}$) masses when fitting the $B^0_s \to K^{*0}\bar{K}^{*0}$ amplitude.

Candidates for $B^0_{s,d} \to K^{*0}\bar{K}^{*0}$ decays are selected using the `Bs2K0stK0stNominalLine` stripping[2] line in the `BhadronCompleteEvent` stream. The stripping line cuts are briefly summarised in Table 3.1.

Figure 3.1 shows the B-candidate invariant mass distribution for stripped events in data. The peaks close to 5400 MeV/c^2 correspond to the B^0_s meson, while the B^0_d decays cannot be seen with such clarity at this early stage.

In LHCb, data streams are stored in two formats: DST (Data Summary Tape) and MDST (Micro Data Summary Tape). While DST files contain the full information on reconstructed objects in an event, MDST files store only specific information for selected events, making them a reduced version of DST.

Relevant decays are simulated via MC methods through the complete chain of the LHCb dataflow, and they are typically referred to as MC. Simulation steps include full details on p–p collisions and hadronisation models, B-hadron decays, or particle interactions when passing through matter. A summary of the various simulated samples used in the analysis is provided in Table 3.2. In the tupling machinery, all MC samples have momentum smearing.

Two kind of samples are especially relevant for the amplitude analysis:

- Signal $B^0_s \to K^{*0}\bar{K}^{*0}$ decays: used to define the signal, which helps in the 4-body mass fit and in the Multivariate Analysis (MVA) used to suppress most of the combinatorial background.

[1] It is very common in particle physics to talk about n-tuples, NTuples, or simply tuples. These are data structures that allow for straightforward access to the parameters of interest in an event. They can be viewed simplistically as a table in a spreadsheet, with each row representing an event and each column a variable.

[2] In LHCb, the *stripping* process applies a series of selection cuts on kinematic, trigger, and other variables to refine generic data streams—such as hadronic or di-muonic streams, which contain events with b- or c-hadrons and di-muon candidates—into specialised datasets customised for specific analyses.

Variable	Stripping cut
$K^{\pm}/\pi^{\pm}$ p_T	> 500 MeV
$K^{\pm}/\pi^{\pm}$ χ^2_{IP}	> 9
$K^{\pm}/\pi^{\pm}$ Ghost Prob	< 0.8
$K^{\pm}$ $\text{DLL}_{K\pi}$	> 2
$\pi^{\pm}$ $\text{DLL}_{K\pi}$	< 0
$K^{*0}/\bar{K}^{*0}$ m	$630 < m < 2230\,\text{MeV}/c^2$
$K^{*0}/\bar{K}^{*0}$ p_T	> 800 MeV
$B^0_{s,d}$ m	$4867 < m < 5867\,\text{MeV}/c^2$
$B^0_{s,d}$ p_T	$> 5000\,\text{MeV}/c$
$B^0_{s,d}$ DOCA	< 0.3 mm
$B^0_{s,d}$ DIRA	> 0.99
$B^0_{s,d}$ $\chi^2_{\text{vtx}}/\text{ndf}$	< 15
$B^0_{s,d}$ χ^2_{IP}	< 25
$B^0_{s,d}$ χ^2_{VD}	> 81

TABLE 3.1: Requirements in the stripping line StrippingBs2K0stK0stNominalLine used to build candidates.

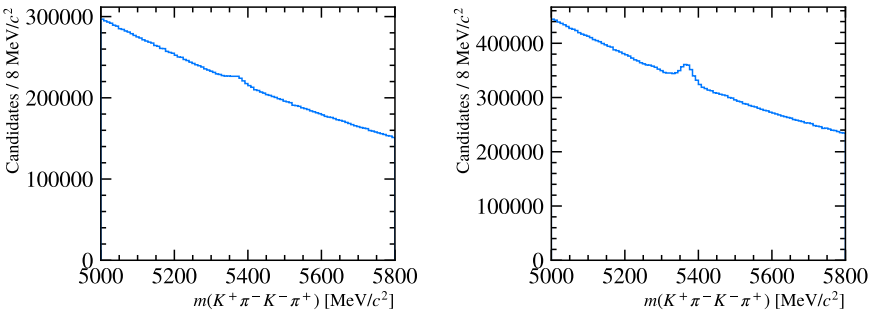

FIGURE 3.1: B-candidate invariant mass distribution of data events passing the stripping requirements for data collected during Run 1 (left) and Run 2 (right). The improved signal-to-background ratio in Run 2 is due to the better PID performance.

Decay	Event Type ID	Type
$B_s^0 \to K^{*0}(892)\bar{K}^{*0}(892)$	13104007	Filtered DST
$B_s^0 \to K^{*0}(892)\bar{K}_0^*(1430)$	13104041	DST
$B_s^0 \to K_0^*(1430)\bar{K}_0^*(1430)$	13104042	DST
$B_s^0 \to \bar{K}^{*0}(892)\phi(1020)$	13104021	DST
$B_s^0 \to \bar{K}^{*0}(892)\rho(770)^0$	13104048	DST
$B_s^0 \to K^+\pi^-K^-\pi^+$ Phase space	13104094	Filtered MDST
$B_d^0 \to K^{*0}(892)\bar{K}^{*0}(892)$	11104002	DST
$B_d^0 \to K^{*0}(892)\phi(1020)$	11104020	MDST
$B_d^0 \to K^{*0}(892)\rho(770)^0$	11104041	MDST
$B_d^0 \to K^+\pi^-K^-\pi^+$	11104094	DST
$\Lambda_b^0 \to pK^-\pi^+\pi^-$	15204011	MDST

TABLE 3.2: Summary of the MC samples used.

- $B^0_{s,d} \to (K^+\pi^-)(K^-\pi^+)$ decays generated flat in phase space: used in the determination of the efficiency across the phase space through a Kernel Density Estimation (KDE) technique.

The main signal MC sample of $B_s^0 \to K^{*0}\bar{K}^{*0}$ decays with event type 13104007 was generated with helicity amplitudes to match those found in Ref. [15]. The MC is filtered to pass the stripping line requirements described in Table 3.1 *except* for the cuts on $\mathrm{DLL}_{K\pi}$, which are applied at a later stage after the PID variables are corrected using the PIDcorr package.

The phase space sample of $B_s^0 \to (K^+\pi^-)(K^-\pi^+)$ decays with event type 13104094 is generated flat in the four-body phase space. It is required that the $m(K^+\pi^-)$ and $m(K^-\pi^+)$ masses are below 1.1 GeV/c^2. Additionally, the same filtering script as above is applied such that all of the stripping line cuts in Table 3.1 are required *except* for the $\mathrm{DLL}_{K\pi}$ cuts.

Due to the nature of the selection and the necessity of having to re-strip the MC samples only full DST samples could be used in the end. The $B_d^0 \to (K^+\pi^-)(K^-\pi^+)$ phase space sample was later generated together with this bunch of samples, and hence it is available in DST format and is re-stripped to remove PID cuts. Regarding backgrounds, rather than generate new DST samples to replace the μDST samples that were already available for $B_d^0 \to \rho^0 K^{*0}$ and $B_d^0 \to \phi K^{*0}$, the full DST $B_s^0 \to \rho^0 K^{*0}$ and $B_s^0 \to \phi K^{*0}$ are used as proxies for the B_d^0 modes. Although the B_s^0 modes for these misIDs are in principle present, they are much more suppressed than the B_d^0 modes and so it should be assumed that misidentified backgrounds with a final state of $K\pi\pi\pi$ or $KKK\pi$ always refer to the B_d^0 decays *physically* but are modelled with the B_s^0 decay MC.

3.1.2 PID CORRECTIONS

The simulation of the detectors dedicated to PID is a non-trivial task and the output PID variables are likely not to be well described in the full simulation of LHCb. Therefore, applying selections on them will produce unavoidable biases. Due to the presence of the PIDK ($\mathrm{DLL}_{K\pi}$) cuts in the stripping line, additional steps are taken to ensure that the PID variables can still be corrected. For the main B_s^0 signal and phase space MC samples (13104007 and 13104094, respectively), a filtering script removes the PIDK cuts from the stripping line. For the rest of the MC samples, as they are full DST, they are re-stripped before running the tupling step to remove all PIDK cuts from the stripping line.

There are three main LHCb packages that use PID calibration data samples to deal with PID in simulations, all based on the track kinematics (p_T and η) and multiplicity (nTracks) of the event of interest – PIDGen, PIDCorr, and PIDCalib2. PIDGen resamples the PID response given a position in the variable space and the distribution of the PID variables in calibration data. PIDCorr constructs a function that transforms the PID variables in simulation such that they are distributed as in calibration data. PIDCalib2 estimates the efficiency of a set of cuts in the PID variables, given the real efficiency from calibration data.

Here the PIDCorr package is used to obtain corrected distributions for the PID variables in MC. These are obtained not only for PIDK but also for ProbNNk, ProbNNpi and ProbNNp, for each of the four final state particles (totalling 16 corrected distributions in total). There is a correction for the well-known discrepancy between the nTracks in data and simulation by passing a scaling factor when running PIDCorr. The scaling factor was determined by looking at the nTracks distribution in signal $B_s^0 \to K^{*0}\bar{K}^{*0}$ simulation and data in Run 1 and Run 2 and dividing the mean of the distribution in data by that of in simulation. The factor determined was the same (to 2 significant figures) in both Run 1 and Run 2 as 1.22.

The output corrected distributions of PIDCorr are used as input to optimise the PID cuts, but the efficiency is measured using PIDCalib2. This choice was made because the agreement between the PIDCorr-corrected ProbNN variables in simulations and sWeighted data was not very good, especially in regions where there are peaks in the data.

3.1.3 KINEMATIC REWEIGHTING

Additional corrections are applied to the MC to more closely align it with data. Specifically, we correct the following distributions in MC:

- p of the B candidate.
- p_T of the B candidate.
- min of all the final state TRACK_CHI2NDOF[3].
- max of all the final state TRACK_CHI2NDOF.

The corrections are obtained with a FoldingReweighter using a GBReweighter as the base from the hep-ml package [74]. The target distribution is obtained

[3]This is the χ^2 per number of degrees of freedom of the best track fit.

by `sWeighting` data where the `sWeights` [75, 76] are derived from a preliminary fit to data described in detail in Sec. 3.1.6. The original distribution is the B_s^0 signal MC sample and the `PIDCorr` corrected stripping line `PIDK` cuts applied. The distributions before and after corrections are shown in Fig. 3.2.

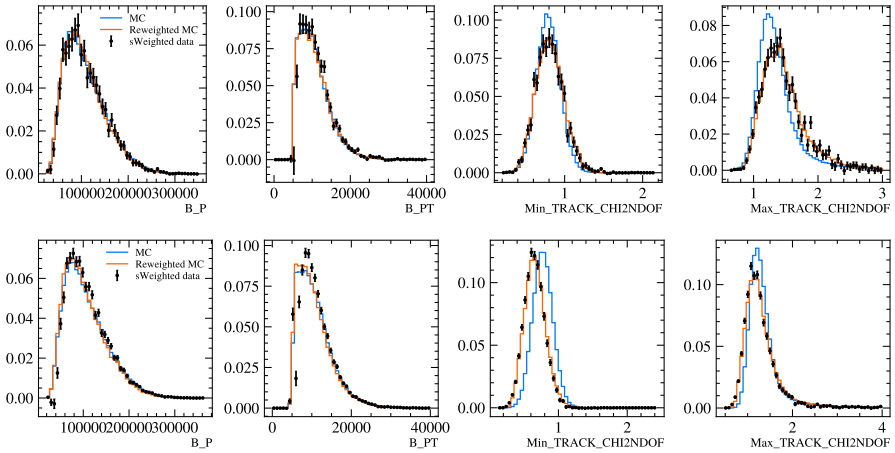

FIGURE 3.2: Variables used to reweight the signal B_s^0 MC before and after kinematic reweighting for Run 1 (top) and Run 2 (bottom).

3.1.4 PRE-SELECTION

An initial selection is applied to both data and MC in the same way. These cuts are designed to exploit "easy gains" by requiring a high signal efficiency (> 95%) whilst removing a good fraction of the background. The trigger requirements used in the data analysed in this thesis are detailed in Table 3.3. The pre-selection cuts are detailed in Table 3.4. Note in particular the cuts under the heading "**Fiducial PID**" are designed to align the PID samples as closely as possible with the PID calibration samples in order to try to ensure that the PID corrections can be reliably used.

A three-body cut on the $m(K^+K^-\pi^\pm)$ invariant masses is used to exclude contamination from the charm contribution $B_s^0 \to (D_s^- \to K^-K^+\pi^-)\pi^+$, which shares the $K^+\pi^-K^-\pi^+$ final state with $B_{s,d}^0 \to K^{*0}\bar{K}^{*0}$. The cut is placed to exclude candidates with $1946.35\,\text{MeV}/c^2 < m(K^+K^-\pi^\pm) < 1990.35\,\text{MeV}/c^2$.

The MC samples are truth-matched, *i.e.*, charged kaons and pions are required to have the corresponding simulation IDs, as well as being produced in the decay of the simulated B-meson, either directly or through the defined intermediate states.

The PV-constrained B mass for pre-selected candidates in data is shown in Fig. 3.3. The total number of pre-selected data candidates is 131 761 in Run 1 and 623 573 in Run 2. Both signal peaks from B_s^0 and B_d^0 decays are visible, although there is still a huge background contamination which needs to be reduced.

L0 Any of:
L0Global TIS – a.l.o. non-signal tracks fired any of the L0 trigger lines
L0Hadron TOS – a.l.o. signal tracks fired the hadronic L0 trigger
Hlt1 Any of:
Hlt1TrackAllL0 TOS – a.l.o. high-quality and high-p_T signal track displaced from PV
Hlt1TrackMVA TOS – like Hlt1TrackAllL0, but with different selections
Hlt1TwoTrackMVA TOS – like Hlt1TrackMVA, but for two tracks
Run 1: Hlt2 Any of:
Hlt2Topo2BodyBBDT TOS – two-body topological trigger, triggered on signal
Hlt2Topo3BodyBBDT TOS – three-body topological trigger, triggered on signal
Hlt2Topo4BodyBBDT TOS – four-body topological trigger, triggered on signal
Run 2: Hlt2 Any of:
Hlt2Topo2Body TOS – two-body topological trigger, triggered on signal
Hlt2Topo3Body TOS – three-body topological trigger, triggered on signal
Hlt2Topo4Body TOS – four-body topological trigger, triggered on signal

TABLE 3.3: Trigger requirements used when selecting candidates. In the descriptions, a.l.o. stands for at least one.

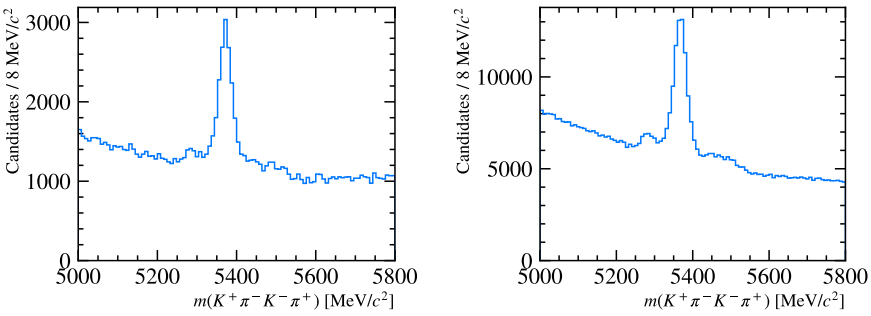

FIGURE 3.3: Reconstructed PV-constrained B-candidate mass for pre-selected data events in Run 1 (left) and Run 2 (right).

B_s^0 Cuts	
$B^0_{s,d}$ (χ^2_{vtx}/ndf)	< 12
$B^0_{s,d}$ (τ)	> 0 ps
$K^\pm/\pi^\pm$ Cuts	
$K^\pm/\pi^\pm$ (χ^2_{track}/ndf)	< 4
Mass Cuts	
$m(B^0_{s,d})$	$5000 < m < 5800\,\text{MeV}/c^2$
$m(K^\pm\pi^\mp)$	$630 < m < 1600\,\text{MeV}/c^2$
$m(K^+K^-\pi^\pm)$	$m < 1946.35$ && $m > 1990.35\,\text{MeV}/c^2$
Fiducial PID	
$K^\pm/\pi^\mp$ η	$1.9 < \eta < 4.9$
$K^\pm/\pi^\mp$ p	$3 < p < 100\,\text{GeV}/c$
$K^\pm/\pi^\pm$ (`hasRich`)	True
$K^\pm/\pi^\pm$ (`InAccMuon`)	True
$K^\pm/\pi^\pm$ (`IsMuon`)	False
`nTracks` (Run 1 only)	< 500
`nSPDHits` (Run 2 only)	< 1000
Other	
$B^0_{s,d}/K^{*0}/\bar{K}^{*0}$ (χ^2_{IP})	> 0
$K^{*0}/\bar{K}^{*0}$ (χ^2_{FD})	> 0
DTF Status	== 0 (fit converged)

TABLE 3.4: Summary of the pre-selection cuts applied to data and all MC samples. FD stands for flight distance.

3.1.5 COMBINATORIAL BACKGROUND SUPPRESSION

An MVA is used to reduce the amount of combinatorial background in the collision data. In this analysis, a Boosted Decision Tree (BDT) is used from the `XGBoost` [77] Python library. In order to ensure the signal MC reflects the data properly, the PID cuts from the stripping line must be applied to the corrected PID variables in the signal MC before the samples are used to train the BDT.

Before training the BDT, two additional steps are required relating to the signal MC samples. Firstly, the MC samples should contain the PID cuts that were removed from the stripping line but now on the corrected PID variables. Additionally, the exact number of simulated events that are generated for each data category (per year and polarity) is somewhat arbitrary, so a weighting procedure is required in order the match the corresponding relative proportions of signal that exist in data. A simplified mass fit is performed on pre-selected data in order to

estimate the number of expected signal events in each data-taking year. This initial mass fit models only three components: signal decays of B_s^0 and B_d^0 to $K^{*0}\bar{K}^{*0}$, and combinatorial background. The fit model and the results for each year is described in more detail in App. B.1.1.
In this analysis, two different BDTs are trained — one for Run 1 (2011 and 2012) and one for Run 2 (2015, 2016, 2017 and 2018). The expected signal yields for each year are taken as a fraction of the total number of expected signal events for that Run and used to weight the signal MC events appropriately. Some MVA algorithms do not perform as well when weights greater than one are used. Therefore, the weights are additionally transformed to down-weight only, as shown in Eq. 3.1

$$\begin{aligned} w_i &= \frac{y_i}{\sum_i y_i} \frac{\sum_i x_i}{x_i} \,, \\ \overline{w}_i &= \frac{w_i}{\mathrm{Max}(w_i)} \,, \end{aligned} \tag{3.1}$$

where $\overline{w}_i$ are the down-weights (w_i the weights), y_i the yields and x_i the number of events for each year i within a Run.

In total, 19 variables are used as input for the BDT. They are listed and described in Table 3.5. A variety of different topological and kinematic variables were tested as input features. Initially, the variables chosen in the Run 1 time-dependent [15] and time-integrated [16] analyses were looked at. In addition to the initial Run 1 variable sets, some isolation variables were trialled. Specifically, the cone p_T-asymmetry variable and the vertex isolation variables. The vertex isolation variables, `SmallestDeltaChi2OneTrack` and `SmallestDeltaChi2TwoTracks`, are constructed by considering adding an additional one or two track(s) to the vertex of interest and saving the smallest change in fit quality ($\delta\chi^2$) as a result of including the extra track(s). For a good vertex fit, which is expected for a signal event, adding additional tracks should significantly change the fit quality of the vertex, whereas for a vertex which is less likely to be signal, adding additional tracks would not make as large an impact. Therefore, small values of these vertex isolation variables are expected for backgrounds and larger values for signal events. The cone isolation variables *e.g.* branch name `B_ptasy_1_50` construct a cone with a half-angle of 1.50 rad around the signal decay vertex. The sum of the p_T of the tracks inside the cone is calculated with and without the signal tracks and this asymmetry is then the value recorded. Different cone radii were looked at (1.5, 1.7 and 1.9 rad) but little difference was found between them and the overlap was significant enough that only one cone radius was considered.

During this data selection it was found that the vertex isolation variables in particular provided a good boost to the discriminating power of the BDT, as shown in Fig. 3.4. Comparisons between the signal and background distributions for the input variables of the BDT are shown in Figs. 3.7 and 3.8. Additionally, the non-χ^2 versions of some variables are also included as well as the χ^2 versions *e.g. both* B_IPCHI2_OWNPV *and* B_IP_OWNPV are included. The correlations between input variables for the signal and background training samples are shown in App. B.1 (see Figs. B.2 and B.3). Whilst some variables show relatively high

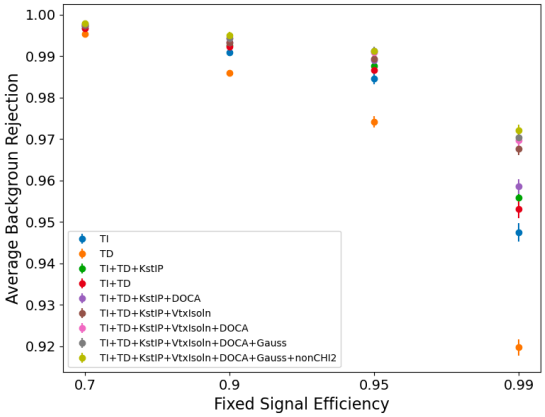

FIGURE 3.4: Background rejection achieved (averaged across the five BDTs) for a given signal efficiency for Run 2. TI refers to the variable set used in the previous time-integrated analysis [16], and TD corresponds to the set explored in the previous time-dependent analysis [15].

correlations, all are providing some unique information as the area under curve score increased when including them. Given that BDTs are generally robust to large variable sets and the increase in performance from their inclusion, it was decided to leave these variables with relatively high correlations in.

For the purposes of the BDT, signal is defined as pre-selected and truth-matched MC samples of $B_s^0 \to K^{*0}(892)\bar{K}^{*0}(892)$ decays. Background is defined as data events in an upper mass sideband of $5600\,\text{MeV}/c^2 < m(K^+\pi^-K^-\pi^+) < 5800\,\text{MeV}/c^2$, as the combinatorial background will dominate in pre-selected data in this mass range.

In order to maximise the use of the available data and simulation samples, k-fold cross-validation is used with $k = 5$ folds. In practice, for each Run, rather than training a single BDT, five BDTs are trained and the background and signal samples are both split into five sub-samples. For each BDT, four of the sub-samples are used for training with the remaining sample used for testing/validation. The outcome is five BDTs, which have collectively been trained using all of the available data (although each BDT only sees 80% each) but each tested/validated with data on which they were not trained. The samples are split into sub-samples using the modulus of their event number (*i.e.* event_number mod 5) which resulted in five pseudo-randomised and approximately equal-sized samples. The event number has the advantage that it can be used to easily recover later which event was used for each BDT.

BDTs are generally quite resilient to overtraining. However, it is still important to check the BDT output to ensure that there is no overtraining. Overtraining is checked by looking at the BDT response for signal and background between the testing and training samples. A Kolmogórov-Smirnov (KS) test is performed and there does not appear to be any significant overtraining (see Figs. 3.5 and 3.6). The KS statistic between two distributions will have a value close to 0 if the two

Variable	Description
$B^0_{s,d}$	
$\log_{10}$(1-B_DIRA_OWNPV)	Pointing angle of the B meson w.r.t. the PV
$\log_{10}$(B_IPCHI2_OWNPV)	Impact parameter χ^2 of the B w.r.t. the PV
$\log_{10}$(B_FDCHI2_OWNPV)	Flight distance χ^2 of the B w.r.t. the PV
B_PT	Transverse momentum of the B
B_IP_OWNPV	Impact parameter of the B w.r.t. the PV
B_FD_OWNPV	Flight distance of the B w.r.t. the PV
B_ETA	Psuedorapidity of the B
B_ENDVERTEX_CHI2_NDOF	The vertex χ^2 of the B per number of degrees of freedom
B_DOCA	Distance of closest approach of the B w.r.t. the PV
$K^{*0}/\bar{K}^{*0}$	
$\log_{10}$(Kst(b)_IPCHI2_OWNPV)	Impact parameter χ^2 of the $K^{*0}/\bar{K}^{*0}$ w.r.t. the PV
Kst(b)_IP_OWNPV	Impact parameter of the $K^{*0}/\bar{K}^{*0}$ w.r.t. the PV
K/π	
MIN_PT_daughters	Minimum p_T of the four daughter particles
$\log_{10}$(Kp_pim_MIN_IPCHI2)	Minimum of K^+ IP-χ^2 and π^- IP-χ^2 w.r.t. the PV
$\log_{10}$(Km_pip_MIN_IPCHI2)	Minimum of K^- IP-χ^2 and π^+ IP-χ^2 w.r.t. the PV
Isolation variables	
B_ptasy_1_50	Asymmetry in sum of p_T of tracks in cone around the decay vertex with and without the signal tracks
B_SmallestDeltaChi2OneTrack	Smallest change in fit quality when adding an additional track to the vertex
B_SmallestDeltaChi2TwoTracks	Smallest change in fit quality when adding an additional two tracks to the vertex

TABLE 3.5: Input variables used in the combinatorial background BDT

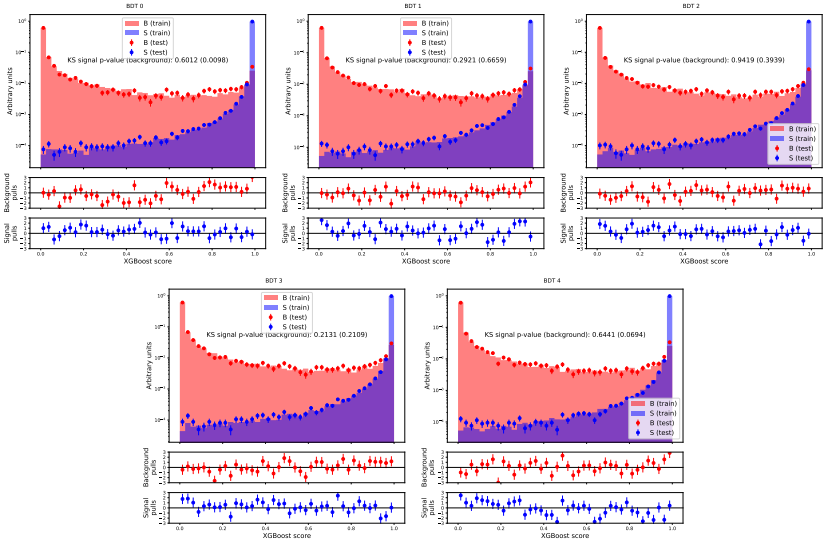

FIGURE 3.5: BDT response with KS test for signal and background for each of the five BDTs trained for Run 1.

distributions are not compatible with being the same. If overtraining has occurred, then the KS statistic between the BDT output for the test sample vs. the training sample would be 0 (the test and train samples have come from the same underlying distribution so their BDT outputs should be similar – if they are not then likely the BDT has overtrained on the test sample). A very high (close to 1) value of the KS statistic suggests that the statistical fluctuations are too small so ideally the value should be 0.5 but anything reasonably bigger than 0 and smaller than 1 is acceptable.

A grid search was performed to try and determine if any performance boost could be found by choosing more optimal values of the hyper-parameters of the BDT. Details of this are described in App. B.1. It was determined that the best parameters (without overtraining) are to use 400 estimators, a max depth of 3 and a learning rate of 0.1.

Once the BDTs have been trained and in order to make sure the BDT does not bias the value of some of these variables, it is important to check that the BDT response does not correlate highly with the variables that will need to be fitted later on. The correlations of each of the potential fit variables with the BDT output are shown in Fig. 3.9. The correlation statistic chosen here is the Kendall Tau test which tests the independence of the output distributions of the two variables. It is clear that the peaking variables (*i.e.* the masses) do not correlate strongly at all with the BDT output, but the decay time and decay time error do. On the one hand, this is not too surprising, as these variables are also a good way to distinguish between signal and background. On the other hand and since this is a time-integrated analysis, possible correlations with time are not of concern, but should be taken into account in future time-dependent analysis. Additional material is presented

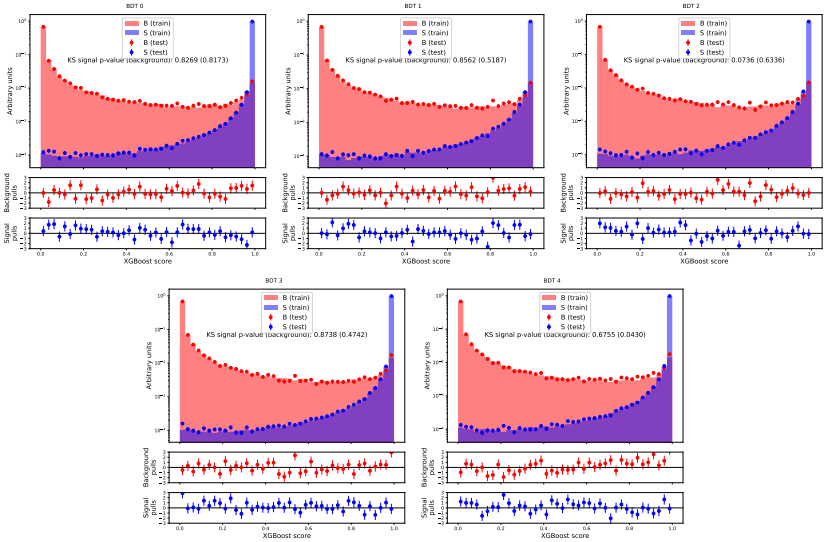

FIGURE 3.6: BDT response with KS test for signal and background for each of the five BDTs trained for Run 2.

in App. B.1.4

It is also desirable to check for correlations between the invariant B mass, which is used for determining the signal and background yields, and the 5D space of independent fit variables (*i.e.* the two-body masses and helicity angles). In particular when deriving `sWeights` from an invariant mass fit it is required that the discriminating variable (the reconstructed B-mass) is statistically independent of the control variables (helicity angles and two-body masses). The Kendall Tau correlations of the suggested fit variable (the PV-constrained B-mass) with the fit variables are shown in Fig. 3.10 which shows no substantial correlation. In Fig. 3.10, it is also clear that the PV-constrained B-mass correlates relatively strongly (in background) with the decay time using the PV *and* mass constraints but does *not* correlate with the PV-only constrained lifetime. Once again, this is not a concern for this analysis but any future time-dependent analysis should therefore choose to fit the PV-only constrained decay time, rather than that obtained with the B-mass constraints, as this does not have any correlation with the discriminating variable (the PV-constrained B-mass).

3.1.6 PRELIMINARY MASS FITS

In order to determine initial signal and misidentified backgrounds yields and hence to optimise the PID cuts described in this section, a preliminary mass fit model is built and fitted to data, including all background contributions considered in the final mass model.

A loose combinatorial BDT cut is applied of 0.2, which keeps 99.9% of signal (estimated from truth-matched MC) while rejecting approximately 78.9% (85.4%)

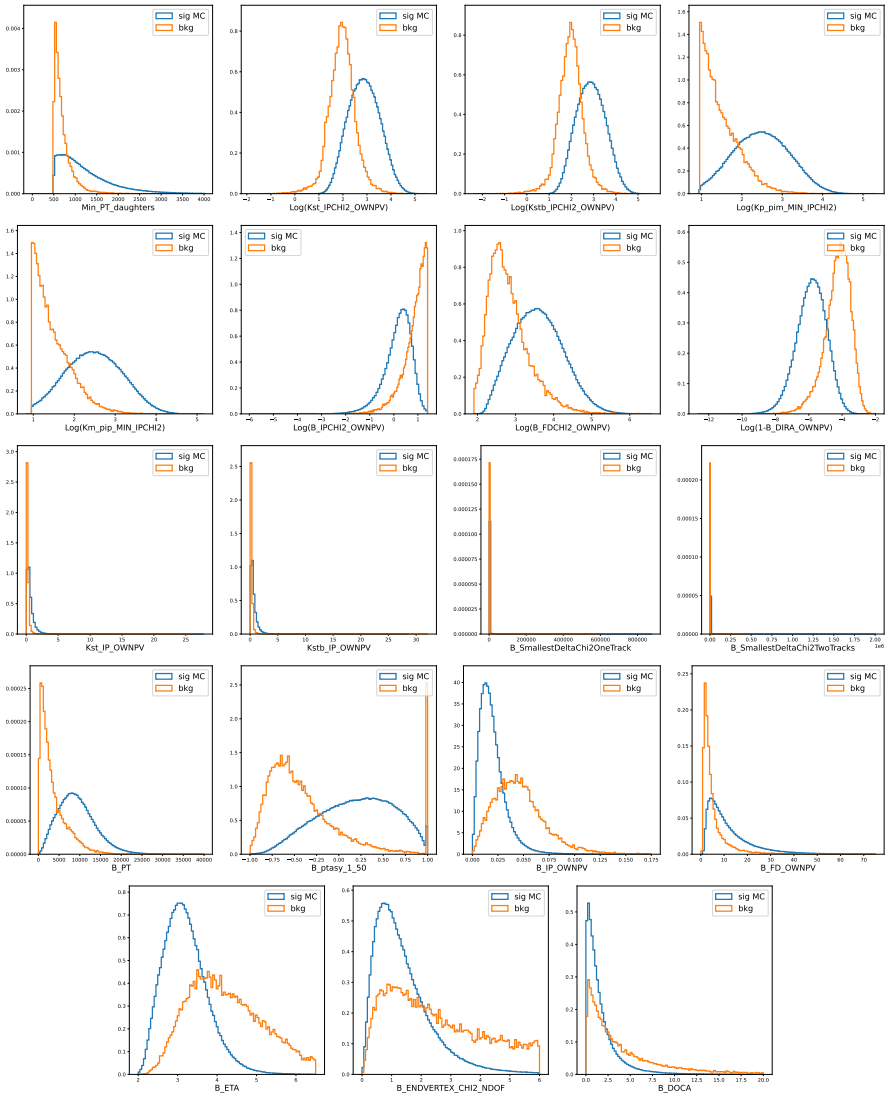

FIGURE 3.7: Distributions of the combinatorial BDT input variables in signal and background for Run 1.

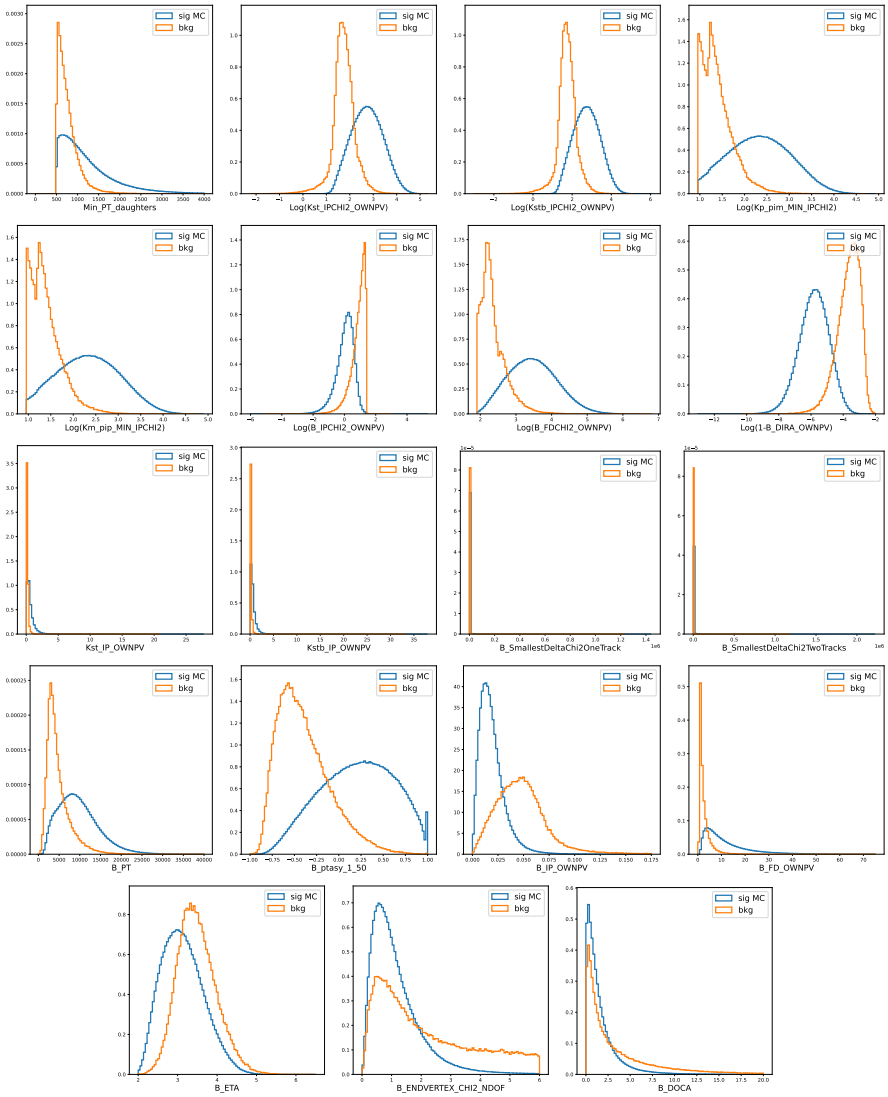

FIGURE 3.8: Distributions of the combinatorial BDT input variables in signal and background for Run 2.

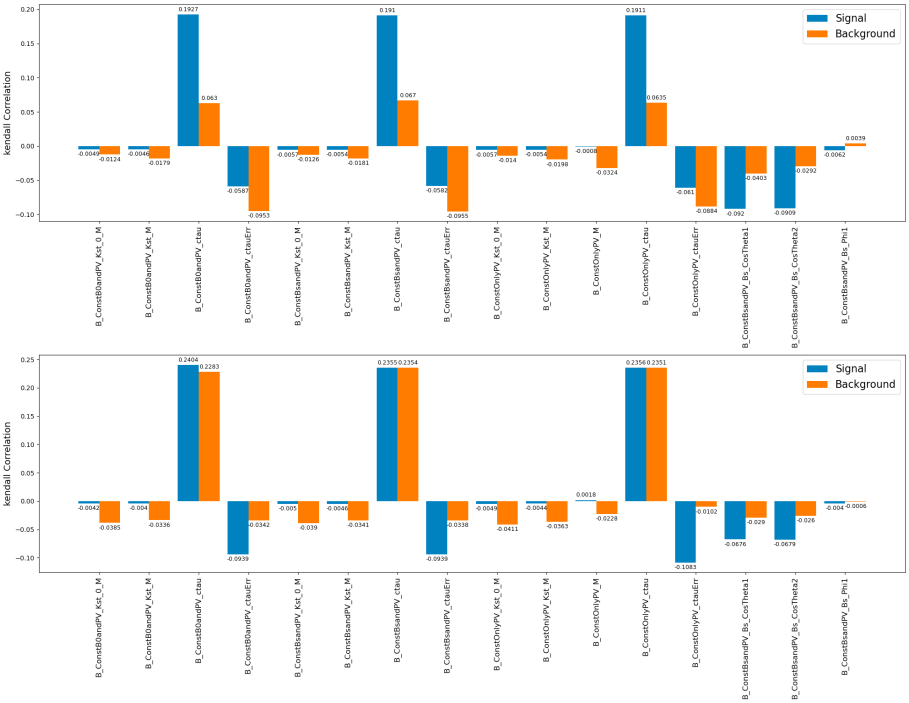

FIGURE 3.9: Correlations (using Kendall Tau statistic) between the possible fit variables and the BDT response for Run 1 (top) and Run 2 (bottom)

of the combinatorial background in Run 1 (Run 2). By removing most of the combinatorial background, the misID contributions become clearer and easier to fit.

Rather than fitting just the nominal 4-body invariant mass, a simultaneous fit is performed between the nominal 4-body mass, $m(K^+\pi^-K^-\pi^+)$, the 4-body mass with the hypothesis of a kaon swapped to a pion, $m(K^\pm\pi^\mp\pi^+\pi^-)$, and with a pion mass hypothesis swap to a kaon, $m(K^+K^-K^\pm\pi^\mp)$. In the $m(K^\pm\pi^\mp\pi^+\pi^-)$ fit, for example, the misID component of $B^0_d \to \rho^0 K^{*0}$ will be a sharp peak, rather than a smeared-out contribution. The main purpose of the simultaneous, preliminary fits is to extract a robust estimate of the misID yields in order to have a starting point for the PID optimisation. The efficiency of the PID cuts on MC can then be used to determine the expected number of misID events in the signal regions for a given set of PID cuts.

The shapes for the signal and misID shapes are fitted in their respective MC samples and then fixed in the fits to data. Depending on the mass projection and decay, the shapes fit to MC are either the Hypatia distribution [78] with $\beta = 0$ and $\zeta = 10^{-5}$ or the Johnson SU function [79]. See Table 3.6 for a list of which shapes are used for each component. The shape of the $B^0_d \to K^{*0}\bar{K}^{*0}$ is taken to be the same as the shape from the fit to $B^0_s \to K^{*0}\bar{K}^{*0}$ MC but shifted down by the mass difference between the B^0_d and B^0_s mesons taken to be 87.42 MeV/c^2 [3]. The same shift is

FIGURE 3.10: Correlations (using Kendall Tau statistic) between the possible fit variables and the PV-constrained B-mass used for fitting for Run 1 (top) and Run 2 (bottom)

applied to extract the shapes for $B_d^0 \to \rho^0 K^{*0}$ from $B_s^0 \to \rho^0 K^{*0}$ MC and $B_d^0 \to \phi K^{*0}$ from $B_s^0 \to \phi K^{*0}$ MC. The shape of the combinatorial background is modelled as an exponential, where the shape parameter floats in the data fits. For the partially reconstructed backgrounds, a dedicated sample of 100 000 $B_s^0 \to K^+\pi^-K^-\pi^+\pi^0$ events was generated with `RapidSim` and a KDE is used to model the shape. The rationale for using a KDE with a dedicated sample is that it then becomes possible to share the yield between the different projections as the shape is known in every projection. The yields of the signal and misID components are shared between the three simultaneous fits. The results of the MC fits are described in Appendix B.1.5. The total list of fit components is as follows:

- $B_s^0 \to K^{*0}\bar{K}^{*0}$
- $B_d^0 \to K^{*0}\bar{K}^{*0}$
- $B_d^0 \to \rho^0 K^{*0}$
- $B_d^0 \to \phi K^{*0}$
- $\Lambda_b^0 \to pK^-\pi^+\pi^-$
- Combinatorial background
- Partially reconstructed background

Additionally, a global shift for the means and scale factor for the widths is allowed to float in the fits to absorb any discrepancies between data and MC. For each

Component	$m(K^+K^-K^\pm\pi^\mp)$	$m(K^+\pi^-K^-\pi^+)$	$m(K^\pm\pi^\mp\pi^+\pi^-)$
$B_s^0 \to K^{*0}\bar{K}^{*0}$	Johnson SU	Hypatia	Johnson SU
$B_d^0 \to K^{*0}\bar{K}^{*0}$	Johnson SU	Hypatia	Johnson SU
$B_d^0 \to \rho^0 K^{*0}$	Johnson SU	Johnson SU	Johnson SU
$B_d^0 \to \phi K^{*0}$	Johnson SU	Johnson SU	Johnson SU
$\Lambda_b^0 \to pK^-\pi^+\pi^-$	Johnson SU	Johnson SU	Johnson SU
Partially reconstructed	KDE	KDE	KDE
Combinatorial	Exponential	Exponential	Exponential

TABLE 3.6: List of which functions were used to fit each component in each mass projection.

projection then the means/widths of each component are:

$$\begin{aligned} \mu_i &= \mu_i^{\mathrm{MC}} + \delta_\mu \ , \\ \sigma_i &= \sigma_i^{\mathrm{MC}} \times S_\sigma \ , \end{aligned} \tag{3.2}$$

where $\mu_i^{\mathrm{MC}}(\sigma_i^{\mathrm{MC}})$ is the mean (width) of the fit to MC and the δ_μ and S_σ are the global shifts and scales respectively that vary globally in each fit projection.

To speed up the fit, a custom fitting framework is built in Python, composed of `numba`-accelerated [80] PDFs, some of which come from the `numba-stats` library, with the fit minimisation performed by `Minuit` via the `iminuit` [81] package. The Hypatia PDFs are costly to evaluate (as there is no analytic integral) and `RooFit` [82] will only evaluate these single-threaded, whereas a `numba`-based implementation allows for parallel evaluation which reduces the time taken for a mass fit from multiple hours to a few minutes.

The results of the simultaneous fit are shown in Figs. 3.11 and 3.12, and the fit parameters are displayed in Table 3.7. Note that the covariance matrix, and hence the uncertainties, from the simultaneous fits reported by `Minuit` and `Hesse`, which is estimated as the inverse of the Hessian matrix, *are not correct* as the same dataset is fitted three times. A bootstrapping method would be necessary to estimate the correct statistical uncertainties. Since only the central values are to be extracted from this part, no effort is made in this respect. As can be seen in Table 3.7, the yield for $\Lambda_b^0 \to pK^-\pi^+\pi^-$ is negative due to a loose PID selection applied before the fit:

- All final state particles have `ProbNNp` < 0.9.
- Both kaons have `ProbNNk` > 0.1.

and so is neglected in the final selected fits.

3.1.7 SELECTION OPTIMISATION

The `PIDCorr` package is used to obtain corrected `ProbNN` variables with more data-like distributions. For each of the final state hadrons, the variables `ProbNNk`, `ProbNNpi`, and `ProbNNp` are used, resulting in a total of 12 variables.

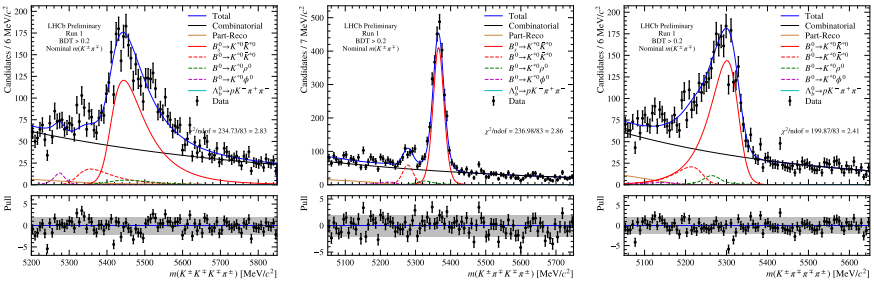

FIGURE 3.11: Results of the simultaneous preliminary fit to Run 1 data. Data is shown in black points, the total fit as a solid blue line, combinatorial as a solid black line, partially reconstructed backgrounds as a solid brown line, $B_s^0 \to K^{*0}\bar{K}^{*0}$ as a solid red line, $B_d^0 \to K^{*0}\bar{K}^{*0}$ as a dashed red line, $B_d^0 \to \rho^0 K^{*0}$ as a dashed green line, $B_d^0 \to \phi K^{*0}$ as a dashed purple line and $\Lambda_b^0 \to pK^-\pi^+\pi^-$ as a solid cyan line.

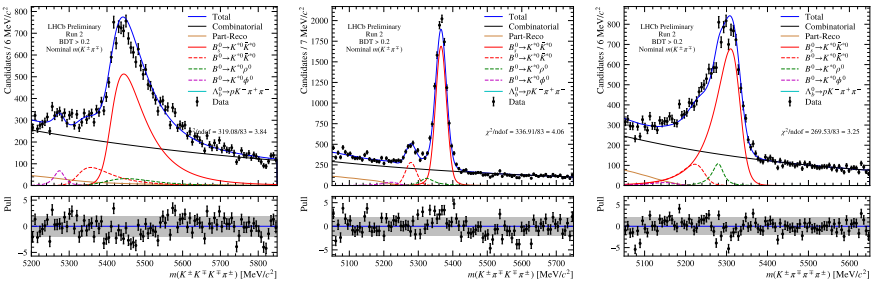

FIGURE 3.12: Results of the simultaneous preliminary fit to Run 2 data. Data is shown in black points, the total fit as a solid blue line, combinatorial as a solid black line, partially reconstructed backgrounds as a solid brown line, $B_s^0 \to K^{*0}\bar{K}^{*0}$ as a solid red line, $B_d^0 \to K^{*0}\bar{K}^{*0}$ as a dashed red line, $B_d^0 \to \rho^0 K^{*0}$ as a dashed green line, $B_d^0 \to \phi K^{*0}$ as a dashed purple line and $\Lambda_b^0 \to pK^-\pi^+\pi^-$ as a solid cyan line.

Searching for the optimal cut in 12+1 dimensions (12 `ProbNN` variables and then the combinatorial BDT) would be extremely time-consuming and difficult to verify. Instead, some of the `ProbNN` variables are combined to roughly correspond to each of the mis-identified decays considered above to reduce the dimensionality to only 3+1.

Parameter	Run 1	Run 2
bs2kstkst_N	2301 ± 61	9595 ± 108
bd2kstkst_N	332 ± 29	1505 ± 53
bd2rhokst_N	119 ± 55	756 ± 87
bd2phikst_N	46 ± 13	227 ± 29
lb2pkpipi_N	-50 ± 3	-41 ± 212
bkg_prec_N	129 ± 28	937 ± 57
kpkp_bkg_comb_N	4107 ± 132	18127 ± 223
kpkp_bkg_comb_alpha	$(166.7 \pm 2) \times 10^{-5}$	$(148.3 \pm 1) \times 10^{-5}$
kpkp_mu_shift	2.7 ± 0.4	3.0 ± 0.2
kpkp_sigma_scale	1.01 ± 0.03	1.00 ± 0.01
kkkp_bkg_comb_N	3942 ± 117	17626 ± 222
kkkp_bkg_comb_alpha	$(1.5 \pm 0.1) \times 10^{-3}$	$(1.22 \pm 0.05) \times 10^{-3}$
kkkp_mu_shift	8.2 ± 2.0	7.6 ± 1.0
kkkp_sigma_scale	0.99 ± 0.03	0.95 ± 0.01
kppp_bkg_comb_N	3361 ± 110	14398 ± 189
kppp_bkg_comb_alpha	$(2.2 \pm 0.1) \times 10^{-3}$	$(1.96 \pm 0.06) \times 10^{-3}$
kppp_mu_shift	5 ± 2	3.4 ± 0.6
kppp_sigma_scale	0.92 ± 0.03	0.91 ± 0.01

TABLE 3.7: Results of the preliminary simultaneous fits to Run 1 and Run 2 data. Note that the quoted uncertainties are incorrect (see text for more details).

- `min_k_ProbNN` = `min(`
  `K1_ProbNNk` × (1 − `K1_ProbNNpi`),
  `K2_ProbNNk` × (1 − `K2_ProbNNpi`)
  `)`
- `min_pi_ProbNN` = `min(`
  `pi1_ProbNNpi` × (1 − `pi1_ProbNNk`),
  `pi2_ProbNNpi` × (1 − `pi2_ProbNNk`)
  `)`
- `max_p_ProbNN` = `max(`
  `K1_ProbNNp, K2_ProbNNp,`
  `pi1_ProbNNp, pi2_ProbNNp`
  `)`

such that `min_k_ProbNN` should mostly correspond to discriminating between signal and $B^0_d \to \rho(770)^0 K^{*0}(892)$ decays, `min_pi_ProbNN` between signal and $B^0_d \to \phi(1020) K^{*0}(892)$ decays and `max_p_ProbNN` which is the `max` of `ProbNNp` over all four final state hadrons should reject Λ^0_b misIDs.

Variable	Optimal cut Run 1	Optimal cut Run 2
BDT	> 0.989	> 0.960
`min_k_ProbNN`	> 0.454	> 0.600
`min_pi_ProbNN`	> 0.273	> 0.047
`max_p_ProbNN`	< 0.563	< 0.949
B^0_d significance	12.6	33.4

TABLE 3.8: Optimal cut points from the 4D `Basin-Hopping` minimisation and the value of the FoM for the B^0_d significance in Run 1 and Run 2. These cut values are used in the full selection.

The Figure of Merit (FoM) to be optimised is the B^0_d significance, defined as

$$\frac{S}{\sqrt{S+B}} \tag{3.3}$$

where S is the expected number of signal events in the signal window and B is the sum of the expected number of combinatorial and mis-identified background events in the same signal window. The choice for the signal window is around the invariant mass of the B^0_d where the window is defined as $\pm 3\sigma$ within the peak. The value of σ is taken from the preliminary fit to data. The measurement of $L_{K^{*0}\bar{K}^{*0}}$ is proportional to the ratio of longitudinal branching fractions and as the B^0_d mode has the smaller yield it seems reasonable to optimise for the significance in the B^0_d window.

The optimal cuts are found by using the `Basin Hopping` [83] algorithm implemented in `SciPy` [84]. This is a global minimisation technique that tries to avoid the optimisation getting stuck on local minima by perturbing the current minima to look for a lower point. This allows to robustly find the most optimal point for the FoM without having to perform a costly 4D grid search.

The pseudo-FoM scans for the significance in the B^0_d window for Run 1 and Run 2 are shown in Figs. 3.13 and 3.14, respectively, and the optimal cut values are shown in Table 3.8. The red-dashed lines representing the optimal cut points from the `Basin-Hopping` minimisation do not quite line up with the peaks from the pseudo-FoM scans. This is to be expected as the scans are effectively optimised in a 3D space with the fourth dimension discretised into 11 points for each of the four plots whereas the `Basin-Hopping` minimisation is looking at the whole 4D space. The FoM scans are more of a cross-check to ensure that the minimisation is going to roughly the correct minimum in a way that can be easily represented without trying to visualise the full 4D space.

3.1.8 PEAKING BACKGROUND VETOES

In addition to the combinatorial background, there are also many specific decays that can contribute to the overall background. Most of these backgrounds

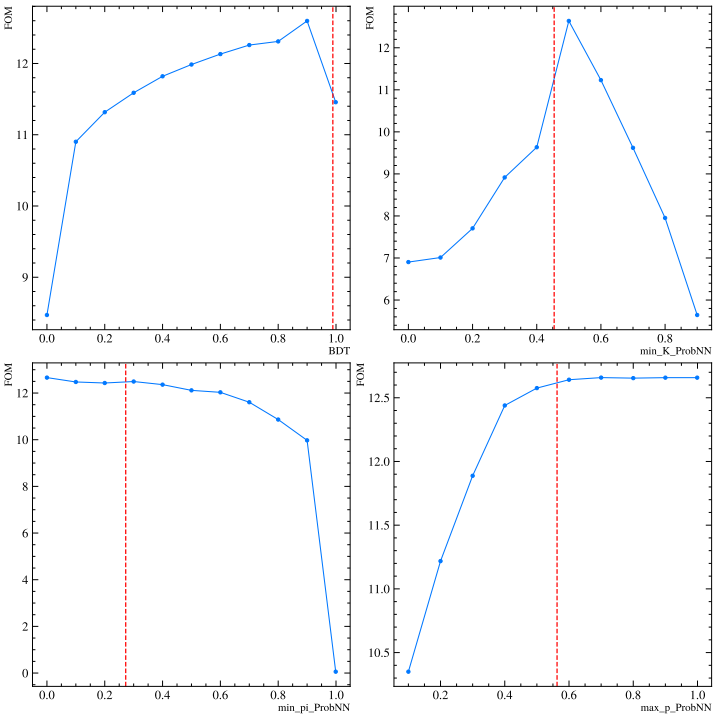

FIGURE 3.13: Pseudo-FoM scans for the 4D selection optimisation for Run 1. The red dashed lines show the optimal point from the `Basin-Hopping` minimisation.

involve the favoured (w.r.t. $b \to s$) $b \to c$ transitions and so most of the considered backgrounds involve charmed hadrons. Although the nominal analysis region in $m(K^{\pm}\pi^{\mp})$ is set below the charm threshold, it is possible that other decays of a B^0_s or B^0_d meson can share a final state with $B^0_{s,d} \to K^{*0}\bar{K}^{*0}$ decays, *i.e.* $K^+\pi^-K^-\pi^+$. In this analysis, backgrounds from $B^0_s \to (D^-_s \to K^-K^+\pi^-)\pi^+$, $B^0_d \to (D^- \to K^+K^-\pi^-)\pi^+, B^0_s \to (D^-_s \to K^-\pi^+\pi^-)K^+, B^0_d \to (D^0 \to K^+K^-)\pi^+\pi^-$, $B^0_d \to (D^0 \to \pi^+\pi^-)K^+K^-$ and any decays with intermediate $\pi^+\,\pi^-$ and $K^-\,K^+$ resonances (for example, ρ^0 and ϕ mesons) may contribute to the different mass spectra. These backgrounds are searched for by constructing the two- and three-body invariant masses $m(K^+K^-)$, $m(\pi^+\pi^-)$, $m(K^+K^-\pi^{\pm})$ and $m(K^{\pm}\pi^+\pi^-)$ and looking for any obvious peaks at the nominal background pole masses.

3.1.8.1 PEAKING BACKGROUNDS IN PRE-SELECTED DATA

The results of these searches in the pre-selected data without the full selection are shown in Figs. 3.15 and 3.16, for Run 1 and Run 2 respectively. Clearly, there is an evident contribution from $D^{\pm}_s$ mesons in the $m(K^+K^-\pi^{\pm})$ invariant mass and from D^0 mesons in the $m(K^+K^-)$ invariant mass. There are perhaps some smaller contributions from $D^{\pm}_s$ in $m(K^{\pm}\pi^-\pi^+)$ and ρ^0 or ω mesons in the $m(\pi^+\pi^-)$ mass which are

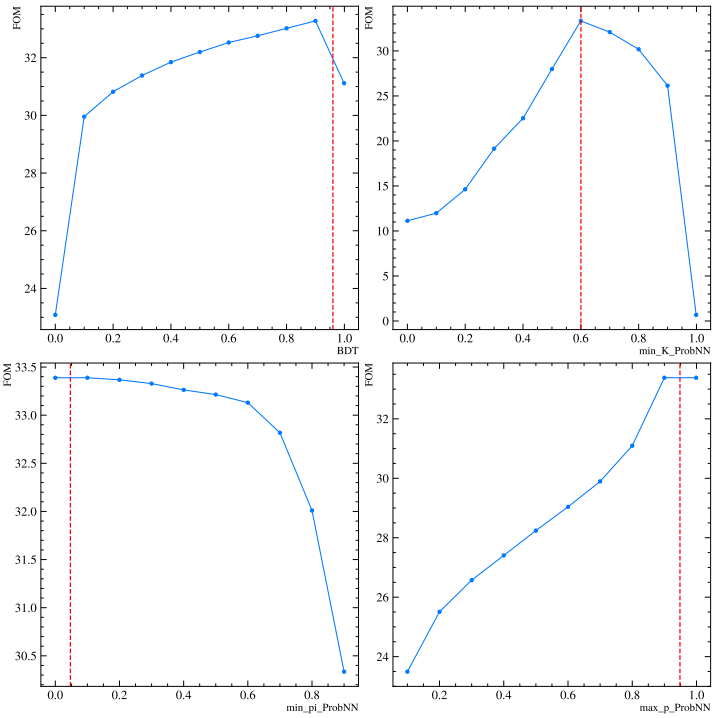

FIGURE 3.14: Pseudo-FoM scans for the 4D selection optimisation for Run 2. The red dashed lines show the optimal point from the `Basin-Hopping` minimisation.

small enough to ignore for now. For the $D_s^{\pm}$ in $m(K^+K^-\pi^{\pm})$ and D^0 in $m(K^+K^-)$, it seems clear from Fig. 3.17 that indeed the $D_s^{\pm}$ mesons are originating from $B_s^0 \to (D_s^- \to K^-K^+\pi^-)\pi^+$ decays and so must be taken into account. However, it is less clear that the D^0 mesons are originating from $B_d^0 \to (D^0 \to K^+K^-)\pi^+\pi^-$ decays as they have a reasonably flat distribution in the four-body spectrum and so should not be accounted for in estimates of the signal yields. For the $D_s^{\pm}$ case, the simplest way to account for these unwanted decays is a mass veto of the $D_s^{\pm}$ peak. A veto is justified as the charmless contribution is approximately zero in the vicinity of the $D_s^{\pm}$ peak so very little signal is being 'lost'. The veto window is determined by fitting a simple Gaussian to the $m(K^+K^-\pi^{\pm})$ invariant mass close to the $D_s^{\pm}$ peak which results in a fit with a mean of $\mu = 1969.0$ with a width $\sigma = 7.28$. The veto is taken as the PDG $D_s^{\pm}$ mass 1968.35 MeV/c^2 $\pm 3\sigma$ from the fit *i.e.* events are required to be outside of the range $1946.35 < m(K^+K^-\pi^{\pm}) < 1990.35$ MeV/c^2, as shown in Fig. 3.18.

In addition to the peaking backgrounds discussed above, there are also possible background contributions from the mis-identification of final state hadrons. The following misIDs are considered: a π has been misID'd as a K, a K has been misID'd as a π and a p has been misID'd as a K. In each of the three cases, the misID is investigated by swapping the mass hypothesis of the final state particle

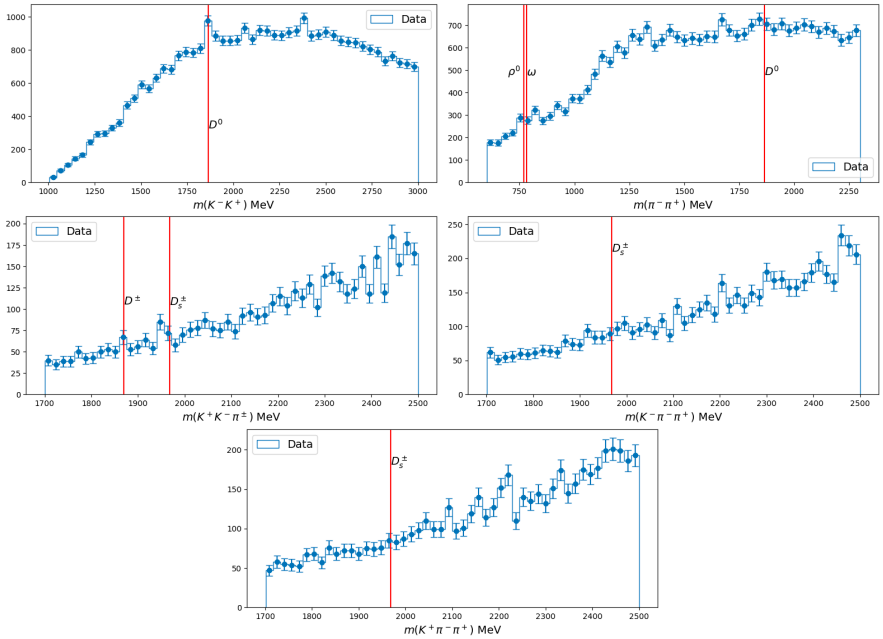

FIGURE 3.15: Invariant masses (with no misID swaps) for Run 1 pre-selected data

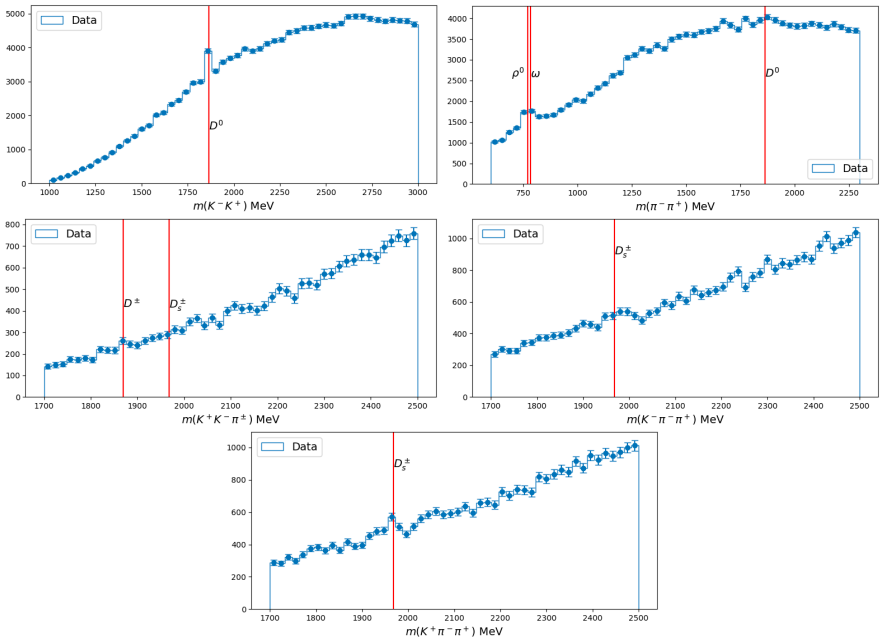

FIGURE 3.16: Invariant masses (with no misID swaps) for Run 2 pre-selected data

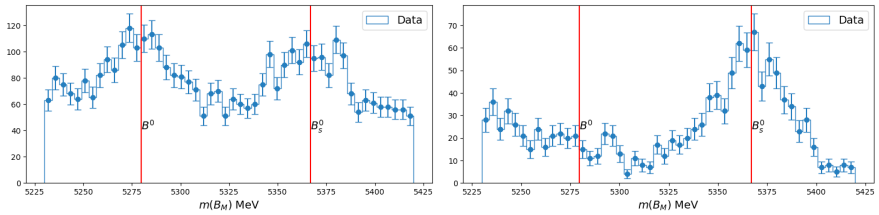

FIGURE 3.17: Reconstructed B-mass in Run 2 for events which fall in the D^0 peak *i.e.* $1850 < m(K^+K^-) < 1890$ (left) and the $D_s^\pm$ peak *i.e.* $1946.35 < m(K^+K^-\pi^\pm) < 1990.35$ (right).

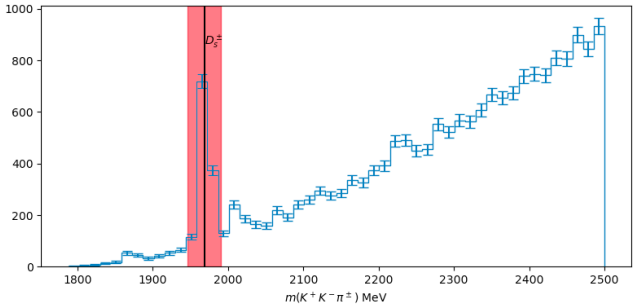

FIGURE 3.18: The mass veto $m(K^+K^-\pi^\pm) < 1946.35$ OR $m(K^+K^-\pi^\pm) > 1990.35$ used to exclude $B_s^0 \to (D_s^- \to K^+K^-\pi^-)\pi^+$ events.

with the highest ProbNN of being the misID'd particle and various three- and the four-body invariant mass spectra are plotted to search for peaking backgrounds. The misID invariant masses for Run 1 and Run 2 are shown in Figs. 3.19 and 3.20 when no PID selection has been applied (except for the loose K_PIDK > 0 and pi_PIDK < -2 cuts in the stripping line). By far the largest background is in the four-body mass spectrum with a K mass hypothesis swapped to a p, which shows a large contribution from Λ_b^0 decays via $\Lambda_b^0 \to pK^-\pi^+\pi^-$ (or possibly with an intermediate Λ_c^+). There is also a sizeable contribution from $D^\pm$ mesons in the $m(K^\pm\pi^\mp\pi^\mp)$ invariant mass where a π has been misID'd as a K (and so a K has been swapped to a π) which most likely originate from $B_d^0 \to (D^- \to K^+\pi^-\pi^-)\pi^+$ decays.

To summarise, a veto is placed on the $m(K^+K^-\pi^\mp)$ mass to veto decays from $B_s^0 \to (D_s^\mp \to K^+K^-\pi^\mp)\pi^\pm$ such that $m(K^+K^-\pi^\pm) \notin [1946.35, 1990.35]\,\text{MeV}/c^2$. The peak in $m(K^+K^-)$ at the D^0 mass was initially ignored and to be checked after the full selection is applied. The peaks seen in invariant masses with a mass hypothesis swap, *i.e.* Λ_b^0 in the $m(pK^-\pi^+\pi^-)$ mass (misID of a p as K^+) and D^+ in the $K^-\pi^+\pi^+$ mass (misID of a K as a π) are also left until after the full PID selection is applied as it is expected it would significantly reduce misID contributions.

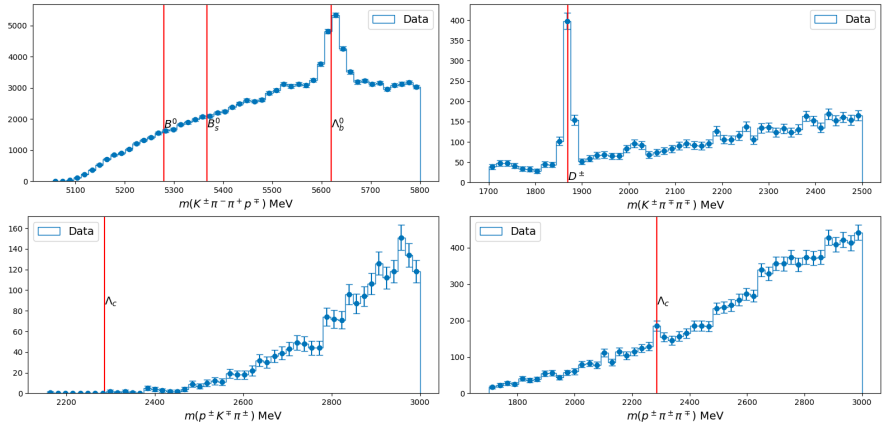

FIGURE 3.19: MisID'd invariant masses for pre-selected Run 1 data.

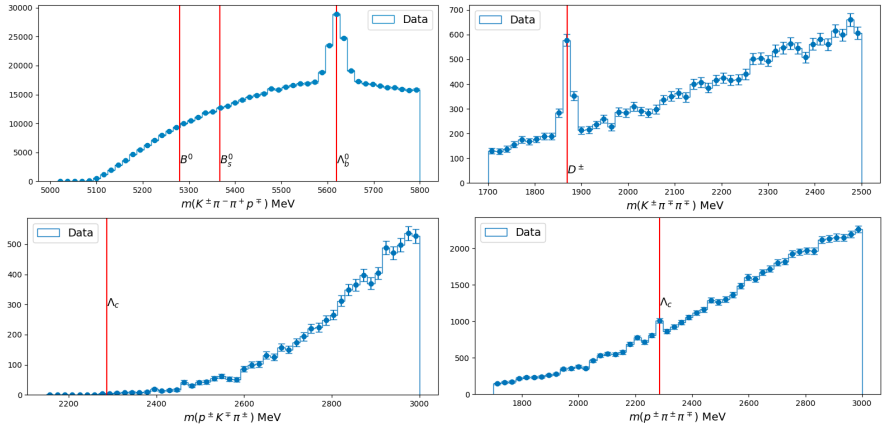

FIGURE 3.20: MisID'd invariant masses for pre-selected Run 2 data.

3.1.8.2 PEAKING BACKGROUNDS IN SELECTED DATA

The procedure of plotting the invariant masses discussed in Sec. 3.1.8.1 is repeated on the fully selected data using the optimal BDT and PID cuts described in Table 3.8. Note in addition, that as used in the nominal signal mass fit described in Sec. 3.1.9, the mass of $m(K^+\pi^-)$ and $m(K^-\pi^+)$ are now constrained to be between $630 < m(K^\pm\pi^\mp) < 1041.5\,\text{MeV}/c^2$ which significantly reduces the mass range of some of the invariant mass combinations. The invariant masses with no mass-hypothesis swaps are shown in Fig. 3.21 for Run 1 and Fig. 3.22 for Run 2. Note that the mass plots for $m(K^+K^-\pi^\pm)$ are no longer included as the tighter $m(K^\pm\pi^\mp)$ mass window excludes all events in the range 1700 – 2500 MeV/c^2 as was used in the original plots. No significant peaks are observed so no further action is taken.

The equivalent mass plots where a particle has had a misID swap are shown in Fig. 3.23 for Run 1 and Fig. 3.24 for Run 2. The 4-body $m(\text{p}K^-\pi^+\pi^-)$ mass is not

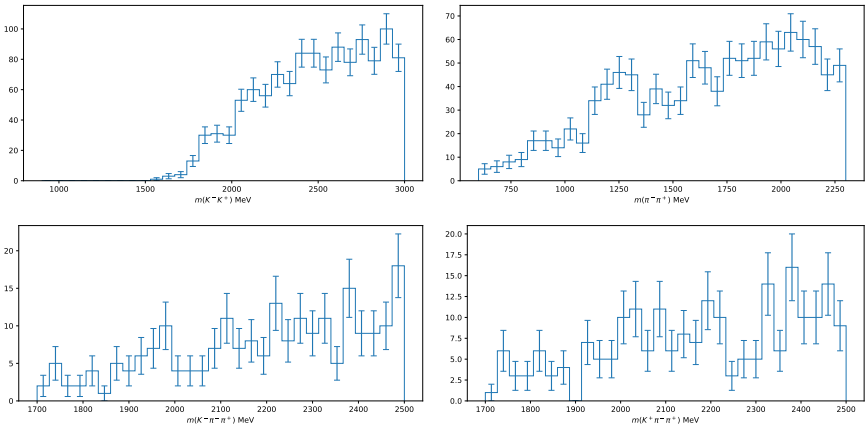

FIGURE 3.21: Invariant masses (with no misID swaps) for Run 1 selected data

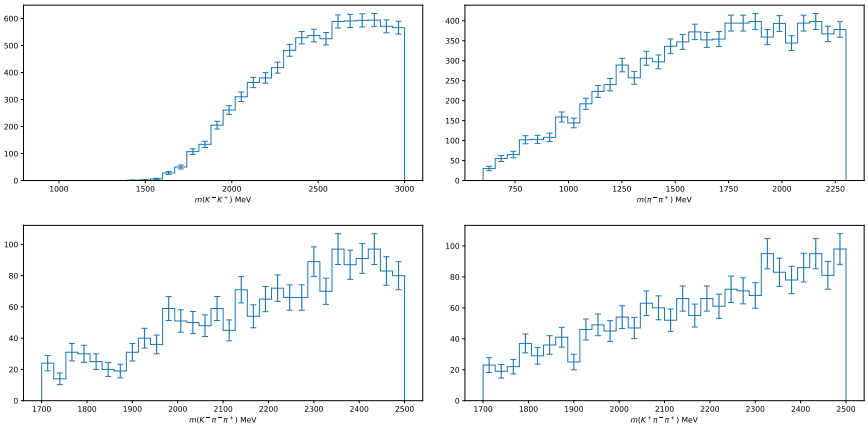

FIGURE 3.22: Invariant masses (with no misID swaps) for Run 2 selected data

included as there was no contribution to it seen in the full mass fit (see Fig. 3.25). Additionally, there is no sign of the $D^{\pm}$ peak seen in pre-selected data so no need for additional vetoes.

3.1.9 $B^0_{s,d} \to (K^+\pi^-)(K^-\pi^+)$ CANDIDATE MASS FIT

Once the MVA optimal selections are in place, the mass fits are performed on the fully selected data using the same framework as described in Sec. 3.1.6 except for the simultaneous part. Therefore the mass fit is set up as follows:

- Signal $B^0_s \to K^{*0}\bar{K}^{*0}$ MC sample with full selection applied is fitted with an Hypatia.
- The misID MC sample of $B^0_s \to \rho^0 K^{*0}$ is fitted with a Johnson SU function but with only the preliminary selection applied (looser BDT cut, no ProbNN

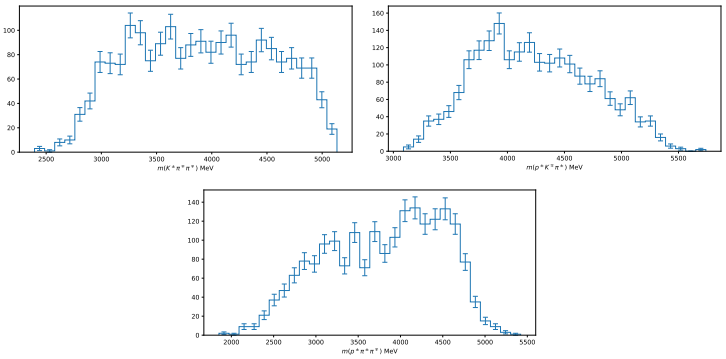

FIGURE 3.23: MisID'd invariant masses for selected Run 1 data.

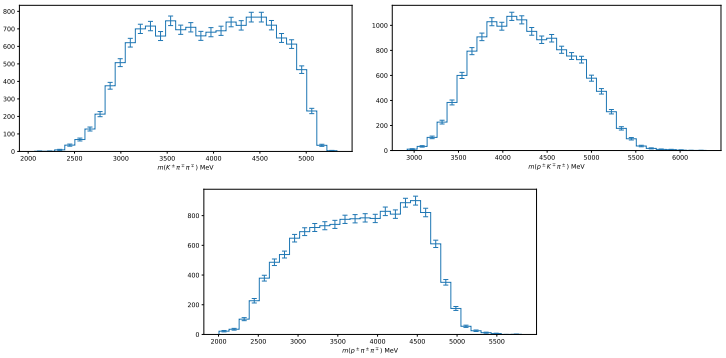

FIGURE 3.24: MisID'd invariant masses for selected Run 2 data.

cuts)

- The misID MC sample of $B_s^0 \to \phi K^{*0}$ is fitted with a Double-Sided Crystal Ball [85] function but with only the preliminary selection applied (looser BDT cut, no `ProbNN` cuts)
- A KDE is used to model the partially reconstructed background from a `RapidSim` sample of $B_s^0 \to K^+\pi^-K^-\pi^+\pi^0$ decays.
- The combinatorial background is modelled with a exponential distribution in Run 2. In Run 1, the level of combinatorial background is so low that it is instead modelled as a flat, horizontal line *i.e.* a linear shape where the slope is fixed to 0 in the fit.
- The component associated with the $\Lambda_b^0 \to pK^-\pi^+\pi^-$ background was consistently found to be near or below 0 for the fully selected data and so this component is dropped for the mass fits.

Full selection is not applied on the misID MC samples since it was found that too few events were left (low efficiency). The tail parameters for the $B_d^0 \to \phi K^{*0}$ and $B_d^0 \to \rho^0 K^{*0}$ are therefore taken from the preliminary fit, with the assumption that the tighter combinatorial BDT cut and `ProbNN` cuts do not significantly affect

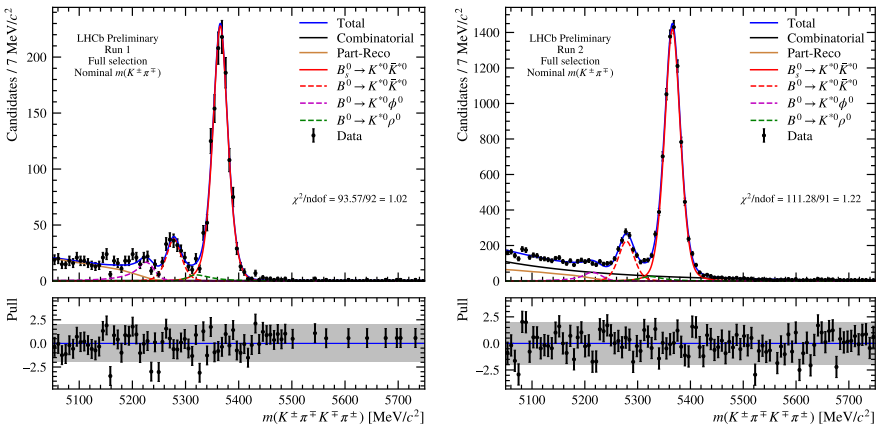

FIGURE 3.25: Results of the fit the $m(K^+\pi^-K^-\pi^+)$ mass for fully selected Run 1 (left) and Run 2 (right) data. The fit components are data (black points), $B_s^0 \to K^{*0}\bar{K}^{*0}$ (solid red line), $B_d^0 \to K^{*0}\bar{K}^{*0}$ (dashed red line), $B_d^0 \to \rho^0 K^{*0}$ (dashed green line), $B_d^0 \to \phi K^{*0}$ (dashed purple line), combinatorial background (solid black line), partially reconstructed background (solid brown line) and the total PDF (solid blue line).

the shape. The position and widths of the peaks are allowed to vary using a global shift and scaling respectively. Note that, as before, B_s^0 MC is used for the misID $B_d^0 \to \rho^0 K^{*0}$ and $B_d^0 \to \phi K^{*0}$ components where the peak is shifted down by the PDG difference in B_s^0 and B_d^0 mass of $87.42\,\text{MeV}/c^2$.

An unbinned extended maximum likelihood fit is performed on the combined Run 1 data and Run 2 data separately. The parameters floating in the fit are:

- Yields of the $B_s^0 \to K^{*0}\bar{K}^{*0}$, $B_d^0 \to K^{*0}\bar{K}^{*0}$, $B_d^0 \to \rho^0 K^{*0}$, $B_d^0 \to \phi K^{*0}$ combinatorial background and partially-reconstructed background components.
- Global peak shift $\delta_\mu = \mu_{\text{data}} - \mu_{\text{MC}}$.
- Global peak scaling $S_\sigma = \sigma_{\text{data}}/\sigma_{\text{MC}}$.
- Combinatorial background decay constant, α, for Run 2.

After cross-checks between performing:

- Simultaneous fit, as was done for the preliminary yields
- Fitting only the $m(K^+\pi^-K^-\pi^+)$ mass and then projecting into the misID masses,

it was determined that for the fully selected fit, fitting the $m(K^+\pi^-K^-\pi^+)$ mass alone provided sufficient control over the background yields.

The fit results can be seen in Fig. 3.25 and with a logarithmic y-axis scale in Fig. 3.26 and the values of the fitted parameters in Table 3.9.

3.2 AMPLITUDE ANALYSIS

The time-integrated amplitude analysis is described throughout this section. The invariant masses of $K^\pm\pi^\mp$ pairs are required to be below the inelastic threshold $m_K + m_\eta = 1042.5\,\text{MeV}/c^2$. No minimum is required, this being the first time in

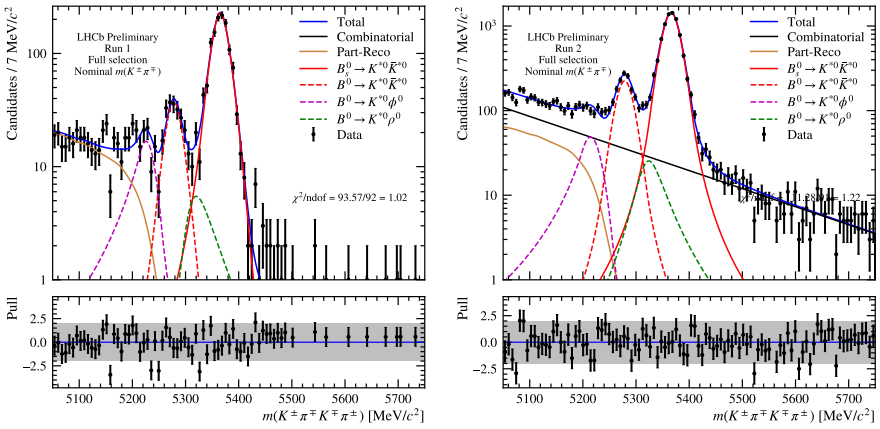

FIGURE 3.26: Results of the fit the $m(K^+\pi^-K^-\pi^+)$ mass for fully selected Run 1 (left) and Run 2 (right) data in a log scale. The fit components are data (black points), $B_s^0 \to K^{*0}\bar{K}^{*0}$ (solid red line), $B_d^0 \to K^{*0}\bar{K}^{*0}$ (dashed red line), $B_d^0 \to \rho^0 K^{*0}$ (dashed green line), $B_d^0 \to \phi K^{*0}$ (dashed purple line), combinatorial background (solid black line), partially reconstructed background (solid brown line) and the total PDF (solid blue line).

Parameter	Run 1	Run 2
bs2kstkst_N	1230 ± 40	8072 ± 108
bd2kstkst_N	202 ± 16	1276 ± 59
bd2rhokst_N	51 ± 24	237 ± 75
bd2phikst_N	135 ± 18	387 ± 48
bkg_prec_N	332 ± 22	1073 ± 325
bkg_comb_N	43 ± 12	3071 ± 426
bkg_comb_alpha	–	$(4.9 \pm 0.4) \times 10^{-3}$
bkg_comb_a	0 (fixed)	–
mu_shift	2.2 ± 0.5	2.9 ± 0.2
sigma_scale	0.83 ± 0.03	1.02 ± 0.01

TABLE 3.9: Results of the fit to fully selected Run 1 and Run 2 data. The combinatorial background is parameterised as a straight line with a slope of 0 *i.e.* a horizontal line in Run 1 whereas in Run 2 it is parameterised with an exponential.

which the region down to the threshold is analysed in these decay channels, in order to have maximum control over scalar contributions. No tensor states are expected in this region, and their possible contribution will eventually be studied in the systematics.

3.2.1 SIGNAL PDF

As was discussed in Sec. 2.6, the total amplitude is modelled as the coherent sum over the different intermediate states,

$$\begin{aligned} A(\Phi_4) &= \sum_i a_i \, A_i(\Phi_4) \, , \\ \bar{A}(\Phi_4) &= \sum_i a_i \, \lambda_i A_i(\bar{\Phi}_4) \, , \end{aligned} \tag{3.4}$$

where the form of $A_i(\Phi_4)$ is detailed in Eq. 2.47.

The PDF describing signal decays is obtained by inserting the amplitude model in Eq. 2.16 and dividing by one of the time integrals, resulting in the following expression:

$$\mathcal{P}_{\text{sig}}(\Phi_4) \propto \left[\left(\left|A(\Phi_4)\right|^2 + \left|\bar{A}(\Phi_4)\right|^2 \right) - 2\,\text{Re}\left(A^*(\Phi_4)\,\bar{A}(\Phi_4) \right) \cdot r_t \right] , \tag{3.5}$$

with

$$r_t(\tau, \Delta\Gamma) \equiv \frac{\int_{t_1}^{t_2} dt\, e^{-t/\tau} \sinh\left(\frac{\Delta\Gamma}{2}\, t\right)}{\int_{t_1}^{t_2} dt\, e^{-t/\tau} \cosh\left(\frac{\Delta\Gamma}{2}\, t\right)} \, . \tag{3.6}$$

The parameters τ, $\Delta\Gamma$ and Δm are fixed throughout the analysis, with their values sourced from Ref. [86] and summarised in Table 3.10. To evaluate the normalisation integral of Eq. 3.5, a flat phase space MC sample of 1M events is generated for each mother meson $B^0_{s,d}$. Formally, this event generation follows Eq. 2.45 and so every conservation law is naturally satisfied. In practice, these large simulation samples are generated rapidly and in parallel using `TGenPhaseSpace`, a class within `ROOT` that implements the `GENBOD` routine [87]. Events are generated in the analysis region and the weight provided by `TGenPhaseSpace`, which is a Jacobian between momentum and mass spaces, is used as input to an accept-reject loop, thereby obtaining a sample uniformly distributed across the phase space.
The integral is thus approximated as

$$\int d\Phi_4\, \mathcal{P}_{\text{sig}}(\Phi_4) \approx \sum_{i=1}^{N} \left[\left(\left|A(\Phi_{4_i})\right|^2 + \left|\bar{A}(\Phi_{4_i})\right|^2 \right) - 2\,\text{Re}\left(A^*(\Phi_{4_i})\,\bar{A}(\Phi_{4_i}) \right) \cdot r_t \right] , \tag{3.7}$$

with an expected error of $O\left(10^{-3}\right)$, according to the sample size. The global factor that considers the integration volume and the number of events is not required, since it would result in a constant scaling in $-2\log\mathcal{L}$, which leaves model parameters unaffected.

Parameter	Value
$\tau_{B_s^0}$	1.520 ± 0.005 ps
$\tau_{B_d^0}$	1.519 ± 0.004 ps
$\Delta\Gamma_s$	0.084 ± 0.005 ps^{-1}
$\Delta\Gamma_d$	0.0007 ± 0.0065 ps^{-1}
Δm_s	17.765 ± 0.006 ps^{-1}
Δm_d	0.5065 ± 0.0019 ps^{-1}

TABLE 3.10: Decay and mixing parameters used throughout this analysis for the B_s^0 and B_d^0 mesons.

The partial waves, $A_i(\Phi_4)$, are not normalised, but a separate program is run once the fit has converged to determine the fit fractions by evaluating the corresponding integral with the same set of integration events. The procedure is best detailed in Sec. 4.1.

3.2.2 DECAY-TIME ACCEPTANCE

Different trigger and offline requirements induce a bias in the B-meson lifetime distribution, being especially strong at short times as shown in Figs. C.1–C.2. This effect has an impact in the determination of the amplitudes by inducing a small, but visible, bias, particularly in the CP-odd ones. This efficiency function is parameterised through cubic b-splines, which are essentially a set cubic polynomials defined in different time regions separated by *knots*, k_i. The number of knots is decided to be 3, and thus the explicit expression can be written as

$$\epsilon_t(t) = \begin{cases} \alpha_{00} + \alpha_{01}\,\tilde{t}_0(t) + \alpha_{02}\,\tilde{t}_0^2(t) + \alpha_{03}\,\tilde{t}_0^3(t) & \text{for } k_0 \le t < k_1 \\ \alpha_{10} + \alpha_{11}\,\tilde{t}_1(t) + \alpha_{12}\,\tilde{t}_1^2(t) + \alpha_{13}\,\tilde{t}_1^3(t) & \text{for } k_1 \le t < k_2 \\ \alpha_{20} + \alpha_{21}\,\tilde{t}_2(t) + \alpha_{22}\,\tilde{t}_2^2(t) + \alpha_{23}\,\tilde{t}_2^3(t) & \text{for } k_2 \le t < k_3 \\ \alpha_{30} + \alpha_{31}\,\tilde{t}_3(t) + \alpha_{32}\,\tilde{t}_3^2(t) + \alpha_{33}\,\tilde{t}_3^3(t) & \text{for } k_3 \le t \le k_4 \end{cases} , \tag{3.8}$$

with

$$\tilde{t}_i(t) \equiv \frac{t - k_i}{k_{i+1} - k_i} \in [0, 1] \, . \tag{3.9}$$

Note that extreme knots correspond to the analysis border, $k_0 \equiv t_1 = 0$ ps and $k_4 \equiv t_2 = 15$ ps; the rest of the knots are placed at lifetimes $k_1 = 0.6$ ps, $k_2 = 1.4$ ps

and $k_3 = 3.0$ ps. Continuity and differentiability imposes the following constraints

$$\begin{aligned}
\alpha_{10} &= \alpha_{00} + \alpha_{01} + \alpha_{02} + \alpha_{03} \,, \\
\alpha_{11} &= \alpha_{01} + 2\alpha_{02} + 3\alpha_{03} \,, \\
\alpha_{12} &= \alpha_{02} + 3\alpha_{03} \,, \\
\alpha_{20} &= \alpha_{10} + \alpha_{11} + \alpha_{12} + \alpha_{13} \,, \\
\alpha_{21} &= \alpha_{11} + 2\alpha_{12} + 3\alpha_{13} \,, \\
\alpha_{22} &= \alpha_{12} + 3\alpha_{13} \,, \\
\alpha_{30} &= \alpha_{20} + \alpha_{21} + \alpha_{22} + \alpha_{23} \,, \\
\alpha_{31} &= \alpha_{21} + 2\alpha_{22} + 3\alpha_{23} \,, \\
\alpha_{32} &= \alpha_{22} + 3\alpha_{23} \,,
\end{aligned} \tag{3.10}$$

which significantly reduces the number of free parameters, from 16 to 7. These free coefficients are determined from a χ^2 fit to the true lifetime distribution in the B_s^0 phase space simulated sample, whose shape is only affected by this acceptance in time unlike the signal MC which is also affected by different CP-even and CP-odd polarisation terms. This lifetime distribution is previously divided by the generation model, quickly obtained with `EvtGen`, and hence the resulting distribution is the efficiency shape. The fit to this histogram is done by year and trigger condition, and only for the B_s^0 meson due to the very small value of $\Delta\Gamma_d$ (see Table 3.10. The results are shown in App. C.1, in Tables C.1–C.12 and Figs. C.1–C.2.

The parameter r_t is then updated to absorb this effect,

$$r_t(\tau, \Delta\Gamma) \longrightarrow r_t^{\text{corr}}(\tau, \Delta\Gamma) \equiv \frac{\int_{t_1}^{t_2} dt\, \epsilon_t(t)\, e^{-t/\tau} \sinh\left(\frac{\Delta\Gamma}{2}\, t\right)}{\int_{t_1}^{t_2} dt\, \epsilon_t(t)\, e^{-t/\tau} \cosh\left(\frac{\Delta\Gamma}{2}\, t\right)} \,. \tag{3.11}$$

Since this efficiency is determined for each data category, the final corrected ratio is calculated as the weighted average of each ratio, where the weight factor is the contribution to the total luminosity,

$$r_t^{\text{avg}} = \frac{1}{\mathcal{L}_{\text{total}}} \left(\mathcal{L}^{\texttt{2011 TOS}}\, r_t^{\texttt{corr 2011 TOS}} + \mathcal{L}^{\texttt{2011 TIS!TOS}}\, r_t^{\texttt{corr 2011 TIS!TOS}} + \dots \right) \,, \tag{3.12}$$

where the total luminosity is the sum of all luminosity factors,

$$\mathcal{L}_{\text{total}} = \mathcal{L}^{\texttt{2011 TOS}} + \mathcal{L}^{\texttt{2011 TIS!TOS}} + \dots \,, \tag{3.13}$$

and these are calculated as the sum of `sWeights`, *i.e.* the number of signal events, for each data category.

3.2.3 EFFICIENCY ACROSS PHASE SPACE

Detection, reconstruction, trigger requirements, and offline selections induce a bias across the phase space, particularly affecting $\cos\theta_{1,2}$ due to the mass difference between $K^\pm$ and $\pi^\mp$. Using the MC sample of pure phase space $B^0_{s,d} \to K^+\pi^-K^-\pi^+$

decays, unbiased by dynamical models, the projections of this efficiency shape can be visualised in the usual 5D space, in Figs. 3.28–3.31. These figures also show the L0 trigger's impact on efficiency: specifically, the efficiency shape differs between `L0HadronTOS` samples and `L0GlobalTIS & !L0HadronTOS` samples.

The normalised PDF, evaluated at a phase space point $\mathbf{x}$ and parameterised by the vector of parameters $\boldsymbol{\theta}$, is weighted by the multidimensional efficiency as

$$\widehat{\mathcal{P}}_{\text{sig}}(\mathbf{x}|\boldsymbol{\theta}) = \frac{\epsilon(\mathbf{x})\,\mathcal{P}_{\text{sig}}(\mathbf{x}|\boldsymbol{\theta})}{\int d\mathbf{y}\,\epsilon(\mathbf{y})\,\mathcal{P}_{\text{sig}}(\mathbf{y}|\boldsymbol{\theta})}\,, \tag{3.14}$$

where the integral in the denominator spans the phase space within the analysis region. Note that the negative likelihood function to be minimised depends only on the parameter vector $\boldsymbol{\theta}$, while efficiency $\epsilon(\mathbf{x})$ has no free parameters. Consequently, the likelihood reads

$$\begin{aligned}
\log\mathcal{L}(\boldsymbol{\theta}) &= \sum_i^N \log\widehat{\mathcal{P}}_{\text{sig}}(\mathbf{x}_i|\boldsymbol{\theta}) \\
&= \sum_i^N \log\left(\epsilon(\mathbf{x}_i)\,\mathcal{P}_{\text{sig}}(\mathbf{x}_i|\boldsymbol{\theta})\right) - \sum_i^N \log\int d\mathbf{y}\,\epsilon(\mathbf{y})\,\mathcal{P}_{\text{sig}}(\mathbf{y}|\boldsymbol{\theta}) \\
&= \sum_i^N \log\epsilon(\mathbf{x}_i) + \sum_i^N \log\mathcal{P}_{\text{sig}}(\mathbf{x}_i|\boldsymbol{\theta}) - N\log\int d\mathbf{y}\,\epsilon(\mathbf{y})\,\mathcal{P}_{\text{sig}}(\mathbf{y}|\boldsymbol{\theta})
\end{aligned} \tag{3.15}$$

where N is the number of data events. The gradient of the likelihood with respect to $\boldsymbol{\theta}$ is then

$$\nabla_{\boldsymbol{\theta}}\log\mathcal{L}(\boldsymbol{\theta}) = \nabla_{\boldsymbol{\theta}}\left[\sum_i^N \log\mathcal{P}_{\text{sig}}(\mathbf{x}_i|\boldsymbol{\theta}) - N\log\int d\mathbf{y}\,\epsilon(\mathbf{y})\,\mathcal{P}_{\text{sig}}(\mathbf{y}|\boldsymbol{\theta})\right]\,. \tag{3.16}$$

This result shows that efficiency affects only the normalisation integral of the signal PDF. Since this integral is evaluated using a toy MC sample over the analysis space, efficiency must be estimated at the specific phase space positions of each event in this integration set.

Efficiency is estimated using a novel technique that leverages the two kind of simulated samples of $B^0_{s,d} \to K^+\pi^-K^-\pi^+$ phase space decays:

- Fully simulated samples: these MC samples, with event types `13104094` for B^0_s and `11104094` for B^0_d, include not only the full LHCb detector response, trigger emulation, and reconstruction strategies that are applied in real data, but also all selection criteria that were applied offline, as described in Sec. 3.1.
- Integration sample: this sample contains the same decays but without any detector information (generator-level simulation). It represents a 'pure physics' scenario, capturing only the theoretical distributions of decays in phase space.

The method consists of mapping the five-dimensional distribution of the variables of Eq. 2.44 in the full-simulated samples to those in the integration sample, where the discrepancies between the two are only given by efficiency effects. Angles are

flat since all involved particles are spin-less, but masses are not and so both samples are weighted by the inverse of the Jacobian of Eq. 2.18 in order to flatten their distributions.

The mapping uses a KDE approach,

$$\hat{\epsilon}(\mathbf{x}_i) \propto \sum_{j=1}^{N} K\left(\mathbf{H}^{-1/2}\ (\mathbf{x}_i - \mathbf{y}_j)\right)\ , \tag{3.17}$$

where N is the number of fully simulated MC events, and $\mathbf{x}$ and $\mathbf{y}$ are 5D vectors representing the toy and full-simulated phase space events, respectively. $\mathbf{H}$ is a 5×5 bandwidth matrix that plays the role of a covariance matrix and through which correlations between variables can be established, and K is a function called kernel. The choice for K, that fortunately does not play a central role in the accuracy, is a Gaussian kernel for the nominal fit,

$$K(\mathbf{x}|\mathbf{H}) \propto |\mathbf{H}|^{-1/2} e^{-\frac{1}{2}\mathbf{x}^T\mathbf{H}^{-1}\mathbf{x}}\ ,$$

and a parabola,

$$K(\mathbf{x}|\mathbf{H}) \propto 1 - \mathbf{x}^T\mathbf{H}^{-1}\mathbf{x}\ ,$$

will be trialled as an alternative kernel for the systematics. Both are shown in Fig. 3.27.

On the other hand, selecting an optimal bandwidth matrix $\mathbf{H}$ is crucial: finer bandwidths improve resolution but are more sensitive to statistical fluctuations, while coarser ones smooth distributions but may overlook narrow structures. The bandwidth matrix for the baseline is manually tweaked by comparing the LHCb simulation versus the integration events weighted by the KDE efficiency weights. For the baseline, $\mathbf{H}$ is manually tweaked by comparing the fully simulated samples to integration events weighted by the KDE-derived efficiency.

For the computation itself, note that a naive algorithm has computational complexity $O(NM)$, where N and M are the number of events of both full-simulated and integration MC samples, respectively, which are quite big. Despite the availability of numerous libraries implementing fast or approximate methods, only few support multidimensional algorithms with reflection techniques. This is the reason why it was decided to use a custom version of `kalepy` [88], which satisfies these requirements along with interesting functionalities such as multidimensional resampling. The core function calculating Eq. 3.17 is accelerated with `Numba`, but even with a parallelisation of loops in CPU it still requires several hours to complete. Since efficiency estimation on each integration event is completely independent of

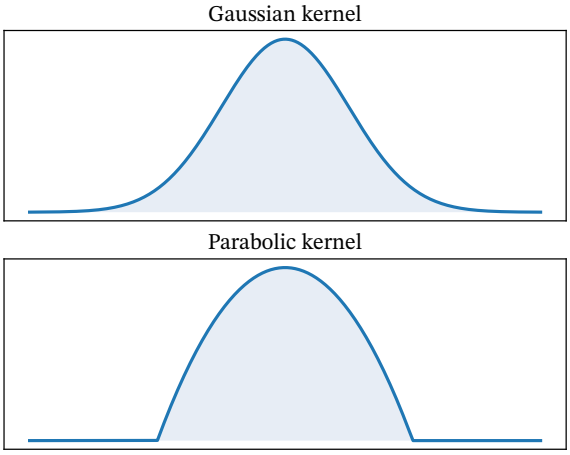

FIGURE 3.27: The two kernel approaches used in the KDE technique to estimate the efficiency across phase space.

the others,

$$\begin{aligned}
\hat{\epsilon}(\mathbf{x}_1) &\propto \sum_{j=1}^{N} K\left(\mathbf{H}^{-1/2}\ (\mathbf{x}_1 - \mathbf{y}_j)\right)\ , \\
\hat{\epsilon}(\mathbf{x}_2) &\propto \sum_{j=1}^{N} K\left(\mathbf{H}^{-1/2}\,(\mathbf{x}_2 - \mathbf{y}_j)\right)\ , \\
&\cdots \\
\hat{\epsilon}(\mathbf{x}_M) &\propto \sum_{j=1}^{N} K\left(\mathbf{H}^{-1/2}\,(\mathbf{x}_M - \mathbf{y}_j)\right)\ ,
\end{aligned} \tag{3.18}$$

then massive parallelisation in GPU is the most appropriate method if the naive approach is to be addressed. For the interoperability between `Python` and `CUDA`, one interesting library was `CuPy` [89] which offered 40x–60x of improvement and worked very well. The Gaussian and parabolic kernels were written in `CUDA-C` and were compiled and fed with data vectors with `CuPy`. After some further research after a while, `CuPy` was superseded by `KeOps` [90] which offers a factor $O(200)$ of improvement with respect to the original implementation and reduces the time to run all efficiencies for both B_s^0 and B_d^0 to approximately two hours, thus no longer being the main bottleneck of the analysis.

The nominal efficiency weights are shown in Figs. 3.32–3.35, for trigger conditions `L0HadronTOS` and `L0GlobalTIS` & `!L0HadronTOS` , respectively. These distributions already have all data/MC corrections, which will be discussed in the next sections. The normalisation integral for the signal PDF is then modified to

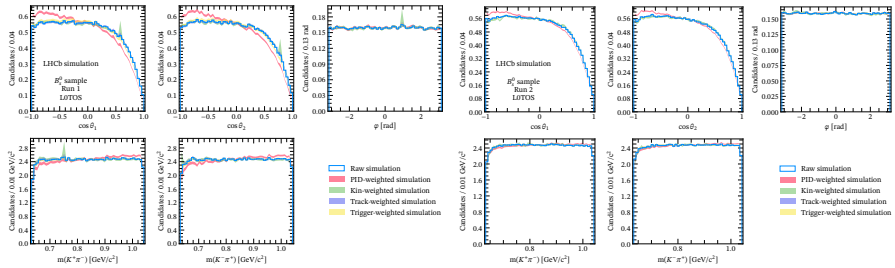

FIGURE 3.28: Raw efficiency shapes from the B_s^0 phase space MC `L0HadronTOS` sample compared to the weighted distributions corrected for different sources of disagreement with data.

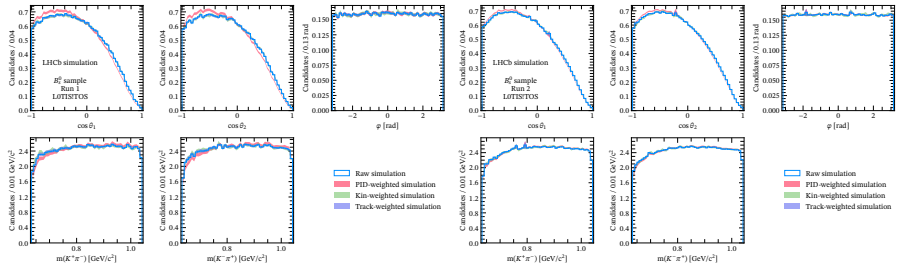

FIGURE 3.29: Raw efficiency shapes from the B_s^0 phase space MC `L0GlobalTIS & !L0HadronTOS` sample compared to the weighted distributions corrected for different sources of disagreement with data.

incorporate this efficiency, as

$$\int d\mathbf{x}\, \epsilon(\mathbf{x})\, \mathcal{P}_{\text{sig}}(\mathbf{x}) \approx \sum_i \hat{\epsilon}(\mathbf{x}_i)\, \mathcal{P}_{\text{sig}}(\mathbf{x}_i)\ . \tag{3.19}$$

Although these efficiency weights are evaluated and saved on disk for all years of data taking and trigger conditions ($6 \times 2 = 12$ sets) to allow fitting separate years/triggers, they are averaged by luminosity in the nominal fit, as is done for the time efficiency,

$$\epsilon^{\text{avg}}(\mathbf{x}) = \frac{1}{\mathcal{L}_{\text{total}}} \left(\mathcal{L}^{2011}_{\texttt{TOS}}\, \epsilon^{2011}_{\texttt{TOS}}(\mathbf{x}) + \mathcal{L}^{2011}_{\texttt{TIS!TOS}}\, \epsilon^{2011}_{\texttt{TIS!TOS}}(\mathbf{x}) + \dots \right)\ , \tag{3.20}$$

and the luminosity factors are calculated as the sum of `sWeights`, either for B_s^0 or for B_d^0, for each data category.

3.2.4 DATA-DRIVEN MC CORRECTIONS

Due to known inaccuracies in the simulation method that give rise to discrepancies between data and MC, some sources of corrections are provided to each of the full-simulated events, in the form of per-event weights. The different sets of weights for each of these sources are calculated independently and, assuming no correlations

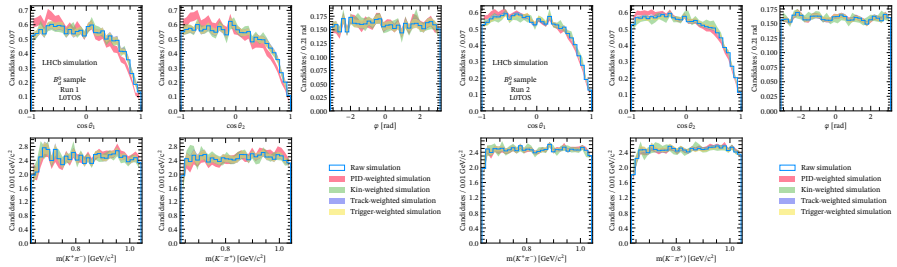

FIGURE 3.30: Raw efficiency shapes from the B^0_d phase space MC `L0HadronTOS` sample compared to the weighted distributions corrected for different sources of disagreement with data.

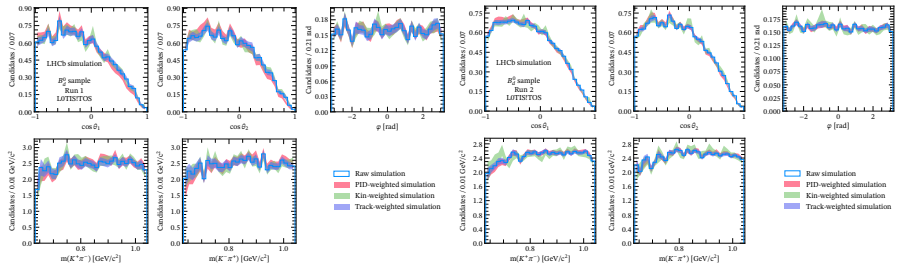

FIGURE 3.31: Raw efficiency shapes from the B^0_d phase space MC `L0GlobalTIS` & `!L0HadronTOS` sample compared to the weighted distributions corrected for different sources of disagreement with data.

between different sources, the total weights are obtained as the product of all sources,

$$w_i^{\text{tot}} = w_i^{\text{src. 1}} \cdot w_i^{\text{src. 2}} \cdots w_i^{\text{src. n}} \ .$$

Finally, these total correction weights correct the efficiency shape in the KDE as

$$\hat{\epsilon}^{\,\text{corr}}(\mathbf{x}_i) \propto \sum_{j=1}^{N} w_j^{\text{tot}} \, K\left(\mathbf{H}^{-1/2}\left(\mathbf{x}_i - \mathbf{y}_j\right)\right) \ . \tag{3.21}$$

3.2.4.1 HADRONIC TRIGGER EFFICIENCY

The L0 hadronic trigger generally shows higher efficiency in MC simulations than in real data, possibly impacting the efficiency shape. Signal candidates are selected by either firing the hadronic trigger (`L0HadronTOS`) or by selecting events where other particles in the event fire the global trigger (`L0GlobalTIS`). With this approach, samples can be split into the disjoint sets `L0HadronTOS` and `L0GlobalTIS & !L0HadronTOS` . The `L0GlobalTIS` sample is considered unbiased with respect to the `L0Hadron` efficiency, and hence it will be used to reweight the `L0HadronTOS` sample using the following approach:

1) Obtain the real `L0HadronTOS` efficiency in the full-simulated phase space samples for all trigger conditions, years of data taking and magnet polarities.

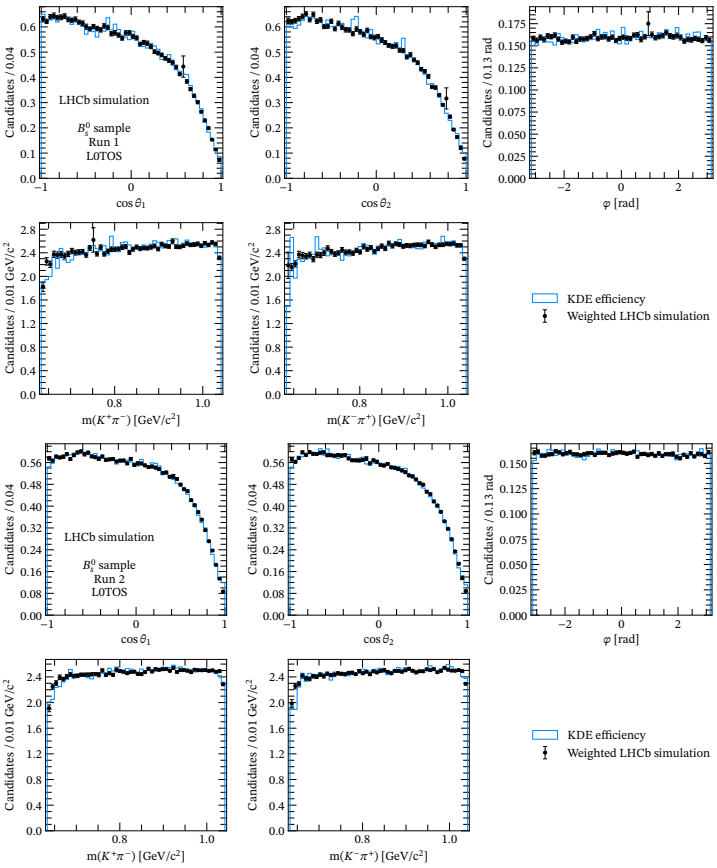

FIGURE 3.32: KDE-efficiency distributions across the phase space versus the data/MC-corrected LHCb MC samples, for the B_s^0 L0HadronTOS sample.

This is done through the LHCb L0Calo tool which evaluates the efficiency as a function of the track ID, magnet polarity, track position at the calorimeter z-projection and the transverse energy deposited in the calorimeter, based on calibration samples from hadronic decays. The tool also considers the probability of overlapping between track clusters, that might result in a positive trigger decision from two tracks that would not fire the trigger.

2) Train a GBReweighter to make the L0GlobalTIS & L0HadronTOS unweighted sample look like L0GlobalTIS sample weighted by its real hadronic efficiency computed in step 1. This is the continuous extension to five dimensions of how trigger efficiency is calculated, $\epsilon = N(\text{TIS \& TOS})/N(\text{TIS})$.
3) Evaluate the trained algorithm on L0HadronTOS events. The resulting set of weights makes the L0HadronTOS subsample look more like real data.

This method was originally developed for the three-body Dalitz analysis of Ref. [91], and the modifications described here correspond to the extension to four-body

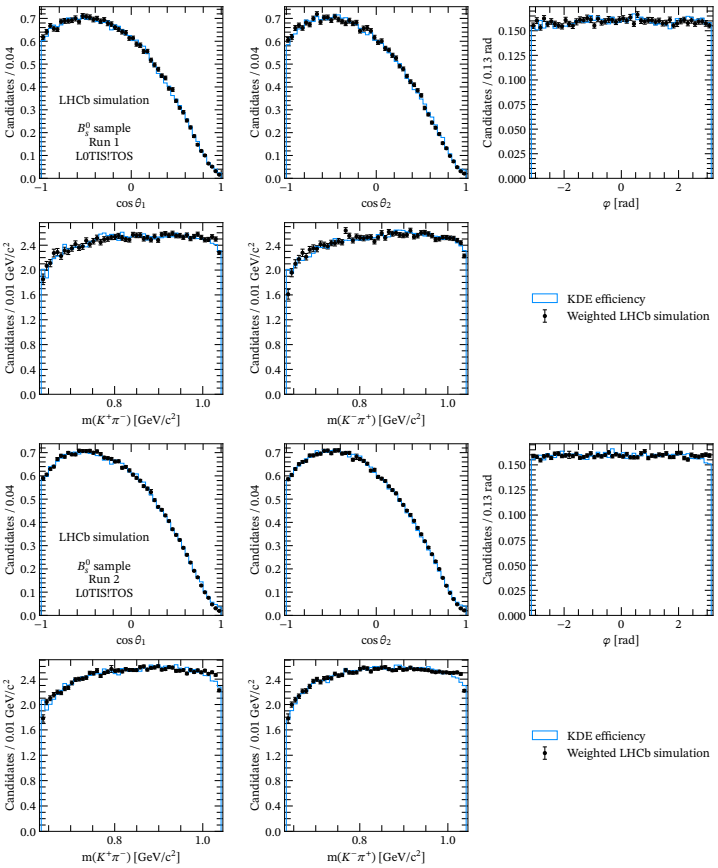

FIGURE 3.33: KDE-efficiency distributions across the phase space versus the data/MC-corrected LHCb MC samples, for the B_s^0 `L0GlobalTIS` & `!L0HadronTOS` sample.

decays, and hence five dimensions in phase space. The hyperparameters used in the `GBReweighter` are the same for every year of data taking, and can be found in Table 3.11. The `GBReweighter` results are shown in Fig. 3.36 for B_s^0 and in Fig. 3.37 for B_d^0. The distributions of weights are shown in Fig. 3.38 for B_s^0 and in Fig. 3.39.

3.2.4.2 TRACKING EFFICIENCY

A correction is applied to the simulation samples to take into account the difference between the LHCb tracking efficiency for real data and MC. These are provided by the LHCb tracking group in the form of correction histograms as functions of the p and η of each charged track, that have been determined by dividing the corresponding efficiency histograms in data and MC. The efficiency per bin is evaluated from mass fits to $J/\psi \to \mu^+\mu^-$ using the tag-and-probe method. The final total weight for a given event, whose signal particles lie in some (p, η) bin, is

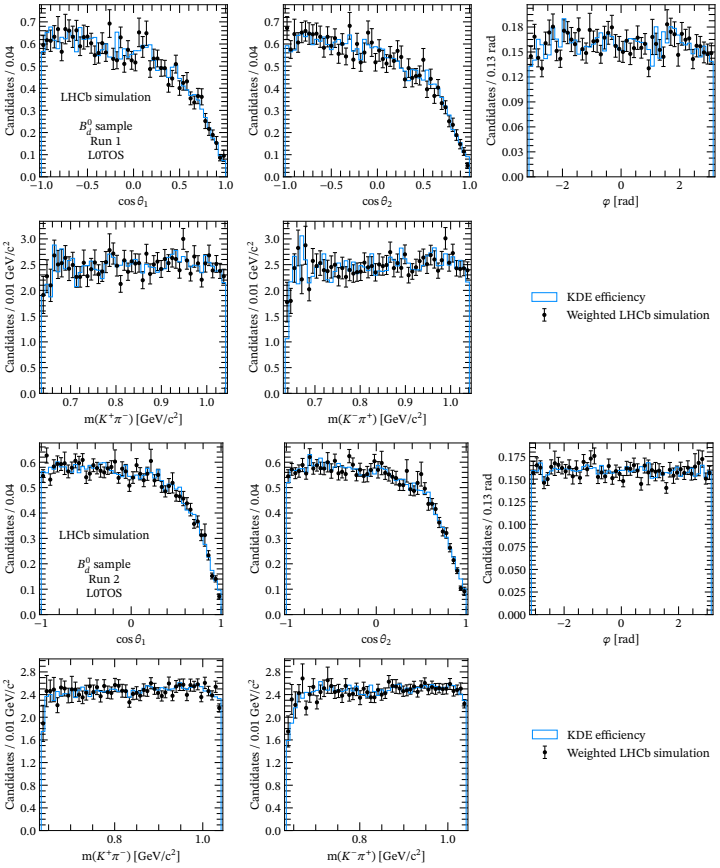

FIGURE 3.34: KDE-efficiency distributions across the phase space versus the data/MC-corrected LHCb MC samples, for the B_d^0 `L0HadronTOS` sample.

Hyperparameter	Value
n_estimators	10
learning_rate	0.1
max_depth	4
min_samples_leaf	10000
subsample	1.0

TABLE 3.11: Hyperparameters used in the `GBReweighter` for the trigger correction to the efficiency.

calculated as

$$w_{\text{tot}}^{\text{track}} = w_{K^+}^{\text{track}} \cdot w_{\pi^-}^{\text{track}} \cdot w_{K^-}^{\text{track}} \cdot w_{\pi^+}^{\text{track}} \, . \tag{3.22}$$

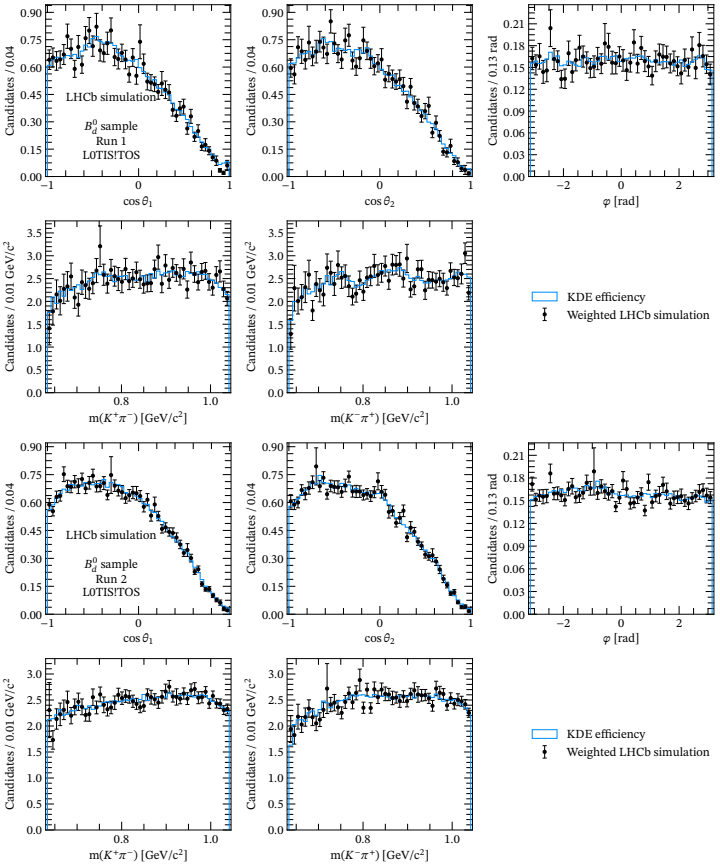

FIGURE 3.35: KDE-efficiency distributions across the phase space versus the data/MC-corrected LHCb MC samples, for the B^0_d `L0GlobalTIS` & `!L0HadronTOS` sample.

If the (p, η) coordinates for a given track lie out of the histogram range, the weight of the nearest bin is assigned. The correction histograms are shown in Fig. 3.40, and the distribution of weights are shown in Fig. 3.41 for B^0_s and Fig. 3.42.

3.2.4.3 PID EFFICIENCY

As described in Sec. 3.1.7, during selection optimisation a figure of merit is maximised in four dimensions in order to remove most of the background: one for the combinatorial MVA response and three for some combinations of PID cuts. Given that PID variables present some mismodeling effects in MC samples, these are not PID-selected. Although one option could be to apply the PID cuts on the corrected variables, it was seen that the agreement between the `PIDCorr`-corrected `ProbNN` variables in simulation vs. `sWeighted` data is not good enough, particularly in the peaking regions. Instead, the per-event efficiency of these cuts is evaluated with `PIDCalib2`, which uses calibration data to know the real efficiency, and this is used

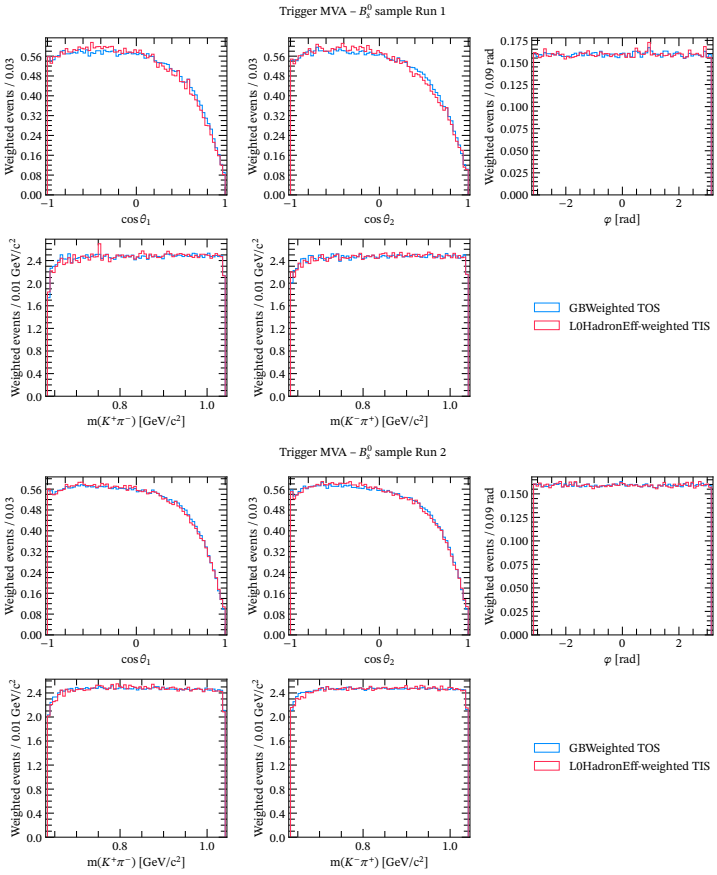

FIGURE 3.36: `L0HadronTOS` sample weighted by the GBWeights to resemble the `L0GlobalTIS` sample, which is weighted by the real hadronic efficiency, for the B_s^0 phase space MC

to reweight the MC, thus emulating the impact of the cuts on "true" distributions. This procedure constitutes the unique information that MC samples have about PID, no further selections are applied.

`PIDCalib2` uses dedicated calibration samples in order to determine the efficiency of a set of given PID cuts. In this case, there are four PID cuts that must be calculated:

- The stripping line `PIDK` cut: `PIDK` > 2 for kaons and `PIDK` < 0 for pions.
- The `min_k_ProbNN` cut.
- The `min_pi_ProbNN` cut.
- The `max_p_ProbNN` cut.

However, there is no option in `PIDCalib2` to calculate the efficiency of a cut that is the minimum or maximum across multiple final state particles. Instead, templates are generated for all possible combinations of the cuts and then those effi-

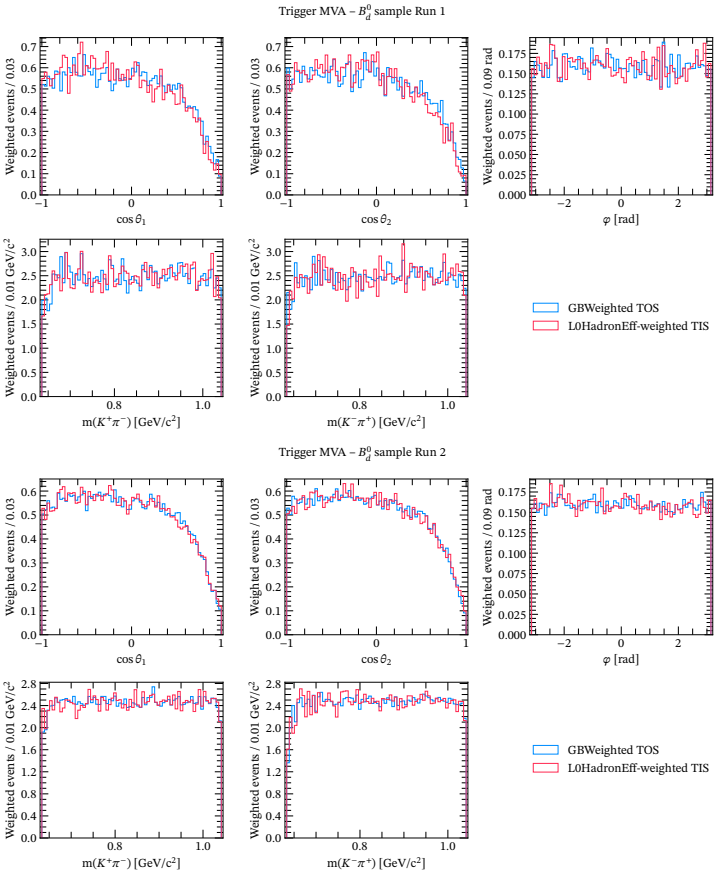

FIGURE 3.37: `L0HadronTOS` sample weighted by the GBWeights to resemble the `L0GlobalTIS` sample, which is weighted by the real hadronic efficiency, for the B_d^0 phase space MC

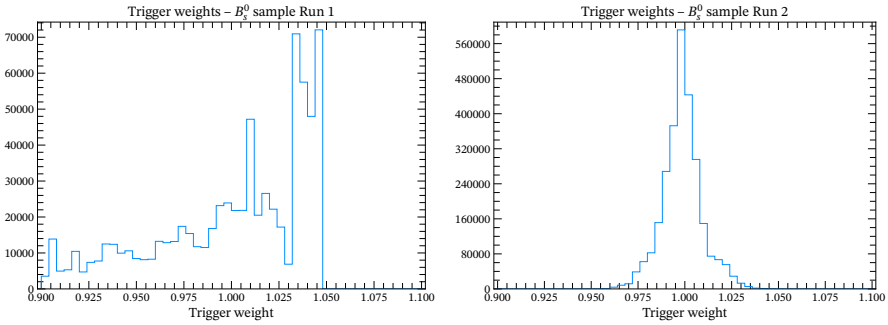

FIGURE 3.38: Distribution of the GBWeights calculated for the trigger correction to the efficiency, for the B_s^0 sample.

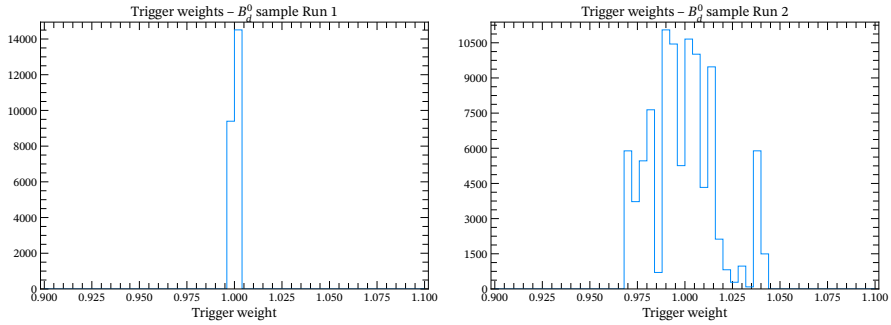

FIGURE 3.39: Distribution of the GBWeights calculated for the trigger correction to the efficiency, for the B_d^0 sample.

ciencies are manually attached to the events in the MC tuples (rather than using the automatic script in `PIDCalib2` to do it). For the $B_s^0 \to (K^+\pi^-)(K^-\pi^+)$ and $B_d^0 \to (K^+\pi^-)(K^-\pi^+)$ MC samples (as well as for signal MC, but it is not relevant here) the following templates are generated in `PIDCalib2`:

- For kaons:
  - `PIDK` > 2
  - `PIDK` > 2 && `K_ProbNNk` $\times (1 -$ `K_ProbNNpi`$) >$ `k_prob`
  - `PIDK` > 2 && `K_ProbNNp` $<$ `p_prob`
  - `PIDK` > 2 && `K_ProbNNk` $\times (1 -$ `K_ProbNNpi`$) >$ `k_prob` && `K_ProbNNp` $<$ `p_prob`.
- For pions:
  - `PIDK` < 0
  - `PIDK` < 0 && `pi_ProbNNpi` $\times (1 -$ `pi_ProbNNk`$) >$ `pi_prob`
  - `PIDK` < 0 && `pi_ProbNNp` $<$ `p_prob`
  - `PIDK` < 0 && `pi_ProbNNpi` $\times (1 -$ `pi_ProbNNk`$) >$ `pi_prob` && `pi_ProbNNp` $<$ `p_prob`,

where `k_prob`, `pi_prob` and `p_prob` are the cut values found from the optimisation for Run 1 and Run 2 from Table 3.8. All of the templates generated with `PIDCalib2` also have, where possible, cuts to align the samples more closely with the stripping line. Note that fiducial cuts were placed to ensure that all events fall within these bins – see Table 3.4 for the signal mode. The templates are generated separately for every year and polarity. The default binning scheme of `PIDCalib2` is used for the nominal determination.

With the above templates, for each event, the `PIDCorr` variables are used to determine which kaon has the lowest `min_k_ProbNN`, which pion has the lowest `min_pi_ProbNN` and which of the four hadrons has the max `max_p_ProbNN`. As previously said, it was determined that the `PIDCorr`-corrected PID variables are not perfect though they should be certainly close enough for these purposes. Now that it is known which hadron is relevant for each cut, the correct template can be selected for each hadron and the PID weight extracted. The total PID weight per

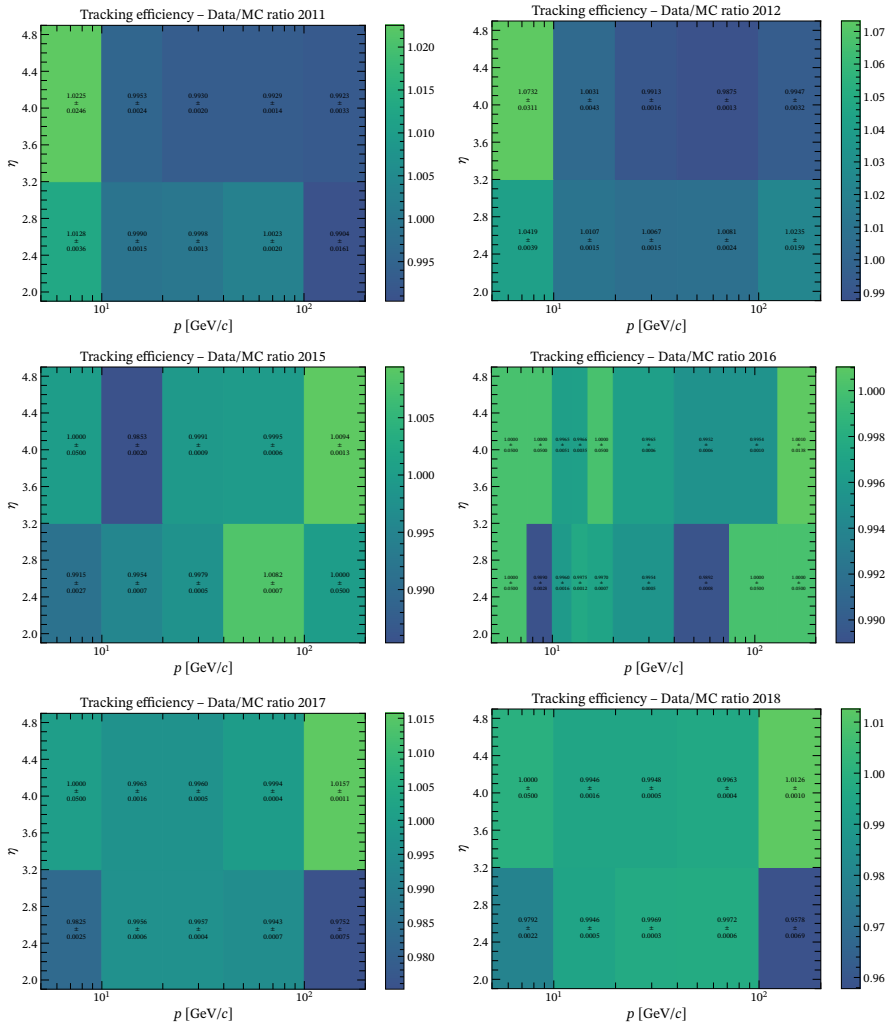

FIGURE 3.40: Data/MC correction histograms for the different years of data taking as functions of p and η.

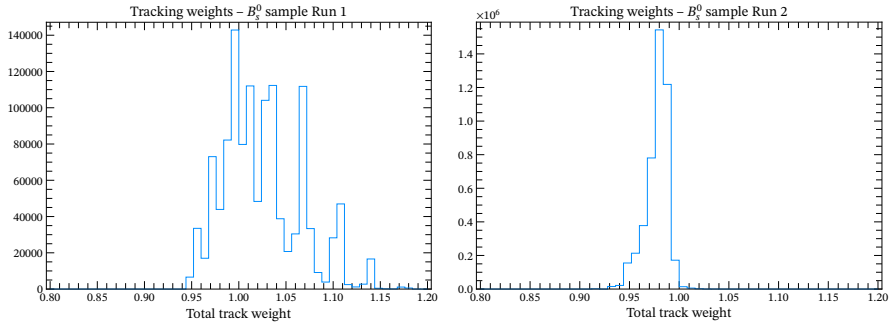

FIGURE 3.41: Distributions of the tracking correction weights, evaluated on B_s^0 phase space MC for the Run 1 sample (left) and Run 2 sample (right).

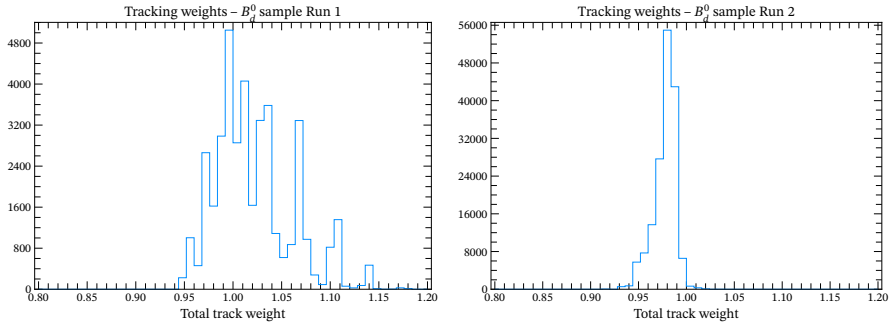

FIGURE 3.42: Distributions of the tracking correction weights, evaluated on B_d^0 phase space MC for the Run 1 sample (left) and Run 2 sample (right).

event is then just the product of weights for each of the four hadrons,

$$w_{\text{tot}}^{\text{PID}} = w_{K^+}^{\text{PID}} \cdot w_{\pi^-}^{\text{PID}} \cdot w_{K^-}^{\text{PID}} \cdot w_{\pi^+}^{\text{PID}} \ . \tag{3.23}$$

3.2.4.4 KINEMATIC REWEIGHTING

The weights calculated in Sec. 3.1.3 are used to align the MC with data in some variables that present known mismodeling, especially some kinematic variables related to the B-meson production. These are obtained by training a `GBReweighter` using the affected variables, with the MC sample as target distribution and `sWeighted` data as original distribution. The MC sample is truth-matched and has the PID selections from the stripping line applied, on the `PIDCorr`-corrected variables.

Once the algorithm is trained, it is applied on the nominal $B_{s,d}^0 \to K^+\pi^-K^-\pi^+$ phase space MC samples thus producing the set of weights that makes the MC resemble the `sWeighted` data on these variables. Alternative configurations for the internal BDT algorithm will be eventually trialled for the systematics.

3.2.5 BACKGROUND MODEL

Initially, the fit strategy was to run a `sWeighted` fit as it is nowadays a very popular method that facilitates a lot the procedures of fitting, plotting, or scanning. However, some issues were accidentally found in some of the amplitude coefficients, and it was investigated in more detail. Intensive studies scanning the likelihood shape for these parameters shed some light on what was going on. The results showed that the `sWeighted` likelihood is not differentiable on these parameters, showing strange jumps up and down and making difficult the estimation of parameters via gradient optimisation methods. Some plots are shown in App. C.2.

To face this problem, a different strategy was considered and the whole analysis pipeline and software was changed to a more traditional approach: the parameterisation of backgrounds during the fit. High-purity signal regions are established for both B_s^0 and B_d^0 mesons, and the remaining backgrounds are parameterised and described across the phase space during the fit. Since the background yields are small enough, simulated samples are generated flat in phase space with `RapidSim` for the corresponding misidentified decay channels. These are then reweighted with the nominal signal models of the corresponding previous LHCb analyses. For the combinatorial background, events in the region with a high four-body invariant mass, which is referred to as the upper sideband region, are used as a proxy for this kind of background, since no further contribution is expected in this region.
These samples act as templates for these backgrounds and describe them in phase space, only their yields are free in the model and they will be fixed to the integral of the PDFs used in the mass fit within the corresponding signal regions. Then, they will be injected in the $-2\log\mathcal{L}$ as negative weights and so they are subtracted from the signal model.

3.2.5.1 SIGNAL REGIONS

The lower (upper) limit for the B_d^0 (B_s^0) region is set from the four-body mass fit parameters values $\mu - 3\sigma$ ($\mu + 3\sigma$), where it should be recalled that $\mu = \mu_{\rm MC} + \delta_\mu$ and $\sigma = \sigma_{\rm MC} \cdot S_\sigma$. The parameters $\mu_{\rm MC}$ and $\sigma_{\rm MC}$ are obtained from a mass fit to signal MC, and δ_μ and S_σ are the data-driven shift and scale that are measured from data. These are actually determined for the B_s^0 meson and propagated to the B_d^0 through their known mass difference, $\Delta m = 87.4\,\text{MeV}/c^2$. The limit between both signal regions is then initially set to $\mu_{B_d^0} + 3\,\sigma_{B_d^0} + \delta_m$, where δ_m is an offset that is fixed to different values in order to get the "optimal" signal window. In summary,

$$\begin{aligned} B_d^0 \text{ region:} &\quad [\,\mu_{B_d^0} - 3\,\sigma_{B_d^0},\ \mu_{B_d^0} + 3\sigma_{B_d^0} + \delta_m\,]\,, \\ B_s^0 \text{ region:} &\quad [\,\mu_{B_d^0} + 3\,\sigma_{B_d^0} + \delta_m,\ \mu_{B_s^0} + 3\sigma_{B_s^0}\,]\,, \\ \delta_m \text{ values:} &\quad [-10, -15, -20, -25, -30, -35]\,\text{MeV}/c^2. \end{aligned} \tag{3.24}$$

All tables with the values obtained in this study are shown in App. C.3. The optimal offset is set to $-25\,\text{MeV}/c^2$, defining both signal regions. The results are shown in Tables 3.12 and 3.13, for Run 1 and Run 2 respectively. Given the back-

Component	Yield in B_s^0 region	Yield in B_d^0 region
$B_s^0 \to K^{*0}\bar{K}^{*0}$	1188 (94%)	4 (2%)
$B_d^0 \to K^{*0}\bar{K}^{*0}$	9 (1%)	186 (75%)
$B_d^0 \to \rho^0 K^{*0}$	59 (5%)	13 (5%)
$B_d^0 \to \phi K^{*0}$	0 (0%)	36 (14%)
Combinatorial	4 (0%)	3 (1%)
Partially reconstructed	0 (0%)	5 (2%)
Retained signal prob.	99%	95%

TABLE 3.12: Yields for the different components in both B_s^0 and B_d^0 signal regions for the Run 1 dataset and offset fixed to the optimal value, which is found to be -25 MeV/c^2. The retained signal probability, which is shown in the last row, is the area under the curve that is retained due to the cuts of the signal region.

Component	Yield in B_s^0 region	Yield in B_d^0 region
$B_s^0 \to K^{*0}\bar{K}^{*0}$	7776 (92%)	44 (3%)
$B_d^0 \to K^{*0}\bar{K}^{*0}$	50 (1%)	1130 (66%)
$B_d^0 \to \rho^0 K^{*0}$	267 (3%)	66 (4%)
$B_d^0 \to \phi K^{*0}$	2 (0%)	77 (5%)
Combinatorial	375 (4%)	373 (22%)
Partially reconstructed	1 (0%)	15 (1%)
Retained signal prob.	99%	94%

TABLE 3.13: Yields for the different components in both B_s^0 and B_d^0 signal regions for the Run 2 dataset and offset fixed to the optimal value, which is found to be -25 MeV/c^2. The retained signal probability, which is shown in the last row, is the area under the curve that is retained due to the cuts of the signal region.

ground contributions that are still present in them, the components $B_d^0 \to \rho^0 K^{*0}$, $B_d^0 \to \phi K^{*0}$, and combinatorial need a description throughout the phase space.

3.2.5.2 $B_d^0 \to \rho^0 K^{*0}$

A `RapidSim` phase space sample of $B_d^0 \to \pi^+\pi^- K^+\pi^-$ decays is generated, requiring each of the four charged tracks to satisfy $p_T > 500\,\text{MeV}/c$. Additionally, the p_T of the $(\pi^+\pi^-)$ and $(K^+\pi^-)$ pairs is required to be greater than $800\,\text{MeV}/c$, and the p_T of the four-body combination greater than $5000\,\text{MeV}/c$.
A physics reweighter is developed based on the signal model described in Ref. [92], where the strong coefficients were measured for the Run 1 dataset. Events are generated with the particle ordering $\pi^+\pi^- K^+\pi^-$, and the sample is required to pass the two-body mass selection criteria after applying pion-to-kaon mass swaps,

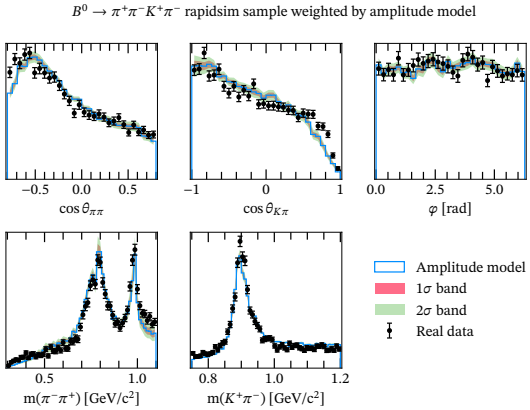

FIGURE 3.43: Agreement between the RapidSim $B^0_d \to \pi^+\pi^-K^+\pi^-$ phase space sample, weighted by the signal model of $B^0_d \to (\pi^+\pi^-)(K^+\pi^-)$, and the sWeighted data points.

as done in real data. The amplitudes A and $\bar{A}$ are generated in equal proportions, determined by a uniform random number. If $\bar{A}$ is chosen, the particle ordering is swapped: 1234 for A becomes 3412 for $\bar{A}$. Parity is handled within the PDF at amplitude level since each contribution has a defined CP eigenvalue, so no inversion of momentum is needed. Numerical integrals of each propagator are precomputed before the reweighting procedure using the Gauss-Kronrod method.

A dedicated RapidSim sample is produced for testing purposes, with all possible selection criteria of the mentioned analysis that can be included in RapidSim. This sample is compared to sWeighted data points extracted from publicly available figures. The agreement is shown in Fig. 3.43, where the 1-σ and 2-σ are derived by generating random Gaussian variations of the strong complex coefficients, considering both statistical and systematic uncertainties.

3.2.5.3 $B^0_d \to \phi K^{*0}$

A similar strategy is followed for this type of background. A RapidSim phase space sample of $B^0_d \to K^+K^-K^+\pi^-$ decays is generated, applying the same selection criteria as used for the $B^0_d \to \pi^+\pi^-K^+\pi^-$ sample.
The physics reweighter is developed based on the signal model described in Ref. [93], where the complex strong coefficients were measured using the 2011 dataset. The methodology for generating equal proportions of A and $\bar{A}$, as well as for handling mass-hypothesis swaps, follows the same approach used for $B^0_d \to \pi^+\pi^-K^+\pi^-$.

Since the PDF employs the same coding strategies as for the $B^0_d \to \rho^0 K^{*0}$ background, a dedicated program is run beforehand to extract the magnitudes and phases of individual amplitudes from their CP-averages and CP-asymmetries.

As with the previous case, a special RapidSim sample is generated for testing purposes, incorporating the relevant selection criteria from the analysis where applicable. This sample is reweighted and compared to sWeighted data points

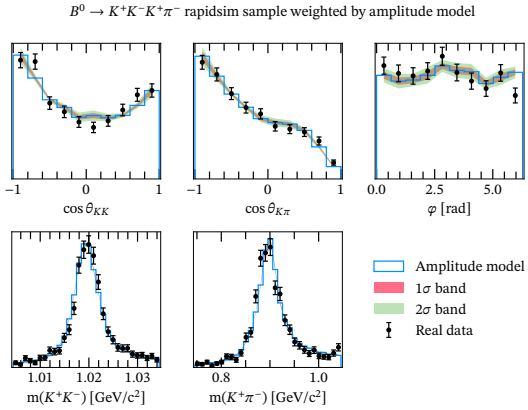

FIGURE 3.44: Agreement between the RapidSim $B^0_d \to K^+K^-K^+\pi^-$ phase space sample, weighted by the signal model of $B^0_d \to (K^+K^-)(K^+\pi^-)$, and the sWeighted data points.

taken from publicly available figures, as shown in Fig. 3.44. The 1-σ and 2-σ bands are determined by varying the complex strong coefficients within their respective 1-σ and 2-σ uncertainties, accounting for both statistical and systematic sources of error.

3.2.5.4 COMBINATORIAL

The events from the upper sideband of the fully selected real dataset are used as a proxy to describe the dynamics of the combinatorial background in the signal regions, since no other contribution are expected there as the four-body mass fit results indicate. Events in this sideband are required to have a PV-constrained four-body invariant mass greater than 5500 MeV/c^2.

While a mismatch in dynamics between different kinematic regions is possible, it is assumed to be minimal due to their relative proximity and the number of events to be handled.

3.2.6 FIT PROCEDURE

The individual amplitudes are constructed as in Eq. 2.47, where the strong coefficients a_i are free parameters of the model. They are parameterised in Cartesian coordinates, $a_i = x_i + iy_i$, since the fit bias studies showed that parameterisation in polar coordinates generate biases for small phases, due to the existence of a boundary close to its value. The component a^S_{VV} is fixed to $(1, 0)$ as a reference for both real and imaginary parts. Initial studies of flavour-integrated fits to toy experiments showed that there is no sensitivity to the imaginary part of a^P_{VV}, so it is fixed to 0 throughout the entire analysis. All weak coefficients λ_i are fixed to $(1, 0)$. As in the quasi-two-body approach, decays of intermediate states are modelled with two-body propagators. Vector contributions, which are dominated by the $K^{*0}(892)$, are modelled with a Breit-Wigner shape, as in Eq. 2.35. The mass and width at the

pole, m_0 and Γ_0, are left free in the fit. Scalar contributions are modelled with the new approach that considers re-scattering and direct production, using Eq. 2.41. The total amplitudes amplitudes for B and $\bar{B}$ are calculated using Eqs. 2.46 and 2.48, respectively. These are inserted in Eq. 3.5, where the correction to time efficiency is evaluated using Eq. 3.11. The normalisation integral is calculated with Eq. 3.19 using MC techniques, and the efficiency for each event is attached using Eq. 3.21. Caching techniques are applied so that the re-evaluation the integral, which is a very CPU-intensive operation, if a lineshape parameter is changed. This saves a lot of time in the minimisation, and in the extreme case where all lineshape parameters are fixed the fit converges in less than a minute. It is efficient to do this because `Minuit 2` only varies two parameters at a time because it needs to evaluate correlations and, if the number of lineshape parameters is relatively smaller than the number of coefficients, it is unlikely that any of the lineshape parameters are changed in a given iteration.

In order to decide how many polynomial coefficient are freed in the lineshape for the scalars, several configurations are trialled and the values of the log-likelihood at each minimum are examined. The coefficients that are not floating have a value of 0, so they do not contribute. The different trials are constructed by freeing an n-order polynomial in the magnitude and all possible polynomials in the phase from 0 to n, leading to 14 different configurations for each B meson. Changes of less than 3σ in the likelihood[4] with respect to the best, as well as fits with inaccurate minima or covariance matrices, are not considered. The results of these studies then suggest freeing $c^{\text{abs}}_{1,2,3,4}$ and $c^{\text{arg}}_{1,2}$ for B^0_s, and c^{abs}_1 and c^{arg}_1 for B^0_d.

So, in summary, the model has 9 free strong coefficients, 2 free BW pole parameters for the vector, and 6 (2) free coefficients for the scalar, that will be determined in the fit to the B^0_s (B^0_d) sample, totalling in 17 free parameters for B^0_s and 13 free parameters for B^0_d. All these parameters are fully independent between B^0_s and B^0_d, as are the data samples.

The background shape estimates, as described in previous sections, are injected in the log-likelihood through the following expression

$$-2\log\mathcal{L}(\theta) = 2\alpha\left[\sum_i^{N_{\text{Data}}}\log\mathcal{P}_{\text{sig}}(\mathbf{x}_i|\theta) - \sum_{\text{cat}}\sum_j^{N^{\text{cat}}_{\text{MC}}} w^{\text{cat}}_j\,\log\mathcal{P}_{\text{sig}}(\mathbf{x}_j|\theta)\right], \tag{3.25}$$

where cat runs over RhoKst, PhiKst and Comb, and

$$\alpha \equiv \frac{-N_{\text{Data}} + \sum_j w^{\text{RhoKst}}_j + \sum_k w^{\text{PhiKst}}_k + \sum_l w^{\text{Comb}}_l}{N_{\text{Data}} + \sum_j \left(w^{\text{RhoKst}}_j\right)^2 + \sum_k \left(w^{\text{PhiKst}}_k\right)^2 + \sum_l \left(w^{\text{Comb}}_l\right)^2} \tag{3.26}$$

guarantees that the statistical errors are correct and are not decreased by the injec-

[4]The p-value is computed with ROOT's `TMath::Prob` using $\Delta\log\mathcal{L}$ and Δn_{dof} as arguments, and then converted to a z-score.

tion of an arbitrary number of MC events. The weights

$$\begin{aligned} w_j^{\text{RhoKst}} &= \frac{N_{\text{RhoKst}}^{\text{Data}}}{N_{\text{RhoKst}}^{\text{MC}}} P_{\text{RhoKst},j}^{\text{MC}} \,, \\ w_k^{\text{PhiKst}} &= \frac{N_{\text{PhiKst}}^{\text{Data}}}{N_{\text{PhiKst}}^{\text{MC}}} P_{\text{PhiKst},k}^{\text{MC}} \,, \end{aligned} \tag{3.27}$$

are the background PDFs, scaled to the actual yields in data, evaluated in the corresponding `RapidSim` phase space samples, while

$$w_l^{\text{Comb}} = \frac{N_{\text{Comb}}^{\text{Data}}}{N_{\text{Comb}}^{\text{SB}}} \tag{3.28}$$

scales the number of combinatorial background events in the sideband to that of data, and does not need any dynamic weighting since it comes from the same data sample. The yields for each background in each signal region are fixed from Tables 3.12 and 3.13.

Before running the baseline fit and in order to avoid local minima, 1000 random sets of input parameters are generated and the fit is run for each of them. To reduce computing time, this search is run using the `Simplex` algorithm in `Minuit 2` with minimisation strategy 1. The parameters for the iteration with least $-2\log\mathcal{L}$ are saved.
The parameters found in the previous step are then used as input to the `Migrad` algorithm with minimisation strategy 2, providing the best estimates for the optimal parameters. After that, the best estimate for the covariance matrix is determined by the `Hesse` algorithm.

CHAPTER 4

RESULTS

The results obtained with the covariant model are shown in this chapter. Final observables are derived from raw amplitudes, such as fit fractions and phase differences, using pseudo-experiments to propagate the statistical uncertainties. A forward-backward asymmetry plot is presented as well.

Some of the main sources of systematic uncertainties are evaluated for the covariant model.

Additionally, this chapter shows the results obtained with the transversity model. As discussed throughout this thesis, these are not directly fitted to data but are derived from the covariant results using pseudo-experiments generated with the central values obtained. The systematic covariance matrix is used to propagate the systematic uncertainties to the transversity observables.

4.1 COVARIANT RESULTS

The values of the fitted complex strong coefficients that weight the partial waves, together with the lineshape parameters, are shown in Table C.25 for B_s^0 and Table C.26 for B_d^0, including statistical uncertainties obtained from the covariance matrix. The complex coefficients are given in both Cartesian coordinates, which are the standard parameters obtained during the amplitude fit, and polar coordinates, which are derived from the former. To avoid excessive CPU workload, neither the spin densities nor the two-body lineshapes are normalised since only the overall normalisation is required by the maximum likelihood principle. Therefore, the magnitude squared of the amplitudes cannot represent a probability. After the fit convergence, the derived and more interesting parameters, fit fractions and phases, are computed by generating pseudo-experiments to propagate the covariance matrix. The fit fractions, which indicate the relative amount of each partial wave

contributing to the total amplitude, are defined as

$$\begin{aligned} f_{ii} &= \frac{1}{N}\int d\Phi_4\, |a_i\, A_i(\Phi_4)|^2 \ , \\ f_{ij} &= \frac{1}{N}\int d\Phi_4\, 2\,\mathrm{Re}\Big(a_i\, a_j^*\, A_i(\Phi_4)\, A_j^*(\Phi_4)\Big) \ , \end{aligned} \tag{4.1}$$

where

$$N \equiv \int d\Phi_4\ |A(\Phi_4)|^2 = \int d\Phi_4 \left|\sum_i a_i\, A_i(\Phi_4)\right|^2 \tag{4.2}$$

is the total amplitude squared integrated across the analysed phase space. By definition, it holds that

$$\sum_{i=1}^{\mathrm{nAmps}} \sum_{j=i}^{\mathrm{nAmps}} f_{ij} = 1 \ . \tag{4.3}$$

The fit fractions calculated here are relative to the $K^{*0}\bar{K}^{*0}$ analysis region. The integrals are evaluated using the set of integration events used to normalise the PDF, without considering any experimental effects. To estimate the statistical error of the fit fractions, 1000 parameter sets are generated using Gaussian random numbers centred around the fit values and distributed according to the fit covariance matrix. The fit fraction matrices are illustrated in Fig. 4.1 for B_s^0 and Fig. 4.2 for B_d^0, where diagonal elements correspond to f_{ii} and off-diagonal elements[1] correspond to f_{ij}, as in Eq. 4.1. As shown, there is a very strong destructive interference between vector-vector S and D waves, exceeding 100%. Nonetheless, the fit fraction of the sum of both waves along with their interference,

$$f_{VV}^{S+D} = f_{VV}^{S} + f_{VV}^{D} + f_{VV}^{SD} \ , \tag{4.4}$$

does make sense and is the result presented in the tables. The total scalar fraction,

$$f_{\mathrm{scalar}} = f_{VS}^{+} + f_{VS}^{-} + f_{SS} \ , \tag{4.5}$$

is presented as well, together with its individual constituents.

The results of the nominal covariant fit are shown in Table 4.1 for B_s^0 and Table 4.2 for B_d^0. These results include the systematic uncertainties computed for this thesis, that will be described in the following sections. Figures 4.3 and 4.5 show the projections of the model in $\cos\theta_1$, $\cos\theta_2$, φ, $m(K^+\pi^-)$ and $m(K^-\pi^+)$ for the B_s^0 and B_d^0 fits, respectively. The same plots are shown in logarithmic scale in Figs. 4.4 and 4.6. As can be seen, there is a fantastic agreement between model and data.

[1] Note that $|a_i + a_j|^2 = |a_i|^2 + |a_j|^2 + \mathrm{Re}(a_i a_j^*) + \mathrm{Re}(a_j a_i^*)$. Consequently, the fit fraction matrix should be symmetric. However, this is simplified by merging the two interference terms into the first one and setting the second term to zero.

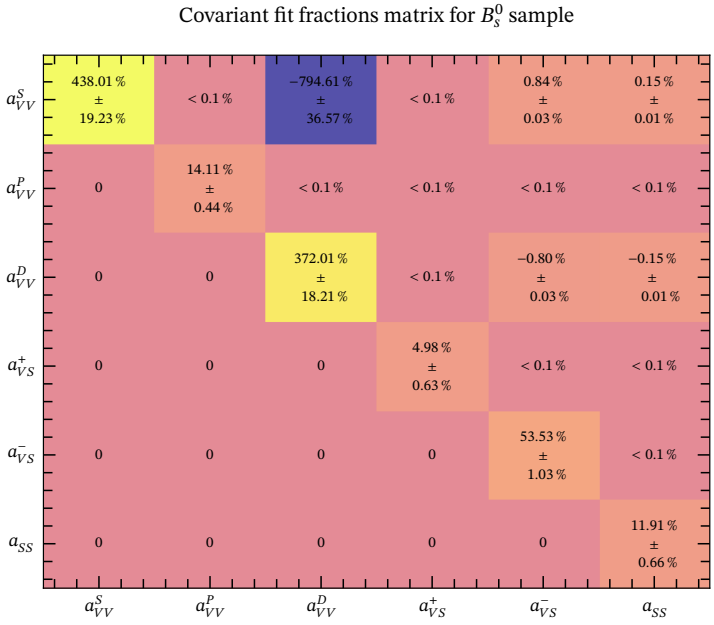

FIGURE 4.1: Fit fraction matrix for the baseline fit to the B_s^0 sample.

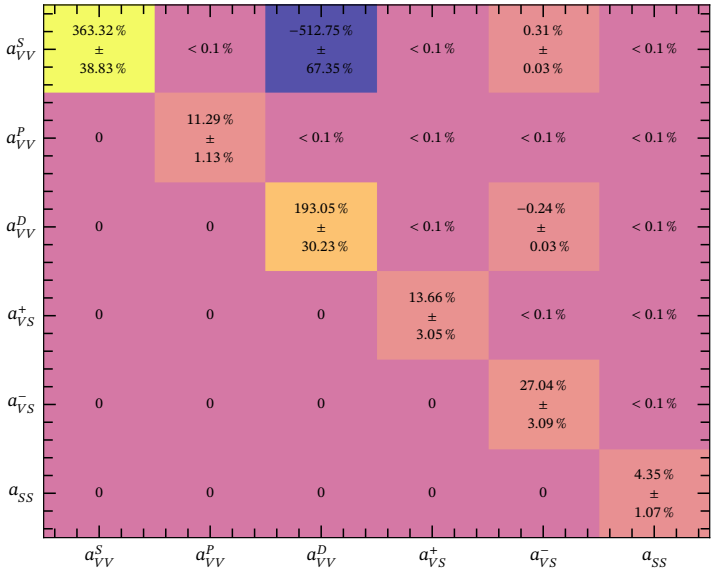

FIGURE 4.2: Fit fraction matrix for the baseline fit to the B_d^0 sample.

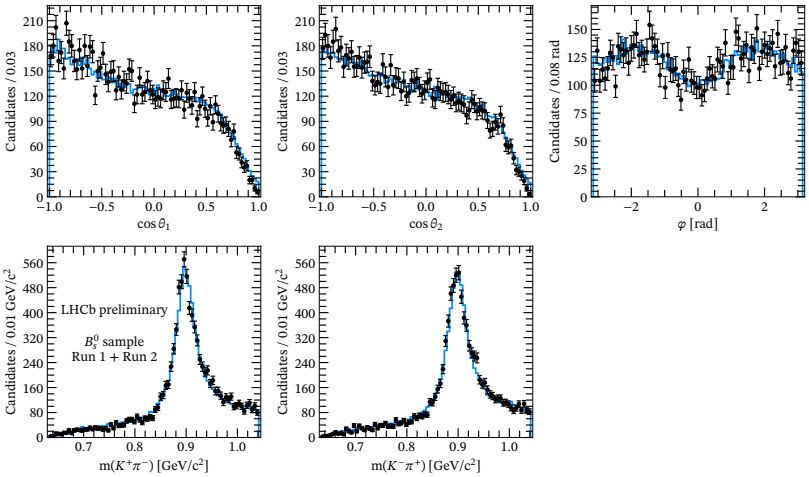

FIGURE 4.3: Projections of the nominal covariant amplitude fit to the B_s^0 sample.

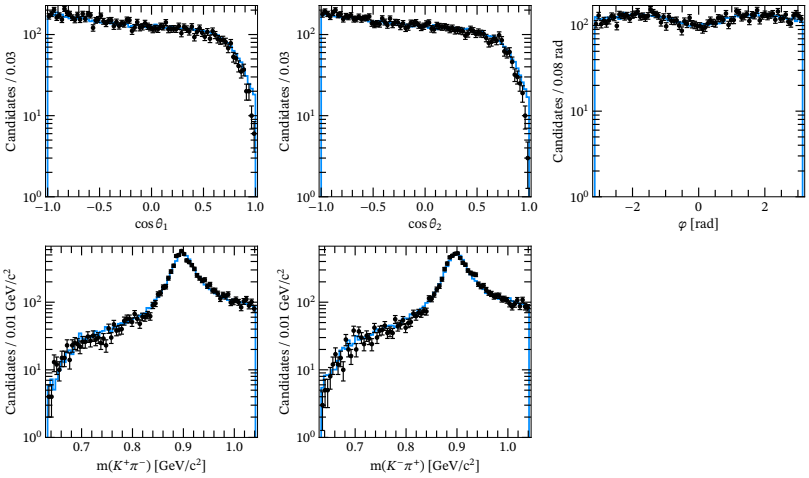

FIGURE 4.4: Projections of the nominal covariant amplitude fit to the B_s^0 sample, in logarithmic scale.

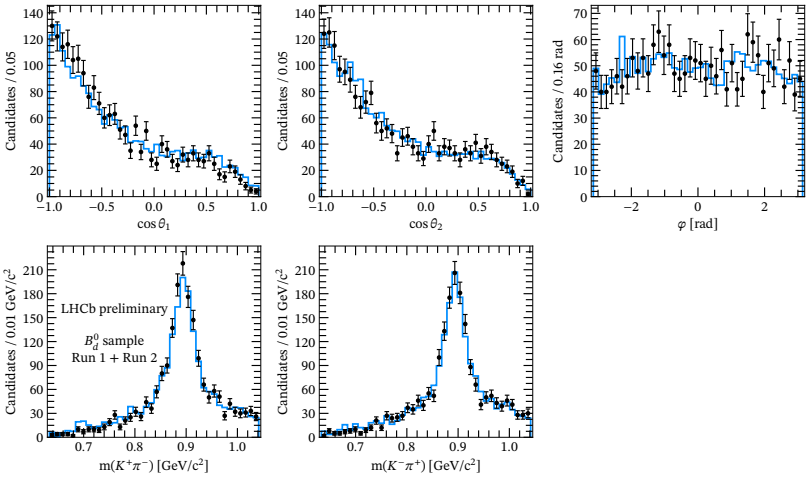

FIGURE 4.5: Projections of the nominal covariant amplitude fit to the B_d^0 sample.

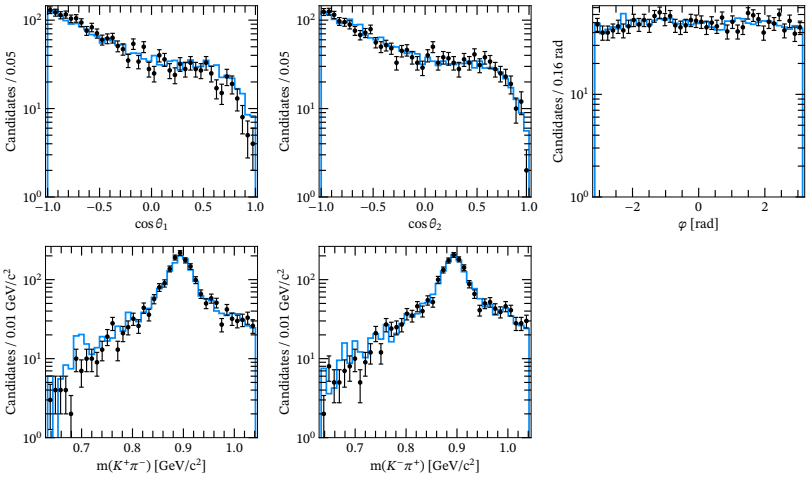

FIGURE 4.6: Projections of the nominal covariant amplitude fit to the B_d^0 sample, in logarithmic scale.

Parameter	Fit value	Parameter	Fit value
$m_{K^{*0}}$	$898.9 \pm 0.3 \pm 0.4\,\mathrm{MeV}/c^2$	$\Gamma_{K^{*0}}$	$44.8 \pm 0.8 \pm 1.5\,\mathrm{MeV}/c^2$
c_1^{abs}	$0.59 \pm 0.04 \pm 0.02$	c_2^{abs}	$0.33 \pm 0.08 \pm 0.04$
c_3^{abs}	$0.21 \pm 0.06 \pm 0.04$	c_4^{abs}	$-0.33 \pm 0.09 \pm 0.03$
c_1^{arg}	$-0.35 \pm 0.09 \pm 0.37$	c_2^{arg}	$0.59 \pm 0.12 \pm 0.26$
f_{VV}^{S+D}	$15.4 \pm 0.7 \pm 0.7\,\%$	f_{VV}^{P}	$14.1 \pm 0.4 \pm 0.5\,\%$
f_{VS}^{+}	$5.0 \pm 0.6 \pm 1.2\,\%$	f_{VS}^{-}	$54 \pm 1.0 \pm 1.6\,\%$
f_{SS}	$11.9 \pm 0.7 \pm 1.3\,\%$	f_{scalar}	$70.5 \pm 0.8 \pm 1.2\,\%$
δ_{VV}^{D}	$-0.071 \pm 0.006 \pm 0.007\,\mathrm{rad}$	δ_{VS}^{+}	$-2.14 \pm 0.08 \pm 0.43\,\mathrm{rad}$
δ_{VS}^{-}	$-3.03 \pm 0.44 \pm 0.41\,\mathrm{rad}$	δ_{SS}	$0.02 \pm 0.06 \pm 0.82\,\mathrm{rad}$

TABLE 4.1: Covariant fit parameters and fractions for the B_s^0 baseline fit. The first uncertainty is statistical and the second is systematic.

Parameter	Fit value	Parameter	Fit value
$m_{K^{*0}}$	$897.5 \pm 0.7 \pm 0.7\,\mathrm{MeV}/c^2$	$\Gamma_{K^{*0}}$	$45.7 \pm 1.7 \pm 3.9\,\mathrm{MeV}/c^2$
c_1^{abs}	$1.012 \pm 0.003 \pm 0.310$	c_1^{arg}	$1.68 \pm 0.14 \pm 0.25$
f_{VV}^{S+D}	$43.6 \pm 2.8 \pm 6.2\,\%$	f_{VV}^{P}	$11.3 \pm 1.1 \pm 2.7\,\%$
f_{VS}^{+}	$14.0 \pm 3.0 \pm 7.1\,\%$	f_{VS}^{-}	$27.1 \pm 3.1 \pm 6\,\%$
f_{SS}	$4.3 \pm 1.1 \pm 2.8\,\%$	f_{scalar}	$45.0 \pm 3.0 \pm 5.1\,\%$
δ_{VV}^{D}	$-0.19 \pm 0.05 \pm 0.13\,\mathrm{rad}$	δ_{VS}^{+}	$-1.5 \pm 0.2 \pm 0.9\,\mathrm{rad}$
δ_{VS}^{-}	$-0.4 \pm 0.1 \pm 1.0\,\mathrm{rad}$	δ_{SS}	$-0.9 \pm 0.2 \pm 2.1\,\mathrm{rad}$

TABLE 4.2: Covariant fit parameters and fractions for the B_d^0 baseline fit. The first uncertainty is statistical and the second is systematic.

4.1.1 FORWARD-BACKWARD ASYMMETRY

The forward-backward asymmetry, A_{FB}, is calculated as

$$A_{\mathrm{FB}} = \frac{N_{\mathrm{F}} - N_{\mathrm{B}}}{N_{\mathrm{F}} + N_{\mathrm{B}}}\,, \tag{4.6}$$

where N_{F} (N_{B}) is the number of events produced forwardly (backwardly), *i.e.*, in positive (negative) values of helicities, $\cos\theta$. There are, naturally, two possible options for this helicity. Each of them can be projected in terms of the corresponding $K\pi$ invariant mass, thus leading to

$$A_{\mathrm{FB}}^{1,2} = \frac{N_{\mathrm{F}}^{1,2} - N_{\mathrm{B}}^{1,2}}{N_{\mathrm{F}}^{1,2} + N_{\mathrm{B}}^{1,2}}\,, \tag{4.7}$$

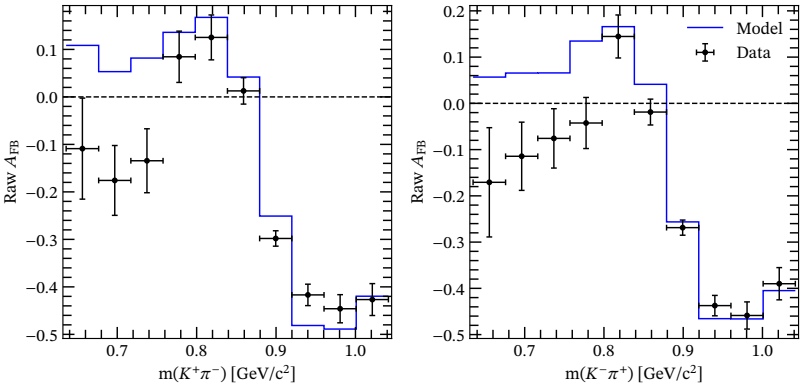

FIGURE 4.7: Raw forward-backward asymmetry for the nominal covariant amplitude fit to the B_s^0 sample.

and

$$N_F^{1,2}(m_{1,2}) = \int_0^1 \left[\mathcal{P}(\Omega, m_{1,2}, m_{2,1}) d\cos\theta_{2,1} dm_{2,1} d\varphi\right] d\cos\theta_{1,2} \,,$$
$$N_B^{1,2}(m_{1,2}) = \int_{-1}^0 \left[\mathcal{P}(\Omega, m_{1,2}, m_{2,1}) d\cos\theta_{2,1} dm_{2,1} d\varphi\right] d\cos\theta_{1,2} \,, \tag{4.8}$$

where $\Omega \equiv (\cos\theta_1, \cos\theta_2, \varphi)$ and $\mathcal{P}(\Omega, m_1, m_2)$ represents the probability density, either for real data or for the signal model whose parameters have been fitted to data.

The result for this analysis, in an attempt to reproduce the work done in Ref. [14], is shown in Fig. 4.7 for the B_s^0 sample. In contrast, the corresponding plot for B_d^0 is less statistically robust due to the limited available data. Note that since there is no parametric efficiency model in this analysis, it becomes a difficult task to estimate the efficiency at each point in the sampled phase space of real data, so the asymmetry is constructed from raw data without any efficiency correction (as was done in that reference). This is the reason why $A_{\rm FB}$ is not symmetric around 0.

There is good agreement in the region across the pole, which was the region analysed in the above-mentioned reference. In the region down to the threshold, although the model closely matches the data, there seem to be some deficits to which this observable seems to show a high sensitivity. Possible explanations to this disagreement at low mass might suggest that the quasi-two-body assumption is broken and hence a more sophisticated model would be needed to describe the interactions between the final state particles. On the experimental side, efficiency loss effects in the limit when $q \to 0$, *i.e.* the low mass $K\pi$ threshold that has not been explored so far, might not be well simulated or not well captured by the KDE.

4.1.2 SYSTEMATIC UNCERTAINTIES

Some of the main systematic variations are evaluated as an estimate of the systematic uncertainties affecting not only the covariant parameters, but also those of

Source	$m_{K^{*0}}$	$\Gamma_{K^{*0}}$	c_1^{abs}	c_2^{abs}	c_3^{abs}	c_4^{abs}
KDE bandwidth	–	0.0002	0.0028	0.0256	0.0070	0.0163
KDE kernel model	0.0003	0.0005	0.0083	0.0068	0.0153	0.0005
PID weights	–	–	0.0022	0.0041	0.0026	0.0031
Lineshape parameters	–	–	0.0113	0.0186	0.0085	0.0008
S-wave model	–	0.0002	–	–	–	–
Alternative bkg. description	0.0002	0.0013	0.0078	0.0198	0.0366	0.0262
Four-body mass fit tails	–	–	0.0003	0.0003	–	0.0007
Four-body mass fit alt. shapes	–	0.0001	0.0017	0.0018	0.0005	0.0040
Fit bias	0.0001	0.0003	0.0016	0.0155	0.0044	0.0127
Total systematic uncertainty	0.0004	0.0015	0.0166	0.0413	0.0415	0.0337
Statistical uncertainty	0.0003	0.0008	0.0388	0.0794	0.0585	0.0890

TABLE 4.3: Summary of the systematic uncertainties for the B_s^0 baseline fit. Errors smaller than 10^{-4} are not shown in the table, though are taken into account in the total systematic uncertainty.

the transversity model. Due to time constraints, not all possible sources could be estimated for this thesis but, hopefully, the remaining ones are not expected to have a strong impact. Sources such as those coming from variations on tracking and trigger weights, which might affect the efficiency across phase space, are not expected to produce large systematics since the weights are very close to 1; contributions from additional resonances, such as tensor states, are not expected to dominate in this analysis region; variations in the impact of the MVA that suppresses most of the combinatorial background are also expected to have a small effect in the amplitudes, since the data samples are selected on high-purity signal regions and some checks seem to show the impact in the 5D space is negligible. Thus, the total systematic uncertainties calculated here, of which most belong to the amplitude analysis part, correspond to a good estimate of the final figures.

The contribution of each source that is considered to the covariant results is shown in Tables 4.3–4.5 for B_s^0 and Tables 4.6–4.8, as well as the total systematic uncertainty which is obtained as square root of the sum of squares (sum of variances). The statistical uncertainty is included as well.

Additionally, the systematic covariance matrix for raw parameters[2] is calculated, for each systematic source, as

$$\Sigma^{\text{i}}_{\text{syst}} = \frac{1}{n_i} \sum_{j=1}^{n_i} \left[\theta^{\text{ref}} - \theta^{\text{alt}_j}\right] \left[\theta^{\text{ref}} - \theta^{\text{alt}_j}\right]^{\intercal} , \tag{4.9}$$

where θ^{ref} is the vector of baseline parameters and θ^{alt_j} is the vector of alternative parameters obtained for experiment j. For each systematic source i there are n_i

[2]Real and imaginary parts of each amplitude coefficient, along with mass parameters.

Source	c_1^{arg}	c_2^{arg}	f_{VV}^{S+D}	f_{VV}^{P}	f_{VS}^{+}	f_{VS}^{-}
KDE bandwidth	0.0022	0.0018	0.0066	0.0605	0.1311	0.3966
KDE kernel model	0.0244	0.0109	0.1682	0.0454	0.2972	0.7061
PID weights	0.0085	0.0071	0.0737	0.0781	0.0251	0.0973
Lineshape parameters	0.0126	0.0043	0.0014	0.0010	0.0008	0.0023
S-wave model	–	–	0.3767	0.2345	0.6522	0.9146
Alternative bkg. description	0.3690	0.2582	0.5323	0.4688	0.8897	1.0725
Four-body mass fit tails	0.0065	0.0060	0.0038	0.0013	0.0073	0.0013
Four-body mass fit alt. shapes	0.0370	0.0348	0.0225	0.0071	0.0383	0.0091
Fit bias	0.0002	0.0107	0.0487	0.0431	0.1205	0.1587
Total systematic uncertainty	0.3720	0.2612	0.6796	0.5371	1.1572	1.6363
Statistical uncertainty	0.0928	0.1210	0.6893	0.4445	0.6267	1.0284

TABLE 4.4: Summary of the systematic uncertainties for the B_s^0 baseline fit. Errors smaller than 10^{-4} are not shown in the table, though are taken into account in the total systematic uncertainty.

Source	f_{SS}	f_{scalar}	δ_{VV}^{D}	δ_{VS}^{+}	δ_{VS}^{-}	δ_{SS}
KDE bandwidth	0.1984	0.0671	0.0008	0.0124	0.0091	0.0156
KDE kernel model	0.1953	0.2136	0.0005	0.0164	0.0258	0.0437
PID weights	0.0210	0.1299	0.0003	0.0016	0.0023	0.0037
Lineshape parameters	0.0005	0.0024	–	0.0064	0.0063	0.0127
S-wave model	0.3487	0.6112	0.0069	0.4052	0.4013	0.8104
Alternative bkg. description	1.1838	1.0011	0.0014	0.1411	0.0621	0.0888
Four-body mass fit tails	0.0136	0.0051	–	0.0002	0.0009	0.0023
Four-body mass fit alt. shapes	0.0770	0.0297	0.0003	0.0012	0.0049	0.0128
Fit bias	0.0327	0.0055	0.0006	0.0099	0.0503	0.0175
Total systematic uncertainty	1.2682	1.2015	0.0072	0.4297	0.4102	0.8170
Statistical uncertainty	0.6591	0.8220	0.0061	0.0785	0.4373	0.0626

TABLE 4.5: Summary of the systematic uncertainties for the B_s^0 baseline fit. Errors smaller than 10^{-4} are not shown in the table, though are taken into account in the total systematic uncertainty.

Source	$m_{K^{*0}}$	$\Gamma_{K^{*0}}$	c_1^{abs}	c_1^{arg}	f_{VV}^{S+D}
KDE bandwidth	0.0001	–	–	0.0358	0.3787
KDE kernel model	–	0.0003	–	0.0674	0.0826
PID weights	–	0.0001	–	0.0013	0.1584
Lineshape parameters	–	–	–	0.0039	0.3172
S-wave model	0.0006	0.0012	–	–	1.7873
Alternative bkg. description	0.0004	0.0037	0.3101	0.2375	5.8531
Four-body mass fit tails	–	0.0002	–	0.0132	0.1745
Four-body mass fit alt. shapes	–	0.0001	–	0.0121	0.1589
Fit bias	–	0.0002	0.0070	0.0090	0.2821
Total systematic uncertainty	0.0007	0.0039	0.3101	0.2503	6.1534
Statistical uncertainty	0.0007	0.0017	0.0034	0.1351	2.8345

TABLE 4.6: Summary of the systematic uncertainties for the B_d^0 baseline fit. Errors smaller than 10^{-4} are not shown in the table, though are taken into account in the total systematic uncertainty.

Source	f_{VV}^{P}	f_{VS}^{+}	f_{VS}^{-}	f_{SS}	f_{scalar}
KDE bandwidth	0.0928	0.1451	0.6649	0.2339	0.2859
KDE kernel model	0.0505	0.0364	0.2799	0.3767	0.1331
PID weights	0.0729	0.0303	0.2846	0.0387	0.2313
Lineshape parameters	0.0126	0.3026	0.0772	0.0437	0.3297
S-wave model	1.6309	6.6464	4.6160	1.3877	3.4181
Alternative bkg. description	2.1568	2.4004	3.7400	2.3568	3.6963
Four-body mass fit tails	0.0188	0.0130	0.1544	0.0137	0.1557
Four-body mass fit alt. shapes	0.0174	0.0125	0.1431	0.0108	0.1415
Fit bias	0.1687	0.0532	0.2094	0.0428	0.1134
Total systematic uncertainty	2.7124	7.0749	5.9992	2.7717	5.0661
Statistical uncertainty	1.1349	3.0477	3.0951	1.0718	2.9869

TABLE 4.7: Summary of the systematic uncertainties for the B_d^0 baseline fit. Errors smaller than 10^{-4} are not shown in the table, though are taken into account in the total systematic uncertainty.

Source	δ^{D}_{VV}	δ^{+}_{VS}	δ^{-}_{VS}	δ_{SS}
KDE bandwidth	0.0275	0.0307	0.0398	0.0573
KDE kernel model	0.0680	0.0542	0.1024	0.1624
PID weights	0.0022	0.0075	0.0084	0.0079
Lineshape parameters	0.0044	0.0072	0.0145	0.0249
S-wave model	0.0830	0.9106	1.0407	2.0449
Alternative bkg. description	0.0589	0.0391	0.0674	0.0374
Four-body mass fit tails	0.0018	0.0024	0.0012	0.0076
Four-body mass fit alt. shapes	0.0016	0.0022	0.0010	0.0071
Fit bias	0.0014	0.0105	0.0030	0.0119
Total systematic uncertainty	0.1256	0.9137	1.0488	2.0527
Statistical uncertainty	0.0460	0.1504	0.1226	0.2102

TABLE 4.8: Summary of the systematic uncertainties for the B^0_d baseline fit. Errors smaller than 10^{-4} are not shown in the table, though are taken into account in the total systematic uncertainty.

alternative sets of fit parameters. The total systematic covariance matrix is then calculated as the sum of the n_{syst} individual matrices,

$$\Sigma^{\text{tot}}_{\text{syst}} = \Sigma^{1}_{\text{syst}} + \cdots + \Sigma^{n_{\text{syst}}}_{\text{syst}} \,. \tag{4.10}$$

This matrix will be used to propagate the systematic uncertainties on covariant parameters to transversity parameters.

4.1.2.1 4-BODY MASS MODEL

The systematic effect due to a mismodeling of the signal and background shapes is evaluated by repeating the four-body mass fit using different shapes for the signal $B^0_s \to (K^+\pi^-)(K^-\pi^+)$ and $B^0_d \to (K^+\pi^-)(K^-\pi^+)$ decays and separately the combinatorial background shape. A double-sided crystal ball is used as an alternative to the Hypatia shape [78] for the signal peaks which is fit to the MC. For the combinatorial background, a second-order Bernstein polynomial [94] is used as an alternative shape to the flat line used in Run 1 and the exponential distribution used in Run 2. The new yields produced by these changes are substituted in the amplitude fit, thus producing a new set of fit parameters. The absolute value of the difference with respect to the baseline values is assigned as a systematic uncertainty.

Additionally, the tail parameters of the Hypatia signal shapes with the nominal model of the Hypatia are also varied at extreme values of all possible combinations of 0 and $\pm 2\sigma$ of their fit values. The sets of yields produced in these mass fits are used to build a covariance matrix, to smooth the effect of these sampling at extreme values, and 100 sets of yields are sampled using a multivariate gaussian. Then, 100 refits are performed, thus assigning the root mean square deviation to baseline as a systematic uncertainty.

4.1.2.2 EFFICIENCY MODEL AND LIMITED MC STATISTICS

Due to the huge size of the simulated samples used to estimate the efficiency across phase space, a specific systematic to directly account for the impact in the efficiency shape is not considered. Instead, the KDE bandwidth matrix is halved to produce a systematic variation in the efficiency shape due to the use of these hyperparameters. Intuitively, finer bandwidths make KDE to be more sensitive to statistical fluctuations, so this already considers a finite MC sample. The systematic uncertainties due to this source are estimated as the distance to baseline parameters.

Additionally, the kernel function used in the KDE is changed from a Gaussian kernel to a parabolic kernel. Once again, the systematic uncertainties are estimated as the distance to baseline parameters.

4.1.2.3 PID WEIGHTS

As discussed, the information about PID on the phase space MC samples used in the efficiency determination comes from the PID weights calculated with `PIDCalib2`, which emulate the PID cuts that are applied on the data. As to estimate systematic variations, two alternative binning schemes, one finer and one coarser, are configured to produce the subsequent two alternative sets of PID weights, followed by new determinations of efficiency and covariant refits. The absolute value of the largest difference between the two sets and the baseline parameters is assigned as systematic uncertainty.

4.1.2.4 LINESHAPE PARAMETERS

The lineshapes used to describe intermediate resonances usually have parameters that are fixed to some values, so they need to be varied within their corresponding uncertainties to see the effect they produce on the measured parameters. In this case, only the coefficients B_0 and B_1 from the re-scattering lineshape in the S-wave model are susceptible to be changed and produce a visible uncertainty, so 100 alternative values for these are generated with Gaussian random numbers and fixed in the covariant fit, which is repeated that many times. The systematic uncertainty is estimated as the root mean square deviation to baseline parameters.

4.1.2.5 S-WAVE MODEL

Another approach for the S-wave, which is widely used by the community, is the LASS parameterisation [95, 96], which consists of a BW to model the $K_0^*(1430)$ and an effective range interaction to describe the non-resonant term

$$T(s) = \sin\delta_F(s)\, e^{i\delta_F(s)} + \sin\delta_R(s)\, e^{i\delta_R(s)}\, e^{2i\delta_F(s)}\ , \tag{4.11}$$

with

$$\delta_F(s) = \cot^{-1}\left[\frac{1}{a\,q(s)} + \frac{r\,q(s)}{2}\right], \qquad \delta_R(s) = \tan^{-1}\left[\frac{m_0\,\Gamma(s)}{m_0^2 - s}\right], \tag{4.12}$$

being $\Gamma(s)$ the particular case of Eq. 2.36 for $L = 0$ and $q(s)$ the breakup momentum given by Eq. 2.19. The constants a and r are called scattering length and effective range, and m_0 and Γ_0 are the mass and width at the pole of the $K_0^*(1430)$. These four are free parameters of the model. While m_0 and Γ_0 can be fixed to known PDG values, as there is no sensitivity to them in this analysis region, a and r depend on the analysis and the specific background levels so they must be determined directly from data.

The covariant fit is repeated using this model, and the difference to baseline is assigned as a systematic uncertainty.

4.1.2.6 ALTERNATIVE BACKGROUND DESCRIPTION

Three background sources have non-negligible contributions in the selected signal regions: $B_d^0 \to \rho^0 K^{*0}$, $B_d^0 \to \phi K^{*0}$, and combinatorial. Initially, 2σ variations of the peaking backgrounds were considered as a systematic uncertainty of the first two, leading to a negligible systematic and confirming the low impact of these backgrounds. Combinatorial is more tricky to estimate, since a change of sideband leads to an unavoidable contribution from other backgrounds. Instead, a `sWeighted` fit is considered as an alternative description for all backgrounds. Since the fit starts at the minimum, it is considered to be a very good alternative estimate. The difference to baseline parameters is assigned as the systematic uncertainty.

4.1.2.7 FIT BIAS

The possibility of the model to present biases is studied in detail by generating 400 pseudo-experiments of the same number of signal events as in data, using the baseline model. These are then re-fitted and pull distributions are constructed, which are shown in App. C.5 for both B_s^0 and B_d^0 mesons. Given that there are little biases but the behaviour is mostly Gaussian, the distance from the mean of the distributions to the baseline values is assigned as systematic uncertainty.

4.2 TRANSVERSITY RESULTS

Although the covariant framework provides enhancements in decay modelling and in systematics, the primary goal of this flavour- and time-integrated amplitude analysis is the measurement of the transversity fractions, and especially f_L, for both B-mesons. The VV partial waves S, P and D are linear combinations of A_0, $A_\parallel$ and $A_\perp$ but the presence of the Blatt-Weisskopf barrier factors in the amplitude model

makes this transformation to become phase-space dependent,

$$\begin{aligned} A_0 &= -\sqrt{\frac{1}{3}} a_{VV}^S \, B_0(\Phi_4) + \sqrt{\frac{2}{3}} a_{VV}^D \, B_2(\Phi_4) \, , \\ A_\perp &= a_{VV}^P \, B_1(\Phi_4) \, , \\ A_\parallel &= \sqrt{\frac{2}{3}} a_{VV}^S \, B_0(\Phi_4) + \sqrt{\frac{1}{3}} a_{VV}^D \, B_2(\Phi_4) \, , \end{aligned} \tag{4.13}$$

so there is no trivial way to move from one basis to another.

The strategy to face this issue consists of generating pseudo-experiments using the total vector-vector amplitude described with the covariant model, using the parameters that were fitted to data (Table C.25 and Table C.26). The time- and flavour-integrated PDF that is used for the fits to data is also used for this MC generation. The transversity parameters are extracted by performing fits to these samples using with the VV transversity model. In this model, the lineshapes describing the vector resonances factorise, and hence a 3D fit is enough to determine the transversity parameters i.e., only the distributions of $\cos\theta_1$, $\cos\theta_2$, φ matter. A complete description of the transversity model, as well as the PDF used in these fits, is provided in App. A. Note that in that appendix, for the sake of generality, a scalar contribution is considered as well, but only the VV part is used in this analysis.

The total number of pseudo-experiments generated is 400. For each of them, only $N_{\rm sig} \times f_{VV}$ events are generated, where $N_{\rm sig}$ is the number of signal candidates determined from the four-body mass fit and f_{VV} is the total VV fit fraction, $f_{VV} = f_{VV}^{S+D} + f_{VV}^P$. This ensures that the transversity parameters are distributed according to the statistics provided by the VV component. Additionally, each pseudo-experiment is generated from the covariant parameters generated using Gaussian random numbers centred at the nominal results and distributed according to $\Sigma_{\rm syst}^{\rm tot}$. Thus, the determined parameters will be distributed according to the total uncertainty, $\sigma_{\rm tot}^2 = \sigma_{\rm stat}^2 + \sigma_{\rm syst}^2$.

For each transversity fit, an intermediate program generates 1000 Gaussian parameter sets distributed according the transversity fit nominal values and covariance matrix, and the derived results, fractions and phases, are calculated for each of them. The mean and the standard deviation are assigned as the nominal fit value and its *total* uncertainty. To separate the contribution of the statistical uncertainty, the same fit and strategy is used on the toys generated for the fit bias study, which are only spread by statistical fluctuations. Of course, only $N_{\rm sig} \times f_{VV}$ events are read for each toy. The systematic uncertainty is then estimated as $\sigma_{\rm syst}^2 = \sigma_{\rm tot}^2 - \sigma_{\rm stat}^2$. The results are shown in Table 4.9 for B_s^0 and Table 4.10 for B_d^0.

The most important observables are the longitudinal polarisation fractions, which are measured to be

$$\begin{aligned} f_L^{B_s^0 \to K^{*0}\bar{K}^{*0}} &= 0.156 \pm 0.012 \pm 0.008 \, , \\ f_L^{B_d^0 \to K^{*0}\bar{K}^{*0}} &= 0.694 \pm 0.022 \pm 0.052 \, . \end{aligned} \tag{4.14}$$

As can be noted, the total systematic uncertainty is much higher for B_d^0 than for B_s^0. This makes sense, as the dominant sources of uncertainty are the S–wave

Parameter	Fit value	Parameter	Fit value
f_L	$0.156 \pm 0.012 \pm 0.008$	$f_\parallel$	$0.350 \pm 0.013 \pm 0.012$
$f_\perp$	$0.494 \pm 0.012 \pm 0.008$	$\delta_\parallel$	$0.71 \pm 0.05 \pm 0.13$ rad

TABLE 4.9: Transversity fit observables for the B_s^0 baseline fit. The first uncertainty is statistical and the second is systematic.

Parameter	Fit value	Parameter	Fit value
f_L	$0.694 \pm 0.022 \pm 0.052$	$f_\parallel$	$0.145 \pm 0.021 \pm 0.019$
$f_\perp$	$0.161 \pm 0.018 \pm 0.049$	$\delta_\parallel$	$0.57 \pm 0.09 \pm 0.34$ rad

TABLE 4.10: Transversity fit observables for the B_d^0 baseline fit. The first uncertainty is statistical and the second is systematic.

model and the background description. The statistics is much lower for B_d^0 than for B_s^0, leading to a less precise determination of the S–wave shape. Additionally, the signal-to-background ratio is significantly worse for B_d^0 than for B_s^0, further contributing to the increased uncertainty.

A preliminary result of $L_{K^{*0}\bar{K}^{*0}}$ can be calculated using the previous result for the ratio of branching fractions between B_s^0 and B_d^0 modes [16],

$$\frac{\mathcal{B}(B_d^0 \to K^{*0}\bar{K}^{*0})}{\mathcal{B}(B_s^0 \to K^{*0}\bar{K}^{*0})} = 0.0758 \pm 0.0064 \,. \tag{4.15}$$

The phase space factor from the definition of $L_{K^{*0}\bar{K}^{*0}}$, in Eq. 1.33, is calculated to be

$$\rho(m_1, m_2) = 1.014 \pm 0.004 \,, \tag{4.16}$$

where the numerical values are taken from Ref. [3]. Thus, using this number, together with the ratio of branching fractions and together with the ratio of longitudinal polarisation fractions measured in this thesis, a preliminary result for this observable is estimated to be

$$L_{K^{*0}\bar{K}^{*0}} = 3.0 \pm 0.5 \,, \tag{4.17}$$

agreeing with the previous experimental determination within 1σ.

Before obtaining the final numbers for publication, the systematic uncertainties related to tracking and trigger weights, additional resonances, and barrier factor radii must be evaluated. These contributions are expected to be small but are particularly time-consuming given the time constraints of this thesis. Additionally, during the review process, further checks may arise before receiving approval for the unblinding of the branching fraction measurement (which was conducted independently of the amplitude analysis) and, consequently, the evaluation of $L_{K^{*0}\bar{K}^{*0}}$.

CHAPTER 5

CONCLUSIONS

The huge amounts of data generated from particle collisions that can be produced nowadays allow the study of all kinds of particle decays, and especially those that are particularly rare, with production probabilities as low as one in a million, or even smaller. Significant efforts are currently being made to achieve high-precision measurements of observables in penguin-dominated decays, especially when SM predictions are available with acceptable theoretical uncertainties. BSM physics may contribute to virtual loops, leading to deviations from SM predictions and providing potential signatures of NP.
The observable $L_{K^{*0}\bar{K}^{*0}}$ was proposed and calculated as the ratio of the longitudinal branching fractions of $B^0_d \to K^{*0}\bar{K}^{*0}$ and $B^0_s \to K^{*0}\bar{K}^{*0}$ decays, which are dominated in the SM by hadronic penguin diagrams and have smaller branching fractions, being accessible only to experiments that massively produce B^0_s and B^0_d mesons. These decay channels have an almost unique property of being related by a U–spin rotation, leading to partial cancellations of hadronic uncertainties. The experimental measurement is much more precise, though new ideas and analysis techniques will be required to provide competitive measurements given the huge statistics that will be collected by the LHC.

This thesis presents the ongoing time-integrated and flavour-untagged amplitude analyses of $B^0_d \to K^{*0}\bar{K}^{*0}$ and $B^0_s \to K^{*0}\bar{K}^{*0}$ decays, whose main goal is the experimental determination of longitudinal polarisation fractions, f_L, for both B–decays. The data analysed were collected by the LHCb experiment using proton–proton collisions produced at centre-of-mass energies of 7, 8, and 13 TeV, with integrated luminosities of 1, 2, and 6 fb^{-1}, respectively. This analysis has had a complete rebranding, since some of the previous measurements for these decays were already dominated by the systematics. The key improvements can be summarised as:

- **Spin description in covariant formalism**
  Transversity amplitudes are not eigenstates of orbital angular momentum L, and hence the production Blatt-Weisskopf barrier factors of the $K^{*0}\bar{K}^{*0}$ inter-

mediate state for the A_0 and $A_\parallel$ states are undefined. In the previous analysis, the $L = 0$ barrier factor was chosen for the baseline, while the alternative form for $L = 2$ had to be trialled in the systematics. Covariant spin amplitudes are eigenstates of L and as such, the appropriate production barrier factor can be applied without further systematic study.

- **New efficiency modelling methods**
  The dominant systematic in the previous time-dependent analysis was related to the sample size used for the determination of the angular efficiency. This time the simulated samples consist of millions of events generated flat in phase space, so this will no longer be the dominant systematic. Besides, a new technique based on KDE is exploited to build the efficiency maps of the integration sample.
- **Fitting the S–wave contribution down to threshold with a new model**
  This analysis focuses on the $K\pi$ mass region near the $K^{*0}(892)^0$ but the analysis is performed right down to the $K\pi$ mass threshold which has not been done before, thus providing a maximum lever arm over scalar contributions. Also, a new model for these scalars, that considers both production and decay mechanisms, is proposed.

The transversity fractions are measured by fitting pseudo-experiments generated the from nominal covariant results, and preliminary results obtained in this thesis with the most important systematic uncertainties are

$$f_L^{B_s^0\to K^{*0}\bar{K}^{*0}} = 0.156 \pm 0.012 \pm 0.008 \,,$$
$$f_L^{B_d^0\to K^{*0}\bar{K}^{*0}} = 0.694 \pm 0.022 \pm 0.052 \,.$$

The B_s^0 longitudinal polarisation fraction is measured with a systematic uncertainty reduction factor of almost 6 compared to the previous time-dependent analysis, which was $0.208 \pm 0.032 \pm 0.046$. As discussed, not all possible systematics have been calculated in this thesis, although a good estimate is provided. The ratio of longitudinal polarisation fractions is measured to be

$$\frac{f_L^{B_s^0\to K^{*0}\bar{K}^{*0}}}{f_L^{B_d^0\to K^{*0}\bar{K}^{*0}}} = 0.225 \pm 0.018 \pm 0.020 \,.$$

The value of this ratio measured by the previous time-integrated analysis, which also analysed both B_s^0 and B_d^0 decays, is $0.331 \pm 0.049 \pm 0.035$. Both values agree within 1.6σ. Given the huge statistics analysed this time, the results are slightly dominated by systematics. However, there is a factor 2 of reduction in the total uncertainty of the f_L ratio with respect to the previous analysis, so all efforts and changes made were finally worthwhile. A preliminary result of $L_{K^{*0}\bar{K}^{*0}}$ is found to be 3.0 ± 0.5, to be compared with the theoretical value, $L^{\text{theo}}_{K^{*0}\bar{K}^{*0}} = 19.53^{+9.14}_{-6.64}$. The experimental value is even lower than the previous one, 4.43 ± 0.92, although the branching fraction measurement of this analysis is still blinded, and consistency checks have not been run yet. It is therefore a little early to draw conclusions.

Looking ahead, Run 3 data will provide massive statistics for two main reasons: 25 fb^{-1}are expected to be collected, and hadronic efficiencies will be higher with

the removal of the hardware trigger. Thus, special attention should be paid to the control of these systematics, and probably the measurement of the ratio of polarisation fractions should be an objective, exploiting partial cancellations of systematic uncertainties.

RESUMO

This chapter contains an extended summary written in Galician.

INTRODUCCIÓN

A física de partículas estuda os constituíntes máis fundamentais da materia, así como as interaccións entre eles. Os avances teóricos e experimentais deron lugar a decenas de descubrimentos durante o século XX. Todo este coñecemento culminou na teoría máis exitosa da física moderna, capaz de describir satisfactoriamente todas as partículas coñecidas e as súas interaccións: o Modelo Estándar da física de partículas.
Esta teoría consegue clasificar nun marco coherente as partículas fundamentais que compoñen o universo coñecido e unificar as interaccións fundamentais que actúan entre elas, exceptuando a gravidade. A forza deste modelo reside no seu poder preditivo e a súa capacidade para explicar unha gran variedade de fenómenos experimentais con gran precisión. Desde procesos de dispersión en colisores ata decaementos de partículas inestables, o Modelo Estándar proporciona unha ferramenta esencial para entender a dinámica do mundo subatómico.

O Modelo Estándar clasifica as partículas en dous grandes grupos, en base ao carácter enteiro ou semi-enteiro dun número cuántico coñecido como *espín*. As partículas con espín semienteiro $(1/2, 3/2, \dots)$ chámanse *fermións*, e as que teñen espín enteiro $(0, 1, 2, \dots)$ son *bosóns*. Os fermións son considerados no Modelo Estándar como os constituíntes fundamentais da materia ordinaria, e pódense categorizar noutros dous grupos máis: os *quarks*, que sinten a interacción forte, e os *leptóns*, que non a sinten. Existen seis tipos, ou *sabores*, fundamentais de quarks: *up* (u), *down* (d), *strange* (s), *charm* (c), *bottom* ou *beauty* (b), e top (t). Os leptóns tamén veñen en seis sabores: electrón (e^-), muón (μ^-), *tau* (τ^-), e os seus correspondentes neutrinos (ν_e, ν_μ, ν_μ). Os quarks teñen un número cuántico chamada *cor*, ou carga de cor, mediante a cal poden interaccionar fortemente. Os quarks nunca foron observados illadamente, senón que forman parte de partículas compostas chamadas *hadróns*. Á sua vez, os hadróns poden estar formados por tres quarks (ou anti-quarks) ou por parellas quark-antiquark, e reciben os nomes de *barións* e *mesóns*.

Os quarks u e d forman un bloque básico dentro do seu sector, e os pares (c, s) e (t, b) parecen ser réplicas de maior masa. O mesmo sucede no sector leptónico, co bloque (e^-, ν_e). A cada un destes pares de partículas chámaselle familia ou

xeración, e, ignorando que teñen distinta masa, todas as familias tanto no sector dos quarks como dos leptóns parece interaccionar de maneira similar. Polo menos, isto sucede así no Modelo Estándar.

A parte dos fermións, os bosóns xogan un papel fundamental no Modelo Estándar. Estes aparecen de xeito natural na teoría para preservar o que se coñece como simetría gauge, polo que moitas veces son coñecidos como bosóns gauge. Son responsables de mediar as interaccións fundamentais entre fermións, estando cada tipo de interacción asociada a un bosón: o fotón (γ) transmite a interacción electromagnética, os bosóns $W^{\pm}$ e Z^0 transmiten a interacción débil por correntes cargadas e neutras, e o gluón (g) transmite a interacción forte. O bosón de Higgs, que foi descuberto no CERN en 2012, é responsable de darlle masa aos fermións e aos bosóns gauge masivos.

A pesar dos éxitos do Modelo Estándar, tamén deixa sen resolver moitas preguntas fundamentais que suxiren a existencia dunha física alén do Modelo Estándar. Entre estas incógnitas destacan a natureza da materia escura, a enerxía escura, a orixe da asimetría materia-antimateria no universo ou a integración da gravidade nun marco cuántico.

Unha das áreas nas que o Modelo Estándar presenta desafíos é a física do sabor, que inclúe o estudo das propiedades e interaccións dos quarks e leptóns. O mecanismo de violación da simetría CP (carga-paridade), predito dentro deste modelo, é insuficiente para explicar completamente a desaparición da antimateria no universo. Esta limitación motiva unha intensa investigación experimental destinada a identificar desviacións respecto ás predicións do Modelo Estándar, que poderían ser signos de nova física.

O EXPERIMENTO LHCB

Neste contexto, o experimento LHCb (Large Hadron Collider beauty), situado no CERN, xoga un papel crucial. O LHC (Large Hadron Collider) é un colisor protón-protón con forma de anel, de 27 quilómetros de circunferencia, que opera a enerxías da orde de varios teraelectronvoltios, que nunca antes foron estudadas. Dous feixes de protóns viaxan en sentidos opostos e coliden en catro puntos específicos dentro do anel, e aí sitúanse catro experimentos, sendo un deles LHCb. Este foi deseñado especificamente para estudar fenómenos relacionados cos quarks pesados, como o quark *beauty* (b) e o quark *charm* (c), LHCb busca desentrañar os procesos fundamentais que rixen a física de sabor. Grazas á súa alta resolución espacial, temporal e na identificación de partículas, o experimento é unha ferramenta esencial para analizar os decaementos raros, as oscilacións de mesóns neutros e outros procesos que poderían revelar discrepancias coas predicións do Modelo Estándar.

O detector consta dun brazo único situado na rexión cara adiante, xa que é cara onde se producen os quarks pesados, b e c, a altas enerxías. O detector consta, á vez, de varios sub-detectores con propósitos moi específicos:

- VELO (Vertex Locator): o buque insignia do experimento. Forma parte do sistema de trazado, e permite reconstruir as trazas que deixan as partículas ao pasar por el. Outra das súas funcións principais é separar os vértices

primarios, onde se producen os mesóns pesados, dos secundarios, onde decaen.
- Imán: dipolo magnético que curva a traxectoria das partículas cargadas segundo a lei de Lorentz, permitindo a identificación da súa carga e o seu momento.
- RICH (Ring Imaging Cherenkov): permite coñecer a masa das partículas cargadas coa condición de ter determinado previamente o seu momento. Funciona en base ao principio de emisión de luz Cherenkov.
- Sistema de trazado: é un conxunto de detectores enfocado a reconstruir as traxectorias que seguen as partículas.
- Sistema de calorimetría: permite medir frear as partículas e medir a enerxía que depositan.
- Sistema de muóns: úsase para identificar muóns e reconstruir a súa traxectoria.

Ademais, LHCb consta dun sistema de disparo, ou *trigger*, para reducir a taxa de sucesos gardados en disco, xa que a gran maioría deles non conteñen nada relevante para o programa de física do experimento. O sistema decide en tempo real, a velocidades absurdas, se un suceso ten que ser gardado ou non. O trigger de LHCb consta de tres etapas, estando cada nivel cada vez máis especializado:
- L0 (Level 0): procesa sucesos a 40 MHz e decide en base a sinais electrónicos nos calorímetros e no sistema de muóns, principalmente. Consegue reducir a taxa de sucesos a 1 MHz.
- HLT1 (High Level Trigger 1): reconstrúe parcialmente as trazas das partículas e fai seleccións básicas.
- HLT2 (High Level Trigger 2): reconstrúe completamente o suceso e permite facer seleccións máis sofisticadas. Permite escribir en disco a unha taxa duns poucos kHz.

ANOMALÍAS DE SABOR NAS DESINTEGRACIÓNS $B^0_{s,d} \to K^{*0}\bar{K}^{*0}$

Unha canle de referencia no estudo de observables con violación das simetrías CP e T é a desintegración dos mesóns B^0_s e B^0_d ao estado final $K^{*0}\bar{K}^{*0}$. Este decaemento ocorre no Modelo Estándar, a orde dominante na expansión en serie, a través dun diagrama de Feynman de tipo pingüín, é dicir, un diagrama con lazos cuánticos virtuais no cal hai unha corrente neutra efectiva que cambia o sabor. Os procesos a nivel de quarks son $b \to sd\bar{d}$ e $b \to ds\bar{s}$, e o diagrama pingüín dominante é de tipo gluónico. A nova física polo tanto ten que estar a escalas de enerxía moi altas ou ter acoplos moi débiles. Polo tanto, hai máis sensibilidade a estes novos operadores en procesos que estean suprimidos, e de aí a importancia dos diagramas de tipo pingüín e a procura de decaementos moi raros.

Estes modos de desintegración teñen un considerable interese na comunidade teórica. Teñen a propiedade moi interesante, e case única, de estar relacionados por unha rotación de sabor, coñecida como *espín U*, entre os quarks b e s. Facendo esta rotación no $B^0_s \to K^{*0}\bar{K}^{*0}$ obtense o $B^0_d \to K^{*0}\bar{K}^{*0}$, e viceversa. A moi altas enerxías esta simetría é perfecta, e a enerxías na escala da masa do quark b está

rota só pola diferenza entre as masas do B_s^0 e B_d^0, que é pequena. Isto é atractivo desde un punto de vista teórico porque as incertezas hadrónicas poden cancelar en boa medida, permitindo mellores predicións do Modelo Estándar.

Aínda que polo que parece as anomalías de sabor en desintegracións semileptónicas desapareceron, deixando de estar as medidas experimentais dos cocientes de taxas de desintegración desviados das predicións do Modelo Estándar, a fenomenoloxía e o coñecemento publicado nesta última década permitiu guiar aos teóricos a desenvolver novos observables para estudar desintegracións de mesóns B sen charm e sen leptóns. Estes preséntanse, para decaementos do tipo $B \to VV$, como cocientes das taxas de desintegración polarizadas lonxitudinalmente. No caso de $B_{s,d}^0 \to K^{*0}\bar{K}^{*0}$, este observable toma a forma de

$$L_{K^{*0}\bar{K}^{*0}} = \mathcal{G}\,\frac{f_L^{B_s^0\to K^{*0}\bar{K}^{*0}}}{f_L^{B_d^0\to K^{*0}\bar{K}^{*0}}}\,\frac{\mathcal{B}(B_s^0 \to K^{*0}\bar{K}^{*0})}{\mathcal{B}(B_d^0 \to K^{*0}\bar{K}^{*0})}\,,$$

onde $\mathcal{G}$ é un factor de espazo fásico, que involucra as masas e os tempos de vida promedio dos mesóns B_s^0 e B_d^0, así como a masa do $K^{*0}(892)$. O produto $f_L \times \mathcal{B}$ é coñecido como taxa de desintegración lonxitudinal, e representa a probabilidade de que os mesóns se desintegren nese estado final no que os vectores están polarizados lonxitudinalmente. A importancia de escoller esta polarización concreta para facer predicións é porque sofren de menos incertezas hadrónicas que os modos transversais, os cales sofren de distintas diverxencias e son máis complicados de calcular. O valor teórico calculado no marco do Modelo Estándar é de $L^{\text{teo}}_{K^{*0}\bar{K}^{*0}} = 19.53^{+9.14}_{-6.64}$. A medida experimental por parte de LHCb en 2019 é, sen embargo, $L^{\text{exp}}_{K^{*0}\bar{K}^{*0}} = 4.43 \pm 0.92$, que é moito máis baixo do que di a teoría. A significancia estatística desta tensión entre teoría e experimento alcanza os 2.6σ, que en termos Gaussianos corresponde a unha probabilidade de concordancia do 1%.

A interpretación que deron os autores teóricos a esta discrepancia é que os acoplos gluónicos que están sendo postos en xogo nesta canle non son universais, senón que as transicións $b \to s$ están dalgún xeito suprimidos fronte a $b \to d$. O valor anómalo tan baixo desta polarización non se pode explicar no Modelo Estándar, e polo tanto mellores medidas e cálculos máis precisos son necesarios para ver si hai Nova Física ou non. Esta tese é está precisamente dedicada a medir os valores de f_L para as dúas desintegracións, de B_s^0 e B_d^0, que xunto cos valores que das taxas de desintegración poderase dar unha medida moito máis precisa de $L_{K^{*0}\bar{K}^{*0}}$.

SELECCIÓN DE DATOS

Aínda que a maior parte da selección de datos foi feita por un estudante de doutoramento dun programa mixto entre as universidades de Warwick (Reino Unido) e Monash (Australia), preséntase aquí para dar contexto á análise de amplitudes. Os datos que serán seleccionados e analizados proveñen do conxunto completo de datos recollido polo experimento LHCb durante o Run 1, que corresponde aos anos

2011–2012, e o Run 2, que corresponde aos anos 2015–2018, resultando en total en 9 fb^{-1}.

A parte da selección céntrase en construír conxuntos de datos de alta pureza a partir de ficheiros b–hadrónicos, é dicir, as saídas do High Level Trigger que son candidatas a conter desintegracións de hadróns cun quark b. Estes ficheiros son filtrados por un conxunto de seleccións básicas, que é coñecido como liña de *stripping*, que buscan catro trazas cargadas compatibles con $K^{\pm}$ e $\pi^{\mp}$ e que utilizan a información da masa dos candidatos a mesóns B e da masa dos estados intermedios compatibles coas resonancias $K^{*0}(892)$, así como información do vértice primario.

Despois do stripping, faise unha pre-selección cunha serie de cortes que manteñen un alto porcentaxe de sinal, os sucesos que queremos buscar, e eliminan un alto porcentaxe de fondo, sucesos moi parecidos aos de sinal que pasan todos os filtros. Nestes cortes úsanse variables cinemáticas, de calidade do vértice e de identificación das partículas (PID).

Fanse simulacións por Monte Carlo (MC) de varios millóns de sucesos tanto do sinal, $B_s^0 \to K^{*0}\bar{K}^{*0}$, como os decaementos do B_s^0 e o B_d^0 ás catro partículas finais tendo en conta unicamente o espazo fásico, $B_{s,d}^0 \to K^+\pi^-K^-\pi^+$. Estas últimas son de especial interese para a análise de amplitudes.

Dado que as variables PID non están ben simuladas, obtense o conxunto de variables corrixidas a través do paquete `PIDCorr`. Isto permite aplicarlles todos os cortes da liña de strippling, a cal contén cortes en PID.

Para cada mostra de MC, é necesario calcular uns pesos cinemáticos (*kinematic weights*) que corrixen as distribucións do momento e momento transverso dos mesóns iniciais B_s^0 e B_d^0, xa que tamén presentan discrepancias cos datos reais. Isto faise a través dun `GBReweighter`, un algoritmo que compara dúas distribucións multidimensionais e calcula uns pesos para que se parezan o máis posible.

O fondo combinatorio, que está composto de conxuntos de catro trazas aleatorias do suceso que pasan todos os cortes, é dominante nas mostras debido ao carácter hadrónico da colisión e as altas enerxías implicadas. É necesario, polo tanto, reducilo ao máximo posible. Para facelo, adéstrase un algoritmo BDT (Boosted Decision Tree) con diferentes variables topolóxicas e cinemáticas do suceso. En realidade, adéstranse dúas BDTs, unha para cada Run. Emprégase a técnica de validaciónj cruzada en k iteracións para asegurar unha robusta separación entre sinal e fondo.

Unha vez calculada a reposta da BDT para cada suceso de datos, é preciso saber cal é o corte óptimo que elimina maior cantidade de fondo sen tirar moito sinal. O resto dos fondos, que principalmente proveñen das desintegracións $B_d^0 \to \rho^0 K^{*0}$, $B_d^0 \to \phi K^{*0}$ e $\Lambda_b^0 \to \text{p}K^-\pi^+\pi^-$, pódense eliminar cortando nas variables PID. A optimización da selección faise polo tanto en catro dimensións, escollendo tres que cualitativamente suprimen os fondos mencionados e outra da resposta da BDT. O número de sucesos de sinal e de fondo determínase mediante un axuste á masa dos catro corpos. Escóllese a significancia estatística como observable a optimizar, sendo o sinal $B_d^0 \to K^{*0}\bar{K}^{*0}$, do que hai menos sucesos pola supresión adicional de CKM.

A maiores, impóñense uns vetos nas ventás de mesóns con charm para evitar

contaminación destas desintegracións.

Unha vez optimizada a selección, realízase un axuste sofisticado á masa dos catro corpos para determinar o número de sucesos de cada contribución, así como para calcular os `sWeights`.

ANÁLISE DE AMPLITUDES INTEGRADA EN TEMPO E SABOR

O núcleo central desta tese corresponde á análise de amplitudes integrada en tempo e sabor das desintegracións $B^0_{s,d} \to (K^+\pi^-)(K^-\pi^+)$, na rexión próxima ao $K^{*0}\bar{K}^{*0}$. O principal obxectivo é medir f_L para as dúas canles de desintegración. Para logralo, proponse un novo modelo de amplitudes, un novo método para estimar a eficiencia no espazo fásico (o que típicamente se coñece como aceptancia angular) e un novo modelo para a contribución escalar, ou onda S.

O conxunto de datos presenta seleccións a dous corpos que aseguren que $m(K^\pm\pi^\mp) < m_K + m_\eta = 1042.5$ MeV/c^2. Este límite superior asegura que non se supere o umbral inelástico, o cal complicaría bastante os perfís de liña para describir as resonancias no espazo fásico. Non se fai ningunha selección no límite inferior, polo que este é o propio umbral cinemático $m_K + m_\pi \approx 633$ MeV/c^2, sendo esta a primeira vez en LHCb na que se analiza o espectro $K\pi$ ata o umbral. Neste rango de masas, non só está presente o $K^{*0}(892)$ senón tamén resonancias escalares moi anchas, como o $K^*_0(1430)$ ou o $K^*_0(700)$ (tamén coñecido como κ). Isto fai que a contribución VV sexa só unha parte dos datos, sendo a contribución vector-escalar e escalar-escalar moito máis grande, en conxunto.

Nesta tese introdúcese o formalismo de espín covariante baseado nas condicións de Rarita-Schwinger para describir os estados de espín. Isto substitúe aos harmónicos esféricos usados nas análises anteriores, sendo un concepto máis xeral e invariante baixo transformacións relativistas. Aínda que o formalismo ten moitos anos, esta é a primeira vez que se usa en LHCb para analizar unha desintegración $B \to VV$. Cada estado de espín é un escalar de Lorentz, e polas súas propiedades pódese calcular tanto no sistema de referencia do mesón B, como nas simulacións de xoguete, como no sistema laboratorio, típico dos datos reais ou as simulacións completas. ten momento angular ben definido, a diferencia das amplitudes de transversidade, polo que se lles pode asignar os factores de barreira centrífugos de Blatt-Weisskopf. Isto é unha diferencia respecto a análises anteriores. No formalismo de transversidade, as amplitudes A_0 e $A_\parallel$ son combinacións lineares das ondas vector-vector S e D, non estando así ben definido o momento angular e sendo imposible de considerar estes factores de barreira. Isto foi o segundo sistemático dominante na anterior análise dependente do tempo.

A amplitude de desintegración total modélase na aproximación do modelo isobar de desintegración de case dous corpos (*quasi-two-body decay*). Nesta aproximación, a amplitude total é a suma coherente sobre todas as ondas parciais que contribúen ao espectro de masas. Hai seis posibles contribucións: tres de VV, dúas de VS e unha de SS. Cada unha delas ten un valor de momento angular ben definido, e polo tanto pódense acoplar os factores de barreira centrífugos de Blatt-Weisskopf. Como base de axuste escóllese o espazo fásico de catro corpos, Φ_4,

que son o conxunto de catro 4-vectores que satisfacen a densidade de espazo fásico. Para modelar a desintegración do vector V úsase unha Breit-Wigner relativista, como é típico. Para modelar o escalar preséntase un novo modelo que considera non só o modelo de re-dispersión $K\pi$–$K\pi$ senón tamén a produción directa dos escalaras na desintegración do B, algo nunca explorado ata o momento.

Para construír a función de densidade de probabilidade (PDF) que modele as desintegracións que se estudan nesta tese, derívase e pártese do modelo PDF dependente de sabor e tempo, que considera non só a desintegración dos mesóns B e o seu conxugado $\bar{B}$, senón tamén a oscilación entre eles. Unha vez feitas as integrais, a expresión é máis sinxela.

Na PDF de sinal hai un termo de cociente entre as dúas integrais no tempo, que dependen dos valores de $\Delta\Gamma$, Δm e τ. Ademáis, a distribución medida dos tempos de vida dos mesóns presenta un perfil de eficiencia ou aceptancia que non é plano ao longo da variable τ. Isto produce un sesgo na determinación dos valores das integrais, baixando o seu valor aproximadamente un 40% e repercutindo na determinación das amplitudes, que tamén se ven afectadas. Para solucionar isto, desenvólvese un modelo de aceptancia no tempo basado en b–splines cúbicas. Este ten unha serie de parámetros que se determinan mediante un axuste á distribución de tempo de vida nas mostras de MC dividido polo modelo de xeración, sendo a distribución resultante xustamente o perfil de eficiencia. Os axustes realízanse por categoría de datos, é dicir, por ano de toma de datos e condición de trigger (`L0TOS` ou `L0TIS!TOS`). Para cada un deles, calcúlase o cociente de integrais temporais corrixido por estes modelos de aceptancia no tempo e despois faise un promedio pesado pola luminosidade aportada por cada mostra, extraendo así o factor de corrección.

Os distintos tipos de selección, tanto online como offline, inducen tamén sesgos no perfil de eficiencia ao longo do espazo fásico, sendo críticamente próxima a cero nos cosenos dos ángulos de helicidade. Isto está perfectamente entendido de análises anteriores, estando relacionado co baixo momento transverso dos pións para $\cos\theta = +1$. O perfil de eficiencia debe ser polo tanto corrixido, e para iso utilízase a mostra de MC de puro espazo fásico. Nestas mostras de simulación no que non hai ningún tipo de resonancia nin efecto dinámico, polo que as proxeccións sobre calquer conxunto de variables determina a forma da eficiencia. As variables escollidas para facer este estudo, así como para proxectar o modelo final de axuste, son os dous ángulos de helicidade, o ángulo entre planos de decaemento e as dúas masas invariantes dos sistemas $K\pi$. O espazo fásico de catro corpos ten cinco graos de liberdade, e esta é unha elección típica en análises $B \to VV$.

A técnica utilizada para determinar a eficiencia multidimensional, que supón unha innovación desta tese, consiste en mapear a distribución destas cinco variables da mostra completamente simulada en LHCb de espazo fásico á mesma mostra sen ningún tipo de efectos de detector. Este mapa faise a través dunha técnica KDE (Kernel Density Estimation), que permite, a partir dunha serie de datos, estimar a densidade de probabilidade en novos puntos. A partir da distribución na mostra completamente simulada estímase a densidade de probabilidade na mostra, que é o perfil de eficiencia. Dado que esta é unha técnica que require moita capacidade de cálculo, adáptase nesta tesa o algoritmo principal de cálculo para executarse en

tarxetas gráficas (GPU).

Impleméntanse varias correccións datos/MC para suplir pequenas carencias, ou comportamentos incorrectos, que teñen as simulacións completas. Estas correccións teñen a forma de pesos por suceso, que multiplican a cada suceso de MC dentro da KDE.

A primeira correspóndese cunha corrección á eficiencia de trigger hadrónico `L0HadronTOS`, que é máis eficiente en simulación que en datos. A partir dun `GBReweighter` e o uso de `L0GlobalTIS`, determínanse uns pesos de corrección.

A segunda é a eficiencia de trazado. Existen dentro do sistema de arquivos do grupo de trazado de LHCb uns histogramas de corrección por traza, calculados a partir de mostras de calibración. A partir deles determínase o peso total, tendo en conta que hai catro trazas no estado final.

Outra é a cinemática do mesón B, que se corrixe cos pesos cinemáticos calculados xa na parte da selección.

E, finalmente, a corrección de PID. Máis que ser unha corrección, corresponde aos cortes feitos nas variables PID durante a selección. Estes non se poden realizar sobre o MC directamente, por estar mal simuladas as variables. En lugar diso, determínase a eficiencia deses cortes en mostras de calibración e faise un repesado con esas eficiencias.

Para realizar o axuste nominal, determínanse a partir dos perfís axustados na parte da seleccións unhas ventás óptimas que conteñen datos de alta pureza das desintegracións do B_s^0 e o B_d^0, con pequenas contaminacións. Os fondos restantes, que básicamente son de malas identificacións e o combinatorio, descríbense durante o axuste de amplitudes. As rexións de sinal son seleccionadas inicialmente a $\pm 3\sigma$ dos valores dos picos respectivos, e o límite entre ambas móvese para obter as mellores relacións sinal-ruído.

Para os fondos $B_d^0 \to \rho^0 K^{*0}$ e $B_d^0 \to \phi K^{*0}$, desenvólvese un programa de repesado baseado nos modelos de amplitudes publicados por LHCb con datos do Run 1. Este programa calcula a PDF sobre mostras de MC de espazo fásico simuladas con `RapidSim`, de $B_d^0 \to K\pi\pi\pi$ e $B_d^0 \to KKK\pi$, respectivamente. Para o fondo combinatorio, tómase unha mostra na rexión de alta masa onde non hai contaminación doutras fontes. Finalmente, inxéctanse todas estas mostras na función de verosimilitude a minimizar con pesos negativos, de forma que están substraídos estatísticamente.

Para o axuste por máxima verosimilitude, ensáianse 1000 axustes previos con algoritmo máis simple dentro de `Minuit 2`, ben chamado `Simplex`, para determinar os parámetros con menor $-2\log\mathcal{L}$. Os parámetros atopados no paso anterior son usados como entrada a unha doble minimización co algoritmo `Migrad`, que determina con moita mellor precisión tanto os parámetros óptimos do modelo como a matriz de covarianza.

RESULTADOS

Despois do axuste, cálculanse as fraccións de axuste realizando as correspondentes integrais de normalización. Os parámetros varíanse 1000 veces con números aleato-

rios Gaussianos cos valores centrais do axuste e a matriz de covarianza, para propagar a incerteza estatística. Isto determina a contribución porcentual de cada compoñente. Neste paso atópase unha forte interferencia entre as ondas vector–vector S e D, polo que o resultado presentado nas tablas inclúe ambas ondas á vez como se fosen unha, sumando a interferencia.

Tamén se calculan as principais fontes de incerteza sistemática. Non foi posible calculalas todas por cuestións de tempo, pero as calculadas deberían ser as principais e dominantes, puidendo ter unha estimación bastante boa da incerteza sistemática final. Estúdanse, por unha banda, como afecta o modelo de axuste de masa do B aos números de sucesos nas rexións de sinal, tanto dos decaementos de sinal como de fondo. Para iso, varíanse 2σ as colas e utilízanse modelos alternativos para describir estes picos. O resto de sistemáticos proveñen da análise de amplitudes, e son principalmente: o ancho de banda da KDE, o modelo da KDE, os pesos de PID, o modelo para o escalar, a descripción alternativa do fondo e o sesgo de axuste.

Non é posible medir os parámetros de transversidade directamente dos resultados covariantes, pois no modelo considerado esta relación é dependente do espazo fásico. A estratexia para medilos consiste en xerar pseudo-experimentos da parte VV do modelo covariante, e facer un fit angular 3D usando as variables $\cos\theta_1$, $\cos\theta_2$, φ. Para propagar a incerteza total, varíanse os parámetros de axuste nominais 1σ usando a matriz de covarianza sistemática cos que se xeran os pseudoexperimentos. O erro estatístico é considerado coa estatística xerada, que provén únicamente da fracción de VV que hai na mostra de datos. Para separar a incerteza estatística da sistemática, faise o mesmo estudo facendo o axuste nos pseudo-experimentos do sistemático do sesgo de axuste, que contén únicamente erros estatísticos.

CONCLUSIÓNS

Esta análise, que xa se fixo con anterioridade en LHCb, sofre importantes cambios e melloras con respecto a análises anteriores.

- **Descripción do espín mediante o formalismo covariante**
  Na anterior análise dependente do tempo o sistemático asociado á non consideración dos factores de barreira foi o segundo dominante. Desta volta, úsase este formalismo para describir ondas parciais que son autoestado do momento angular e que permiten asociarlles os factores centrífugos, sen estudo sistemático posterior.
- **Novo modelado de eficiencia** O sistemático dominante na anterior análise dependente do tempo viña da estatística considerada no MC para determinar a eficiencia. Esta vez a estatística non é un problema, contando con millóns de sucesos. Ademáis, preséntase unha técnica novidosa para construir os mapas de eficiencia baseado na KDE.
- **Axuste do escalar ata o umbral cun novo modelo** Esta análise é a primeira en LHCb en baixar ata o umbral $K\pi$, o que permite ter máximo control para axustar os perfís que modelan a forte compoñente escalar. Ademáis, proponse un novo modelo que considera tanto o mecanismo de produción

destas resonancias como o de decaemento.
Os valores medidos da fracción total de vector e escalar e están de acordo con valores medidos anteriormente. As fraccións de polarización lonxitudinais, f_L, que é o principal obxectivo desta tese, mídense cos valores de

$$f_L^{B_s^0 \to K^{*0}\bar{K}^{*0}} = 0.156 \pm 0.012 \pm 0.008 \,,$$
$$f_L^{B_d^0 \to K^{*0}\bar{K}^{*0}} = 0.694 \pm 0.022 \pm 0.052 \,.$$

A incerteza sistemática é case seis veces menor que a do análise dependente do tempo anterior, polo que o esforzo da renovación desta análise parece que merece a pena. O cociente destas dúas, que é parte do observable $L_{K^{*0}\bar{K}^{*0}}$, é

$$\frac{f_L^{B_s^0 \to K^{*0}\bar{K}^{*0}}}{f_L^{B_d^0 \to K^{*0}\bar{K}^{*0}}} = 0.225 \pm 0.018 \pm 0.020 \,. \tag{5.1}$$

O cociente medido na análise anterior integrado en tempo, que tamén mediu as dúas desintegracións de B_s^0 e B_d^0 usando os datos do Run 1, é de

$$\frac{f_L^{B_s^0 \to K^{*0}\bar{K}^{*0}}}{f_L^{B_d^0 \to K^{*0}\bar{K}^{*0}}} = 0.331 \pm 0.049 \pm 0.035 \,. \tag{5.2}$$

Ambos valores están de acordo en 1.6σ. A mellora na incerteza total é dun factor 2, sendo a medida feita nesta nesta tese a máis precisa ata o momento.

BIBLIOGRAPHY

[1] X. Fan et al. “Measurement of the Electron Magnetic Moment”. In: *Phys. Rev. Lett.* 130 (7 2023), p. 071801. DOI: 10.1103/PhysRevLett.130.071801. URL: https://link.aps.org/doi/10.1103/PhysRevLett.130.071801 (Cited on page 1).

[2] E. Noether. “Invariante Variationsprobleme”. ger. In: *Nachrichten von der Gesellschaft der Wissenschaften zu Gottingen, Mathematisch-Physikalische Klasse* 1918 (1918), pp. 235–257. URL: http://eudml.org/doc/59024 (Cited on page 2).

[3] S. Navas et al. “Review of particle physics”. In: *Phys. Rev* D110.8 (2024), p. 030001. DOI: 10.1103/PhysRevD.110.030001 (Cited on pages 4, 5, 53, 105, 133).

[4] Barbara Schmidt and Matthias Steinhauser. “CRunDec: A C++ package for running and decoupling of the strong coupling and quark masses”. In: *Computer Physics Communications* 183.9 (Sept. 2012), pp. 1845–1848. ISSN: 0010-4655. DOI: 10.1016/j.cpc.2012.03.023. URL: http://dx.doi.org/10.1016/j.cpc.2012.03.023 (Cited on page 5).

[5] B. Adeva Andany. *The Electroweak Unification Theory: Course in nine lectures*. Liberlibro.com A.C., 2019. ISBN: 9788417934057. URL: https://books.google.es/books?id=JmKWDwAAQBAJ (Cited on page 6).

[6] Andrzej J. Buras. *Gauge Theory of Weak Decays: The Standard Model and the Expedition to New Physics Summits*. Cambridge University Press, 2020 (Cited on page 6).

[7] F. Halzen and Alan D. Martin. *QUARKS AND LEPTONS: AN INTRODUCTORY COURSE IN MODERN PARTICLE PHYSICS*. 1984. ISBN: 978-0-471-88741-6 (Cited on page 6).

[8] Lincoln Wolfenstein. “Parametrization of the Kobayashi-Maskawa Matrix”. In: *Physical Review Letters* 51.21 (Nov. 1983), pp. 1945–1947. DOI: 10.1103/physrevlett.51.1945 (Cited on page 10).

[9] Luiz Vale Silva. *2023 update of the extraction of the CKM matrix elements*. 2024. arXiv: 2405.08046 [hep-ph]. URL: https://arxiv.org/abs/2405.08046 (Cited on page 11).

[10] J. Charles et al. "CP violation and the CKM matrix: assessing the impact of the asymmetric B factories". In: *The European Physical Journal C* 41.1 (May 2005), pp. 1–131. ISSN: 1434-6052. DOI: 10.1140/epjc/s2005-02169-1. URL: http://dx.doi.org/10.1140/epjc/s2005-02169-1 (Cited on page 11).

[11] *CKMfitter group web page*. URL: http://ckmfitter.in2p3.fr (Cited on page 11).

[12] Pietro Colangelo et al. *Flavour anomalies, correlations, hadronic uncertainties, and all that*. 2024. arXiv: 2401.02796 [hep-ph]. URL: https://arxiv.org/abs/2401.02796 (Cited on page 12).

[13] Asier Pereiro Castro. "f_L measurements with $B \to VV$ decays at LHCb". In: *PoS* CKM2021 (2023), p. 117. DOI: 10.22323/1.411.0117 (Cited on page 12).

[14] R. Aaij et al. "Measurement of CP asymmetries and polarisation fractions in $B_s^0 \to K^{*0}\overline{K}^{*0}$ decays". In: *JHEP* 07 (2015), p. 166. DOI: 10.1007/JHEP07(2015)166. arXiv: 1503.05362 [hep-ex] (Cited on pages 13, 22, 29, 37, 97).

[15] R. Aaij et al. "First measurement of the CP-violating phase $\phi_s^{d\bar{d}}$ in $B_s^0 \to (K^+\pi^-)(K^-\pi^+)$ decays". In: *JHEP* 03 (2018), p. 140. DOI: 10.1007/JHEP03(2018)140. arXiv: 1712.08683 [hep-ex] (Cited on pages 13, 15, 22, 23, 29, 37, 41, 46, 47).

[16] R. Aaij et al. "Amplitude analysis of the $B_{(s)}^0 \to K^{*0}\overline{K}^{*0}$ decays and measurement of the branching fraction of the $B^0 \to K^{*0}\overline{K}^{*0}$ decay". In: *JHEP* 07 (2019), p. 032. DOI: 10.1007/JHEP07(2019)032. arXiv: 1905.06662 [hep-ex] (Cited on pages 13, 15, 22, 29, 46, 47, 105).

[17] B. Aubert et al. "Observation of $B^0 \to K^{*0}\overline{K}^{*0}$ and Search for $B^0 \to K^{*0}K^{*0}$". In: *Phys. Rev. Lett.* 100 (8 2008), p. 081801. DOI: 10.1103/PhysRevLett.100.081801. URL: https://link.aps.org/doi/10.1103/PhysRevLett.100.081801 (Cited on page 13).

[18] R. Aaij et al. "Measurement of lepton universality parameters in $B^+ \to K^+\ell^+\ell^-$ and $B^0 \to K^{*0}\ell^+\ell^-$ decays". In: *Phys. Rev.* D108 (2023), p. 032002. DOI: 10.1103/PhysRevD.108.032002. arXiv: 2212.09153 [hep-ex] (Cited on page 13).

[19] R. Aaij et al. "Test of Lepton Universality in $b \to s\ell^+\ell^-$ Decays". In: *Phys. Rev. Lett.* 131 (2023), p. 051803. DOI: 10.1103/PhysRevLett.131.051803. arXiv: 2212.09152 [hep-ex] (Cited on page 13).

[20] Aritra Biswas et al. "A new puzzle in non-leptonic B decays". In: *JHEP* 06 (2023), p. 108. DOI: 10.1007/JHEP06(2023)108. arXiv: 2301.10542 [hep-ph] (Cited on page 13).

[21] Marcel Algueró et al. "A new B-flavour anomaly in $B_{d,s} \to K^{*0}\bar{K}^{*0}$: anatomy and interpretation". In: *JHEP* 04 (2021), p. 066. DOI: 10.1007/JHEP04(2021)066. arXiv: 2011.07867 [hep-ph] (Cited on pages 13, 14).

[22] M. Algueró et al. "Anatomy of a new anomaly in non-leptonic B decays". In: *55th Rencontres de Moriond on QCD and High Energy Interactions*. May 2021. arXiv: 2105.11837 [hep-ph] (Cited on page 13).

[23] Bhubanjyoti Bhattacharya et al. "Searching for new physics with $\bar{b} \to \bar{s}$ $B_s^0 \to V_1 V_2$ penguin decays". In: *Physical Review D* 88.1 (July 2013). DOI: 10.1103/physrevd.88.016007 (Cited on pages 14, 15, 130).

[24] Robert Fleischer. "Extracting CKM phases from angular distributions of B(d,s) decays into admixtures of CP eigenstates". In: *Phys. Rev. D* 60 (1999), p. 073008. DOI: 10.1103/PhysRevD.60.073008. arXiv: hep-ph/9903540 (Cited on page 14).

[25] Robert Fleischer and Michael Gronau. "Studying new physics amplitudes in charmless B(s) decays". In: *Phys. Lett. B* 660 (2008), pp. 212–216. DOI: 10.1016/j.physletb.2007.12.028. arXiv: 0709.4013 [hep-ph] (Cited on page 14).

[26] Sebastien Descotes-Genon, Joaquim Matias, and Javier Virto. "Penguin-mediated $B_{d,s} \to VV$ decays and the $B_s - \bar{B}_s$ mixing angle". In: *Phys. Rev. D* 76 (2007). [Erratum: Phys.Rev.D 84, 039901 (2011)], p. 074005. DOI: 10.1103/PhysRevD.76.074005. arXiv: 0705.0477 [hep-ph] (Cited on page 14).

[27] Sebastien Descotes-Genon, Joaquim Matias, and Javier Virto. "An analysis of $B_{d,s}$ mixing angles in presence of New Physics and an update of $B_s \to \bar{K}^{0*} anti - K^{0*}$". In: *Phys. Rev. D* 85 (2012), p. 034010. DOI: 10.1103/PhysRevD.85.034010. arXiv: 1111.4882 [hep-ph] (Cited on page 14).

[28] Bhubanjyoti Bhattacharya et al. "Measuring β_s with $B_s \to K^{0(*)}\bar{K}^{0(*)}$ – a Reappraisal". In: *Phys. Lett. B* 717 (2012), pp. 403–408. DOI: 10.1016/j.physletb.2012.09.054. arXiv: 1203.3435 [hep-ph] (Cited on page 14).

[29] Michael Gronau. "U spin symmetry in charmless B decays". In: *Phys. Lett. B* 492 (2000), pp. 297–302. DOI: 10.1016/S0370-2693(00)01119-9. arXiv: hep-ph/0008292 (Cited on page 14).

[30] Yuval Grossman et al. "$B_s^0 \to K^0 \overline{K}^0$ beyond the Standard Model". In: (July 2024). arXiv: 2407.13506 [hep-ph] (Cited on page 14).

[31] M. Ciuchini, M. Pierini, and L. Silvestrini. "$B_s \to K^{*0}\bar{K}^{*0}$ CP Asymmetries: Golden Channels for New Physics Searches". In: *Physical Review Letters* 100.3 (Jan. 2008). DOI: 10.1103/physrevlett.100.031802 (Cited on page 14).

[32] Lyndon Evans and Philip Bryant. "LHC Machine". In: *Journal of Instrumentation* 3.08 (2008), S08001. DOI: 10.1088/1748-0221/3/08/S08001. URL: https://dx.doi.org/10.1088/1748-0221/3/08/S08001 (Cited on page 16).

[33] G. Aad et al. "Observation of a new particle in the search for the Standard Model Higgs boson with the ATLAS detector at the LHC". In: *Physics Letters B* 716.1 (2012), pp. 1–29. ISSN: 0370-2693. DOI: https://doi.org/10.1016/j.physletb.2012.08.020. URL: https://www.sciencedirect.com/science/article/pii/S037026931200857X (Cited on page 16).

[34] S. Chatrchyan et al. "Observation of a new boson at a mass of 125 GeV with the CMS experiment at the LHC". In: *Physics Letters B* 716.1 (2012), pp. 30–61. ISSN: 0370-2693. DOI: https://doi.org/10.1016/j.physletb.2012.08.021. URL: https://www.sciencedirect.com/science/article/pii/S0370269312008581 (Cited on page 16).

[35] R. Aaij et al. "Study of the doubly charmed tetraquark T_{cc}^+". In: *Nature Communications* 13 (2022), p. 3351. DOI: 10.1038/s41467-022-30206-w. arXiv: 2109.01056 [hep-ex] (Cited on page 17).

[36] R. Aaij et al. "Observation of a $J/\psi\Lambda$ resonance consistent with a strange pentaquark candidate in $B^- \to J/\psi\Lambda\bar{p}$ decays". In: *Phys. Rev. Lett.* 131 (2023), p. 031901. DOI: 10.1103/PhysRevLett.131.031901. arXiv: 2210.10346 [hep-ex] (Cited on page 17).

[37] R. Aaij et al. "Measurement of the W boson mass". In: *JHEP* 01 (2022), p. 036. DOI: 10.1007/JHEP01(2022)036. arXiv: 2109.01113 [hep-ex] (Cited on page 17).

[38] R. Aaij et al. "Search for lepton-flavour-violating decays of Higgs-like bosons". In: *Eur. Phys. J.* C78 (2018), p. 1008. DOI: 10.1140/epjc/s10052-018-6386-8. arXiv: 1808.07135 [hep-ex] (Cited on page 17).

[39] R. Aaij et al. "Search for exotic massive long-lived particles decaying semileptonically at $\sqrt{s} = 13$ TeV". In: *Eur. Phys. J.* C82 (2022), p. 373. DOI: 10.1140/epjc/s10052-022-10186-3. arXiv: 2110.07293 [hep-ex] (Cited on page 17).

[40] *LHCb : Technical Proposal*. Geneva: CERN, 1998. URL: https://cds.cern.ch/record/622031 (Cited on page 17).

[41] A. Augusto Alves Jr. et al. "The LHCb Detector at the LHC". In: *JINST* 3 (2008), S08005. DOI: 10.1088/1748-0221/3/08/S08005 (Cited on page 17).

[42] Rhorry Gauld. "Understanding forward B hadron production". In: *Journal of High Energy Physics* 2017.5 (May 2017). ISSN: 1029-8479. DOI: 10.1007/jhep05(2017)084. URL: http://dx.doi.org/10.1007/JHEP05(2017)084 (Cited on page 17).

[43] Christian Elsasser. *$\bar{b}b$ production angle plots*. URL: https://lhcb.web.cern.ch/speakersbureau/html/bb_ProductionAngles.html (Cited on page 18).

[44] Rolf Lindner. "LHCb layout. LHCb schema". LHCb Collection. 2008. URL: https://cds.cern.ch/record/1087860 (Cited on page 18).

[45] P R Barbosa-Marinho et al. *LHCb VELO (VErtex LOcator): Technical Design Report*. Technical design report. LHCb. Geneva: CERN, 2001. URL: https://cds.cern.ch/record/504321 (Cited on page 17).

[46] S Amato et al. *LHCb RICH: Technical Design Report*. Technical design report. LHCb. Geneva: CERN, 2000. URL: https://cds.cern.ch/record/494263 (Cited on page 19).

[47] N Brook et al. *LHCb RICH1 Engineering Design Review Report*. Tech. rep. Geneva: CERN, 2005. URL: https://cds.cern.ch/record/897981 (Cited on page 19).

[48] M Adinolfi et al. *LHCb RICH 2 engineering design review report*. Tech. rep. revised version number 1 submitted on 2002-05-21 14:24:22. Geneva: CERN, 2002. URL: https://cds.cern.ch/record/691478 (Cited on page 19).

[49] S Amato et al. *LHCb magnet: Technical Design Report*. Technical design report. LHCb. Geneva: CERN, 2000. URL: https://cds.cern.ch/record/424338 (Cited on page 20).

[50] J. Andre et al. "Status of the LHCb magnet system". In: *IEEE Transactions on Applied Superconductivity* 12.1 (2002), pp. 366–371. DOI: 10.1109/TASC.2002.1018421 (Cited on page 20).

[51] J. Andre et al. "Status of the LHCb dipole magnet". In: *IEEE Transactions on Applied Superconductivity* 14.2 (2004), pp. 509–513. DOI: 10.1109/TASC.2004.829705 (Cited on page 20).

[52] R Antunes-Nobrega et al. *LHCb reoptimized detector design and performance: Technical Design Report*. Technical design report. LHCb. Geneva: CERN, 2003. URL: https://cds.cern.ch/record/630827 (Cited on page 20).

[53] J Gassner, M Needham, and O Steinkamp. *Layout and Expected Performance of the LHCb TT Station*. Tech. rep. Geneva: CERN, 2004. URL: https://cds.cern.ch/record/728548 (Cited on page 20).

[54] P R Barbosa-Marinho et al. *LHCb inner tracker: Technical Design Report*. Technical design report. LHCb. revised version number 1 submitted on 2002-11-13 14:14:34. Geneva: CERN, 2002. URL: https://cds.cern.ch/record/582793 (Cited on page 20).

[55] P R Barbosa-Marinho et al. *LHCb outer tracker: Technical Design Report*. Technical design report. LHCb. Geneva: CERN, 2001. URL: https://cds.cern.ch/record/519146 (Cited on page 20).

[56] "LHCb detector performance". In: *International Journal of Modern Physics A* 30.07 (Mar. 2015), p. 1530022. ISSN: 1793-656X. DOI: 10.1142/s0217751x15300227. URL: http://dx.doi.org/10.1142/S0217751X15300227 (Cited on page 20).

[57] S Amato et al. *LHCb calorimeters: Technical Design Report*. Technical design report. LHCb. Geneva: CERN, 2000. URL: https://cds.cern.ch/record/494264 (Cited on page 20).

[58] P R Barbosa-Marinho et al. *LHCb muon system: Technical Design Report*. Technical design report. LHCb. Geneva: CERN, 2001. URL: https://cds.cern.ch/record/504326 (Cited on page 21).

[59] *LHCb muon system: addendum to the Technical Design Report*. Technical design report. LHCb. Geneva: CERN, 2003. URL: https://cds.cern.ch/record/600536 (Cited on page 21).

[60] *LHCb muon system: second addendum to the Technical Design Report*. Technical design report. LHCb. Submitted on 9 Apr 2005. Geneva: CERN, 2005. URL: https://cds.cern.ch/record/831955 (Cited on page 21).

[61] R Antunes-Nobrega et al. *LHCb trigger system: Technical Design Report*. Technical design report. LHCb. revised version number 1 submitted on 2003-09-24 12:12:22. Geneva: CERN, 2003. URL: https://cds.cern.ch/record/630828 (Cited on page 21).

[62] R. Aaij et al. "First observation of the decay $B_s^0 \to K^{*0}\bar{K}^{*0}$". In: *Phys. Lett.* B709 (2012), p. 50. DOI: 10.1016/j.physletb.2012.02.001. arXiv: 1111.4183 [hep-ex] (Cited on page 22).

[63] Gustavo C. Branco, Luis Lavoura, and Joao P. Silva. *CP Violation*. Vol. 103. 1999. ISBN: 978-1-383-02075-5, 978-0-19-850399-6 (Cited on page 26).

[64] Frank von Hippel and C. Quigg. "Centrifugal-Barrier Effects in Resonance Partial Decay Widths, Shapes, and Production Amplitudes". In: *Phys. Rev. D* 5 (3 1972), pp. 624–638. DOI: 10.1103/PhysRevD.5.624. URL: https://link.aps.org/doi/10.1103/PhysRevD.5.624 (Cited on page 30).

[65] William Rarita and Julian Schwinger. "On a Theory of Particles with Half-Integral Spin". In: *Phys. Rev.* 60 (1 1941), pp. 61–61. DOI: 10.1103/PhysRev.60.61. URL: https://link.aps.org/doi/10.1103/PhysRev.60.61 (Cited on page 31).

[66] Charles Zemach. "Use of Angular-Momentum Tensors". In: *Phys. Rev.* 140 (1B 1965), B97–B108. DOI: 10.1103/PhysRev.140.B97. URL: https://link.aps.org/doi/10.1103/PhysRev.140.B97 (Cited on page 31).

[67] S. U. Chung. "General formulation of covariant helicity-coupling amplitudes". In: *Phys. Rev. D* 57 (1 1998), pp. 431–442. DOI: 10.1103/PhysRevD.57.431. URL: https://link.aps.org/doi/10.1103/PhysRevD.57.431 (Cited on page 31).

[68] M. Williams. "Numerical object oriented quantum field theory calculations". In: *Computer Physics Communications* 180.10 (Oct. 2009), 1847–1852. ISSN: 0010-4655. DOI: 10.1016/j.cpc.2009.05.017. URL: http://dx.doi.org/10.1016/j.cpc.2009.05.017 (Cited on page 34).

[69] José R. Peláez and Arkaitz Rodas. "Dispersive $\pi K \to \pi K$ and $\pi\pi \to K\bar{K}$ amplitudes from scattering data, threshold parameters, and the lightest strange resonance κ or $K_0^*(700)$". In: *Physics Reports* 969 (2022), pp. 1–126. ISSN: 0370-1573. DOI: https://doi.org/10.1016/j.physrep.2022.03.004. URL: https://www.sciencedirect.com/science/article/pii/S0370157322001053 (Cited on page 34).

[70] S Mandelstam et al. "Isobar approximation of production processes". In: *Annals of Physics* 18.2 (1962), pp. 198–225. ISSN: 0003-4916. DOI: https://doi.org/10.1016/0003-4916(62)90067-2. URL: https://www.sciencedirect.com/science/article/pii/0003491662900672 (Cited on page 37).

[71] David J. Herndon, Paul Söding, and Roger J. Cashmore. "Generalized isobar model formalism". In: *Phys. Rev. D* 11 (11 1975), pp. 3165–3182. DOI: 10.1103/PhysRevD.11.3165. URL: https://link.aps.org/doi/10.1103/PhysRevD.11.3165 (Cited on page 37).

[72] J.J. Brehm. "Unitarity and the isobar model: Two-body discontinuities". In: *Annals of Physics* 108.2 (1977), pp. 454–476. ISSN: 0003-4916. DOI: https://doi.org/10.1016/0003-4916(77)90023-9. URL: https://www.sciencedirect.com/science/article/pii/0003491677900239 (Cited on page 37).

[73] Wouter D. Hulsbergen. "Decay chain fitting with a Kalman filter". In: *Nuclear Instruments and Methods in Physics Research Section A: Accelerators, Spectrometers, Detectors and Associated Equipment* 552.3 (Nov. 2005), 566–575. ISSN: 0168-9002. DOI: 10.1016/j.nima.2005.06.078. URL: http://dx.doi.org/10.1016/j.nima.2005.06.078 (Cited on page 39).

[74] A. Rogozhnikov. "Reweighting with Boosted Decision Trees". In: *J. Phys. Conf. Ser.* 762.1 (2016). https://github.com/arogozhnikov/hep_ml. DOI: 10.1088/1742-6596/762/1/012036. arXiv: 1608.05806 [physics.data-an] (Cited on page 42).

[75] M. Pivk and F.R. Le Diberder. "sPlot: A statistical tool to unfold data distributions". In: *Nuclear Instruments and Methods in Physics Research Section A: Accelerators, Spectrometers, Detectors and Associated Equipment* 555.1–2 (Dec. 2005), 356–369. ISSN: 0168-9002. DOI: 10.1016/j.nima.2005.08.106. URL: http://dx.doi.org/10.1016/j.nima.2005.08.106 (Cited on page 43).

[76] Yuehong Xie. *sFit: a method for background subtraction in maximum likelihood fit*. 2009. arXiv: 0905.0724 [physics.data-an]. URL: https://arxiv.org/abs/0905.0724 (Cited on page 43).

[77] Tianqi Chen and Carlos Guestrin. "XGBoost: A Scalable Tree Boosting System". In: *Proceedings of the 22nd ACM SIGKDD International Conference on Knowledge Discovery and Data Mining*. KDD '16. San Francisco, California, USA: ACM, 2016, pp. 785–794. ISBN: 978-1-4503-4232-2. DOI: 10.1145/2939672.2939785. URL: http://doi.acm.org/10.1145/2939672.2939785 (Cited on page 45).

[78] Diego Martínez Santos and Frédéric Dupertuis. "Mass distributions marginalized over per-event errors". In: *Nucl. Instrum. Meth.* A764 (2014), pp. 150–155. DOI: 10.1016/j.nima.2014.06.081. arXiv: 1312.5000 [hep-ex] (Cited on pages 53, 101).

[79] N. L. JOHNSON. "SYSTEMS OF FREQUENCY CURVES GENERATED BY METHODS OF TRANSLATION". In: *Biometrika* 36.1-2 (June 1949), pp. 149–176. ISSN: 0006-3444. DOI: 10.1093/biomet/36.1-2.149. eprint: https://academic.oup.com/biomet/article-pdf/36/1-2/149/513258/36-1-2-149.pdf. URL: https://doi.org/10.1093/biomet/36.1-2.149 (Cited on page 53).

[80] Siu Kwan Lam, Antoine Pitrou, and Stanley Seibert. "Numba: A llvm-based python jit compiler". In: *Proceedings of the Second Workshop on the LLVM Compiler Infrastructure in HPC*. 2015, pp. 1–6 (Cited on page 55).

[81] Piti Ongmongkolkul (@piti118) et al. *iminuit - A Python interface to MINUIT [**1975CoPhC..10..343J**]*. [Online; accessed 2018.03.05]. 2012–. URL: https://github.com/iminuit/iminuit (Cited on page 55).

[82] Wouter Verkerke and David Kirkby. *The RooFit toolkit for data modeling*. 2003. arXiv: physics/0306116 [physics.data-an]. URL: https://arxiv.org/abs/physics/0306116 (Cited on page 55).

[83] David J. Wales and Jonathan P. K. Doye. "Global Optimization by Basin-Hopping and the Lowest Energy Structures of Lennard-Jones Clusters Containing up to 110 Atoms". In: *The Journal of Physical Chemistry A* 101.28 (1997), pp. 5111–5116. DOI: 10.1021/jp970984n. eprint: https://doi.org/10.1021/jp970984n. URL: https://doi.org/10.1021/jp970984n (Cited on page 58).

[84] Pauli Virtanen et al. "SciPy 1.0: Fundamental Algorithms for Scientific Computing in Python". In: *Nature Methods* 17 (2020), pp. 261–272. DOI: 10.1038/s41592-019-0686-2 (Cited on page 58).

[85] Tomasz Skwarnicki. "A study of the radiative cascade transitions between the Upsilon-prime and Upsilon resonances". DESY-F31-86-02. PhD thesis. Institute of Nuclear Physics, Krakow, 1986 (Cited on page 65).

[86] Y. Amhis et al. "Averages of b-hadron, c-hadron, and τ-lepton properties as of 2021". In: *Phys. Rev.* D107 (2023). updated results and plots available at https://hflav.web.cern.ch, p. 052008. DOI: 10.1103/PhysRevD.107.052008. arXiv: 2206.07501 [hep-ex] (Cited on page 68).

[87] Frederick E James. *Monte Carlo phase space*. CERN Academic Training Lecture. CERN, Geneva, 1 May 1968. Geneva: CERN, 1968. DOI: 10.5170/CERN-1968-015. URL: https://cds.cern.ch/record/275743 (Cited on page 68).

[88] Luke Zoltan Kelley. "kalepy: a Python package for kernel density estimation, sampling and plotting". In: *Journal of Open Source Software* 6.57 (2021), p. 2784. DOI: 10.21105/joss.02784. URL: https://doi.org/10.21105/joss.02784 (Cited on page 72).

[89] Ryosuke Okuta et al. "CuPy: A NumPy-Compatible Library for NVIDIA GPU Calculations". In: *Proceedings of Workshop on Machine Learning Systems (LearningSys) in The Thirty-first Annual Conference on Neural Information Processing Systems (NIPS)*. 2017. URL: http://learningsys.org/nips17/assets/papers/paper_16.pdf (Cited on page 73).

[90] Benjamin Charlier et al. "Kernel Operations on the GPU, with Autodiff, without Memory Overflows". In: *Journal of Machine Learning Research* 22.74 (2021), pp. 1–6. URL: http://jmlr.org/papers/v22/20-275.html (Cited on page 73).

[91] Roel Aaij et al. "Dalitz plot analysis of $B_s^0 \to \overline{D}^0 K^- \pi^+$ decays". In: *Phys. Rev. D* 90 (2014). Comments: 44 pages, 15 figures; added reference for companion paper, p. 072003. DOI: 10.1103/PhysRevD.90.072003. arXiv: 1407.7712. URL: https://cds.cern.ch/record/1746552 (Cited on page 76).

[92] R. Aaij et al. "Study of the $B_d^0 \to \rho(770)^0 K^{*0}(892)$ decay with an amplitude analysis of $B_d^0 \to (\pi^+\pi^-)(K^+\pi^-)$ decays". In: *JHEP* 05 (2019), p. 026. DOI: 10.1007/JHEP05(2019)026. arXiv: 1812.07008 [hep-ex] (Cited on page 86).

[93] R. Aaij et al. "Measurement of polarization amplitudes and CP asymmetries in $B_d^0 \to \phi(1020)^0 K^{*0}(892)$". In: *JHEP* 05 (2014), p. 069. DOI: 10.1007/JHEP05(2014)069. arXiv: 1403.2888 [hep-ex] (Cited on page 87).

[94] George M. Phillips. “Bernstein Polynomials”. In: *Interpolation and Approximation by Polynomials*. New York, NY: Springer New York, 2003, pp. 247–290. ISBN: 978-0-387-21682-9. DOI: 10.1007/0-387-21682-0_7. URL: https://doi.org/10.1007/0-387-21682-0_7 (Cited on page 101).

[95] P. Estabrooks. “Where and what are the scalar mesons?” In: *Phys. Rev. D* 19 (9 1979), pp. 2678–2685. DOI: 10.1103/PhysRevD.19.2678. URL: https://link.aps.org/doi/10.1103/PhysRevD.19.2678 (Cited on page 102).

[96] D. Aston et al. “A study of $K^-\pi^+$ scattering in the reaction $K^-p \to K^-\pi^+n$ at 11 GeV/c”. In: *Nuclear Physics B* 296.3 (1988), pp. 493–526. ISSN: 0550-3213. DOI: https://doi.org/10.1016/0550-3213(88)90028-4. URL: https://www.sciencedirect.com/science/article/pii/0550321388900284 (Cited on page 102).

[97] Aaron Meurer et al. “SymPy: symbolic computing in Python”. In: *PeerJ Computer Science* 3 (Jan. 2017), e103. ISSN: 2376-5992. DOI: 10.7717/peerj-cs.103. URL: https://doi.org/10.7717/peerj-cs.103 (Cited on page 130).

[98] ALAKABHA DATTA and DAVID LONDON. “TRIPLE-PRODUCT CORRELATIONS IN B→V1V2 DECAYS AND NEW PHYSICS”. In: *International Journal of Modern Physics A* 19.15 (June 2004), 2505–2544. ISSN: 1793-656X. DOI: 10.1142/s0217751x04018300. URL: http://dx.doi.org/10.1142/S0217751X04018300 (Cited on page 130).

APPENDIX A

ANGULAR DISTRIBUTION IN THE TRANSVERSITY BASIS

The amplitude for a four-body B-decay through vector, V, and scalar, S, resonances is built as the coherent sum of all possible intermediate states

$$A = A_{VV} + A_{VS} + A_{SV} + A_{SS} \ . \tag{A.1}$$

The vector-vector component has three possible states and is given, in the transversity formalism, as

$$A_{VV} = A_0 + A_{\parallel} + A_{\perp} \ . \tag{A.2}$$

The vector-scalar and scalar-vector configurations are not eigenstates of CP, so the following combinations are considered,

$$A^{\pm}_{VS} = \frac{A_{VS} \pm A_{SV}}{\sqrt{2}} \ . \tag{A.3}$$

Equation A.1 now reads

$$A = A_0 + A_{\parallel} + A_{\perp} + A^{+}_{VS} + A^{-}_{VS} + A_{SS} \ . \tag{A.4}$$

Each individual amplitude A_i is given by the product of an angular term and mass term, weighted by a complex coefficient a_i,

$$A_i = a_i \, f_i(\theta_1, \theta_2, \varphi) g_i(m_1, m_2) \ , \tag{A.5}$$

where $f_i(\theta_1, \theta_2, \varphi)$ are spherical harmonics given by the corresponding spin-orbit configurations and $g_i(m_1, m_2)$ describe the intermediate resonances across the phase space.

In this configuration, the total amplitude is described by

$$\begin{aligned} A = & -\frac{3N}{4\pi}\Bigg[\Big(A_0\cos\theta_1\cos\theta_2 + \frac{A_\parallel}{\sqrt{2}}\sin\theta_1\sin\theta_2\cos\varphi \\ & + i\frac{A_\perp}{\sqrt{2}}\sin\theta_1\sin\theta_2\sin\varphi\Big)\mathcal{M}_V(m_1)\mathcal{M}_V(m_2) \\ & - \frac{A^+_{VS}}{\sqrt{6}}\Big(\cos\theta_1\mathcal{M}_V(m_1)\mathcal{M}_S(m_2) - \cos\theta_2\mathcal{M}_S(m_1)\mathcal{M}_V(m_2)\Big) \\ & + \frac{A^-_{VS}}{\sqrt{6}}\Big(\cos\theta_1\mathcal{M}_V(m_1)\mathcal{M}_S(m_2) + \cos\theta_2\mathcal{M}_S(m_1)\mathcal{M}_V(m_2)\Big) \\ & - \frac{A_{SS}}{3}\mathcal{M}_S(m_1)\mathcal{M}_S(m_2)\Bigg], \end{aligned} \tag{A.6}$$

where N is a normalisation constant and $\mathcal{M}_{V,S}$ are the lineshapes describing the dynamics in the two-body masses for spins 1 and 0, respectively. Looking at the angular terms, it is easy to deduce that $A_\perp$ and A^+_{VS} are CP-odd, while the rest of the amplitudes are CP-even. The scalar-scalar component shows no helicity structure.

The time-dependent differential decay rate can be obtained by inserting Eq. A.6 in Eq. 2.15. The essential aspects of the phenomenology are not time-related and hence can be studied more comfortably at $t = 0$ where only the term $|A|^2$ has to be calculated, thus simplifying the expressions without any loss of generality. Furthermore, for the objectives of this thesis, the propagators can be integrated and disappear from Eq. A.6; they can be restored at any time by coupling to each raw amplitude the corresponding propagator. Thus, the angular distribution is given by the following PDF

$$\begin{aligned} \left.\frac{d^4\Gamma}{dt\, d\cos\theta_1\, d\cos\theta_2\, d\varphi}\right|_{t=0} &= \iint dm_1 dm_2 \left.\frac{d^6\Gamma}{dt\, d\cos\theta_1 d\cos\theta_2\, d\varphi\, dm_1 dm_2}\right|_{t=0} \\ &= |A|^2 = \frac{9}{8\pi}\sum_{i=1}^{21} K_n X_n(\cos\theta_1, \cos\theta_2, \varphi)\ , \end{aligned} \tag{A.7}$$

where K_n are products of amplitudes at $t = 0$ and X_n functions of the angles. Note that for n amplitude contributions there are $\binom{n}{2}+n = \frac{1}{2}(n^2+n)$ terms when squaring. For $n = 6$ amplitudes, 21 terms are expected as in this case. In related analyses such as $B^0_s \to J/\psi\,\phi$, where only three VV states exist along with the VS state, or $B^0_s \to \phi\phi$ where three VV states along with VS and SS states are possible, only 10 and 15 terms need to be considered, respectively.
Note that the normalisation constant N has been chosen in such a way that

$$\iiint d\cos\theta_1\, d\cos\theta_2\, d\varphi \left[\left.\frac{d^4\Gamma}{dt\, d\cos\theta_1\, d\cos\theta_2\, d\varphi}\right|_{t=0}\right] = \sum_{i=1}^{6}|a_i|^2\ , \tag{A.8}$$

where the integration is done in the region with $-1 \le \cos\theta_{1,2} < 1$ and $0 \le \varphi < 2\pi$.

The expressions for each term of K_n and X_n are shown in Table A.1, and their partial integrals, which are interesting for plotting individual contributions, are

shown in Table A.2. The numerical content of these tables were obtained analytically by the author of this thesis using `SimPy` [97], but it may be helpful for interested readers to see also Ref. [23] for additional information, such as time-dependent modifications.

It is worth noting that some of the terms are Triple Products (TPs), which are scalar observables formed from the product of three T-odd vectors, such as spins or momenta. A TP can be expressed as

$$C_T = \vec{v}_1 \cdot \left(\vec{v}_2 \times \vec{v}_3\right) \ . \tag{A.9}$$

Since TPs are constructed from T-odd vectors, they are also T-odd themselves and may provide signals of CP violation, assuming the conservation of CPT symmetry. Asymmetries can be constructed from differences of TPs, called TPAs, which take the form

$$A_T = \frac{\Gamma(C_T > 0) - \Gamma(C_T < 0)}{\Gamma(C_T > 0) + \Gamma(C_T < 0)} \ , \tag{A.10}$$

where Γ is the decay rate of the process. In the context of the angular distribution in the transversity basis, these asymmetries are of the form of

$$A_T \propto \mathrm{Im}\left[A_1 A_2^*\right] \ , \tag{A.11}$$

where A_1 and A_2 are amplitudes with opposite CP eigenvalues and thus A_T is CP-odd, $\eta = \eta_1\eta_2 = -1$. As detailed in Ref. [98], these observables may have terms that can be non-zero even if polarisation-dependent weak phases are present but there is no strong-phase difference. This issue can be addressed by considering the flavour-integrated observable, the so-called "true" TPAs,

$$A_T^{\mathrm{true}} = \frac{1}{2}\left(A_T + \bar{A}_T\right) \ , \tag{A.12}$$

where $\bar{A}_T$ is the asymmetry constructed from the CP-conjugated process. Let A_1 and A_2 be two amplitudes with opposite CP eigenvalues, which can be parameterised as

$$\begin{aligned} A_1 &= |A_1|\, e^{i(\delta_1+\phi_1)} \ , \\ A_2 &= |A_2|\, e^{i(\delta_2+\phi_2)} \ , \end{aligned} \tag{A.13}$$

where δ_i and ϕ_i are their corresponding strong and weak phases, respectively. The true TPA is then given by

$$\begin{aligned} A_T^{\mathrm{true}} &= \mathrm{Im}\left(A_1 A_2^* - \bar{A}_1 \bar{A}_2^*\right) \\ &= |A_1||A_2|\,\mathrm{Im}\left(e^{i(\delta_1+\phi_1)} e^{-i(\delta_2+\phi_2)} - e^{i(\delta_1-\phi_1)} e^{-i(\delta_2-\phi_2)}\right) \\ &= |A_1||A_2|\,\mathrm{Im}\left(e^{i(\Delta\delta+\Delta\phi)} - e^{i(\Delta\delta-\Delta\phi)}\right) \\ &= |A_1||A_2|\,\mathrm{Im}\left(e^{i\Delta\delta}\left(e^{i\Delta\phi} - e^{-i\Delta\phi}\right)\right) \\ &= 2|A_1||A_2|\,\mathrm{Im}\left(\left(\cos\Delta\delta + i\sin\Delta\delta\right) i\sin\Delta\phi\right) \\ &\propto \cos\Delta\delta\,\sin\Delta\phi \ , \end{aligned} \tag{A.14}$$

which indeed has the desirable behaviour in terms of sensitivity to weak-phase differences. Note that it is the "i" factor in $A_\perp$ what generates the Im (...) terms; terms with Re (...) have different behaviour and are not interesting. Of course, such weak-phase differences are *strictly forbidden* in the SM (all Feynman diagrams sharing the same CKM couplings), and therefore the experimental observation of any non-zero asymmetry will unequivocally manifest the presence of NP.

n	K_n	$X_n(\cos\theta_1, \cos\theta_2, \varphi)$
1	$\lvert A_0\rvert^2$	$\cos^2\theta_1 \cos^2\theta_2$
2	$\lvert A_\parallel\rvert^2$	$\frac{1}{2}\sin^2\theta_1 \sin^2\theta_2 \cos^2\varphi$
3	$\lvert A_\perp\rvert^2$	$\frac{1}{2}\sin^2\theta_1 \sin^2\theta_2 \sin^2\varphi$
4	$\mathrm{Re}\left[A_\parallel A_0^*\right]$	$\frac{1}{2\sqrt{2}}\sin 2\theta_1 \sin 2\theta_2 \cos\varphi$
5	$\mathrm{Im}\left[A_\perp A_0^*\right]$	$-\frac{1}{2\sqrt{2}}\sin 2\theta_1 \sin 2\theta_2 \sin\varphi$
6	$\mathrm{Im}\left[A_\perp A_\parallel^*\right]$	$-\frac{1}{2}\sin^2\theta_1 \sin^2\theta_2 \sin 2\varphi$
7	$\lvert A_{VS}^+\rvert^2$	$\frac{1}{6}(\cos\theta_1 - \cos\theta_2)^2$
8	$\mathrm{Re}\left[A_{VS}^+ A_{SS}^*\right]$	$\frac{\sqrt{2}}{3\sqrt{3}}(\cos\theta_1 - \cos\theta_2)$
9	$\mathrm{Re}\left[A_{VS}^+ A_{VS}^{-*}\right]$	$\frac{1}{3}(\cos^2\theta_1 - \cos^2\theta_2)$
10	$\mathrm{Re}\left[A_{VS}^+ A_0^*\right]$	$-\frac{\sqrt{2}}{\sqrt{3}}\cos\theta_1 \cos\theta_2 (\cos\theta_1 - \cos\theta_2)$
11	$\mathrm{Re}\left[A_{VS}^+ A_\parallel^*\right]$	$-\frac{1}{\sqrt{3}}\sin\theta_1 \sin\theta_2 \cos\varphi (\cos\theta_1 - \cos\theta_2)$
12	$\mathrm{Im}\left[A_\perp A_{VS}^{+*}\right]$	$\frac{1}{\sqrt{3}}\sin\theta_1 \sin\theta_2 \sin\varphi (\cos\theta_1 - \cos\theta_2)$
13	$\lvert A_{VS}^-\rvert^2$	$\frac{1}{6}(\cos\theta_1 + \cos\theta_2)^2$
14	$\mathrm{Re}\left[A_{VS}^- A_{SS}^*\right]$	$\frac{\sqrt{2}}{3\sqrt{3}}(\cos\theta_1 + \cos\theta_2)$
15	$\mathrm{Re}\left[A_{VS}^- A_0^*\right]$	$-\frac{\sqrt{2}}{\sqrt{3}}\cos\theta_1 \cos\theta_2 (\cos\theta_1 + \cos\theta_2)$
16	$\mathrm{Re}\left[A_{VS}^- A_\parallel^*\right]$	$-\frac{1}{\sqrt{3}}\sin\theta_1 \sin\theta_2 \cos\varphi (\cos\theta_1 + \cos\theta_2)$
17	$\mathrm{Im}\left[A_\perp A_{VS}^{-*}\right]$	$\frac{1}{\sqrt{3}}\sin\theta_1 \sin\theta_2 \sin\varphi (\cos\theta_1 + \cos\theta_2)$
18	$\mathrm{Re}\left[A_{SS} A_\parallel^*\right]$	$-\frac{\sqrt{2}}{3}\sin\theta_1 \sin\theta_2 \cos\varphi$
19	$\mathrm{Im}\left[A_\perp A_{SS}^*\right]$	$\frac{\sqrt{2}}{3}\sin\theta_1 \sin\theta_2 \sin\varphi$
20	$\mathrm{Re}\left[A_{SS} A_0^*\right]$	$-\frac{2}{3}\cos\theta_1 \cos\theta_2$
21	$\lvert A_{SS}\rvert^2$	$\frac{1}{9}$

TABLE A.1: Explicit expressions for K_n and X_n, which define the angular distribution.

Looking again at Table A.1, four different TPAs can be constructed from the interference between $A_\perp$ and the four CP-even amplitudes. The first two, corresponding to terms 5 and 6, arise from interference between vector-vector components, while the other two, corresponding to terms 17 and 19, originate in interference

n	$\int X_n(\Omega)\, d\cos\theta_2\, d\varphi$	$\int X_n(\Omega)\, d\cos\theta_1\, d\varphi$	$\int X_n(\Omega)\, d\cos\theta_1\, d\cos\theta_2$	$\int X_n(\Omega)\, d\Omega$
1	$\frac{4}{3}\pi\cos^2\theta_1$	$\frac{4}{3}\pi\cos^2\theta_2$	$\frac{4}{9}$	$\frac{8\pi}{9}$
2	$\frac{2}{3}\pi\sin^2\theta_1$	$\frac{2}{3}\pi\sin^2\theta_2$	$\frac{8}{9}\cos^2\varphi$	$\frac{8\pi}{9}$
3	$\frac{2}{3}\pi\sin^2\theta_1$	$\frac{2}{3}\pi\sin^2\theta_2$	$\frac{8}{9}\sin^2\varphi$	$\frac{8\pi}{9}$
4	0	0	0	0
5	0	0	0	0
6	0	0	$-\frac{8}{9}\sin 2\varphi$	0
7	$\frac{\pi}{9}(3\cos 2\theta_1 + 5)$	$\frac{\pi}{9}(3\cos 2\theta_2 + 5)$	$\frac{4}{9}$	$\frac{8\pi}{9}$
8	$\sqrt{\frac{32}{27}}\pi\cos\theta_1$	$-\sqrt{\frac{32}{27}}\pi\cos\theta_2$	0	0
9	$\frac{2\pi}{9}(3\cos 2\theta_1 + 1)$	$-\frac{2\pi}{9}(3\cos 2\theta_2 + 1)$	0	0
10	$\sqrt{\frac{32}{27}}\pi\cos\theta_1$	$-\sqrt{\frac{32}{27}}\pi\cos\theta_2$	0	0
11	0	0	0	0
12	0	0	0	0
13	$\frac{\pi}{9}(3\cos 2\theta_1 + 5)$	$\frac{\pi}{9}(3\cos 2\theta_2 + 5)$	$\frac{4}{9}$	$\frac{8\pi}{9}$
14	$\sqrt{\frac{32}{27}}\pi\cos\theta_1$	$\sqrt{\frac{32}{27}}\pi\cos\theta_2$	0	0
15	$-\sqrt{\frac{32}{27}}\pi\cos\theta_1$	$-\sqrt{\frac{32}{27}}\pi\cos\theta_2$	0	0
16	0	0	0	0
17	0	0	0	0
18	0	0	$-\frac{\pi^2}{6\sqrt{2}}\cos\varphi$	0
19	0	0	$\frac{\pi^2}{6\sqrt{2}}\sin\varphi$	0
20	0	0	0	0
21	$\frac{4\pi}{9}$	$\frac{4\pi}{9}$	$\frac{4}{9}$	$\frac{8\pi}{9}$

TABLE A.2: Partial and total integrals of each X_n term, with $\Omega \equiv (\cos\theta_1, \cos\theta_2, \varphi)$. Integrals are evaluated in the whole available phase space, *i.e.*, $-1 \leq \cos\theta_{1,2} < 1$ and $0 \leq \varphi < 2\pi$

between vector and scalar.

APPENDIX B

DATA SELECTION

This appendix collects extra plots and details that may be interesting to show/comment on but disrupt the flow of the main text in Sec. 3.1.

B.1 ADDITIONAL COMBINATORIAL BDT MATERIAL

Further details about the BDT are shown in this section.

B.1.1 DATA/MC YIELD CORRECTIONS

A simplified mass model is developed to weight the signal MC of $B_s^0 \to K^{*0}\bar{K}^{*0}$ decays in order to match the corresponding signal proportions in real data. The model consists of the following components:

- A $B_s^0 \to K^{*0}\bar{K}^{*0}$ component modelled as a Gaussian with a floating mean, standard deviation and yield *i.e.* Gauss $\left(\mu_{B_s^0}, \sigma_{B_s^0}, N_{B_s^0}\right)$.
- A $B_d^0 \to K^{*0}\bar{K}^{*0}$ component modelled as a Gaussian with the same standard deviation as the B_s^0 mode, the same mean as the B_s^0 mode but offset by the PDG value [3] for the mass difference $m_{B_s^0} - m_{B_d^0} = 87.38\,\text{MeV}/c^2$ and floating yield *i.e.* Gauss $\left(\mu_{B_s^0} - 87.38, \sigma_{B_s^0}, N_{B_d^0}\right)$.
- A combinatorial background component modelled as a smoothly decaying exponential *i.e.* $\exp(\alpha\, m_B)$ with a floating yield.

The results are shown in Fig. B.1.

B.1.2 CORRELATION BETWEEN INPUT FEATURES

Statistical correlations between input features for signal and background categories are shown in Figs. B.2 and B.3, for Run 1 and Run 2, respectively.

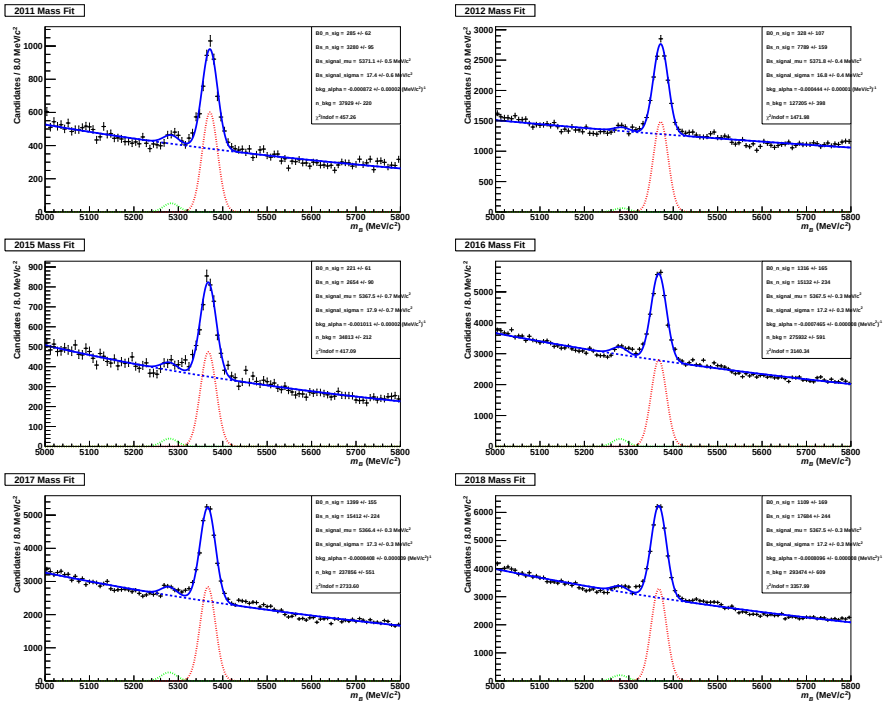

FIGURE B.1: Initial mass fits to estimate the signal yields for each year in order to correctly weight the signal MC

B.1.3 COMBINATORIAL BDT GRID SEARCH

The hyper-parameters considered were the number of estimators (trees), the learning rate and the maximum depth of the trees. The parameter space considered consisted of:

- learning rates in {0.01, 0.1, **0.3**, 0.6}
- number of estimators in {100, **200**, 400, 1000}
- max depth in {**3**, 5, 10},

where the **bold** values are the default values. Additionally, three metrics were chosen to assess the performance of the BDTs: the balanced accuracy, the area under the ROC curve and the negative log-loss. The results of this search are shown in Figs. B.4–B.7. It is clear that the value of hyper-parameters does not offer much difference to the overall BDT performance provided they are reasonably close to the default values.

B.1.4 CORRELATIONS BETWEEN BDT RESPONSE AND TIME VARIABLES

As was found in Sec. 3.1.5, the BDT response present some correlations with the B-meson decay time and the decay time error. As a check of this, the output distributions of the decay time with the PV and B_s^0 mass constraint are shown in

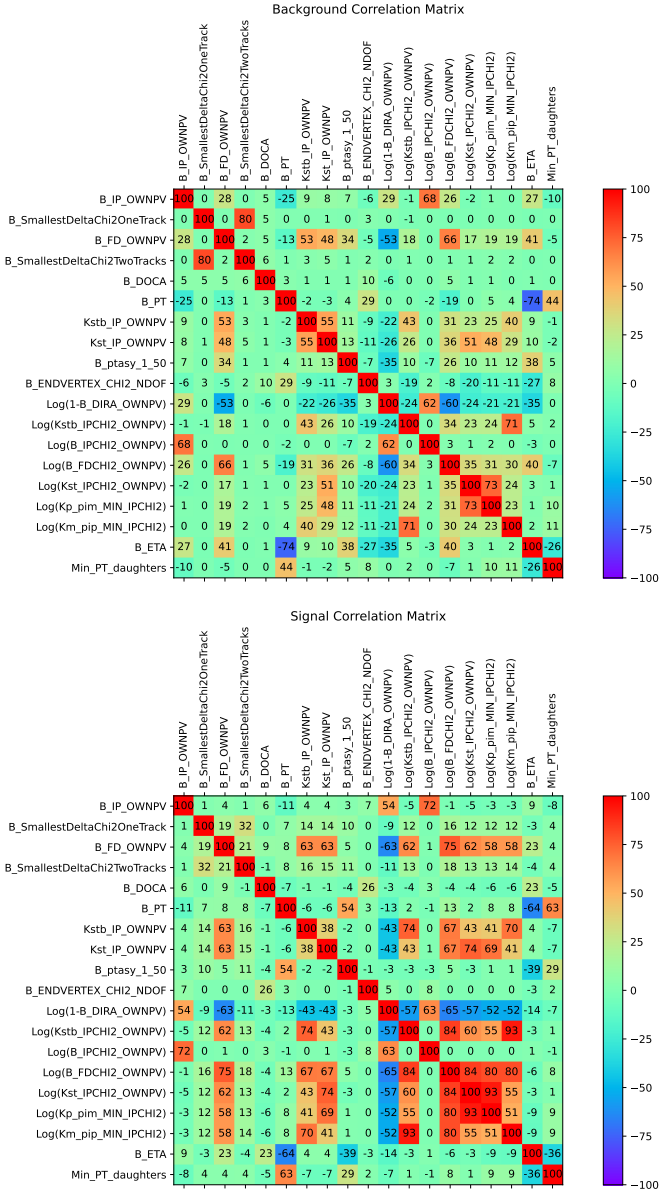

FIGURE B.2: Input variable correlations for Run 1 in background (top) and signal (bottom).

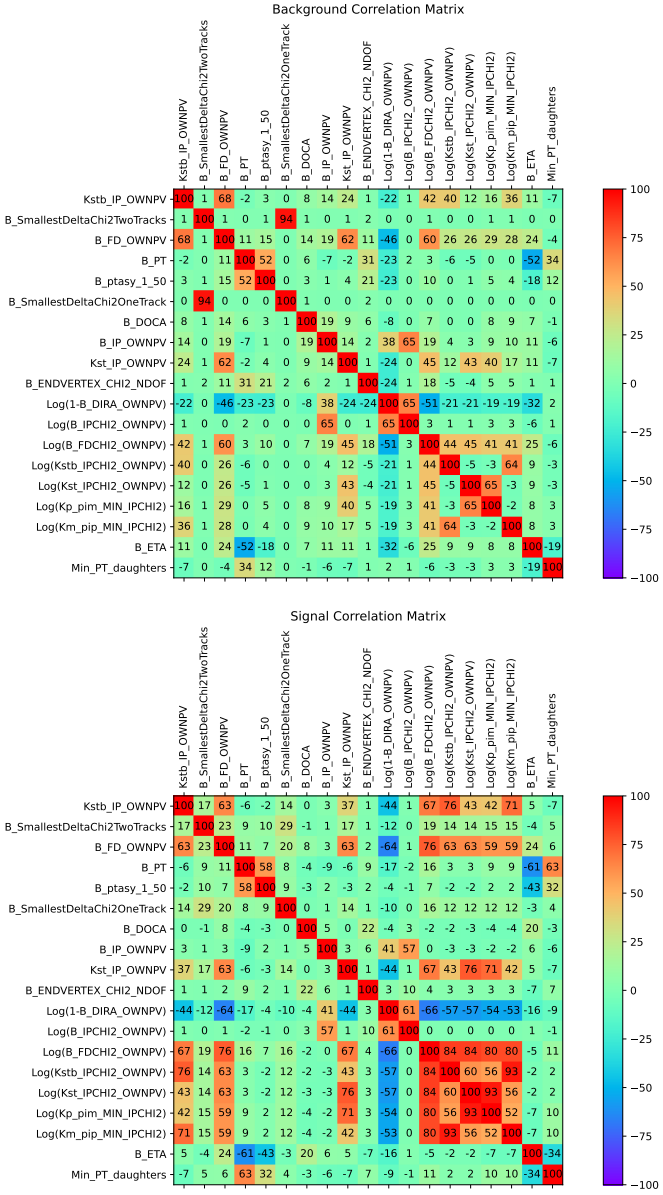

FIGURE B.3: Input variable correlations for Run 2 in background (top) and signal (bottom).

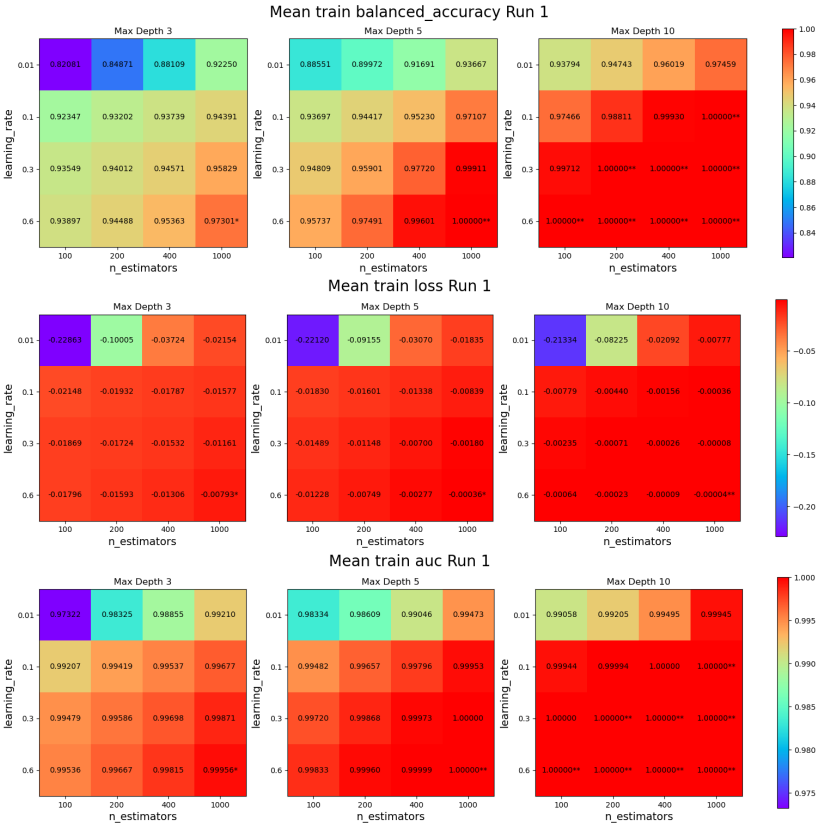

FIGURE B.4: Grid search results for the combinatorial BDT for Run 1

Fig. B.8 under a range of cuts on the BDT response for truth-matched signal MC. There is a small shift in the decay time distributions which can easily be taken into account later. As this is a time-integrated analysis, possible correlations with time are not of concern, but should be taken into account in future time-dependent analysis.

B.1.5 MC SHAPES FOR PRELIMINARY FIT

The fits to the MC samples for the preliminary fit are shown in Figs. B.9 for Run 1 and B.10 for Run 2 and the fit results are displayed in Tables B.1 to B.4.

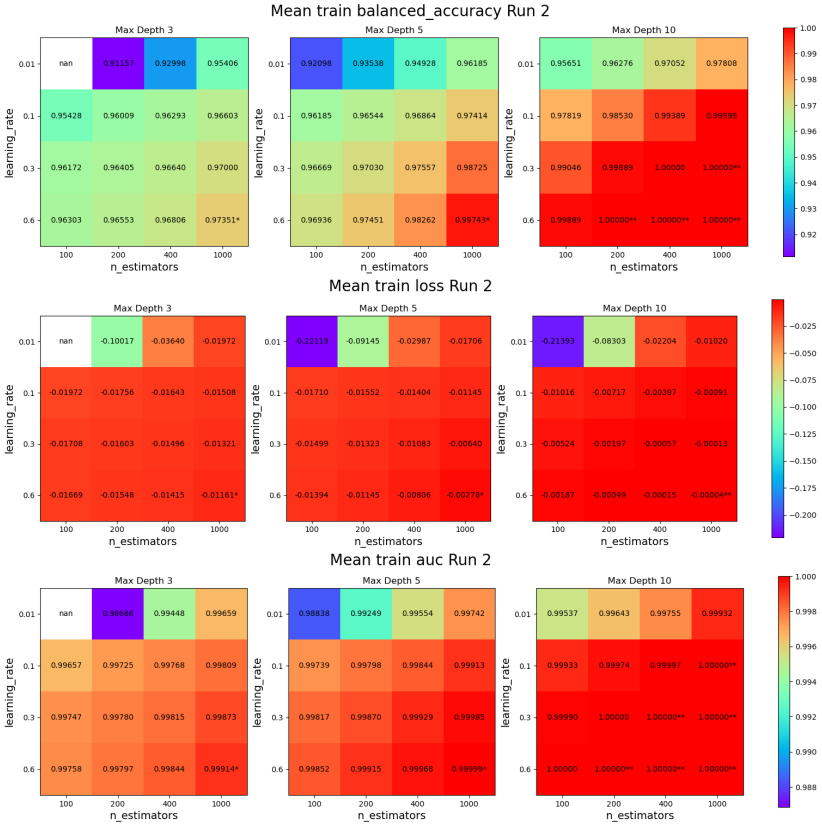

FIGURE B.5: Grid search results for the combinatorial BDT for Run 2

TABLE B.1: Results for the fit to signal MC with a Hypatia shape with preliminary selection for Run 1 and Run 2. Parameters with an * are fixed in the fit.

Fit parameter	Run 1	Run 2
mu	5368.44 ± 0.06	5368.73 ± 0.01
sigma	17.12 ± 0.06	16.5 ± 0.01
beta	$0 \pm -^*$	$0 \pm -^*$
zeta	$10^{-5} \pm -^*$	$10^{-5} \pm -^*$
lb	6.27 ± 0.001	6.185 ± 0.004
al	2.216 ± 0.005	2.057 ± 0.004
nl	$3.0 \pm -^*$ 0	$3.0 \pm -^*$
ar	2.039 ± 0.004	2.374 ± 0.003
nr	$3.0 \pm -^*$	$3.0 \pm -^*$

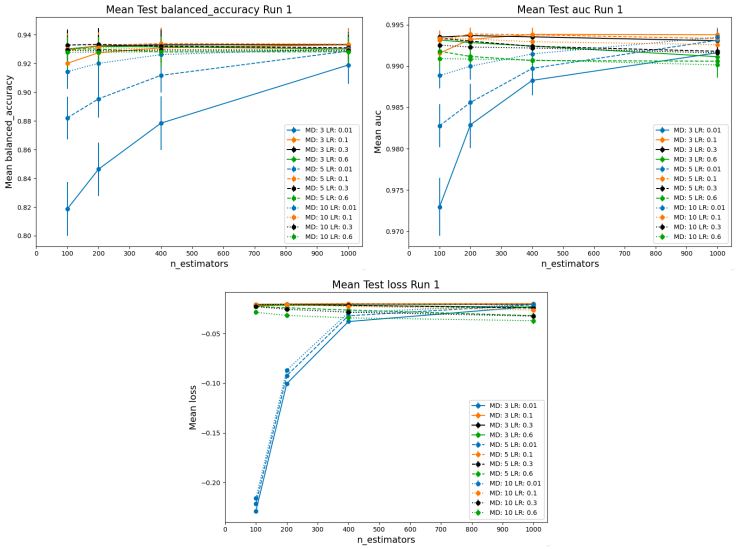

FIGURE B.6: Grid search results for the combinatorial BDT for Run 1 with MD=max depth and LR=learning rate.

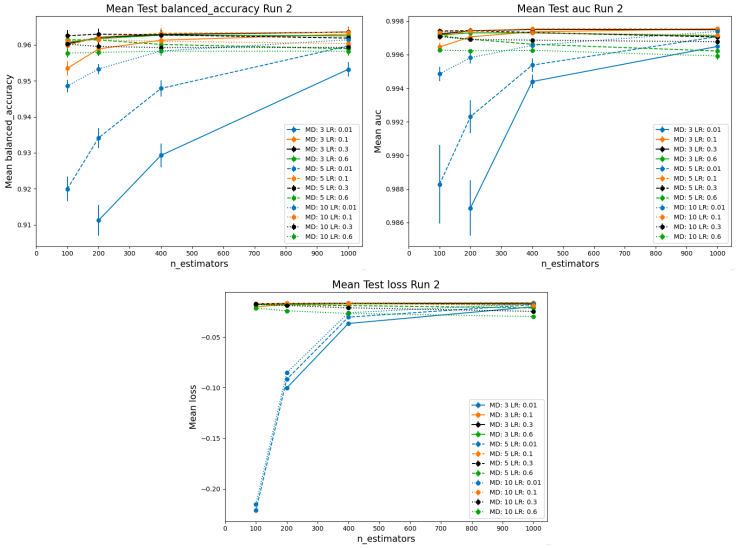

FIGURE B.7: Grid search results for the combinatorial BDT for Run 2 with MD=max depth and LR=learning rate..

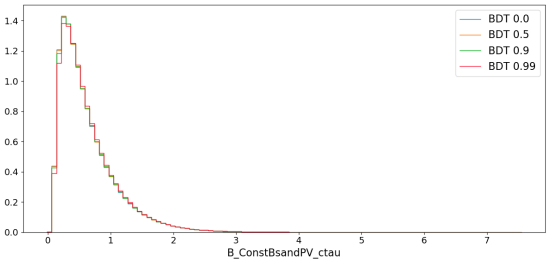

FIGURE B.8: Example of decay time distribution from pre-selected Run 2 data with a variety of cuts on the BDT output.

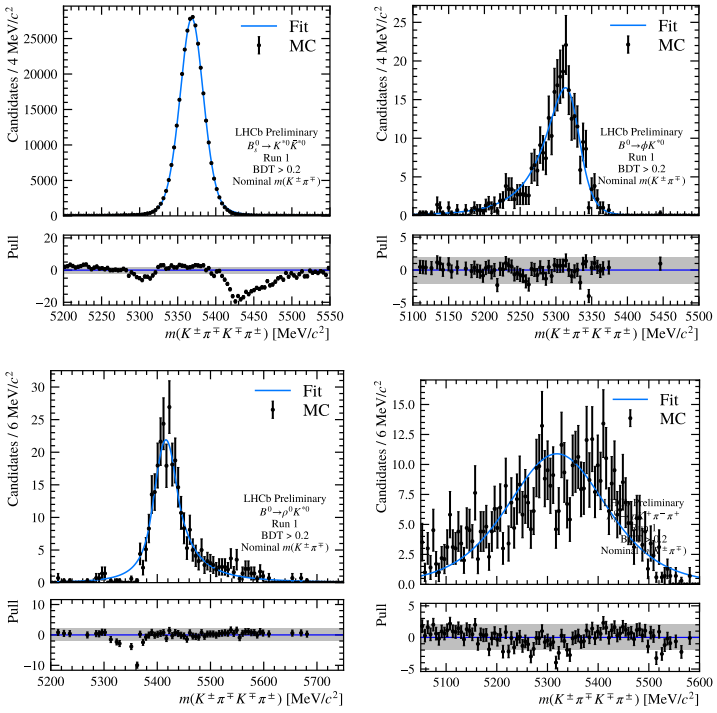

FIGURE B.9: Fits to the MC samples with preliminary selection applied for the signal sample (top left), $B_s^0 \to \phi K^{*0}$ sample (top right), $B_s^0 \to \rho^0 K^{*0}$ (bottom left) and $\Lambda_b^0 \to pK^-\pi^+\pi^-$ (bottom right) for Run 1.

TABLE B.2: Results for the fit to $B_s^0 \to \phi K^{*0}$ MC with a Johnson SU with preliminary selection for Run 1 and Run 2.

Fit parameter	Run 1	Run 2
mu	5328 ± 5	5321 ± 2
sigma	29 ± 4	26 ± 2
gamma	1.0 ± 0.2	0.67 ± 0.06
delta	1.3 ± 0.1	1.05 ± 0.04

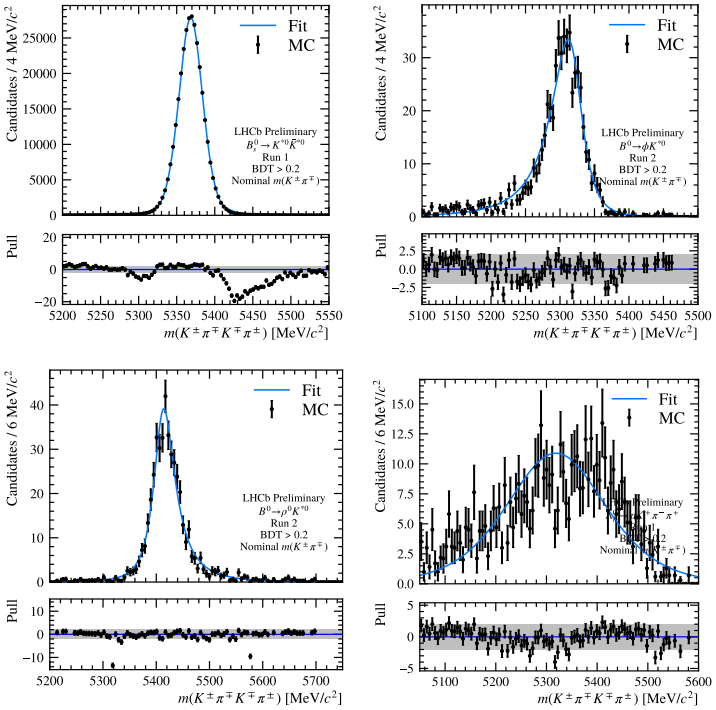

FIGURE B.10: Fits to the MC samples with preliminary selection applied for the signal sample (top left), $B_s^0 \to \phi K^{*0}$ sample (top right), $B_s^0 \to \rho^0 K^{*0}$ (bottom left) and $\Lambda_b^0 \to pK^-\pi^+\pi^-$ (bottom right) for Run 2.

TABLE B.3: Results for the fit to $B_s^0 \to \rho^0 K^{*0}$ MC with a Johnson SU with preliminary selection for Run 1 and Run 2.

Fit parameter	Run 1	Run 2
mu	5396 ± 4	5411 ± 1
sigma	30 ± 4	23 ± 2
gamma	−1.0 ± 0.2	−0.32 ± 0.05
delta	1.2 ± 0.1	0.92 ± 0.04

TABLE B.4: Results for the fit to $\Lambda_b^0 \to pK^-\pi^+\pi^-$ MC with a Johnson SU with a preliminary selection for Run 1 and Run 2. Parameters with an * are fixed in the fit.

Fit parameter	Run 1	Run 2
mu	5319 ± 4	5279 ± 3
sigma	200 ± 2	200 ± 2
gamma	0 ± −*	0 ± −*
delta	1.91 ± 0.05	1.94 ± 0.04

APPENDIX C

AMPLITUDE ANALYSIS

This appendix collects extra plots and details that may be interesting to show/comment on but disrupt the flow of the main text in Sec. 3.2.

C.1 LIFETIME FITS

The χ^2 fits to the lifetime distribution are presented in this section. The true lifetime distribution of full simulated B_s^0 phase space samples is divided by the corresponding generator-level MC, which is simulated with `EvtGen`, to obtain the distribution of the time efficiency. The model used to describe this efficiency as a function of the decay-time, which is detailed in Sec. 3.2.2, is then fitted to this distribution through a χ^2 fit. The numerical results are shown in Tables C.1–C.12, and the fit projection are shown in Figs. C.1 and C.2.

Parameter	Fit value
α_{00}	-0.04545 ± 0.00011
α_{01}	0.13694 ± 0.00027
α_{02}	-0.08294 ± 0.00017
α_{03}	$0.01925 \pm 8.4e-05$
α_{13}	0.00865 ± 0.00018
α_{23}	-0.00262 ± 0.00054
α_{33}	-0.0004 ± 0.0072

TABLE C.1: Time efficiency coefficients for fit to 2011 `L0HadronTOS` sample.

Parameter	Fit value
α_{00}	-0.06104 ± 0.00013
α_{01}	0.17605 ± 0.00038
α_{02}	-0.05679 ± 0.00025
α_{03}	0.00042 ± 0.00012
α_{13}	0.01857 ± 0.00027
α_{23}	-0.0035 ± 0.0008
α_{33}	-0.0432 ± 0.0089

TABLE C.2: Time efficiency coefficients for fit to 2012 `L0HadronTOS` sample.

Parameter	Fit value
α_{00}	$-0.025 \pm 8e-05$
α_{01}	0.0809 ± 0.0002
α_{02}	-0.05913 ± 0.00011
α_{03}	$0.01641 \pm 5.5e-05$
α_{13}	0.00319 ± 0.00012
α_{23}	-0.00025 ± 0.00037
α_{33}	0.0024 ± 0.0062

TABLE C.3: Time efficiency coefficients for fit to 2015 `L0HadronTOS` sample.

Parameter	Fit value
α_{00}	-0.0262 ± 0.0012
α_{01}	0.0281 ± 0.0059
α_{02}	0.2082 ± 0.0082
α_{03}	-0.1104 ± 0.0033
α_{13}	0.0465 ± 0.0012
α_{23}	-0.0138 ± 0.0017
α_{33}	0.025 ± 0.014

TABLE C.4: Time efficiency coefficients for fit to 2016 `L0HadronTOS` sample.

Parameter	Fit value
α_{00}	-0.0208 ± 0.0012
α_{01}	-0.0138 ± 0.0061
α_{02}	0.3121 ± 0.0085
α_{03}	-0.1559 ± 0.0035
α_{13}	0.0592 ± 0.0013
α_{23}	-0.0188 ± 0.0019
α_{33}	0.042 ± 0.015

TABLE C.5: Time efficiency coefficients for fit to 2017 `L0HadronTOS` sample.

Parameter	Fit value
α_{00}	-0.0317 ± 0.0011
α_{01}	0.0580 ± 0.0057
α_{02}	0.178 ± 0.008
α_{03}	-0.1016 ± 0.0032
α_{13}	0.0494 ± 0.0012
α_{23}	-0.0177 ± 0.0017
α_{33}	0.030 ± 0.013

TABLE C.6: Time efficiency coefficients for fit to 2018 `L0HadronTOS` sample.

Parameter	Fit value
α_{00}	-0.0246 ± 0.0001
α_{01}	0.05600 ± 0.00022
α_{02}	-0.02048 ± 0.00014
α_{03}	$0.00239 \pm 6.8e-05$
α_{13}	0.00330 ± 0.00015
α_{23}	0.00126 ± 0.00045
α_{33}	-0.0241 ± 0.0068

TABLE C.7: Time efficiency coefficients for fit to 2011 `L0GlobalTIS` & `!L0HadronTOS` sample.

Parameter	Fit value
α_{00}	-0.01456 ± 0.00013
α_{01}	-0.00328 ± 0.00031
α_{02}	0.09129 ± 0.00021
α_{03}	-0.04160 ± 0.00011
α_{13}	0.00867 ± 0.00023
α_{23}	0.00157 ± 0.00069
α_{33}	-0.0112 ± 0.0084

TABLE C.8: Time efficiency coefficients for fit to 2012 `L0GlobalTIS` & `!L0HadronTOS` sample.

Parameter	Fit value
α_{00}	$-0.01059 \pm 7.9e-05$
α_{01}	0.01939 ± 0.00016
α_{02}	$0.00034 \pm 8.7e-05$
α_{03}	$-0.00326 \pm 4.4e-05$
α_{13}	$0.00347 \pm 9.4e-05$
α_{23}	-0.0008 ± 0.0003
α_{33}	-0.0028 ± 0.0051

TABLE C.9: Time efficiency coefficients for fit to 2015 `L0GlobalTIS` & `!L0HadronTOS` sample.

Parameter	Fit value
α_{00}	0.00772 ± 0.00013
α_{01}	-0.10831 ± 0.00038
α_{02}	0.27033 ± 0.00028
α_{03}	-0.11451 ± 0.00014
α_{13}	0.0257 ± 0.0003
α_{23}	-0.00788 ± 0.00088
α_{33}	-0.00 ± 0.01

TABLE C.10: Time efficiency coefficients for fit to 2016 `L0GlobalTIS` & `!L0HadronTOS` sample.

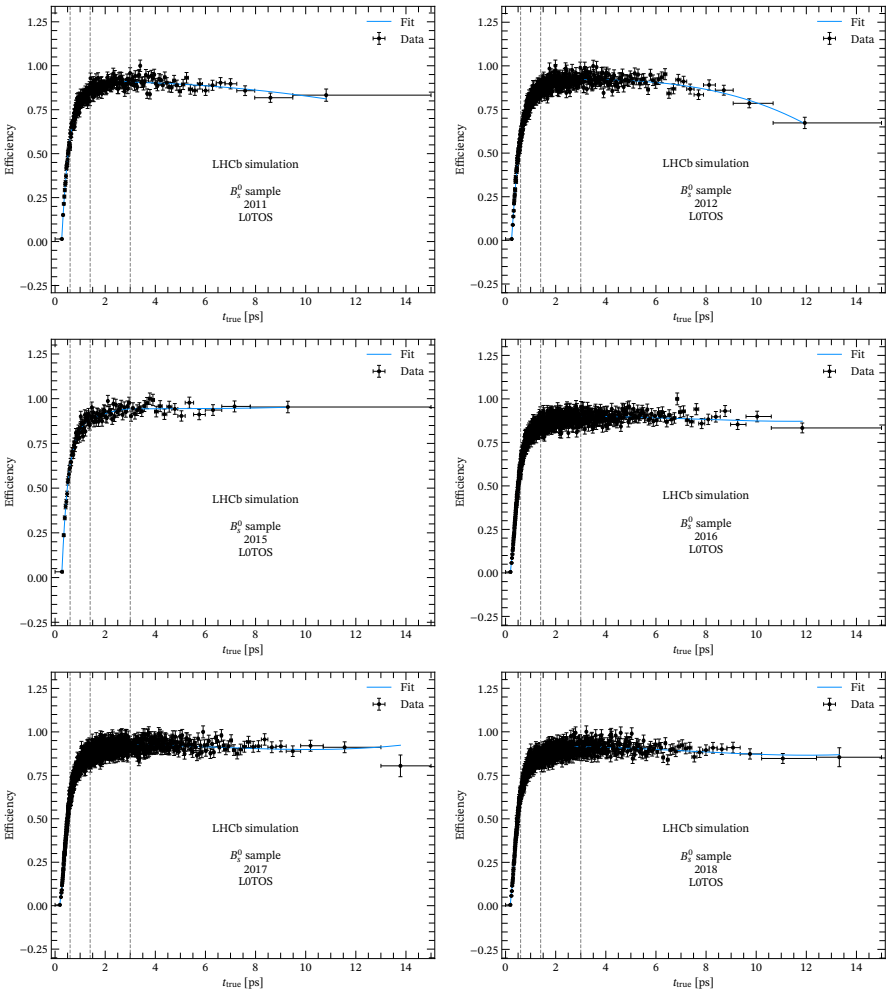

FIGURE C.1: Fits to time acceptance distributions evaluated on B_s^0 phase space MC for the `L0HadronTOS` sample.

C.2 SWEIGHTED FITS

As discussed in Sec. 3.2.5, the initial strategy considered a `sWeighted` fit. However, it was found that the shape of the $-2\log\mathcal{L}$ misbehaves when is `sWeighted`. This was discovered by accident when running likelihood scans for two different reasons. One was the search for multiple solutions in some of the amplitude coefficients. For each scan point, corresponding to a fixed value of the parameter, several fits are run and then the lowest value for the likelihood is recorded, otherwise large fluctuations are observed. Some of the results using the whole data sample (Run 1 and Run 2) and the B_s^0 weight are shown in Fig. C.3, where very strange shapes and abrupt jumps are observed. The other reason was that after switching to polar coordinates

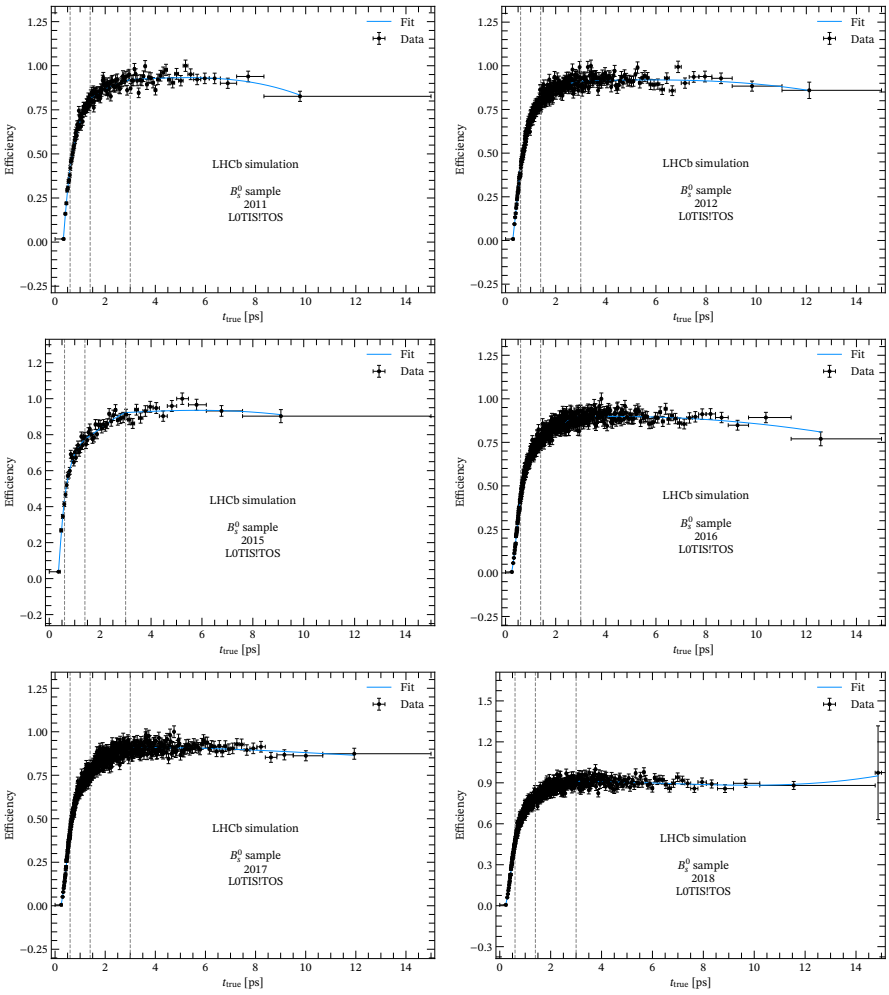

FIGURE C.2: Fits to time acceptance distributions evaluated on B_s^0 phase space MC for the `L0GlobalTIS & !L0HadronTOS` sample.

in the strong coefficients the observed value for the phase of the VS^- wave was very close to π, with the available statistical precision. Although every value is possible, special values such as 0 or π for these phases might indicate something is going wrong, since this has never been observed before in this channel (though all phases were referred to A_0). This prompted several intensive studies of this phase, for which an example using the B_s^0 weight is shown in Fig. C.4–left, but ended up being a coincidence, as shown in Fig. C.4–right where the weight was set to 1 for the whole sample (and therefore all backgrounds are absorbed by the signal). Additionally, the behaviour was very different between Run 1 and Run 2, as can be seen in Fig. C.5. It looks like the jump is caused by this sample.

Moreover, the B_d^0 weight showed that using `sWeights` is not compatible with

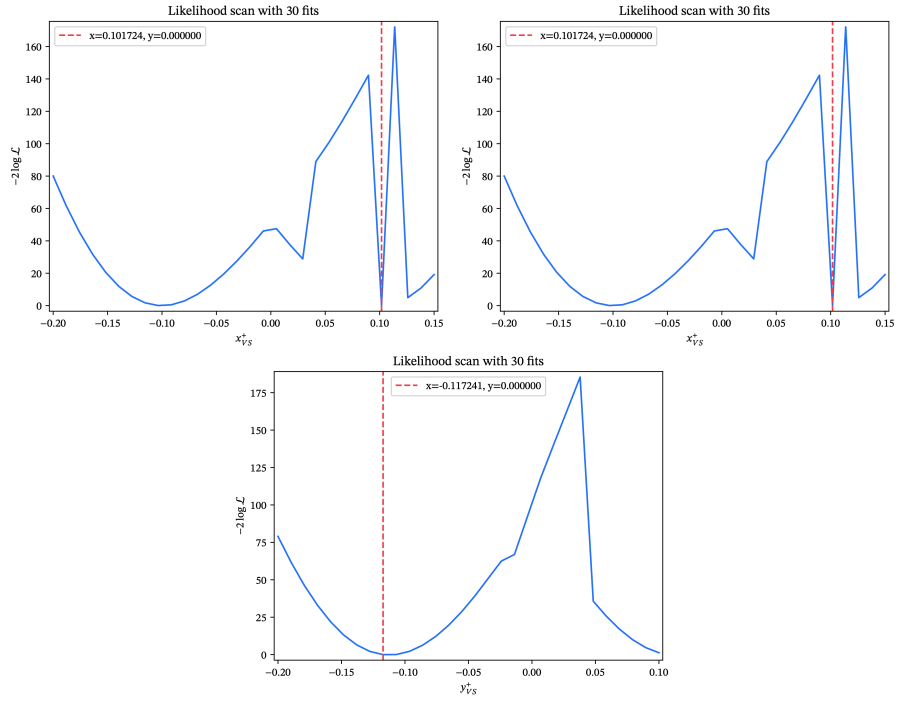

FIGURE C.3: B^0_s–sWeighted likelihood scans of some of the amplitude coefficients, which are parameterised in Cartesian coordinates, using all available data samples. In the notation used in these plots, x and y refers to real and imaginary parts, respectively. For the scans, the parameter space is divided in 30 points and 10 fits are run for each point.

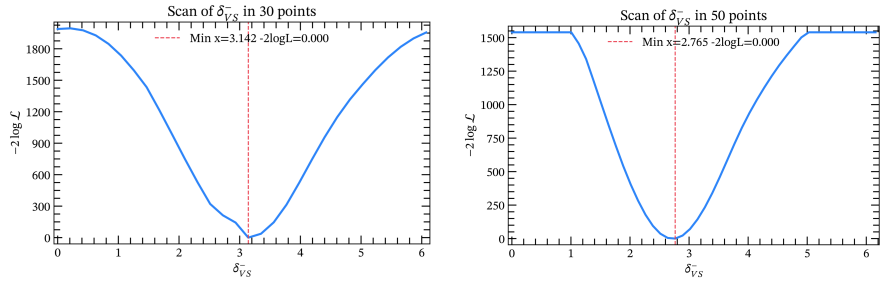

FIGURE C.4: B^0_s–sWeighted (left) and unweighted (right) likelihood scans of the phase difference of A^-_{VS} with respect to A^S_{VV}, using all available data samples. The parameter space is divided in 30 (50) points for the weighted (unweighted) scan, and 100 fits are run for each point.

Parameter	Fit value
α_{00}	0.0207 ± 0.0015
α_{01}	-0.1700 ± 0.0068
α_{02}	0.3617 ± 0.0089
α_{03}	-0.1498 ± 0.0035
α_{13}	0.0314 ± 0.0011
α_{23}	-0.0108 ± 0.0016
α_{33}	0.013 ± 0.013

TABLE C.11: Time efficiency coefficients for fit to 2017 `L0GlobalTIS` & `!L0HadronTOS` sample.

Parameter	Fit value
α_{00}	0.0082 ± 0.0014
α_{01}	-0.1088 ± 0.0064
α_{02}	0.2780 ± 0.0083
α_{03}	-0.1196 ± 0.0033
α_{13}	0.030 ± 0.001
α_{23}	-0.0131 ± 0.0015
α_{33}	0.036 ± 0.012

TABLE C.12: Time efficiency coefficients for fit to 2018 `L0GlobalTIS` & `!L0HadronTOS` sample.

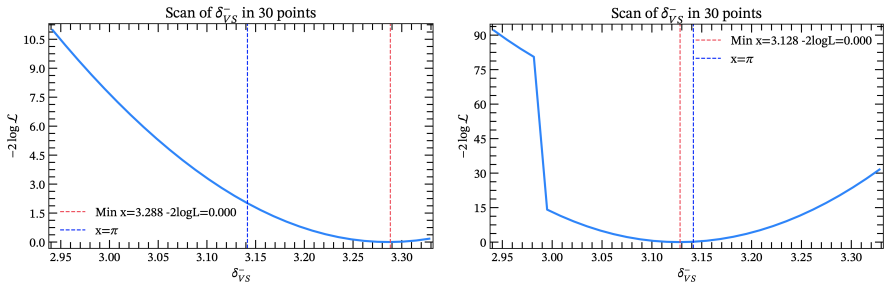

FIGURE C.5: B_s^0–`sWeighted` likelihood scans of the phase difference of A_{VS}^- with respect to A_{VV}^S, using the Run 1 (left) and Run 2 (right) data samples. The parameter space is divided in 30 points, and 100 fits are run for each point.

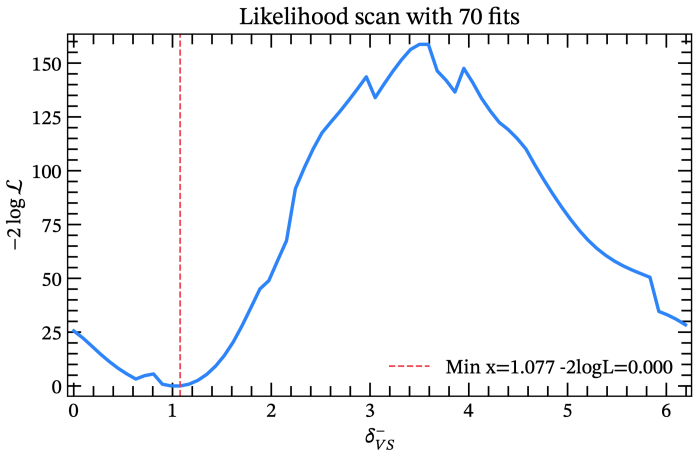

FIGURE C.6: B^0_d–sWeighted likelihood scan of the phase difference of A^{-}_{VS} w.r.t. A^{S}_{VV}, using all available data samples. The parameter space is divided in 70 points, and 300 fits are run for each point.

gradient-based optimisation methods for this analysis, as shown in Fig. C.6. This plot is obtained using all available statistical power and running 300 fits per scan point. It is not a matter of randomness, it is a real effect. The probabilities of falling in local minima are high enough to rule out this method.

C.3 YIELD STUDY FOR SIGNAL REGION SELECTION

All tables of the yields obtained for the B^0_s and B^0_d signal regions are found here, from Table C.13 to Table C.24, for the offset study running from $-10\,\mathrm{MeV}/c^2$ to $-35\,\mathrm{MeV}/c^2$.

C.4 RAW FIT RESULTS

The nominal results of the covariant fit are shown in this section, in Table C.25 for B^0_s and Table C.26 for B^0_d.

C.5 FIT BIAS STUDY

A set of 400 pseudoexperiments is generated from the nominal covariant fit results, each having the same statistics as in real data. These samples are re-fitted with the nominal model. Then, pulls are calculated for each fit parameter and shown in Fig. C.7 for B^0_s and Fig. C.8 for B^0_d.

Offset = −10 MeV/c^2		
Component	Yield in B_s^0 region	Yield in B_d^0 region
$B_s^0 \to K^{*0}\bar{K}^{*0}$	1179 (96%)	13 (5%)
$B_d^0 \to K^{*0}\bar{K}^{*0}$	2 (0%)	193 (70%)
$B_d^0 \to \rho^0 K^{*0}$	47 (4%)	25 (9%)
$B_d^0 \to \phi K^{*0}$	0 (0%)	36 (13%)
Combinatorial	4 (0%)	3 (1%)
Partially reconstructed	0 (0%)	5 (2%)
Retained signal prob.	98%	98%

TABLE C.13: Yields for the different components in both B_s^0 and B_d^0 signal regions for the Run 1 dataset and offset fixed to −10 MeV/c^2. The retained signal probability, which is shown in the last row, is the area under the curve that is retained due to the cuts of the signal region.

Offset = −15 MeV/c^2		
Component	Yield in B_s^0 region	Yield in B_d^0 region
$B_s^0 \to K^{*0}\bar{K}^{*0}$	1184 (95%)	9 (3%)
$B_d^0 \to K^{*0}\bar{K}^{*0}$	3 (0%)	192 (72%)
$B_d^0 \to \rho^0 K^{*0}$	51 (4%)	21 (8%)
$B_d^0 \to \phi K^{*0}$	0 (0%)	36 (14%)
Combinatorial	4 (0%)	3 (1%)
Partially reconstructed	0 (0%)	5 (2%)
Retained signal prob.	99%	97%

TABLE C.14: Yields for the different components in both B_s^0 and B_d^0 signal regions for the Run 1 dataset and offset fixed to −15 MeV/c^2. The retained signal probability, which is shown in the last row, is the area under the curve that is retained due to the cuts of the signal region.

Offset $= -20$ MeV/c^2		
Component	Yield in B_s^0 region	Yield in B_d^0 region
$B_s^0 \to K^{*0}\bar{K}^{*0}$	1186 (95%)	6 (2%)
$B_d^0 \to K^{*0}\bar{K}^{*0}$	5 (0%)	190 (74%)
$B_d^0 \to \rho^0 K^{*0}$	55 (4%)	17 (7%)
$B_d^0 \to \phi K^{*0}$	0 (0%)	36 (14%)
Combinatorial	4 (0%)	3 (1%)
Partially reconstructed	0 (0%)	5 (2%)
Retained signal prob.	99%	96%

TABLE C.15: Yields for the different components in both B_s^0 and B_d^0 signal regions for the Run 1 dataset and offset fixed to -20 MeV/c^2. The retained signal probability, which is shown in the last row, is the area under the curve that is retained due to the cuts of the signal region.

Offset $= -25$ MeV/c^2		
Component	Yield in B_s^0 region	Yield in B_d^0 region
$B_s^0 \to K^{*0}\bar{K}^{*0}$	1188 (94%)	4 (2%)
$B_d^0 \to K^{*0}\bar{K}^{*0}$	9 (1%)	186 (75%)
$B_d^0 \to \rho^0 K^{*0}$	59 (5%)	13 (5%)
$B_d^0 \to \phi K^{*0}$	0 (0%)	36 (14%)
Combinatorial	4 (0%)	3 (1%)
Partially reconstructed	0 (0%)	5 (2%)
Retained signal prob.	99%	95%

TABLE C.16: Yields for the different components in both B_s^0 and B_d^0 signal regions for the Run 1 dataset and offset fixed to -25 MeV/c^2. The retained signal probability, which is shown in the last row, is the area under the curve that is retained due to the cuts of the signal region.

Offset $= -30$ MeV/c^2		
Component	Yield in B_s^0 region	Yield in B_d^0 region
$B_s^0 \to K^{*0}\bar{K}^{*0}$	1189 (94%)	3 (1%)
$B_d^0 \to K^{*0}\bar{K}^{*0}$	14 (1%)	181 (76%)
$B_d^0 \to \rho^0 K^{*0}$	62 (5%)	10 (4%)
$B_d^0 \to \phi K^{*0}$	0 (0%)	36 (15%)
Combinatorial	4 (0%)	3 (1%)
Partially reconstructed	0 (0%)	5 (2%)
Retained signal prob.	99%	92%

TABLE C.17: Yields for the different components in both B_s^0 and B_d^0 signal regions for the Run 1 dataset and offset fixed to -30 MeV/c^2. The retained signal probability, which is shown in the last row, is the area under the curve that is retained due to the cuts of the signal region.

Offset $= -35$ MeV/c^2		
Component	Yield in B_s^0 region	Yield in B_d^0 region
$B_s^0 \to K^{*0}\bar{K}^{*0}$	1190 (93%)	3 (1%)
$B_d^0 \to K^{*0}\bar{K}^{*0}$	23 (2%)	172 (76%)
$B_d^0 \to \rho^0 K^{*0}$	64 (5%)	8 (3%)
$B_d^0 \to \phi K^{*0}$	0 (0%)	36 (16%)
Combinatorial	5 (0%)	2 (1%)
Partially reconstructed	0 (0%)	5 (2%)
Retained signal prob.	99%	87%

TABLE C.18: Yields for the different components in both B_s^0 and B_d^0 signal regions for the Run 1 dataset and offset fixed to -35 MeV/c^2. The retained signal probability, which is shown in the last row, is the area under the curve that is retained due to the cuts of the signal region.

Offset = −10 MeV/c^2		
Component	Yield in B_s^0 region	Yield in B_d^0 region
$B_s^0 \to K^{*0}\bar{K}^{*0}$	7707 (94%)	114 (6%)
$B_d^0 \to K^{*0}\bar{K}^{*0}$	13 (0%)	1168 (60%)
$B_d^0 \to \rho^0 K^{*0}$	204 (2%)	129 (7%)
$B_d^0 \to \phi K^{*0}$	1 (0%)	78 (4%)
Combinatorial	313 (4%)	435 (22%)
Partially reconstructed	1 (0%)	15 (1%)
Retained signal prob.	98%	97%

TABLE C.19: Yields for the different components in both B_s^0 and B_d^0 signal regions for the Run 2 dataset and offset fixed to −10 MeV/c^2. The retained signal probability, which is shown in the last row, is the area under the curve that is retained due to the cuts of the signal region.

Offset = −15 MeV/c^2		
Component	Yield in B_s^0 region	Yield in B_d^0 region
$B_s^0 \to K^{*0}\bar{K}^{*0}$	7739 (93%)	81 (4%)
$B_d^0 \to K^{*0}\bar{K}^{*0}$	19 (0%)	1161 (63%)
$B_d^0 \to \rho^0 K^{*0}$	227 (3%)	106 (6%)
$B_d^0 \to \phi K^{*0}$	1 (0%)	78 (4%)
Combinatorial	333 (4%)	415 (22%)
Partially reconstructed	1 (0%)	15 (1%)
Retained signal prob.	98%	97%

TABLE C.20: Yields for the different components in both B_s^0 and B_d^0 signal regions for the Run 2 dataset and offset fixed to −15 MeV/c^2. The retained signal probability, which is shown in the last row, is the area under the curve that is retained due to the cuts of the signal region.

Offset $= -20$ MeV/c^2		
Component	Yield in B_s^0 region	Yield in B_d^0 region
$B_s^0 \to K^{*0}\bar{K}^{*0}$	7761 (92%)	59 (3%)
$B_d^0 \to K^{*0}\bar{K}^{*0}$	30 (0%)	1150 (65%)
$B_d^0 \to \rho^0 K^{*0}$	249 (3%)	85 (5%)
$B_d^0 \to \phi K^{*0}$	2 (0%)	77 (4%)
Combinatorial	354 (4%)	394 (22%)
Partially reconstructed	1 (0%)	15 (1%)
Retained signal prob.	99%	96%

TABLE C.21: Yields for the different components in both B_s^0 and B_d^0 signal regions for the Run 2 dataset and offset fixed to -20 MeV/c^2. The retained signal probability, which is shown in the last row, is the area under the curve that is retained due to the cuts of the signal region.

Offset $= -25$ MeV/c^2		
Component	Yield in B_s^0 region	Yield in B_d^0 region
$B_s^0 \to K^{*0}\bar{K}^{*0}$	7776 (92%)	44 (3%)
$B_d^0 \to K^{*0}\bar{K}^{*0}$	50 (1%)	1130 (66%)
$B_d^0 \to \rho^0 K^{*0}$	267 (3%)	66 (4%)
$B_d^0 \to \phi K^{*0}$	2 (0%)	77 (5%)
Combinatorial	375 (4%)	373 (22%)
Partially reconstructed	1 (0%)	15 (1%)
Retained signal prob.	99%	94%

TABLE C.22: Yields for the different components in both B_s^0 and B_d^0 signal regions for the Run 2 dataset and offset fixed to -25 MeV/c^2. The retained signal probability, which is shown in the last row, is the area under the curve that is retained due to the cuts of the signal region.

Offset $= -30$ MeV/c^2		
Component	Yield in B_s^0 region	Yield in B_d^0 region
$B_s^0 \to K^{*0}\bar{K}^{*0}$	7787 (91%)	34 (2%)
$B_d^0 \to K^{*0}\bar{K}^{*0}$	84 (1%)	1096 (68%)
$B_d^0 \to \rho^0 K^{*0}$	283 (3%)	51 (3%)
$B_d^0 \to \phi K^{*0}$	2 (0%)	76 (5%)
Combinatorial	397 (5%)	351 (22%)
Partially reconstructed	1 (0%)	15 (1%)
Retained signal prob.	99%	91%

TABLE C.23: Yields for the different components in both B_s^0 and B_d^0 signal regions for the Run 2 dataset and offset fixed to -30 MeV/c^2. The retained signal probability, which is shown in the last row, is the area under the curve that is retained due to the cuts of the signal region.

Offset $= -35$ MeV/c^2		
Component	Yield in B_s^0 region	Yield in B_d^0 region
$B_s^0 \to K^{*0}\bar{K}^{*0}$	7794 (90%)	26 (2%)
$B_d^0 \to K^{*0}\bar{K}^{*0}$	139 (2%)	1042 (68%)
$B_d^0 \to \rho^0 K^{*0}$	295 (3%)	38 (3%)
$B_d^0 \to \phi K^{*0}$	3 (0%)	76 (5%)
Combinatorial	419 (5%)	329 (22%)
Partially reconstructed	1 (0%)	15 (1%)
Retained signal prob.	99%	87%

TABLE C.24: Yields for the different components in both B_s^0 and B_d^0 signal regions for the Run 2 dataset and offset fixed to -35 MeV/c^2. The retained signal probability, which is shown in the last row, is the area under the curve that is retained due to the cuts of the signal region.

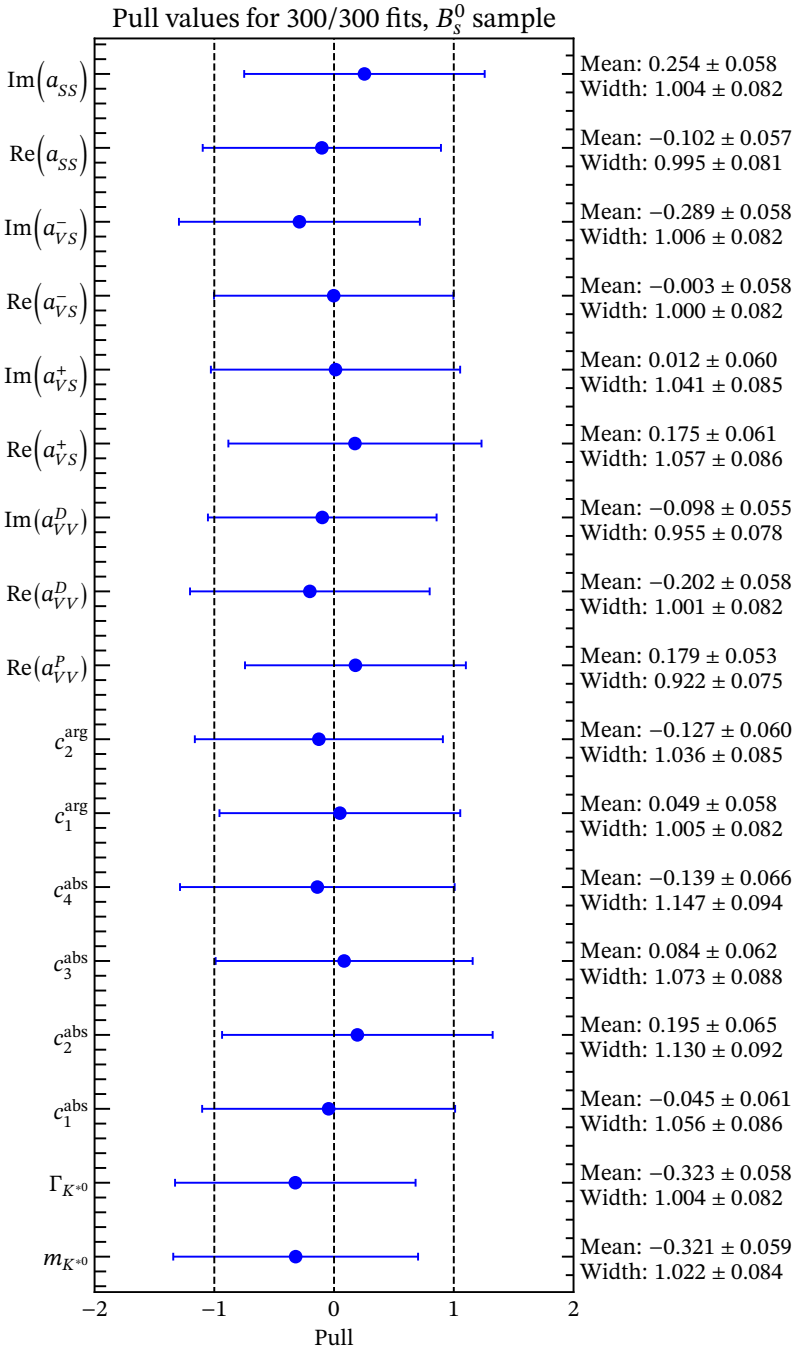

FIGURE C.7: forward-backward asymmetry for the nominal covariant amplitude fit to the B_s^0 sample.

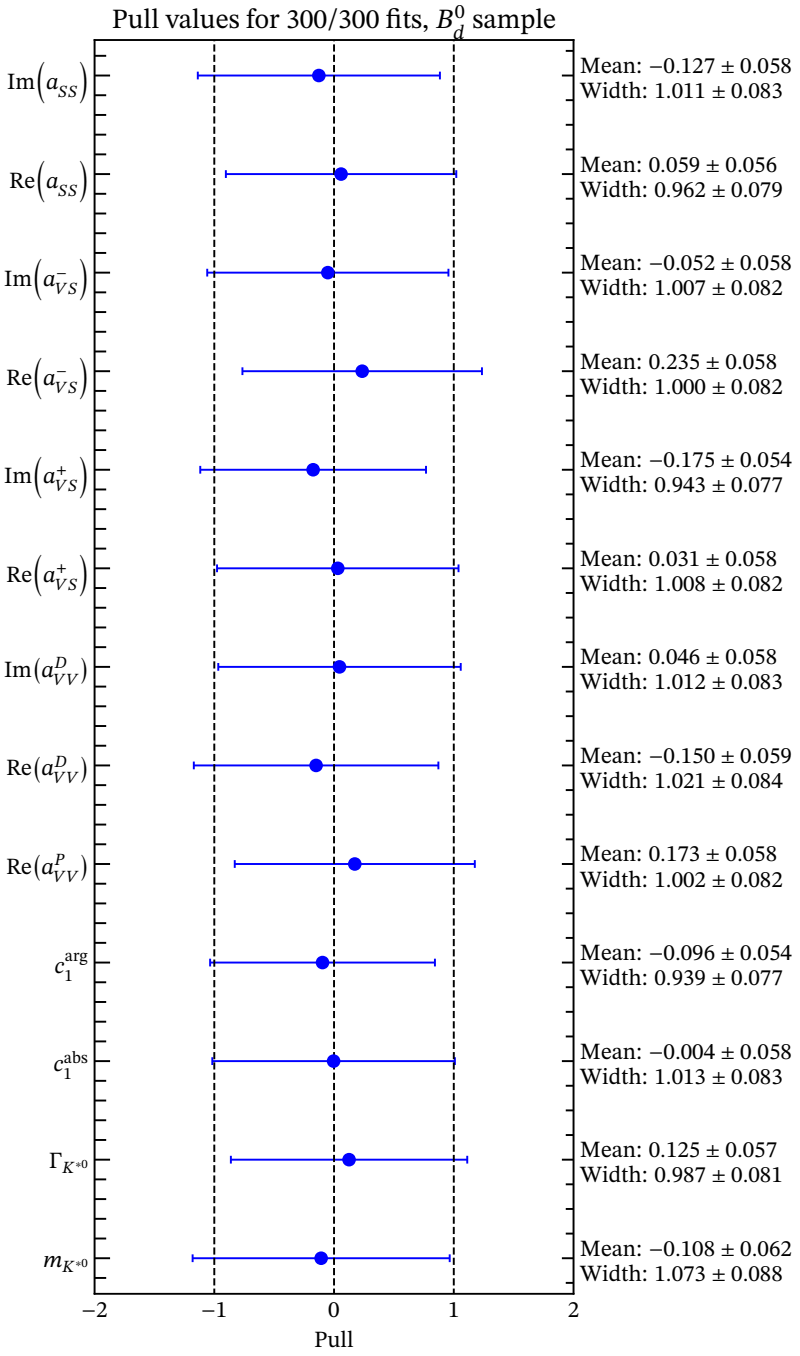

FIGURE C.8: Raw forward-backward asymmetry for the nominal covariant amplitude fit to the B_d^0 sample.

Parameter	Fit value	Parameter	Fit value
$m_{K^{*0}}$	$898.9 \pm 0.3\,\mathrm{MeV}/c^2$	$\Gamma_{K^{*0}}$	$44.8 \pm 0.8\,\mathrm{MeV}/c^2$
c_1^{abs}	0.59 ± 0.04	c_2^{abs}	0.33 ± 0.08
c_3^{abs}	0.21 ± 0.06	c_4^{abs}	-0.33 ± 0.09
c_1^{arg}	-0.35 ± 0.09	c_2^{arg}	0.59 ± 0.12
$\mathrm{Re}(a_{VV}^S)$	1 (fixed)	$\mathrm{Im}(a_{VV}^S)$	0 (fixed)
$\mathrm{Re}(a_{VV}^P)$	1.599 ± 0.046	$\mathrm{Im}(a_{VV}^P)$	0 (fixed)
$\mathrm{Re}(a_{VV}^D)$	9.395 ± 0.062	$\mathrm{Im}(a_{VV}^D)$	-0.664 ± 0.058
$\mathrm{Re}\left(a_{VS}^+\right)$	-0.069 ± 0.010	$\mathrm{Im}\left(a_{VS}^+\right)$	-0.1084 ± 0.0085
$\mathrm{Re}\left(a_{VS}^-\right)$	-0.419 ± 0.012	$\mathrm{Im}\left(a_{VS}^-\right)$	-0.047 ± 0.017
$\mathrm{Re}\left(a_{SS}\right)$	0.00783 ± 0.00033	$\mathrm{Im}\left(a_{SS}\right)$	0.00018 ± 0.00050
$\left\|a_{VV}^S\right\|$	1 (fixed)	δ_{VV}^S	0 (fixed)
$\left\|a_{VV}^P\right\|$	1.599 ± 0.046	δ_{VV}^P	0 (fixed)
$\left\|a_{VV}^D\right\|$	9.419 ± 0.062	δ_{VV}^D	-0.071 ± 0.006 rad
$\left\|a_{VS}^+\right\|$	0.1286 ± 0.0090	δ_{VS}^+	-2.14 ± 0.08 rad
$\left\|a_{VS}^-\right\|$	0.422 ± 0.013	δ_{VS}^-	-3.03 ± 0.44 rad
$\left\|a_{SS}\right\|$	0.00783 ± 0.00033	δ_{SS}	0.02 ± 0.06 rad

TABLE C.25: Raw covariant parameters obtained for the B_s^0 baseline fit. The strong coefficients are given in Cartesian coordinates, as implemented in the fit, and in polar coordinates, which are derived from the former.

Parameter	Fit value	Parameter	Fit value
$m_{K^{*0}}$	$897.5 \pm 0.7\,\mathrm{MeV}/c^2$	$\Gamma_{K^{*0}}$	$45.7 \pm 1.7\,\mathrm{MeV}/c^2$
c_1^{abs}	1.012 ± 0.003	c_1^{arg}	1.68 ± 0.14
$\mathrm{Re}\left(a_{VV}^{S}\right)$	1 (fixed)	$\mathrm{Im}\left(a_{VV}^{S}\right)$	0 (fixed)
$\mathrm{Re}\left(a_{VV}^{P}\right)$	1.55 ± 0.13	$\mathrm{Im}\left(a_{VV}^{P}\right)$	0 (fixed)
$\mathrm{Re}\left(a_{VV}^{D}\right)$	7.31 ± 0.23	$\mathrm{Im}\left(a_{VV}^{D}\right)$	-1.41 ± 0.37
$\mathrm{Re}\left(a_{VS}^{+}\right)$	0.010 ± 0.033	$\mathrm{Im}\left(a_{VS}^{+}\right)$	-0.224 ± 0.027
$\mathrm{Re}\left(a_{VS}^{-}\right)$	0.291 ± 0.027	$\mathrm{Im}\left(a_{VS}^{-}\right)$	-0.122 ± 0.039
$\mathrm{Re}\left(a_{SS}\right)$	0.00286 ± 0.00082	$\mathrm{Im}\left(a_{SS}\right)$	-0.00382 ± 0.00085
$\left\lvert a_{VV}^{S}\right\rvert$	1 (fixed)	δ_{VV}^{S}	0 (fixed)
$\left\lvert a_{VV}^{P}\right\rvert$	1.55 ± 0.13	δ_{VV}^{P}	0 (fixed)
$\left\lvert a_{VV}^{D}\right\rvert$	7.44 ± 0.24	δ_{VV}^{D}	$-0.19 \pm 0.05\,\mathrm{rad}$
$\left\lvert a_{VS}^{+}\right\rvert$	0.224 ± 0.027	δ_{VS}^{+}	$-1.5 \pm 0.2\,\mathrm{rad}$
$\left\lvert a_{VS}^{-}\right\rvert$	0.316 ± 0.029	δ_{VS}^{-}	$-0.4 \pm 0.1\,\mathrm{rad}$
$\left\lvert a_{SS}\right\rvert$	0.00477 ± 0.00084	δ_{SS}	$-0.9 \pm 0.2\,\mathrm{rad}$

TABLE C.26: Raw covariant parameters obtained for the B_d^0 baseline fit. The strong coefficients are given in Cartesian coordinates, as implemented in the fit, and in polar coordinates, which are derived from the former.

ACKNOWLEDGMENTS

I would like to thank everyone who helped to make this project possible.

First of all thanks to my supervisors, Bernardo and Jeremy, who introduced me to this topic before I started my Master's degree and supported me in my research over the last five years. None of this work would have been possible without their guidance and expertise in the field. Thanks to Diego and Veronika, for their help when I needed it and for the opportunities they gave me to grow as a scientist. Thanks to the people of the KstKst team for their assistance and insightful ideas, and especially to Matthew with whom I have worked closely and who has provided enormous help along the way.

Thanks to Julián for his help and guidance, not only in particle physics but also in daily life matters in foreign countries. Thanks to Marta for her closeness, for making me feel at home in Milano, and for pointing me to the *brodo*. Thanks to David *sexta-feira* for his help and support and, more importantly, for his memes.

Quero agradecer tamén aos meus compañeiros do mellor despacho no que se investigaron todo tipo de temas, tanto científicos como non científicos, ata o nivel máis fundamental: o 26. O que empezou como unha secta xirando ao redor dun (*do*) editor de código acabou sendo unha estupenda relación de amizade cos que compartir os bos e malos momentos do doutoramento. Grazas tanto á subdivisión *old guard*, Adrián, Alexandre, Gabi, Gonzalo e Marcos, como á nova, Alberto, Andrés, Moncho, Pablo e Saúl. Quero facer mención especial a Alberto e Saúl, cos que compartín vida máis aló da investigación e dos bares, e á sub-subdivisión *Uviéu*, Moncho e Pablo, cos que teño pasado moitas aventuras e desventuras e dos que sempre é agradable escoitar unha opinión. Agradecer tamén ao balón e á *cañita de fons*, non vos esqueceremos.

Grazas ao resto de xente do IGFAE, e especialmente a Vero e Ale por eses primeiros anos post-pandémicos. A Alberto, Manu e Saúl polas quentadas astronómicas en PdB/RdC. A Carlos, Emilio, Eloi e Erlantz pola carallada, axuda e manutención en St. Genis/Genève. Grazas tamén aos demáis amigos que me acompañaron estes anos. Aos de física, a.k.a. os aguatequers, aos astrólogos, Aitor e David, e aos de sempre, Bieito, Iván e Roi.

Por último, quero agradecer á miña familia, en especial a meus pais, meus tíos e meus avós, polo seu apoio incondicional en todas as miñas decisións. E a Cris, por aguantarme, escoitarme e apoiarme durante este longo camiño.

A time-integrated and flavour-untagged amplitude analysis is performed to four-body decays of the neutral mesons Bs and Bd, using data collected by the LHCb experiment in Run 1 and Run 2. Observables to be measured include the investigation of an anomaly in the polarisation of vector resonances when they arise from decays of Bs and Bd mesons, which seems to point to a break in the universality of the gluonic couplings to the different quark generations in the Standard Model.

The project includes several innovations, such as the description of partial waves in a covariant framework, the parameterisation of the efficiency across phase space using a GPU-accelerated KDE technique, and a new model for the strong scalar component present in data.